



## Simulation of a Network Circulars Patch Antennas for the Wireless Communications

Adnane Latif

Cadi Ayyad University, Marrakech, Morocco  
E-mail: [a.latif@uca.ma](mailto:a.latif@uca.ma), [latif\\_adnane@yahoo.fr](mailto:latif_adnane@yahoo.fr)

### Abstract:

The objective of this paper is the design a linear network of 3 circular patch antennas and the study its radiation diagrams which is formed by multiplying a diagram of a single patch antenna by the factor of a linear network in the two planes E and H. In fact, the change excitation phase  $\beta$  which is considered as very important parameter in the patch antenna network design is adjusted while all the other factors are fixed, thus, the different radiation diagrams of the network in two planes are obtained.

**Keywords:** Patch antenna, Array antennas, Wireless communications, Radiation Diagramm, Simulation of antenna network.

### 1. Introduction

The use of a single patch antenna is often insufficient to meet the constraints imposed by radiation. Specific characteristics such as high gain or a main lobe comply can usually be obtained only by grouping several sources radiating to form a system called "network". A network of antennas consists of a group of identical sources. The spacing of the sources called "network step" which is a basic parameter in the design of a network patch antenna.

These sources are fed by a splitter (distribution system) which defines a law of supply in module and in phase. The major advantage of the network of antennas is the ability to create a radiation beam adjustable and shaped in all directions according to the law of supply and the number of elements. The group in the simplest network is obtained with a number of identical sources that are deduced from each other by translation to form linear networks and plans.

For the linear network, we seek to conform the radiation diagram only in the plane containing the sources. In a modification of the radiation diagram over the entire hemisphere, the elementary sources must be arranged in the two-dimensional network.

In an antennas network, the energy is distributed between various sources radiating in a given law: the radiation characteristics of the system depends on the radiation diagram of the base element, the coefficients of excitation in amplitude and in phase on each source and the distance between elements.

These networks consist of circular radiating elements connected in chain with each other by short cut of microstrip line. The supply network of the antenna will aim to bring energy to the various sources according to the law of weighting (balance). The simplest technique is to feed the radiating elements by microstrip lines.

## 2. Radiation Diagram of a Network of Circular Patch Antenna

A linear network with uniform spacing is illustrated in Figure 1.1 where  $N$  isotropic radiating elements are excited by a plane wave generated from source situated in a far field. The field radiated by an antenna network is the vector summation of fields radiated by each element. By properly selecting the spacing between the elements and power law, we can change the directivity and the radiation direction of the network.

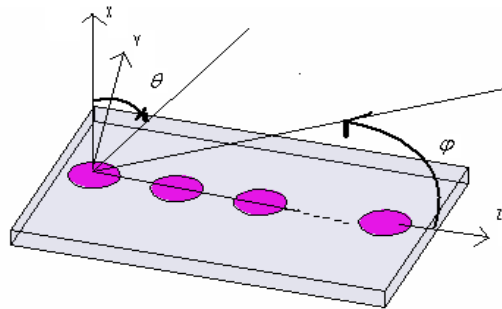


Figure 1 .Network of  $N$  circular patch aligned along the  $z$  axis

$\theta$ : The angle between the  $z$  axis is the direction of radiation

$\phi$ : The angle between the projection of the direction of radiation and  $x$ -axis

$\beta$ : The phase of current between two successive elements in the network

## 3. Simulation of a Linear Network Formed by Three Circular Patch Antennas

The simulation of linear network will be made on two softwares MATLAB and PCAAD. The used parameters of this antenna are:

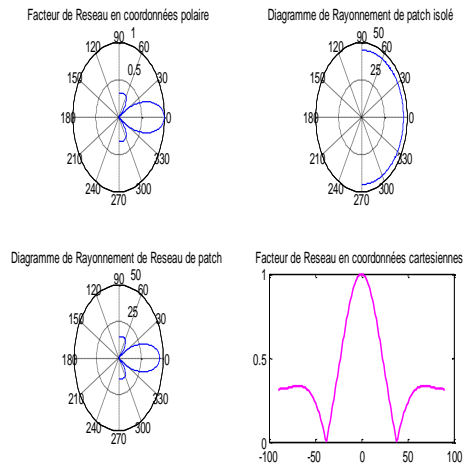
The ray of the patch	$a = 3\text{cm}$
The dielectric constant	$\epsilon_r = 2.33$
The thickness dielectric	$h = 0.159\text{cm}$
Frequency of resonance	$f_r = 2.3\text{ GHz}$
Length of wave	$\lambda = 3\text{cm}$

For this network the number of patches is  $N = 3$  is the spacing between the elements is fixed at  $7\text{cm}$ . The results of the program developed in MATLAB are mounted in the figures 2 and 3, in which visualizes the network factor of the 3 antennas patch polar coordinates and Cartesian coordinates, and the radiation diagram of a single circular patch antenna and the radiation diagram of the network of 3 circular patch antennas.

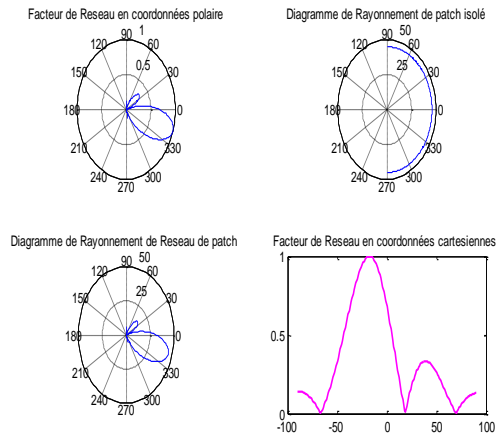


### 3.1 In the E Plane( $\varphi=0$ )

For different values of phase network  $\beta$ , it visualizes the diagram of radiation observed in the network plan E. The result is shown on the figures below:



$$\beta = 0,360^\circ$$



$$\beta = 45^\circ$$



Facteur de Réseau en coordonnées polaire

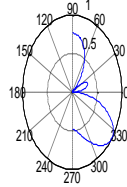


Diagramme de Rayonnement de patch isolé

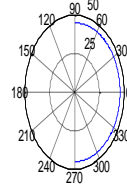
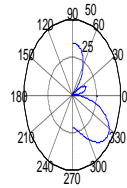
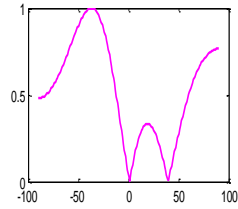


Diagramme de Rayonnement de Réseau de patch



Facteur de Réseau en coordonnées cartésiennes



$$\beta = 90^\circ$$

Facteur de Réseau en coordonnées polaire

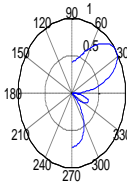


Diagramme de Rayonnement de patch isolé

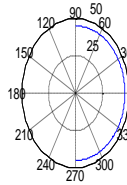
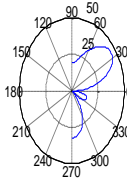
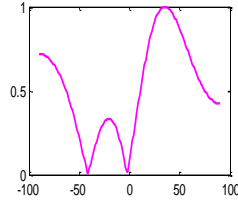


Diagramme de Rayonnement de Réseau de patch



Facteur de Réseau en coordonnées cartésiennes



$$\beta = 130^\circ$$

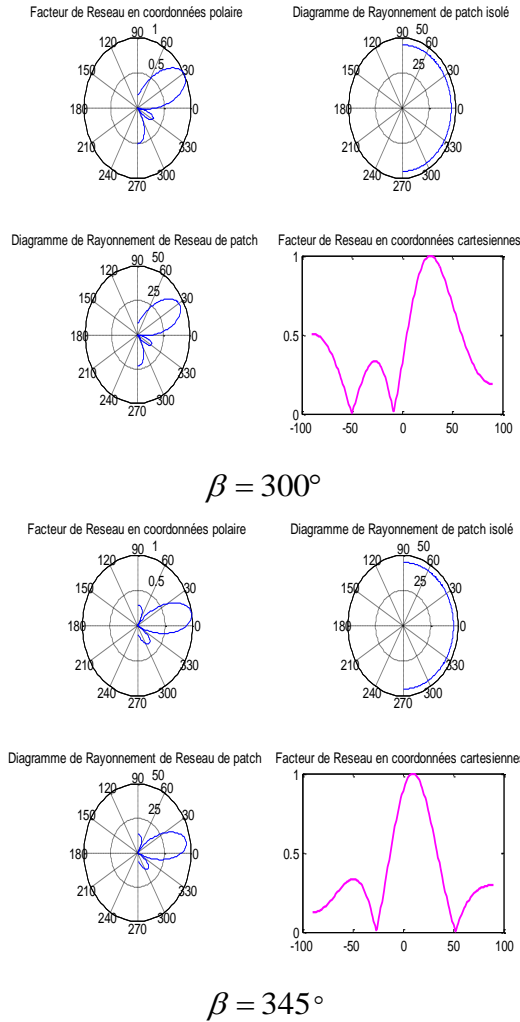


Figure 2. Diagram of radiation linear network with  $N = 3$  in the E plane (MATLAB)

For the results we have found for the same values of phase network  $\beta$  using the software PCAAD are shown below Fig.3:

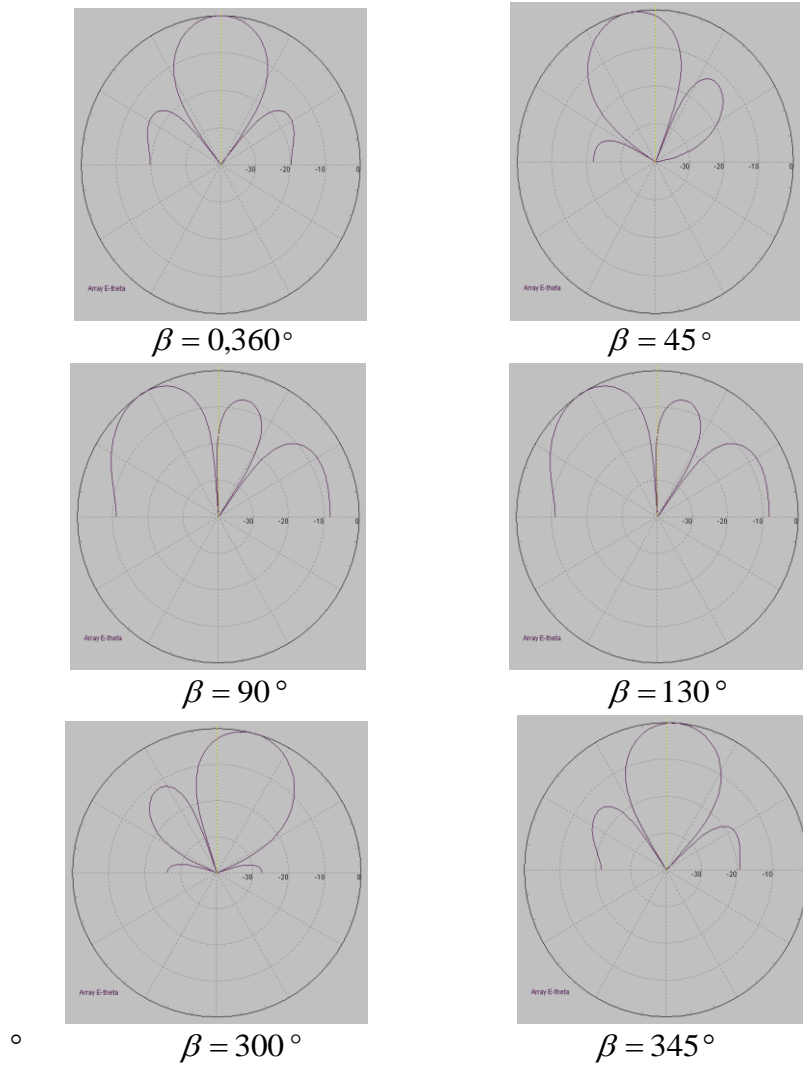
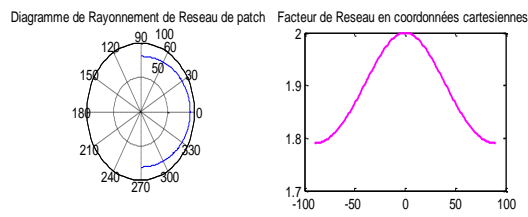
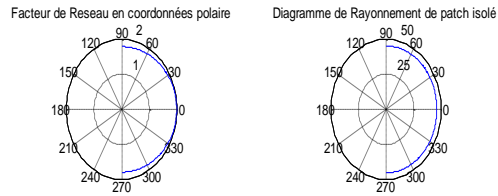


Figure 3. Diagram of radiation linear network with  $N = 3$  in the E plane (PCAAD)

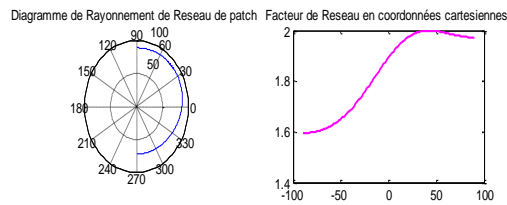
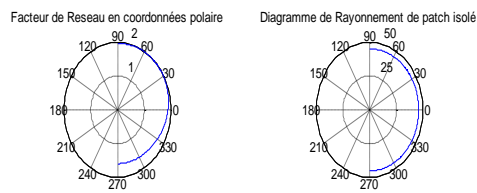
One observes from these figures that the simulation results for a linear array of 3 three antennas circular patch found by our program developed in MATLAB and the results found by the software PCAAD are almost the same

### 3.2 In the H Plane ( $\varphi=90^\circ$ )

For different values of phase network  $\beta$ , it visualizes the diagram of radiation observed in the network plan H. The result is shown on the figures below:



$$\beta = 0,360^\circ$$



$$\beta = 45^\circ$$



Facteur de Réseau en coordonnées polaire

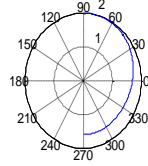


Diagramme de Rayonnement de patch isolé

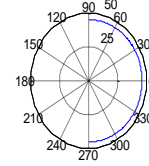
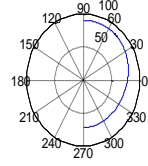
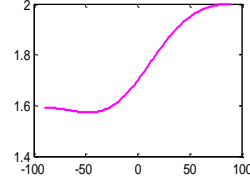


Diagramme de Rayonnement de Réseau de patch



Facteur de Réseau en coordonnées cartésiennes



$$\beta = 90^\circ$$

Facteur de Réseau en coordonnées polaire

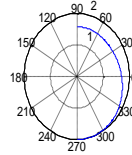


Diagramme de Rayonnement de patch isolé

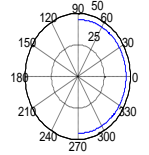
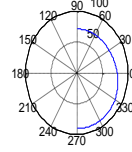
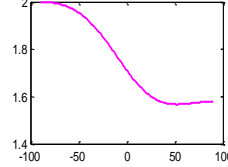


Diagramme de Rayonnement de Réseau de patch

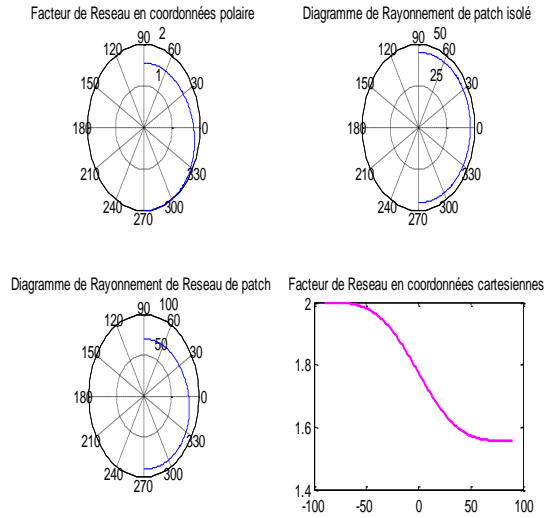


Facteur de Réseau en coordonnées cartésiennes

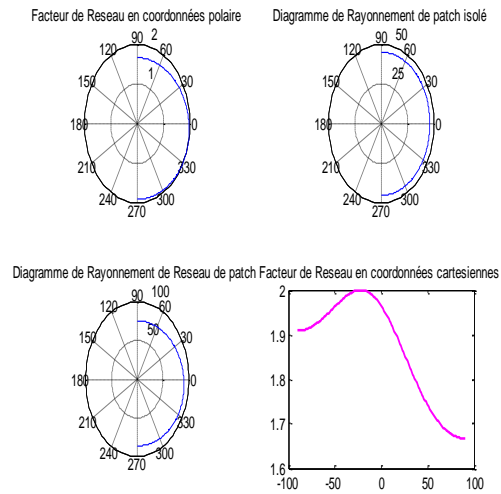


$$\beta = 130^\circ$$





$$\beta = 300^\circ$$



$$\beta = 345^\circ$$

Figure 4. Diagram of radiation linear network with  $N = 3$  in the E plane (MATLAB)

For the results we have found for the same values of phase network  $\beta$  using the software PCAAD are shown below Figure 5:

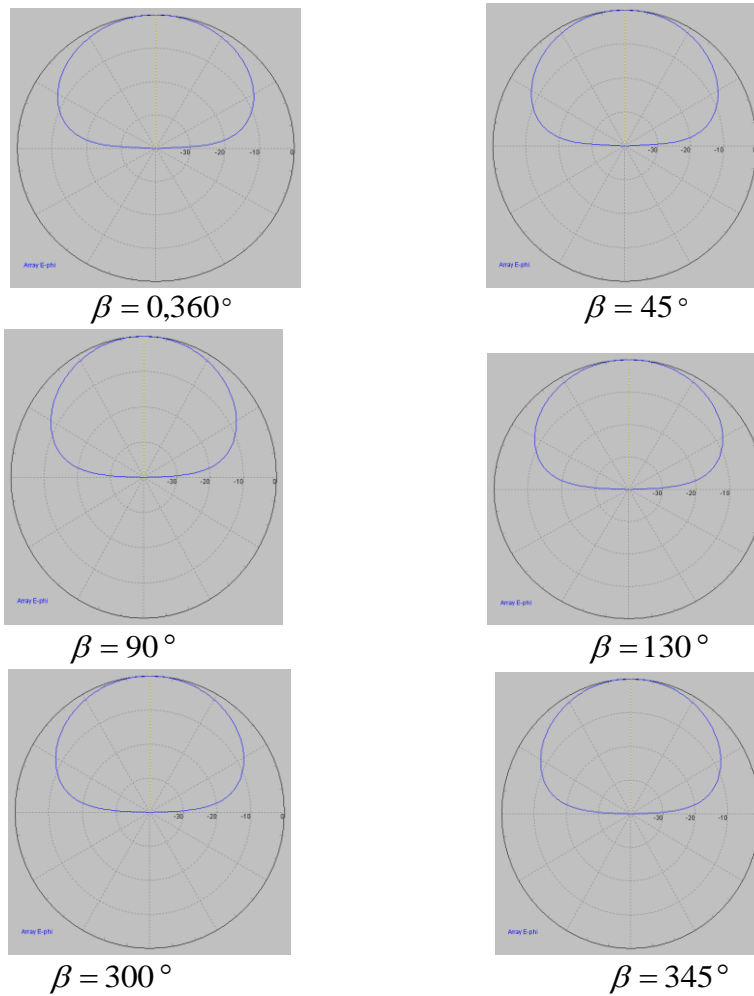


Figure 5. Diagram of radiation linear network with  $N = 3$  in the H plane (PCAAD)

The simulation results for the linear network of 3 circular patch antennas in H plan our program developed in MATLAB and the results found by the PCAAD software are almost the same.



#### 4. Conclusions

**In E plane:** According to the result given by the software PCAAD and those found by MATLAB: We observe that the phase variation of excitation influences only on the directivity pattern. a good directivity of the radiation diagram is observed for  $\beta = 0$  (12.0 dB). We observe also an increase in modulus of the deflection angle is obtained by varying the phase excitation from  $\beta = 0^0$  (where the deflection angle equal to  $0^0$ ) to  $\beta = 130^0$  (or deviation angle equal to  $33^0$ ) after it decreases from  $\beta = 300^0$  (where deflection angle equal to  $15^0$ ). On the main lobe amplitude is reduced by increasing the phase excitation from  $\beta = 0^0$  to  $\beta = 130^0$  at the same time the amplitude of side lobes increases, but the main lobe amplitude starts has increased from  $\beta = 300^0$ .

**In H plane:** According to the result given by the software MATLAB and PCAAD: It is observed that an increase in excitation phase has an effect only on the directivity of the network diagram, on the other hand the width of 3dB beam remains constant during this phase variation of excitation ( $76.7^\circ$ ) as well as deflection angle of main lobe is always zero ( $0^\circ$ ). In order the directivity remains constant for the value  $\beta = 0^\circ, 45^\circ$  (its value equal to 12dB), begins to decline after increasing the excitation phase ( $\beta = 90^\circ$  for the value of directivity is 11.8dB, for  $\beta = 130^\circ$  No value of directivity is 11.1dB), after beginning to increase for  $\beta = 300^\circ$  (11.9dB), and  $\beta = 345^\circ$  (12dB).

#### References

1. D.M. Pozar and D.H.Schaubert, *New York, IEEE Press*, 1995.
2. K.Huie, *Thesis submitted to the faculty of the Virginia Polytechnic Institute and State University in partial fulfilment of the requirements for the degree of Master of Science in Electrical Engineering, January, 2002*
3. C.A. Balanis, 2<sup>nd</sup> Edition, *John Wiley & Son, Inc 1997*.
4. F.T. Ulaby, *Prentice Hall, 1999*.
5. A. Constantine - Balanis, 3<sup>rd</sup> Edition *John Wiley & Sons Inc 2005*.
6. W.F. Richards, Van Nostrand Reinhold Co., *New York, 1989*.
7. J.R. James and P.S. Hall, *I.E.E. Electromagnetic Waves Series 28, Peter Peregrinus LTD 1989*
8. Constantine A. Balanis, *John Wiley & Son, Inc, 2008*.
9. E.H Newman, and P.Tylythan, *1981*.
10. R.F. Harrington, *New York, 1968*.





## Resonances and patterns within the kINPen-MED atmospheric pressure plasma jet

Victor J Law, A Chebbi, F T O'Neill and D P Dowling

School of Mechanical and Materials Engineering, University College Dublin,  
Belfield, Dublin 4, Ireland.

E-mail: [victor.law@ucd.ie](mailto:victor.law@ucd.ie)

**Abstract:** The kINPen MED atmospheric pressure plasma jet is now undergoing clinical studies that are designed to investigate its suitability as a device for use in plasma medicine treatments. This paper describes dimensionless studies of the synchronizing oscillatory gas flow through the nozzle followed by electro-acoustic measurements coupled with the discharge photo emission. The plasma jet operates in the burst mode of 2.5 KHz (duty cycle = 50%), within a neutral argon Strouhal number of 0.14 to 0.09 and Reynolds number of 3570 to 5370. In this mode the jet acts like a plasma actuator with an anisotropic far field noise pattern that is composed of radiated noise centered at 17.5 kHz; +20 dB, and the expanding visible plasma plume and cooled gas recombine along the jet axial flow (1-2 kHz peak that diminishes at a rate of  $-1.7 \text{ dB.kHz}^{-1}$ ).

**Keywords:** atmospheric pressure plasma jet, plasma medicine, gas flow dynamics, acoustic resonance.

### 1. Introduction

Cold atmospheric plasmas have shown enormous potential in Plasma Medicine for surface sterilization, for wound healing, for blood coagulation and in cancer treatment [1, 2]. This paper is focused on an atmospheric pressure plasma jet (APPJ) system called kINPen MED, which is being targeted for use in Plasma Medicine [3]. However to keep the medical device safe and easy to handle the fixed repetitive pulsed power source is used and the gas supply is limited to argon flow rate of 4-6 standard liters per minute (SLM). To help underpin the ongoing clinical trials this paper presents dimensionless analysis of the jet along with the jets electro-acoustic and polychromic emission.

It has been shown that within the cold limit of ions that the speed of sound can be approximated to the neutral gas molecular temperature [4, 5], see equation 1. Here the fluctuation in the speed of neutrals and ions generate both sound waves and an oscillatory electric field, both of which contribute to the overall local sound pressure level. In the plasma production zone the difference between neutrals and ions, is that the latter (and electrons) absorb electrical energy from the electrical electro-magnetic field as the plasma gas expands and loses electrical energy, when the electrical power is turned off. Whereas the neutral gas gains energy thereby allowing radicals and metastable species to be formed from the electron-neutral energy transfer per second in the plasma volume and so the electron-neutral reaction acts as an acoustic source. In The kinPen09 [3] and the Med version an argon plasmas comprises  $\text{Ar}^+$  ions and hydroxyl (OH) radicals.



$$c_{sound} = \sqrt{\frac{\gamma RT_{gas}}{M}} \quad (1)$$

Where  $S_{ound}$  is the speed of sound in the gas medium,  $R$  is the gas constant ( $8.314 \text{ J K}^{-1} \text{ mol}^{-1}$ ),  $T_{gas}$  is the gas temperature in Kelvin,  $M$  is the molar mass in kilograms per mole of the gas (argon =  $0.03994 \text{ kg mole}^{-1}$ ), and  $\gamma$  adiabatic constant of the gas (argon and helium = 1.6).

The Strouhal number ( $St$ ) [11, 12] of the kINPen MED was compared with 5 other commercial APPJs: the kINPen09 [3], the PVA Tepla air Plasma-Pen<sup>TM</sup> [6], the air-PlasmaTreat<sup>TM</sup> [7, 8], and two helium linear jets [9, 10]. The  $St$  is a dimension-less measure as defined in equation (1), where  $f_d$  is the drive frequency, and  $D$  is the length scale of the nozzle diameter and  $v$  is the gas (in this argon) velocity. Thus for  $St \sim 1$ , the drive frequency is synchronized through the nozzle orifice to the velocity of the gas exiting the nozzle. For low  $St$ , the quasi steady state of the gas dominates the oscillation. And at high values of  $St$  the viscosity of the gas dominates fluid flow (“fluid plug”). Thus  $St$  acts as a comparator when the jets have similar values of  $D$ . Of the 5 plasma jets studied only the kINPen MED has a compound nozzle (double open-end ceramic tube within a steel-steel outer body with a central electrically driven wire electrode. The linear jets are configured as double open-ended glass tubes.

$$St = \frac{f_d D}{v} \quad (2)$$

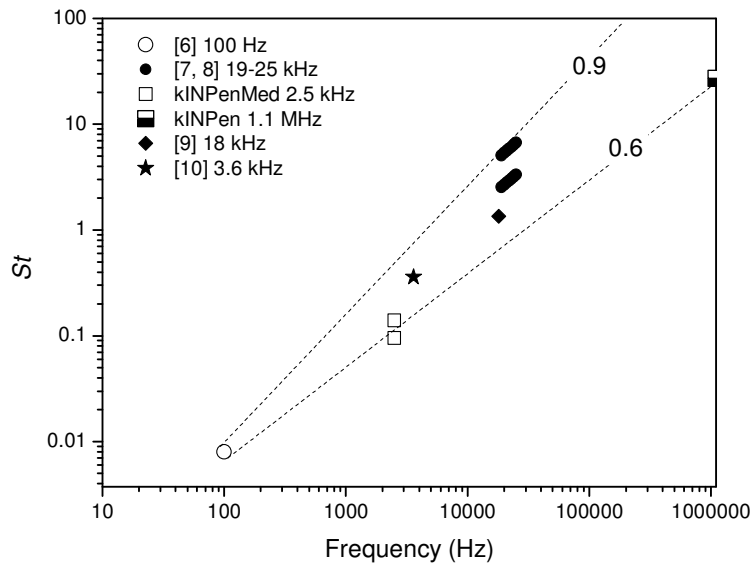


Fig 1:  $St$  numbers for 6 air and helium APPJs as a function of  $f_d$  and  $D$ : 1.7 to 4 mm.



Figure 1 show the log-log graph relationship between  $St$  and  $f_d$  for the 6 APPJs, which have a  $D$  value between 1.7 to 4 mm. There are two observations of note within the plot. First, the gas type (air, argon and helium) are normalized through their gas velocities (equation 2) and thus there is gas correlation; Second using the Plasma-Pen as references point two interpolation lines are used to map the upper and lower boundary of the data points with the kINPen forming the lower rate boundary ( $\exp^{0.6}$ ) and the PlasmaTreat<sup>TM</sup> forming the upper rate boundary ( $\exp^{0.9}$ ). From these observations and an examination of equation 1, it can be deduced that the rates corresponded to the length scale  $D$ .

## 2. Experiments

As with aircraft jet engines, low frequency driven APPJs produce two types of acoustic emission patterns within the overall radiated noise emission. The acoustic noise patterns originate from the jet nozzle and from axially aligned jet turbulence. To measure the aircraft jet engine noise patterns the jet engine is normally placed within an anechoic chamber and both near-field microphones and a linear array of far field microphones in are used to measure the noise pattern [11, 12]. In contrast the acoustic noise of APPJs has been measured with a single microphone in some preferred position with the result that the boundary between the two acoustic production sources is ill-defined. Furthermore there has no report of an APPJ being employed as plasma actuator, where the  $St$  is an indicator of the acoustic spectrum is attenuation.

For the purpose of this study, a single condenser mini-microphone is used to measure both the electro-magnetic emission and acoustic emission from kINPen MED which uses argon as the ionization gas. The microphone acts as both an E-probe and a sound energy sensor, where both measured quantities are distance dependent. In ordered to capture the nozzle Omni-directional sound energy and sound energy being propagated along the discharge axis, acoustic far field measurement is scaled to a distance of 20 x the jet diameter between 90° perpendicular to the jet exit nozzle to 180° where the microphone is facing the gas flow. From a process control perspective 90° position has a number of advantages; (a) the microphone measures the radiated plasma sound energy emanating from the nozzle; (b) the microphone does not mechanically interfere with the movement of the jet over the treatment surface and; (c) the 90° allows capture of the deflected sound energy from the treated surface to be used as a nozzle to surface height indicator [7, 8], thus by inference the treated surface temperature. In addition to the electro-acoustic measurements, a photodiode (PD) is used to evaluate the jets time-dependent polychromic emission and acoustic pattern is correlated with “overspill” [13] of the plasma jet on treated Polyethylene-terephthalate (PET) polymer using water contact angle measurements. Finally the electro-acoustic and PD measurements were digitally processed using LabVIEW software and correlated as previously described [7, 14].

## 3. Results

### 3.1. Electro-acoustic analysis

Figure 2 shows the typical electro-acoustic from the APPJ at a microphone angle  $90^\circ$  with the plasma turned-off, and on, with the argon flowing at 5 SLM (nozzle velocity =  $36.78 \text{ m.s}^{-1}$ ) in both cases. For the plasma conditions the first feature of note is that the  $f_d$  (2.5 kHz) has Q-factor ( $f/\Delta f \sim 100$ ) followed by its harmonics: here observed up to 20 kHz. The second feature of note is that 5<sup>th</sup> and 6<sup>th</sup> harmonic of the  $f_d$  straddle the broad asymmetric structure ( $f/\Delta f \sim 35$ ) centered on 17.5 kHz. Turning off the electric power to the nozzle not only removes the drive frequency component but also reduces the broadband structure at 17.5 kHz by 20 dB. An independent measurement using a sound pressure level meter (YF-20) indicates this reduction equates a drop of 4 to 6 dB in the audible range. A photo of the argon discharge and ceramic nozzle is shown as an insert in figure 2.

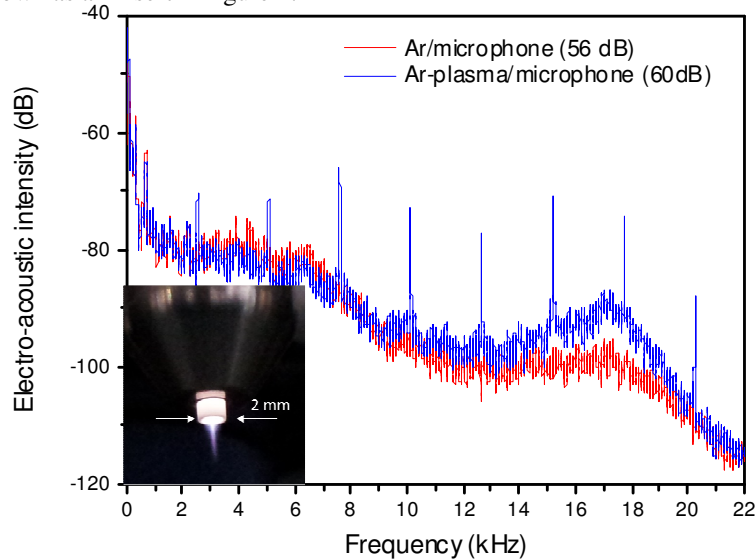


Fig 2: Argon plasma formed using the kINPen MED along with the associated plasma acoustic response.

Using the 2 electro-acoustic traces and the knowledge of the nozzle geometry it possible to model the acoustic response ( $f_n$ ) and its overtones ( $f_n$ ) of the nozzle of as either an open-ended gas column (equation 3) or as a Helmholtz resonator (equation 4) [7]. At room temperature ( $20^\circ\text{C}$ ) the speed of sound ( $c$ ) in argon and air equates to  $323$  to  $346 \text{ m.s}^{-1}$ .

$$f_n = \frac{nc}{m(L + 0.6r)} \quad 3$$



$$f_o = \frac{c}{2\pi} \sqrt{\frac{A}{LV_o}} \quad 4$$

In equations 3:  $L$  is the length of the ceramic tube beyond the drive electrode (0.01 m), and  $r$  is the tube radius end-correction (0.0005 m). Lastly  $m$  denotes the resonate mode within the tube (1 = fullwave and 2 = halfwave resonant mode etc...) and  $n$  is the overtone number. Whereas in equation 4:  $A$  is the area of nozzle, and  $V_o$  is the volume of the nozzle.

Equations 3 yields a value range of  $f_n$  between 16.5 to 17.7 kHz for a halfwave resonant mode ( $m=2$ ). This calculation agrees well with the broad acoustic peak at 17.5 kHz which is enhanced in amplitude by onset of the plasma. By comparison equation 4 yields a  $f_o$  range between 2.57 and 2.75 kHz which is a factor of 5-6 times lower than the observed broadband response. This comparison of the two mathematical models suggests that the open ended nozzle model provides the most representative and robust visualization of the nozzle acoustic response.

### 3.2. Photodiode analysis

Using a Hamamatsu MPPC photo diode (PD) with a rise time of 10 ns and a spectral range between 320 and 900 nm we now turn to the examining the effect of 2.5 kHz pulse drive frequency on the time-dependent plasma polychromic emission. Discharge emission was collected via a fibre optic and collimating lens focused at the plasma discharge at 1 mm downstream of the nozzle exit.

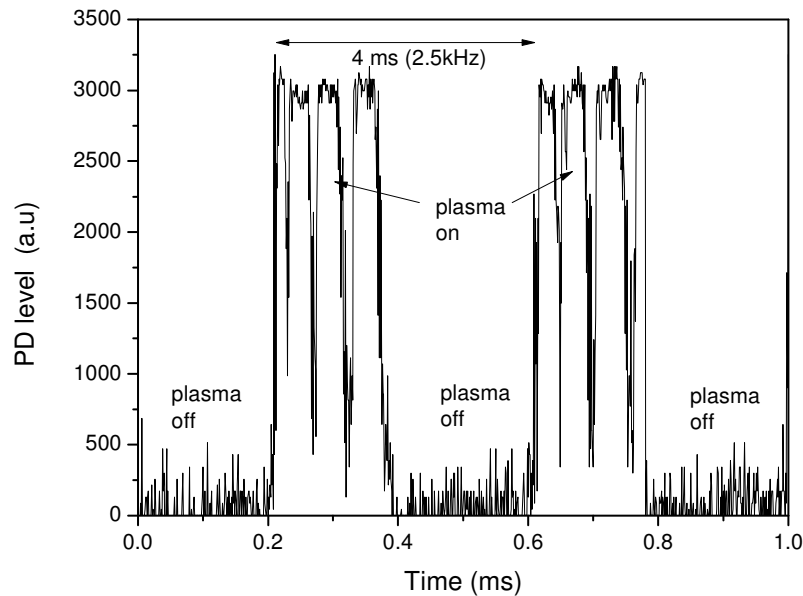


Fig 3: kINPen MED polychromic emission at 1 mm from nozzle.

The measurement results for 5 SLM of argon is shown in figure 3. Here it can be seen that the polychromatic emission has a 2.5 kHz pulse; with a periodic duty cycle of 50% response (duration of the emission to the total period of a repeat signal) with an envelope rise- and fall-time of microseconds. Within the emission envelope four dips in emission can be also seen. The flat top of the pulse enveloped appears to represent the DBD self-current-limiting characteristic that prevents spark formation within the reactor tube. That is, the plasma is extinguished unless the magnitude of the applied voltage continuously increases. For limited range investigated, varying the argon flow rate from 4 to 6 SLM does not alter the height of the envelope or the emission between the envelopes; nor does it alter the drive (2.5 kHz) or harmonics frequencies.

### 3.3. Anisotropic acoustic emission pattern

With the drive frequency and its harmonics isolated from the acoustic emission response, the next sets of measurements are aimed to delineate the radiated sound energy from the jet turbulence sound energy. The delineation is achieved by recording electro-acoustic measurement between 90 and 180° (in-line) in steps of 10° degrees. The results of these measurements are shown in figure 4. Here it can be seen that the sound radiation energy does not alter significantly from 90 to 160°. The 170° measurement however increases in amplitude and exhibits a number of additional resonances peaks. In the case of the 180° the measurement acoustic noise amplitude has increased above the electrical emission resulting in the loss of electrical information. In this position, resonance information is also lost and noise amplitude becomes inversely proportional to frequency at a rate of  $-1.7 \text{ dB.kHz}^{-1}$ . The peak at 1.5 kHz varies by  $\pm 1 \text{ kHz}$  due to the jet gas flow dynamics over the microphone body.

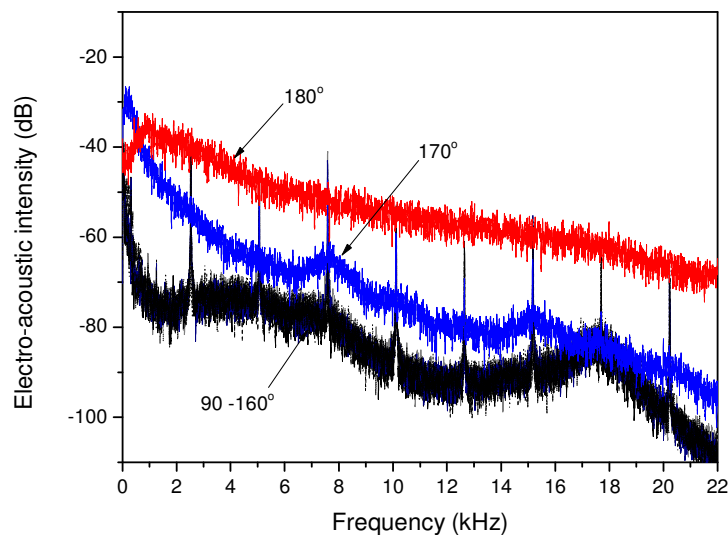


Fig 4: 90 to 180° far field measurements.

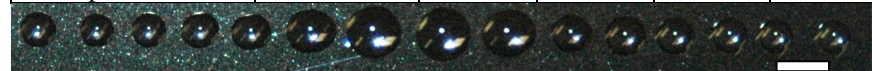
The measurements reveal that the neutral argon flow forms an expanding cone

with internal angle of 10 degrees to the jet axis. This is in contrast to the 10 mm in length visible pencil-like plasma plume, see figure 2 picture insert.

An investigation was carried out to determine the correlation between the area / diameter treated by the kINPen MED gas plume and the water contact angle of the PET placed under the jet. Measurements were obtained 1 hour after plasma treatment as a function of the gap distance (5, 10, and 15 mm) between the jet and the PET substrate. The contact angle obtained for the untreated PET was 85°. Table 1 shows the results of the measurements and the computed internal cone angle for the treatment gap. This limited gap distance analysis reveals that the treated diameter is much larger than the pencil-like diameter of the plasma plume (~ 2 mm), with an overspill ratio (plasma/treatment diameter) of 8 to 10. The treatment becomes less effective with gap distance. Correlating these results with the acoustic mapping it appears that the argon gas passing through the plasma zone and entering the expanding argon cone has a chemical ‘spillover effect’ on the surface properties of PET thus possibly differentiating between ion exposure and radicals and metastable treatment mechanisms.

Table 1: PET WCA as a function gap distance. The photograph demonstrates the increased water droplet width after the plasma treatment (2 mm scale bar).

	No Plasma	5 mm	10 mm	15 mm	20 mm
WCA	85°	45°	59°	70°	
Overspill diameter	N/A	16 mm	20 mm	18 mm	
Treatment angle	N/A	160	90	62	
Overspill ratio	N/A	8	10	9	



#### 4. Conclusion

This paper examined the kINPen MED argon flow dynamics using dimensionless analysis, electro-acoustic and photodiode measurements. The  $St$  analysis of the plasma jet (with 5 other APPJs with similar nozzle diameters ( $D = 1.7$  to  $4$  mm)) reveal similar nozzle oscillating flow mechanisms that produce  $St$  values that are proportionally to  $\text{Hz}^{(0.6 \text{ to } 0.9)}$  between 100 Hz to 1.1 MHz where the rate is defined by the scale length of the nozzle. Electro-acoustic and polychromic emission measurements reveal the APPJ nozzle is operating with a low  $St < 0.5$  for an argon flow of 4-6 SLM. The nozzle resonant frequency can be modeled as a closed end column where resonance amplitude undergoes amplification when plasma is applied. One possible mechanism for this acoustic amplification may be due to electric winds [4] that are generated by the positive and negative edges of the drive pulse and which are synchronized to the neutral argon velocity to produce an enhanced molecular vibration at the nozzle exit. The plasma jet therefore appears to act like a dielectric barrier discharge plasma actuator. Electro-acoustic far field pattern measurements reveal an anisotropic acoustic emission which is composed of sound radiation energy from the nozzle and the axially aligned gas jet pressure. It has been shown that gas passing



through the visible plasma zone and entering the expanding argon cone alters the hydrophobicity of PET when placed cone region.

### Acknowledgement

This work is partially supported by Science Foundation Ireland Grant 08/SRCI1411 and the Enterprise Ireland Commercialisation Programme.

### References

1. M. G. Kong, G. Kroesen, G. Morfill, T. Nosenko, T. Shimizu T, J. van Dijk and J. L. Zimmermann. Plasma medicine: an introductory review, *New J. Phys.* 11, 115012, 2009.
2. M. Vandamme, E. Robert, S. Pesnel, S. Barbosa, S. Dozias, J. Sobilo, S. Lerondel, A. Le Pape, J. M. Pouvesle. Antitumor Effect of Plasma Treatment on U87 Glioma Xenografts: Preliminary Results, *Plasma Processes and Polymers* 7(3-4), 264-273, 2010.
3. K.-D. Weltmann, E. Kindel, R. Brandenburg, C. Meyer, R. Bussiahn, C. Wilke, and T. von Woedtke. Atmospheric pressure plasma jet for medical therapy: plasma parameters and risk estimation. *Contrib. Plasma Phys.* 49(9), 631-640, 2009.
4. M. Fitaire and T. D. Mantei. Some experimental results on acoustic wave propagation in a plasma. *Physics of Fluids.* 15(3), 464-469, 1972.
5. V. J. Law, C. E. Nwankire, D. P. Dowling, and S Daniels. Acoustic emission within an atmospheric helium discharge jet. *Chaos Theory: Modeling, Simulation and Applications.* 255-264. Eds: C. H. Skiadas, I. Dimotikalis and C. Skiadas. (Publisher: World Scientific 2011).
6. V. J. Law. Interdisciplinary Symposium on Complex Systems, 11-13<sup>th</sup> September Prague, Czech Republic 2013.
7. V. J. Law, F. T. O'Neill and D. P. Dowling. Evaluation of the sensitivity of electro-acoustic measurements for process monitoring and control of an atmospheric pressure plasma jet system. *PSST.* 20(3), 035024, 2011.
8. V. J. Law, F. T. O'Neill, D. P. Dowling Atmospheric pressure plasma acoustic moment analysis. *Complex systems* 20(2), 181-193 (Complex systems, Publications, Inc 2011).
9. J. L. Walsh, F. Iza, N. B. Janson, V. J. Law and M. G. Kong. Three distinct modes in a cold atmospheric pressure plasma jet. *J, Phys, D: Appl, Phys* 43(7), 075201 (14pp), 2010.
10. N. O'Connor and S. Daniels. Passive acoustic diagnostics of an atmospheric pressure linear field jet including analysis in the time-frequency domain. *J Appl. Phys* 110, 013308, 2011.
11. V. F. Kopiev, V. A. Bityurin, I. V. Belyaev, S. M. Godin, M. Yu. Zaitsev, A. I. Klimov, V. A. Kopiev, I. A. Moralev, and N. N. Ostrikov. Jet noise control using the dielectric barrier discharge plasma actuators. *Acoustical Physics.* 58(4), 434-441, 2012.
12. M. Samimy, J.-H. Kim, J. Kastner, I. Adamovich, and Y. Utkin. Active Control of a Mach 0.9 Jet for noise mitigation using plasma actuators. *AIAA J.* 45( 4), 890-901, 2007.
13. J. F. Kolb, A. M. Mattson, C. M. Edelbute, X. H. Muhammad and L. C. Heller. Cold dc-operated air plasma jet for the inactivation of infectious microorganisms. *IEEE PS* 40(11), 3007-3026. 2012.
14. V. J. Law, M. Donegan and B. Creaven. Acoustic metrology: from atmospheric plasma to solo percussive irish dance. *CMSIM Journal.* 4, 663-670, 2012.



## Bursting Dynamics of Pancreatic $\beta$ -cells with Electrical and Chemical Couplings

Qishao Lu <sup>1,\*</sup>, Pan Meng<sup>2</sup>

- 1) Department of Dynamics and Control, Beihang University, Beijing 100191, China
- 2) Department of Mathematics, Guangdong College of Pharmacy, Guangzhou 510224, China

\* E-mail: [qishaolu@hotmail.com](mailto:qishaolu@hotmail.com)

**Abstract:** Pancreatic  $\beta$ -cells located in islets of Langerhans in the pancreas are responsible for the synthesis and secretion of insulin in response to a glucose challenge. Bursting electrical activity is also important for pancreatic  $\beta$ -cells as it leads to oscillations in the intracellular free calcium concentration, which in turn leads to oscillations in insulin secretion. The minimal model for a single pancreatic  $\beta$ -cell was extended by introducing one additional ionic current was considered. The synchronization behaviors of two identical pancreatic  $\beta$ -cells connected by electrical (gap-junction) and chemical (synaptic) couplings, respectively, are investigated based on bifurcation analysis by extending the fast-slow dynamics from single cell to coupled cells. Various firing patterns are produced in coupled cells under proper coupling strength when a single cell exhibits tonic spiking or square-wave bursting individually, no matter the cells are connected by electrical or chemical coupling. The above analysis of bursting types and the transition may provide us with better insight into understanding the role of coupling in the dynamic behaviors of pancreatic beta-cells.

**Keywords:** Pancreatic  $\beta$ -cell, Coupling, Calcium oscillation, Bursting, Synchronization, Transition.

### 1. Introduction

Pancreatic  $\beta$ -cells located in islets of Langerhans in the pancreas are responsible for the synthesis and secretion of insulin in response to a glucose challenge. Like nerve and endocrine cells, pancreatic  $\beta$ -cells are electrically excitable and the electrical firing patterns typically come in the form of bursting, characterized by an active phase of fast spiking followed by a quiescent phase without spiking. It is well-known that bursting can be exhibited by a wide range of nerve and endocrine cells and is likely one of the most important and distinctive firing patterns in dynamic behaviors. Bursting electrical activity is also important for pancreatic  $\beta$ -cells as it leads to oscillations in the intracellular free  $\text{Ca}^{2+}$  concentration, which in turn leads to oscillations in insulin secretion.

### 2. The Model

The minimal model for a single pancreatic  $\beta$ -cell was extended by introducing one additional ionic current, namely, the ATP-sensitive  $\text{K}^+$  current  $I_{K(ATP)}$ . This modified model described by the following equations:

$$\tau \frac{dv}{dt} = -I_{Ca}(v) - I_k(v, n) - I_s(v, s) - I_{K(ATP)}(v, p) \quad (1)$$

$$\tau \frac{dn}{dt} = \lambda[n_\infty(v) - n] \quad (2)$$

$$\tau_s \frac{ds}{dt} = s_\infty(v) - s \quad (3)$$

Three variables in this system are the membrane potential ( $v$ ), the delayed rectifier activation ( $n$ ), and a very slow variable  $s$  which has been postulated to be the intracellular  $\text{Ca}^{2+}$ . Depending on the value of the parameter  $g_s$ , the system either undergoes a spiking solution or generates bursting oscillations, both of which can be explained by using fast-slow dynamics analysis.

### 3. Main Results

The synchronization behaviors of two identical pancreatic  $\beta$ -cells connected by electrical (gap-junction) and chemical (synaptic) couplings, respectively, are investigated based on bifurcation analysis and numerical simulations by extending the fast-slow dynamics from single cell to coupled cells. Various firing patterns are produced in coupled cells under proper coupling strength when a single cell exhibits tonic spiking or square-wave bursting



individually, no matter the cells are connected by electrical or chemical coupling.

For two electrically coupled cells, when an isolated single cell exhibits continuous spiking individually, with the coupling strength increasing, there exists synchronization transition path including at least four different synchronous states, including two kinds of bursting synchronization with totally different bifurcation structure of the fast subsystem, and another two synchronous spiking regimes with continuous anti-phase and in-phase rhythms, respectively.

For two chemically coupled cells, two spiking cells can transit to bursting under weak chemical coupling condition. Moreover, an interesting inverse period-adding bursting sequence is found when the isolated cell exhibits square-wave bursting. In addition, the two-cell model with proper chemical coupling strength can produce the “fold/Hopf” type of bursting.

In summary, on the one hand, cells could burst synchronously for both weak electrical and chemical couplings when an isolated single cell exhibits tonic spiking itself. Especially, for electrically coupled cells, under the variation of the coupling strength there exist complex transition processes of synchronous firing patterns, including the anti-phase continuous spiking, then another type of bursting, and finally the in-phase tonic spiking. On the other hand, it is shown that when an individual cell exhibit square-wave bursting, modest coupling strength can make the electrically coupled system generate “fold/Hopf” bursting via “fold/fold” hysteresis loop while the chemically coupled system generate “fold/Hopf” bursting. Especially, chemically coupled bursters could exhibit inverse period-adding bursting sequence.

#### 4. Conclusion

The above analysis of bursting types and the transition may provide us with better insight into understanding the role of coupling in the dynamic behaviors of pancreatic  $\beta$ -cells. It is noticed that these results are obtained when the slow variables of two cells are very near and could be taken as the bifurcation parameter. In fact, this assumption is valid mostly except the inverse period-adding bursting sequence occurring in the chemically coupled situation. The latter case is worthy of further research.

#### References

1. F. Ashcroft and P. Rorsman. Electrophysiology of the pancreatic  $\beta$ -cell, *Prog. Biophys. Molec. Biol.*, vol. 54, 87–143, 1989.
2. T. A. Krasimira, C. L. Zimlik, R. Bertram and A. Sherman. Diffusion of calcium and metabolites in pancreatic islets: Killing oscillations with a pitchfork, *J. Biophys.*, vol. 90, 3434-3446, 2006.
3. H. P. Meissner, Electrophysiological evidence for coupling between  $\beta$ -cells of pancreatic islets, *Nature*, vol. 262, 502–504, 1976.
4. A. Sherman and J. Rinzel. Model for synchronization of pancreatic beta-cells by gap junctions, *J. Biophys.*, vol. 59, 547-559, 1991.
5. A. Sherman and J. Rinzel. Rhythmogenic effects of weak electrotonic coupling in neuronal models, *Proc. Natl. Acad. Sci. USA*, vol. 89, 2471-2474, 1992.
6. A. Sherman. Anti-phase, asymmetric and aperiodic oscillations in excitable cells - I. Coupled bursters, *Bull. Math. Biol.* vol. 56, 811–835, 1994.
7. D. Terman. The transition from bursting to continuous spiking in excitable membrane models, *J. Nonlinear Sci.*, vol. 2, 135–182, 1992.
8. E. M. Izhikevich. Neural excitability, spiking and bursting, *Int. J. Bifur. and Chaos*, vol. 10, 1171-1266, 2000.
9. P. Meng, Q. S. Lu, and Q. Y. Wang, Dynamical analysis of bursting oscillations in the Chay-Keizer model with three time scales, *Science China: Series E*, vol. 54, 1–9, 2011.



## Chaos Cryptography: Relation Of Entropy With Message Length and Period

George Makris<sup>1</sup>, Ioannis Antoniou<sup>2</sup>

Complex Systems Analysis Laboratory, Mathematics Department, Aristotle  
University, 54124, Thessaloniki, Greece

<sup>1</sup>E-mail: [geormak@outlook.com](mailto:geormak@outlook.com)

<sup>2</sup>E-mail: [iantonio@math.auth.gr](mailto:iantonio@math.auth.gr)

**Abstract:** Chaos cryptography is implemented by torus automorphisms with strictly positive entropy production. For any given entropy production  $h > 0$  we explicitly construct integer valued automorphisms with entropy  $h(S) \geq h$ . We identify compatibility conditions between the values of the entropy production and the lengths of the messages in terms of the grid size and we propose constructive ways to encrypt messages of arbitrary length in terms of torus automorphisms with any given desired entropy production. We moreover prove that the restrictions of chaotic maps with the same entropy have the same period for a fixed grid size.

**Keywords:** Entropy, Cryptography, Chaos, Cryptography with Chaos.

### 1. Introduction

Chaos cryptography was proposed by Shannon in his classic 1949 mathematical paper on Cryptography where used chaotic maps as models - mechanisms for symmetric key encryption. Of course Shannon did not employ the term Chaos which emerged in the 1970s. This remarkable intuition was based on the paradigm of the Baker's map introduced by Hopf in 1934 as a simple deterministic mixing model with statistical regularity. Shannon observed that using chaotic maps, encryption is achieved via successive mixing of the initial information which is uniformly "spread" all over the available state space. In this way it is becoming exponentially hard to recover the initial message if the reverse transformation is not known. Baker's map is the simplest example of chaotic Torus Automorphisms with constant Entropy production equal to one bit at every step. The Entropy production theory of Torus Automorphisms and general Chaotic maps was developed later by Kolmogorov and his group [Arnold and Avez, 1968; Katok ea, 1995; Lasota ea, 1994], following Shannon's earlier foundation of Information Theory in 1948. Baker's map has also served as a toy model for understanding the problem of Irreversibility in Statistical Mechanics [Prigogine, 1980]. Chaos cryptography with 2-dimensional maps deal with image encryption [Guan D. ea, 2005; Xiao G. ea, 2009] and text encryption [Kocarev ea, 2003; Kocarev ea, 2004; Kocarev L. and Lian S., 2011; Li S., 2003]. We have proposed a new implementation method for Chaos Cryptography based on Chaotic torus automorphisms, applicable for both image and text encryption simultaneously [Makris G, Antoniou I, 2012a] and designed torus automorphisms with desired entropy production [Makris G, Antoniou I, 2012b]. Part of these results is summarized in section 1.



As the grid discretizations of chaotic Torus automorphisms are periodic, for effective implementation we have to examine the conditions for reliable cryptography implementation. The objectives of this work are: a) to examine the dependence of the period on the entropy production and on the grid size (Section 2), b) to provide conditions for admissible grid discretizations (Section 3) and c) to provide algorithms for the construction of integer torus automorphisms with desired entropy production (Appendix A) and for adapting the image size to the appropriate grid size (Appendix B) for customized implementation of chaotic cryptography).

The automorphisms of the 2-torus  $Y = [0,1) \times [0,1)$  are defined by the formula:

$$S : Y \rightarrow Y : \begin{bmatrix} x_{n+1} \\ y_{n+1} \end{bmatrix} = A \begin{bmatrix} x_n \\ y_n \end{bmatrix} \pmod{1}, n \in \mathbb{N} \quad (1)$$

Where  $A = \begin{bmatrix} a & b \\ c & d \end{bmatrix}$  is a real invertible matrix with inverse:

$$A^{-1} = \frac{1}{ad-bc} \begin{bmatrix} d & -b \\ -c & a \end{bmatrix}$$

Chaotic Torus automorphisms (1) have one eigenvalue greater than 1, according Pesin's 1977 Formula.

**Lemma:**

- 1) The class of chaotic automorphisms (1) with  $ad - bc = 1$  consists of the matrices:

$$A = \begin{bmatrix} a & b \\ \frac{ad-1}{b} & d \end{bmatrix}, a \in \mathbb{R}, b \in \mathbb{R} - \{0\}, d > 2 - a \quad (2)$$

- 2) The entropy production of the Chaotic automorphisms (2) is:

$$h = \log_2 \lambda_1 = \log_2 \frac{(a+d) + \sqrt{(a+d)^2 - 4}}{2} = \log_2 \frac{tr(A) + \sqrt{(tr(A))^2 - 4}}{2},$$

$$a \in \mathbb{R}, b \in \mathbb{R}, d > 2 - a \text{ (or } tr(A) > 2) \quad (3)$$

- 3) The chaotic automorphisms (2) are expressed in terms of the entropy production as a parameter  $h$  by the formula:

$$A = \begin{bmatrix} a & b \\ \frac{a \cdot (2^h + 2^{-h} - a) - 1}{b} & 2^h + 2^{-h} - a \end{bmatrix}, a \in \mathbb{R}, b \in \mathbb{R} - \{0\}, h > 0 \quad (4)$$

- 4) For the class of chaotic automorphisms  $A$  with one eigenvalue greater than 1 and  $ad - bc = -1$  we have the corresponding formulas:





$$A = \begin{bmatrix} a & b \\ \frac{ad+1}{b} & d \end{bmatrix}, a \in \mathbb{R}, b \in \mathbb{R} - \{0\}, d > -a \quad (5)$$

$$h = \log_2 \lambda_1 = \log_2 \frac{(a+d) + \sqrt{(a+d)^2 + 4}}{2} = \log_2 \frac{tr(A) + \sqrt{(tr(A))^2 + 4}}{2},$$

$$a \in \mathbb{R}, b \in \mathbb{R}, d > -a \text{ (or } tr(A) > 0) \quad (6)$$

$$A = \begin{bmatrix} a & b \\ \frac{a \cdot (2^h - 2^{-h} - a) + 1}{b} & 2^h - 2^{-h} - a \end{bmatrix}, a \in \mathbb{R}, b \in \mathbb{R} - \{0\}, h > 0 \quad (7)$$

Formulas (2),(3),(4) are proven in [Makris G, Antoniou I, 2012b]. The corresponding formulas for the case  $ad - bc = -1$  are obtained in a similar way. From formulas (3),(6) we see that

**Corollary**

Two Chaotic Torus Automorphisms have the same Entropy Production (are isomorphic), if and only if they have the same trace

**2. Entropy production and the period of the discretization restrictions of integer Torus Automorphisms**

The implementation of cryptographic algorithms requires discretization of the chaotic maps onto the selected  $N \times N$  grid. In order to preserve the grid structure we shall consider torus automorphisms with integer matrix elements. Given a desired entropy production value not less than  $h$  we may construct integer torus automorphisms with entropy production  $h$  from formulas (4),(7) using the algorithms presented in appendix A.

The coordinates of pixels are elements of the  $N \times N$  lattices  $\mathbb{Z}_N \times \mathbb{Z}_N$ . The restriction of any integer torus automorphism to  $\mathbb{Z}_N \times \mathbb{Z}_N \pmod N$ :

$$\begin{bmatrix} x' \\ y' \end{bmatrix} = A \begin{bmatrix} x \\ y \end{bmatrix} \pmod N = \begin{bmatrix} a & b \\ c & d \end{bmatrix} \begin{bmatrix} x \\ y \end{bmatrix} \pmod N \quad (8)$$

is a periodic transformation, called the  $N \times N$  discretization automorphism of (1). The period of the discretization automorphisms (8) is the minimal number  $T$  which satisfies the formula:

$$\begin{bmatrix} a & b \\ c & d \end{bmatrix}^T \pmod N = I_2 = \begin{bmatrix} 1 & 0 \\ 0 & 1 \end{bmatrix} \quad (9)$$

**Theorem 1:** All discretization automorphisms (8) with the same trace have the same period  $T$  which depends only on the size  $N$  of the grid.

Proof:



First we shall show that the discretization automorphisms (8) of isospectral matrices have the same period. It is enough to show that the matrices A (9) and

$$\Delta = \begin{bmatrix} \lambda_1 & 0 \\ 0 & \lambda_2 \end{bmatrix} \quad (10)$$

define discretization automorphisms (8) with the same period. We have:

$$A = B^{-1} \cdot \Delta \cdot B$$

Where B is a diagonalization transformation of A.

If T is the period of (8), from (9) and (10) we have:

$$A^T = (B^{-1} \cdot \Delta \cdot B)^T = B^{-1} \cdot \Delta^T \cdot B$$

and:

$$\begin{bmatrix} a & b \\ c & d \end{bmatrix}^{-T} \pmod{N} = \left( B^{-1} \begin{bmatrix} \lambda_1^T & 0 \\ 0 & \lambda_2^T \end{bmatrix} B \right) \pmod{N} = \begin{bmatrix} 1 & 0 \\ 0 & 1 \end{bmatrix}$$

Therefore:

$$\begin{bmatrix} \lambda_1^T & 0 \\ 0 & \lambda_2^T \end{bmatrix} \pmod{N} = \begin{bmatrix} 1 & 0 \\ 0 & 1 \end{bmatrix}$$

Therefore the discretizations (8) of  $\Delta$  and A have the same period T. From the eigenvalue formulas (3) and (6), we see that the eigenvalues  $\lambda_1, \lambda_2$  depend only on the trace of A. Therefore any two matrices with the same trace define discretizations (8) with the same period. ■

### 3. Entropy Production and Grid size

We observe that torus automorphisms with different entropy production may have identical discretizations (8). For example, applying formula (6) we see that

the torus automorphisms with matrices  $A_1 = \begin{bmatrix} 2 & 1 \\ 4093 & 2047 \end{bmatrix}$  and

$A_2 = \begin{bmatrix} 2 & 1 \\ 93 & 47 \end{bmatrix}$  have entropy productions  $h_1 = 11.0007$

and  $h_2 = 5.6141$  correspondingly. However their discretizations (8) to the grid  $100 \times 100$  are identical:

$$\begin{bmatrix} 2 & 1 \\ 4093 & 2047 \end{bmatrix} \pmod{100} \equiv \begin{bmatrix} 2 & 1 \\ 93 & 47 \end{bmatrix} \pmod{100}.$$

The same is true for the grids  $200 \times 200$ ,  $500 \times 500$ ,  $1000 \times 1000$  and others.

This is an undesirable fact because only equivalent chaotic torus automorphisms should have identical grid discretization (8). We found that this requirement is true only for certain values of the entropy production h and grid size N. The result is the following:



**Theorem 2:** An necessary and sufficient condition for one to one correspondence between torus automorphisms and their grid discretizations (8) is:  $N > \max\{a, b, c, d\}$  (11)

Equivalently in terms of entropy production, using (3) and (6) we have the conditions:

$$N > \max \left\{ a, b, 2^h + 2^{-h} - a, \frac{a \cdot (2^h + 2^{-h} - a) - 1}{b} \right\} \text{ for } \det(A) = 1 \quad (12)$$

$$N > \max \left\{ a, b, 2^h - 2^{-h} - a, \frac{a \cdot (2^h - 2^{-h} - a) + 1}{b} \right\} \text{ for } \det(A) = -1 \quad (13)$$

**Prof:**

$$\begin{aligned} \begin{bmatrix} a & b \\ c & d \end{bmatrix} \begin{bmatrix} x \\ y \end{bmatrix} (\text{mod } N) &= \begin{bmatrix} a \pmod{N} & b \pmod{N} \\ c \pmod{N} & d \pmod{N} \end{bmatrix} \begin{bmatrix} x \\ y \end{bmatrix} (\text{mod } N) = \\ &= \begin{bmatrix} v_a & v_b \\ v_c & v_d \end{bmatrix} \begin{bmatrix} x \\ y \end{bmatrix} (\text{mod } N) \end{aligned}$$

As the remainders  $v_a, v_b, v_c, v_d$  are always not greater than a,b,c,d

correspondingly, we have:  $tr \begin{bmatrix} a & b \\ c & d \end{bmatrix} = a + d \geq v_a + v_d = tr \begin{bmatrix} v_a & v_b \\ v_c & v_d \end{bmatrix}$

Therefore, from (3) and (6) we have:  $h \begin{bmatrix} a & b \\ c & d \end{bmatrix} \geq h \begin{bmatrix} v_a & v_b \\ v_c & v_d \end{bmatrix}$

$h \begin{bmatrix} a & b \\ c & d \end{bmatrix} = h \begin{bmatrix} v_a & v_b \\ v_c & v_d \end{bmatrix}$  if and only if:  $a < N$  and  $b < N$  and  $c < N$  and  $d < N$ ,

from which follows the desired result. ■

The natural question now arises what are the possible values of entropy production for automorphisms satisfying (11)

Without significant loss of generality we consider the simpler class of integer torus automorphisms with  $b = 1$ . Formulas (12) and (13) are written :

$$h < \log_2 \left[ (a + N) + \sqrt{(a + N)^2 - 4} \right] - 1, \quad 0 < a < N, \quad \det(A) = 1 \quad (14)$$

$$h < \log_2 \left[ (a + N) + \sqrt{(a + N)^2 + 4} \right] - 1, \quad 0 < a < N, \quad \det(A) = -1 \quad (15)$$

Therefore given the grid size  $N$  we know the maximal entropy production from (14),(15) for automorphisms with  $b=1$  and conversely given a desired entropy production value we know the minimal grid size from (12),(13). The relation

between entropy production and grid size is shown in figure 1. We shall call the discretizations (8) with grid size  $N \times N$  admissible discretizations if and only if the conditions (12) , (13) hold.

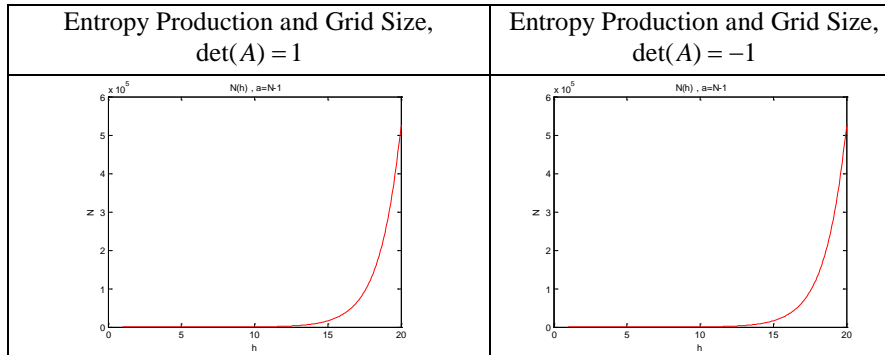


Figure 1: Entropy Production and Grid Size

In case the grid  $N \times N$  for admissible discretization (8) of the constructed torus automorphisms is larger than the message size  $n \times m$  we may enlarge and adapt the message size to the grid size using the algorithm presented in appendix B.

## 5. Conclusions

After extending our previous results [Makris G, Antoniou I, 2012b] on the entropy production on torus automorphisms (Lemma and Corollary), we show that the period of grid discretizations of chaotic automorphisms depends only on the entropy production and on the grid size (Theorem 1). In order to avoid the undesirable fact that torus automorphisms with different entropy production may have the same discretization, we provide a necessary and sufficient condition of admissible grid discretizations (Theorem 2). For customized implementation of chaotic cryptography, we provide algorithms for the construction of integer torus automorphisms with desired entropy production (Appendix A) and for adapting the image size to the appropriate grid size (Appendix B). These results are necessary for implementation of chaotic cryptographic algorithms of desired entropy production. Based on Theorem 2 and Appendix B we can automatically adapt the message size to admissible discretization for effective cryptography.

## References

1. Akritas P., Antoniou I., Pronko G., "On the Torus Automorphisms: Analytic Solution, Computability and Quantization", Chaos, Solitons and Fractals 12,(2001) 2805-2814
2. Arnold, V. I. and Avez, A., Ergodic Problems of Classical Mechanics Benjamin, New York , 1968



3. Guan Z. H., Huang F., and Guan W.. Chaos-based image encryption algorithm. *Physics Letters A*, Vol. 346, Issues 1-3,( 2005), pp 153-157.
4. Dyson FJ, Falk H., Period of a discrete cat mapping. *Am Math Monthly* 1992;2(99):603-14
5. Hopf E., On Causality, Statistics and Probability, *J. Math. and Phys.* 13, (1934), 51-102.
6. Katok A., Hasselblatt B., *Introduction to the Modern Theory of Dynamical Systems*, Cambridge University Press, Cambridge, UK , 1995
7. Kocarev L., Sterjev M., Amato P., RSA ENCRYPTION ALGORITHM BASED ON TORUS AUTOMORPHISMS, *IEEE, ISCAS (2004)*, IV 577-580.
8. Kocarev L., Tasev Z., and Makraduli J., "Public-Key Encryption and Digital-Signature Schemes Using Chaotic Maps", 16th European Conference on Circuits Theory and Design, September 1 – September 4, 2003, Krakow, Poland, ECCTD 2003.
9. Kocarev, L., Lian, S., *Chaos-Based Cryptography. Theory, Algorithms and Applications*, Studies in Computational Intelligence, Vol. 354, (2011), ISBN 978-3-642-20542-2, Berlin.
10. Lasota A. and Mackey M., *Chaos, Fractals, and Noise*, Springer-Verlag New York, 1994.
11. Li, S., *Analyses and New Designs of Digital Chaotic Ciphers*. Ph.D. thesis, School of Electronic and Information Engineering, Xi'an Jiaotong University, Xi'an, China, 2003
12. Makris G., Antoniou I., 2012, "Cryptography with Chaos", *Chaotic Modeling and Simulation (CMSIM)*, VOL 1: 169-178, 2012, ISSN 2241-0503.
13. Makris G., Antoniou I., 2012, "Cryptography with Entropy Producing Maps", 6th World Congress of NonLinear Analysts, IFNA 2012, 25 June - 1 July, Athens, Greece
14. Pesin Ya. B., Characteristic Lyapunov exponents and smooth ergodic theory, *Russ. Math. Surv.* 32:4, (1977), 55-112
15. Prigogine I., *From Being to Becoming*, Freeman, New York, 1980
16. Shannon C. , *A Mathematical Theory of Communication*. *Bell System Technical Journal*, vol. 27, pp. 379–423, 623–656 (1948); Shannon C. and Weaver W., *Mathematical Theory of Communication*, Univ of Illinois Press, Urbana, Ill (1949).
17. Shannon, C., *Communication Theory of Secrecy Systems*. *Bell System Technical Journal*, Vol.28, Issue 4, (1949), pp 656–715.
18. Smale S., "Differentiable dynamical systems". *Bulletin of the American Mathematical Society* 73: (1967) 747–817.
19. Smale S., Finding a horseshoe on the beaches of Rio, *Mathematical Intelligencer* 20, (1998), 39-44
20. Xiao, D., Liao, X., Wei, P., Analysis and improvement of a chaos-based image encryption algorithm. *Chaos, Solitons & Fractals*, Vol. 40, Issue 5, (2009), pp 2191-2199.



## Appendix A: Construction of integer torus automorphisms with entropy production not less than any desired positive real number

Torus automorphisms have been applied to  $N \times N$  grids and the periods has been related to the grid size  $N$  [Vivaldi, 1989; Dyson FJ and Falk H, 1992; Akritas ea, 2001; Antoniou ea, 1997; Xiao ea, 2009]. According to formula (2) we should have  $\frac{ad-1}{b} \in \mathbb{Z}$  for any integer values  $a, b, d$ , ie. :  $(ad) \bmod b = 1$

For any given entropy production  $h > 0$  we construct integer matrixes  $A$  with entropy  $h(A) \geq h$  according to the following algorithm.

### Algorithm 1. Construction of integer matrices $A$ with $\det(A) = 1$

Step 0: inputs:  $h \in (0, \infty)$ ,  $a, b \in \mathbb{Z}$

Step 1: Set  $x = \lceil \text{tr}(A) \rceil = \lceil 2^h + 2^{-h} \rceil$ ,  $\lceil z \rceil$  is the ceiling of  $z$

Step 2: Set  $d = x - a$

Step 3: if  $[d > 2 - a \text{ and } (b = 1 \text{ or } (ad) \bmod b = 1)]$  goto Step 9

Step 4: if  $[a \bmod b \neq 0 \text{ and } b \bmod a \neq 0]$  goto Step 7

Step 5: Set  $x = x + 1$  and  $d = x - a$

Step 6: goto Step 3

Step 7: Set  $a = a + 1$  and  $d = x - a$

Step 8: goto Step 3

Step 9: return  $A = \begin{bmatrix} a & b \\ \frac{ad-1}{b} & d \end{bmatrix}$

Step 10: return  $\lambda_1(A) = \frac{(a+d) + \sqrt{(a+d)^2 - 4}}{2}$

Step 11: return  $h(A) = \log_2 \lambda_1(A)$

Input			Output		
$h$	$a$	$b$	$A = \begin{bmatrix} a & b \\ \frac{ad-1}{b} & d \end{bmatrix}$	$\lambda_1(A)$	$h(A)$
<b>1.2</b>	1	1	$A = \begin{bmatrix} 1 & 1 \\ 1 & 2 \end{bmatrix}$	2.6180	<b>1.3885</b>
<b>1.2</b>	2	3	$A = \begin{bmatrix} 2 & 3 \\ 1 & 2 \end{bmatrix}$	3.7321	<b>1.9000</b>



<b>3.5</b>	1	1	$A = \begin{bmatrix} 1 & 1 \\ 10 & 11 \end{bmatrix}$	11.9161	<b>3.5748</b>
<b>3.5</b>	5	1	$A = \begin{bmatrix} 5 & 1 \\ 34 & 7 \end{bmatrix}$	11.9161	<b>3.5748</b>
<b>3.5</b>	5	3	$A = \begin{bmatrix} 5 & 3 \\ 13 & 8 \end{bmatrix}$	11.9161	<b>3.5748</b>
<b>11</b>	2	1	$A = \begin{bmatrix} 2 & 1 \\ 4093 & 2047 \end{bmatrix}$	2049	<b>11.0007</b>

Table 1: Examples of **Algorithm 1**

According to formula (4) we should have  $\frac{ad+1}{b} \in \mathbb{Z}$  for any integer values

$a, b, d$ , i.e. :  $(ad+1) \bmod b = 0 \Rightarrow (ad) \bmod b = b-1$

**Algorithm 2. Construction of integer matrices A with  $\det(A) = -1$**

Step 0: inputs:  $h \in (0, \infty)$ ,  $a, b \in \mathbb{Z}$

Step 1: Set  $x = \lceil \text{tr}(A) \rceil = \lceil 2^h - 2^{-h} \rceil$ ,  $\lceil z \rceil$  is the ceiling of  $z$

Step 2: Set  $d = x - a$

Step 3: if  $[d > -a \text{ and } (b=1 \text{ or } (ad) \bmod b = b-1)]$  goto Step 9

Step 4: if  $[a \bmod b \neq 0 \text{ and } b \bmod a \neq 0]$  goto Step 7

Step 5: Set  $x = x + 1$  and  $d = x - a$

Step 6: goto Step 3

Step 7: Set  $a = a + 1$  and  $d = x - a$

Step 8: goto Step 3

Step 9: return  $A = \begin{bmatrix} a & b \\ \frac{ad+1}{b} & d \end{bmatrix}$

Step 10: return  $\lambda_1(A) = \frac{(a+d) + \sqrt{(a+d)^2 + 4}}{2}$

Step 11: return  $h(A) = \log_2 \lambda_1(A)$

Input			Output		
$h$	$a$	$b$	$A = \begin{bmatrix} a & b \\ \frac{ad+1}{b} & d \end{bmatrix}$	$\lambda_1(A)$	$h(A)$
<b>1.2</b>	1	1	$A = \begin{bmatrix} 1 & 1 \\ 2 & 1 \end{bmatrix}$	2.4142	<b>1.2716</b>



<b>1.2</b>	2	3	$A = \begin{bmatrix} 2 & 3 \\ 1 & 1 \end{bmatrix}$	3.3028	<b>1.7237</b>
<b>3.5</b>	1	1	$A = \begin{bmatrix} 1 & 1 \\ 12 & 11 \end{bmatrix}$	12.0828	<b>3.5949</b>
<b>3.5</b>	5	1	$A = \begin{bmatrix} 5 & 1 \\ 36 & 7 \end{bmatrix}$	12.0828	<b>3.5949</b>
<b>3.5</b>	5	3	$A = \begin{bmatrix} 5 & 3 \\ 12 & 7 \end{bmatrix}$	12.0828	<b>3.5949</b>
<b>11</b>	2	1	$A = \begin{bmatrix} 2 & 1 \\ 4093 & 2046 \end{bmatrix}$	2048	<b>11.0000</b>

Table 2: Examples of **Algorithm 2**

### Appendix B: Algorithm to Enlarge image size from $(n \times m)$ to $(N \times N)$ :

Step 0: inputs:  $(image, N, c)$ , N: new image size, c: color of new pixels

Step 1: calculate  $(n, m)$  = image size

Step 2:  $W_h = N - n$

Step 3: Create a new blank image1 with size  $\left(\frac{W_h}{2} \times m\right)$  and color c to every pixel.

Step 4: Create a new image2 with vertical quote of three images:

$$image2 = \begin{pmatrix} image1 \\ image \\ image1 \end{pmatrix}. \text{ Image2 size} = (N \times m)$$

Step 5:  $W_w = N - m$




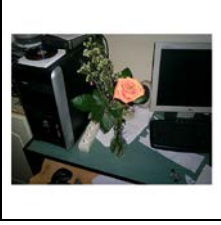
Step 6: Create a new blank image3 with size  $\left(\frac{W_w}{2} \times N\right)$  and color c to every pixel.

Step 7: Create a new\_image with horizontal quote of three images :  
 $new\_image = (image3 \ image2 \ image3)$  . new\_image size =  $(N \times N)$

<b>Image</b>	<b>Image1</b>	<b>Image2</b>	<b>Image3</b>
(342 x 454)	(79 x 454)	(500 x 454)	(500 x 23)





				
<b>Inputs</b>	<b>New_image</b> (500 x 500)		<b>Output</b>	
Image $N=500$ $c=white$  <u>Calculations</u> $W_n = N - n = 158$ $W_w = N - m = 46$			New_image	

The advantage of adding pixels in an image is to keep the original information.





## Chaos Based Water Marked Image Encryption

Mahalinga V. Mandi, Dileep D

Dr. Ambedkar Institute of Technology, Bangalore, India

E-mail: [mvmandi@yahoo.com](mailto:mvmandi@yahoo.com)

**Abstract:** Digital image watermarking along with image encryption is a growing research area. The use of chaos in image watermarking and image encryption algorithms has seen tremendous advantages. In this paper a chaos based image watermarking to provide authentication and chaos based watermarked image encryption to provide security is proposed. The performance of the image watermarking and encryption is mainly based on the randomness properties of chaotic binary sequences. Chaotic binary sequences are derived from chaotic discrete sequences using logistic map equation. In order for a complex imaging system to cope with these concerns, a cryptography algorithm able to manage the vast amounts of data involved in image processing is required. This paper proposes a new image watermarked encryption algorithm based on Logistic map equation, in which the key space is  $2^{212}$  which improves the security against exhaustive attacks. Also good encryption speed is achieved using the proposed algorithm. The experimental results and the security analysis including Key space, Information entropy and key sensitivity proves that the proposed algorithm is secure, authenticated and more efficient.

**Keywords:** Watermarking, Image encryption, Logistic map, Chaos

### 1. Introduction

The growth of the digital technology and the associated need for information integrity, authenticity and secrecy encourages the development of secure image encryption systems. After the advent of the Internet and especially nowadays, security of data and protection of privacy has become a major concern for everyone's life. Combining the properties of cryptography and chaos theory it is possible to design an image encryption algorithm that provides security, authentication and privacy in image and video applications. Cryptography deals with watermarking techniques to provide authentication and encryption techniques to provide security. Chaos theory provides the suitable non linear binary sequences that can be applied to watermarking and encryption algorithm. Chaos is a deterministic, random like process found in non-linear, dynamical system which is non-periodic, non-converging and bounded. Chaotic signals are random like but they are produced by deterministic systems and can be reproduced. Chaotic systems are sensitive to initial conditions and thus even with a small difference in initial conditions will lead to the generation of very different signals from the same dynamical system. The broad band, noise like nature of chaos offers several advantages when used for generating key stream for watermark and encryption algorithm. Chaotic sequences are non-repeatable; if only part of the sequence is recovered then it is nearly impossible to



regenerate the whole sequence. This means that any unintended receiver subjected to these sequences will encounter noise like waveforms whose spectrum have no features that can be exploited for signal interception.

The chaos based image watermarking and encryption is discussed in [1] – [6] and [12] – [13]. A watermarking procedure for digital image in the Complex Wavelet Domain is discussed in [1]. The proposed watermark algorithm needs three keys: a sub-image, a random location matrix and spread spectrum watermark. The first and the second ones ensure the security of watermarking procedure and the third one guarantees its robustness.

A new robust watermarking scheme based on a chaotic function and a correlation method for detection, operating in the frequency domain is discussed in [2]. This scheme is blind and comparing to other chaos related watermarking methods, experimental results exhibit satisfactory robustness against a wide variety of attacks such as filtering, noise addition, geometric manipulations and JPEG compression with very low quality factors. The scheme also outperforms traditional frequency domain embedding both in terms of robustness and quality.

A digital image watermark algorithm based on discrete wavelet transform and chaos theory is referred [3]. During the embedding of the watermarking, discrete wavelet transform is done firstly and extract low frequency part as the embedding field; then the chaotic sequence is used to encrypt the watermark and transform the encrypted part and extract the low frequency; finally, embed the low frequency part into that of the original image.

An efficient, secure color image coder incorporating Color-SPIHT (C-SPIHT) compression and partial encryption is presented in [4]. Confidentiality of the image data is achieved by encrypting only the significance bits of individual wavelet coefficients for  $K$  iterations of the C-SPIHT algorithm. By varying  $K$ , the level of confidentiality vs. processing overhead can be controlled.

A new approach for image encryption based on chaotic logistic maps in order to meet the requirements of the secure image transfer is discussed in [5]. Here an external secret key of 80-bit and two chaotic logistic maps are employed. The initial conditions for the both logistic maps are derived using the external secret key by providing different weightage to all its bits.

A digital image encryption algorithm four array chaotic array is presented in [6] and uses chaotic maps to generate four value chaotic array whose size as big as image.

Combined with two chaotic maps, a novel alternate structure is applied to image cryptosystem in paper [7]. A general cat-map is used for permutation and diffusion, as well as the OCML (one-way coupled map lattice), which is applied

for substitution. These two methods are operated alternately in every round of encryption process, where two sub-keys employed in different chaotic maps are generated through the master-key spreading.

A paper on the utilization Pixels Arrangement and Random Permutation to encrypt medical image for transmission security is presented in [8]. The objective of this scheme is to obtain a high speed computation process and high security. In this paper a new chaos based watermarked image encryption algorithm is proposed. First the watermark is embedded in the image and then the image is encrypted using two steps, first the image is position permuted and then the substitution is done by XOR<sup>ring</sup> each pixel. The key streams are generated using logistic map equation.

The organization of the paper is as follows. Section 2 discusses the architecture of the proposed scheme. Section 3 presents experimental results. Security analysis is discussed in section 4. Finally the paper is concluded in section 5.

## 2. Architecture

Fig. 1 shows the block diagram of chaos based image encryption scheme with embedded watermark. In this diagram there are two parts. One that is used to embed the watermark in the plain image using LSB insertion and the other that encrypts the watermarked image using chaotic logistic map equation. LSB insertion is randomly done and the LSB keystream is generated using chaotic logistic map equation. The advantage of using LSB insertion is that it is possible to embed a large watermark as compared to other techniques. In the watermarked image encryption, mainly two steps are involved. First the image is position permuted and then the substitution is done by Bitwise XOR<sup>ring</sup> each pixel with Key stream 3 to obtain an encrypted image. The Key stream 1 is used for row permutation and Key stream 2 is used for column permutation. Generation of Key streams is explained in Section 2.1.

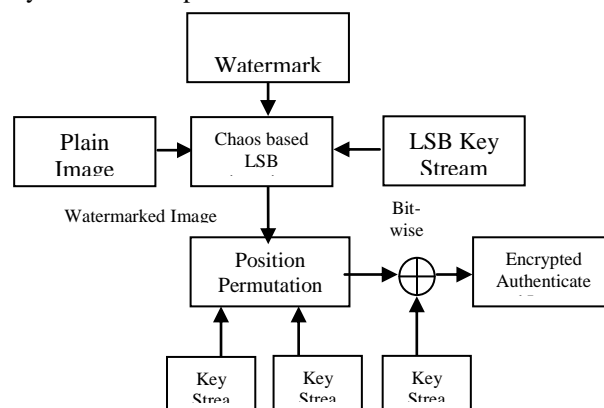


Fig. 1. Proposed Encryption Scheme

Fig. 2 shows the watermark extraction. Here the decryption of the watermarked image is exactly the reverse process and the same Key streams are used. The watermark is also extracted with the same LSB Key stream. It is also possible to know whether the watermark/image is tampered by comparing the extracted watermark and the reference watermark. Hence the proposed algorithm not only provides the required security but also provides the authentication.

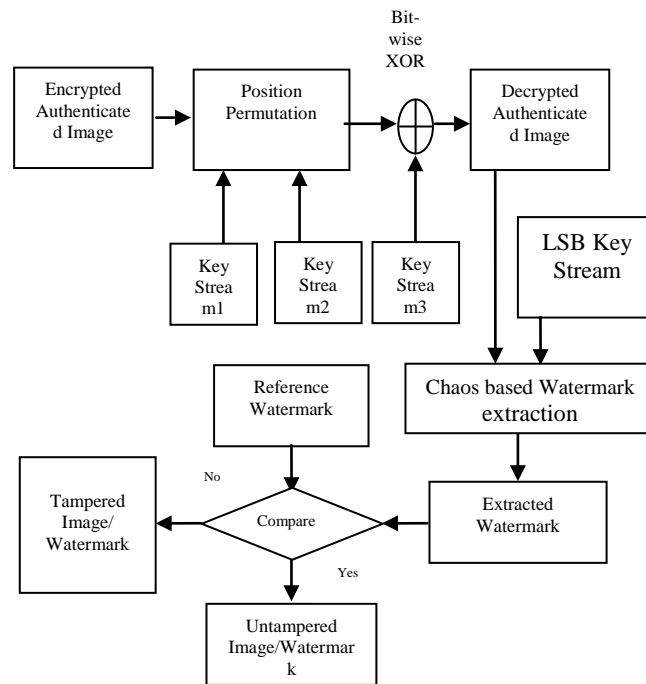


Fig. 2. Watermark detection

### 2.1. Key stream generator

Key stream generator is as shown in Fig. 3. In this paper Logistic map is used for generating chaotic real valued discrete sequence by selecting a key.

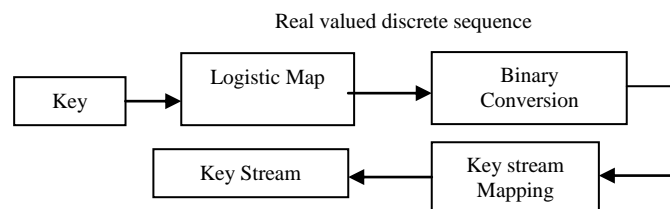


Fig. 3. Key Stream Generation



The most commonly used chaotic map is Logistic map equation is given by,

$$x_{k+1} = r * x_k * (1 - x_k), \quad 0 < x < 1 \quad (1)$$

where  $x_0$  is the initial value,  $r$  is the bifurcation parameter and depending on the value of  $r$ ,  $x_0$  the dynamics of the generated chaotic sequence can change dramatically. For  $3.57 < r \leq 4$ , the sequence is found to be non periodic and non-converging [9]. The probability density function of Logistic map is symmetric and hence the binary conversion is done as shown in equation (2).

$$\begin{aligned} b_i &= 0 \text{ for } x_k < 0.5 \\ \text{and } b_i &= 1 \text{ for } x_k \geq 0.5 \end{aligned} \quad (2)$$

where  $0 < i < n$ ,  $n$  = length of the chaotic sequence.

Key = {key1, key2, key3} is composed of three sub-keys, where sub-key1 is used as initial value for generating key stream1, sub-key2 is used as initial value for generating key stream2 and sub-key3 is used as initial value for generating key stream3. Key stream mapping for generating key stream1, 2 and 3 are as shown in Fig. 4.

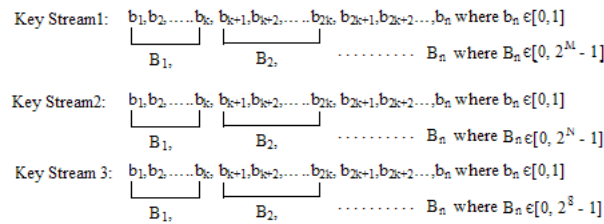


Fig. 4. Key Stream Mapping

Where  $B_1, B_2, \dots$  etc denotes decimal numbers obtained by combining  $k$ -binary numbers for each streams respectively. Thus if the Image to be encrypted is of size  $2^M \times 2^N$  then required length of key Stream 1 which is used for row permutation is  $2^M$  and the range is  $[0, 2^M - 1]$ , required length of key Stream 2 used for column permutation is  $2^N$  and the range is  $[0, 2^N - 1]$  and the required length of key Stream 3 which is used for bitwise XOR<sup>ring</sup> is  $2^M \times 2^N \times 8$  and the range is  $[0, 255]$ .

During the key stream 1 and 2 generation, it must be guaranteed that there is no duplicate element in the two streams by discarding the repeated sequence. The LSB key stream is similar to key stream 3 and mainly depends on the size of the watermark.

### 3. Experimental Results

In order to test this algorithm we considered standard 512 X 512 Lena bmp image. In this Lena image a watermark 'R' of size 14 X 14 is embedded. The  $r$

value is taken as 3.99 and the initial values to generate key streams 1, 2 and 3 respectively is taken as  $\text{key} = \{\text{key1}, \text{key2}, \text{key3}\} = \{0.6532245, 0.9874562, 0.416745\}$ . For generating the LSB key stream the initial value is taken as 0.62343242.

Fig. 5 shows the input image, watermark embedded image, watermark and watermark extract.

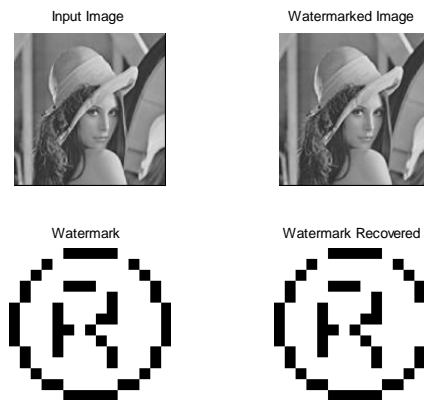


Fig. 5. Input image and Watermark

Fig. 6 to Fig. 9 shows the histogram of the input image, encrypted image, encrypted image histogram and decrypted image respectively.

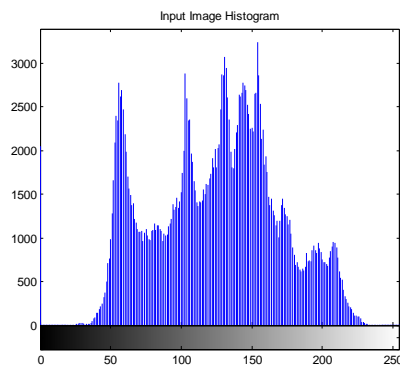


Fig. 6. Input Image Histogram

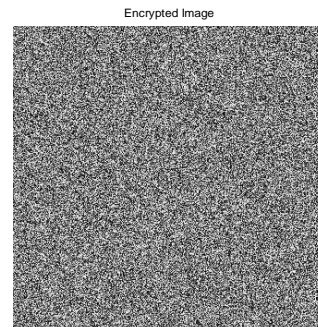


Fig. 7. Encrypted Image



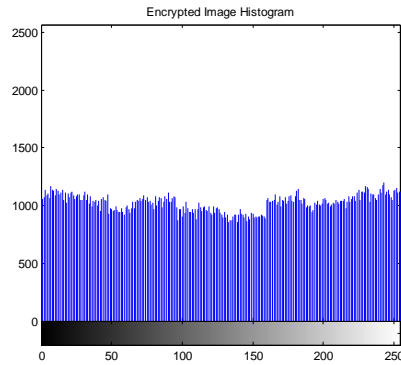


Fig. 8. Encrypted image histogram



Fig. 9. Decrypted image

The encryption and Decryption time in Matlab for a 512 X 512 bmp image was found to be 0.679 seconds.

#### 4. Security Analysis

A good encryption schemes should resist all kinds of known attacks such as known/chosen plain text attacks, cipher text only attack, statistical attack and various brute force attacks. We will present some security analysis on the proposed encryption scheme in this section.

##### 4.1. Key space analysis

Considering most commonly used PC platform as an example, the computation precision is 16 decimal digits, therefore a chaos-based cryptosystem can only provides  $10^{16} \approx 2^{53}$  size key space [10], which is a little smaller than DES( $2^{56}$ ) and by far smaller than AES( $2^{128}$ ). Since key = {key1, key2, key3} and LSB key which is composed of four sub-keys, the key space size is  $(10^{16})^4 \approx 2^{212}$ , which is larger than the acknowledged most security AES algorithm. Besides, the scheme is secure against known/chosen-plaintext attack, since it adopts both permutation and substitution operations.

##### 4.2. Information entropy

Entropy of a random image source is expected to be eight for an image in which each pixel is 8-bits [11]. The entropy of the input image in was found to be 7.3465 and the entropy of the encrypted image was found to be 7.9963, which is very close to the theoretical value. The entropy of the encrypted image of the proposed scheme is very close to the ideal one. Also the entropy of the watermarked image is equal to 7.3466 which is almost same as that of the input image.

### 4.3. Key Sensitivity

A good crypto-system should be sufficiently sensitive to small changes in the key. In the proposed scheme with a small change in the key it is not possible to decrypt the image. This was observed by selecting the key = {0.6532245, 0.9874562, 0.41674500001} and by decrypting the image with a wrong key, key3 is not possible. Fig. 10 shows the decrypted image with a wrong key and its histogram.

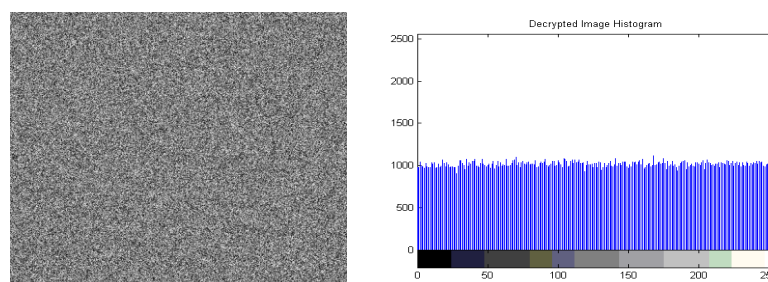


Fig. 10. Decrypted image and its histogram with a wrong key

## 5 Conclusions

In this paper a new a good performance chaos based security algorithm for images is proposed. The algorithm proposed in this paper provides security as well as authenticity. The advantage of this algorithm is that the key space is enlarged to  $2^{212}$ , which improves the security against exhaustive attack and also the good encryption speed which is enhances the performance when image size is large. The entropy of the encrypted image of the proposed scheme is very close to the ideal one and hence the encrypted image appears to be highly random which is observed from the histogram of encrypted image. The simulation result shows that the proposed scheme has very good key sensitivity which provides good security for color images. By comparing the extracted watermark with the reference watermark it is easy to find whether the image/watermark is tampered or not.

## Acknowledgement

The authors would like to thank the Principal, Management, SPFU and NPIU for sponsoring the authors to present the paper in the International Conference CHAOS 2013 under the World Bank Funded Project TEQIP-2.

## References

1. S. Mabtoul , E. Ibn-Elhaj , D. Aboutajdine, “A Blind Chaos-Based Complex Wavelet-Domain Image Watermarking Technique”, Proc. Int Jnl. of Computer Science and Network Security, VOL.6 No.3, pp. 134-139, March 2006



2. E. Chrysochos, V. Fotopoulos, and A. N. Skodras, Robust Watermarking of Digital Images Based on Chaotic Mapping and DCT”.
3. Qiang Wang, Qun Ding, Zhong Zhang and Lina Ding, “Digital Image Encryption Research Based on DWT and Chaos”, Proc. Fourth IEEE Int. Conf. on Natural Computation, pp. 494-498, 2008.
4. Karl Martin, Rastislav Lukac, Konstantinos N. Plataniotis, “Efficient encryption of wavelet-based coded color images”, Jnl. Pattern Recognition Society, Elsevier, pp. 1111 – 1115, 2006.
5. N.K. Pareek, Vinod Patidar, and K.K. Sud, “Image encryption using chaotic logistic map”, Jnl. Image and Vision Computing, Elsevier, pp. 926–934, 2006.
6. Gao Shan-qing, Zhang Shi-jie, Liu Bin, Luo Xiang-yang and Liu Fen-lin, ” An Image Encryption Algorithm based on Four-value Chaotic Array”, Jnl. Image and Graphics, Vol. II, No. 2, pp. 244-250, Feb. 2006.
7. Zhang YiWei1, Wang YuMin & Shen XuBang, “A chaos-based image encryption algorithm using alternate structure”, Springer, Vol. 50, No. 3, pp. 334-341, June 2007.
8. Koredianto Usman, Hiroshi Juzoji, Isao Nakajima, Soegijardjo Soegidjoko, Mohamad Ramdhani, Toshihiro Hori and Seiji Igi, “Medical Image Encryption Based on Pixel Arrangement and Random Permutation for Transmission Security”, IEEE, pp. 244-247, 2007.
9. Mahalinga V.Mandi, R. Murali K.N.Haribhat,” Chaotic functions for generating binary sequences and their suitability in Multiple Access”, Proc. IEEE-ICCT 2006, Vol. 1, pp.217-220.
10. Chong Fu, Zhiliang Zhu, ”A Chaotic Image encryption scheme based on circular bit shift method”, The 9th International Conference for Young Computer Scientists, IEEE Computer Society, pp. 3057 – 3061, 2008.
11. Xu Shu-Jiang, Wang Ying-Long, Wang Ji-Zhi, Tian Min,” A Novel Image Encryption Scheme Based on Chaotic Maps”, Proc. IEEE-ICSP 2008, pp. 1014 – 1018.
12. Soumaya Al-Maadees, Afnan Al-Ali and Turki Abdalla, “A New Chaos-Based Image-Encryption and Compression Algorithm”, Journal of Electrical and Computer Engineering, Volume 2012 (2012), Article ID 179693, 11 pages, DOI:10.1155/2012/179693.
13. Chen Zaiping, Li Haifen, Dong Enzeng and Du Yang, “Hyper-Chaos Based Image Encryption Algorithm”, 2nd IEEE International Conference on Intelligent Human-Machine Systems and Cybernetics (IHMSC), 2010, Volume: 2, pp. 188 – 191.





**Maximova Marina**

South-Russian State Technical University (Novocherkassk Polytechnic Institute), Faculty of Socio-Humanitarian Knowledge, Department of Philosophy

Email: [aspera-86@mail.ru](mailto:aspera-86@mail.ru)

## **An attractor and a superattractor in the contemporary pan-humanitarian space**

**Abstract:** The work purpose is clearing up the possibility of adequate use of the applied synergetics results in the sphere of philosophical and social knowledge. On the basis of the contemporary Russian researchers' works the author analyzes the concept of an attractor and a superattractor as the goal of a complex system, considers prospects of synergetics methodology use in the epistemological scientific field.

**Keywords:** attractor, superattractor, synergetics, socio-humanitarian systems, post-nonclassical paradigm

**1. Introduction:** One of the major defining concepts in the contemporary synergetics, namely the attractor, can be developed in the area of both applied and abstract and philosophical knowledge. An attractor as an emergent formation shows qualitative changes in the process of evolutionary development of any system, including non-natural, general social systems. According to the author, an attractor represents a system innovation [1,2], - a conceptual change in the system which radically alters its behaviour.

For more "evident" confirmation of the idea the author offers to use the Darwinian concept of selection which if applied to socio-humanitarian systems is interpreted as occurrence of bifurcation points, branching of the system associated with uncertainty in its further development when the most suitable variant satisfying the "natural" laws of development defines further vector of movement. The system evolution process is a process of movement on the way chosen in the bifurcation point. Thus, the universal mechanism of evolution is revealed at the moment of bifurcation by selecting structures capable of bringing the system to a totally new level. An attractor, or an innovation is a conceptual change most suitable for novelty features. Such an attractor represents rather stable state of the system, a balance between instability and steady state.

**2. Essence of the attractor in socio-humanitarian systems.** In comparison with applied synergetics, use of synergetic methodology in humanitarian knowledge has a number of peculiarities. In particular, social systems have a higher level of complexity as they include "the human" factor, namely a role of a man as the subject of knowledge. Taking into account such a feature of «human» systems it is offered to consider the attractor to be not a point but K. Lorenz's strange attractor having a limited area of its existence, a certain field of possible decisions. If, by analogy with applied synergetics, the attractor is understood to be the system goal, it will allow to show pluralistic character of social processes with a great number of various goals at different levels of the action.

Laws of social systems functioning are associated with processes of apprehending by the subject the activity results in its total variety. In this case it is inevitably necessary to touch upon the question on the goal essence and on necessity of its understanding change according to scientific trends of the postnonclassical scientific paradigm. If we understand the social system goal to be the strange attractor, it is necessary to reveal its features in this context.



First, it is necessary to note conventionality of the concept of the local goal of self-organizing systems of any nature. The concept of the goal assumes availability of an external subject which sets this goal. Sinergetic systems of such a subject do not have and cannot have. Therefore, in accordance with the results of the researches [3], complex self-organizing systems of a social nature can be referred to the group of teleonomic systems. These are systems which evolve to some final condition without a specific initial programme.

In this case, the concept of "the goal" can be defined as an internally determined condition of a social system and a direction of its change and development, that is the system trend to the order. In the process of evolutionary development the similar "goal" reasons play the increasing role, accordingly the factors named the order parametres, become complicated as well. Along with their complication, the system "goals" become more complicated, their quantity set by the strange attractor increases.

Every social attractor forms its area of attraction, therefore intrasystem relations based on coherent collective movement of the system components arise.

**3.A superattractor and its meaning in the contemporary reality.** According to N.I. Moiseyev [4], a social system can have a great number of attractors. Proceeding from it, it is logical to differentiate local attractors as intermediate goals of evolutionary processes, and global, that is consolidating the whole process of the system functioning. Taking into account complexity of non-natural systems, it seems to be pertinent to clear up social parametres of such a global attractor as a goal-like structure.

In this connection Russian scientist V.P. Bransky [5] determines the concept of a superattractor. A superattractor is fundamentally important when considering social systems as it defines availability of the global "goal" of the whole system which can be understood as a general meaning of the evolution. A global attractor (a superattractor) can be presented as an asymptotically stable point in the evolution spiral which movement incessantly approaches this point.

The incessant aiming for a superattractor is caused by complexity of its nature, non-linearity of movement to it. In the interpretation of social processes V.P. Bransky understands a superattractor as a limit of the mankind cultural development, a meaning of global self-organization, the order and chaos synthesis, more precisely, the order which is stable against the chaos.

The concept of a superattractor defines the system integrity, representing the concept of holistic synergistic system world outlook.

According to V.P. Bransky, a superattractor is a much broader category in comparison with the concept of the system goal. In the conception of synergistic historicism [5] a superattractor is interpreted as a public ideal and analyzed particularly from the view point of its subjective spiritual characteristics associated with axiological categories. According to such conception, the most general concept concerning social processes is the concept of the ideal including a number of value and world outlook characteristics.

From this view point the ideal acquires a global comprehensive character. V.P. Bransky notes that in the XX-th century philosophy there was a trend to replace the concept of "the ideal" with the concepts of "the project", "the plan" that does not correspond to global essential characteristics of the ideal – a superattractor including all the scale of axiological categories, such as value, meaning, truth, as well as a doubtless strategic component.

Taking into account the complex nature of a superattractor in social systems, in my opinion, it is pertinent to make emphasis on understanding of a superattractor as the global goal of the system dealing with world outlook and value systems in the social processes. In this case the term "the ideal" in the best way possible corresponds to such a concept including complex subjective social characteristics.



So, from the view point of synergetics and the conception offered by V.P. Bransky, development can be interpreted as the directed non-linear movement to a superattractor fulfilled through the change of local attractors by means of self-organization.

For example, for today, such a broad social phenomenon as globalization can be understood, proceeding from the synergistic paradigm, as a social self-organization of the wide range.

The concept of a global superattractor of the social system is used as a consolidating parametre uniting the scope of self-organization processes at various being levels and determining the evolution in its integrity. On this basis the contemporary synergistic world outlook becomes truly holistic: any object is as the universal component which "strives" for a superattractor.

**4. Conclusion.** Defining an attractor as one of the crucial concepts of the contemporary synergetics in the pan-humanitarian supplement is caused by its goal-like behaviour and backbone characteristics. In this context the concept of «a superattractor» offered by the Russian philosophical school, which allows to interpret the unified process of the universal evolution from the view point of the synergistic methodology is challenging.

#### References:

- 1.Maksimova M.V. Innovation and synergistic reconstruction of evolutionary epistemology S. Tulmina. Scientific thought of the Caucasus.- 2010,- No. 1, pp.56-60
- 2.Maksimova M.V. Innovations in synergetics of socio-humanitarian processes. CHAOS 2009 : Chaotic Modeling and Simulation : Books of Abstracts International Conference, Chania Crete Greece, June 1-5, 2009 / Editor Christos H. Skiadas.- Chania Crete Greece, 2009.- p.47
- 3.Mamchur E.N. Spontaneity and teleologism. Spontaneity and determinism. Institute of Philosophy at the Russian Academy of Sciences. – M.: Nauka, 2006. – pp. 225–248.
- 4.Moiseyev N.N. Farewell to simplicity / N.N. Moiseyev. – M.: Agraf, 1998. – p. 474.
- 5.Bransky V.P. Globalisation and synergistic historicism. St. Petersburg: Politekhnik, 2004. – p. 400.







## Weak Regularized Solutions to Stochastic Cauchy Problems\*

Irina V. Melnikova<sup>1</sup> and Uljana A. Alekseeva<sup>2</sup>

<sup>1</sup> Ural Federal University, Institute of Mathematics and Computer Sciences, 620083 Ekaterinburg, Lenina av., 51, Russia  
(E-mail: [Irina.Melnikova@usu.ru](mailto:Irina.Melnikova@usu.ru))

<sup>2</sup> Ural Federal University, Institute of Mathematics and Computer Sciences, 620083 Ekaterinburg, Lenina av., 51, Russia  
(E-mail: [Uljana.Alekseeva@usu.ru](mailto:Uljana.Alekseeva@usu.ru))

**Abstract.** The Cauchy problem for systems of differential equations with stochastic perturbations is studied. Weak regularized solution are constructed for the case of systems with operators generating  $R$ -semigroups; generalized and mild solutions are introduced.

**Keywords:** white noise process; Wiener process; weak, regularized, generalized and mild solutions; Gelfand-Shilov spaces.

### 1 Introduction

Let  $(\Omega, \mathcal{F}, P)$  be a random space. We consider the Cauchy problem for the systems of differential equations with stochastic perturbations:

$$\frac{\partial X(t, x)}{\partial t} = A \left( i \frac{\partial}{\partial x} \right) X(t, x) + BW(t, x), \quad t \in [0, T], \quad x \in \mathbb{R}, \quad (1)$$

$$X(0, x) = f(x), \quad (2)$$

where  $A \left( i \frac{\partial}{\partial x} \right)$  is a matrix operator:  $A \left( i \frac{\partial}{\partial x} \right) = \{A_{jk} \left( i \frac{\partial}{\partial x} \right)\}_{j, k=1}^m$  generating different type systems in the Gelfand-Shilov classification [3],  $A_{jk} \left( i \frac{\partial}{\partial x} \right)$  are linear differential operators in  $L_2(\mathbb{R})$  of finite orders;  $\mathcal{W} = \{\mathcal{W}(t), t \geq 0\}$  is a random process of white noise type in  $L_2^n(\mathbb{R})$ :  $\mathcal{W}(t) = (\mathcal{W}_1(t, x, \omega), \dots, \mathcal{W}_1(t, x, \omega))$ ,  $x \in \mathbb{R}$ ,  $\omega \in \Omega$ ;  $B$  is a bounded linear operator from  $L_2^n(\mathbb{R})$  to  $L_2^m(\mathbb{R})$ ;  $f$  is an  $L_2^m(\mathbb{R})$ -valued random variable;  $X = \{X(t), t \in [0, T]\}$  is an  $L_2^m(\mathbb{R})$ -valued stochastic process  $X(t) = (X_1(t, x, \omega), \dots, X_m(t, x, \omega))$ ,  $x \in \mathbb{R}$ ,  $\omega \in \Omega$ , which is to be determined.

This problem usually is not well-posed for several reasons. The first one is caused by the fact that the differential operators  $A \left( i \frac{\partial}{\partial x} \right)$  generally do not generate semigroups of class  $C_0$  and the corresponding homogeneous Cauchy problem is not uniformly well-posed in  $L_2^m(\mathbb{R})$ , they generate only some regularized semigroups. By this reason we look for a regularized solution of (1)–(2). The second reason is the irregularity of a white noise process, because of this we need to consider not the original equation (1) but the integrated one, that is

\* The work was supported by the Ministry of Education and Science of Russian Federation (Program 1.1016.2011) and by RFBR, project 13-01-00090



an equation in the Ito form with a Wiener process  $W$  being a kind of primitive of white noise  $\mathcal{W}$ :

$$X(t, x) = f(x) + \int_0^t A \left( i \frac{\partial}{\partial x} \right) X(\tau, x) d\tau + BW(t, x), \quad t \in [0, T], \quad x \in \mathbb{R}. \quad (3)$$

In addition, we can not expect the stochastic inhomogeneity be in the domain of  $A \left( i \frac{\partial}{\partial x} \right)$ , by this reason we have to explore weak regularized solutions to the integrated problem (3).

## 2 Necessary definitions and preliminary results

We consider the problem (1)–(2) as an important particular case of the abstract Cauchy problem

$$X'(t) = AX(t) + BW(t), \quad t \in [0, T], \quad X(0) = f, \quad (4)$$

and the problem (3) as that of the abstract integral one (written as usually in the form of differentials):

$$dX(t) = AX(t)dt + BdW(t), \quad t \in [0, T], \quad X(0) = f, \quad (5)$$

with  $A$  being the generator of a regularized semigroup in a Hilbert space  $H$ , especially an  $R$ -semigroup (see, exp., Melnikova[4], Melnikova and Anufrieva[6]). Thus, we continue investigations of Da Prato[2], Melnikova *et al.* [5], Alshanskiy and Melnikova[1]. We assume in this paper  $H = L_2^m(\mathbb{R})$ .

**Definition 1.** Let  $A$  be a closed operator and  $R$  be a bounded linear operator in  $L_2^m(\mathbb{R})$  with a densely defined  $R^{-1}$ . A strongly continuous family  $S := \{S(t), t \in [0, \tau]\}$ ,  $\tau \leq \infty$ , of bounded linear operators in  $L_2^m(\mathbb{R})$  is called an  $R$ -regularized semigroup (or  $R$ -semigroup) generated by  $A$  if

$$S(t)Af = AS(t)f, \quad t \in [0, \tau), \quad f \in \text{dom } A, \quad (6)$$

$$S(t)f = A \int_0^t S(\tau)f ds + Rf, \quad t \in [0, \tau), \quad f \in L_2^m(\mathbb{R}). \quad (7)$$

The semigroup is called *local* if  $\tau < \infty$ .

**Definition 2.** Let  $Q$  be a symmetric nonnegative trace class operator in  $L_2^n(\mathbb{R})$ . An  $L_2^n(\mathbb{R})$ -valued stochastic process  $\{W(t), t \geq 0\}$  is called a  $Q$ -Wiener process if

(W1)  $W(0) = 0$   $P_{\text{a.s.}}$ ;

(W2) the process has independent increments  $W(t) - W(s)$ ,  $0 \leq s \leq t$ , with normal distribution  $\mathcal{N}(0, (t - s)Q)$ ;

(W3)  $W(t)$  has continuous trajectories  $P_{\text{a.s.}}$

**Definition 3.** Let  $\{\mathcal{F}_t, t \leq \infty\}$  be a filtration defined by  $W$ . An  $L_2^m(\mathbb{R})$ -valued  $\mathcal{F}_t$ -measurable process  $X = \{X(t), t \in [0, T]\}$  is called a *weak  $R$ -solution* of



the problem (3) with  $A \left( i \frac{\partial}{\partial x} \right)$  generating an  $R$ -semigroup  $\{S(t), t \in [0, \tau]\}$  in  $L_2^m(\mathbb{R})$  if the following conditions are fulfilled:

- 1) for each  $t \in [0, T], k = \overline{1, m}, \int_0^t \|X_k(\cdot, \tau)\|_{L_2(\mathbb{R})} d\tau < \infty P_{a.s.}$ ;
- 2) for each  $g \in \text{dom } A^*, X$  satisfies the weak regularized equation:

$$\langle X(t), g \rangle = \langle Rf, g \rangle + \int_0^t \langle X(\tau), A^*g \rangle d\tau + \langle RBW(t), g \rangle P_{a.s.}, \quad t \in [0, T]. \quad (8)$$

It is proved by Melnikova and Alshanskiy[1] that a weak  $R$ -solution of the abstract stochastic Cauchy problem (5) with densely defined  $A$  being the generator of an  $R$ -semigroup and  $W$  being a  $Q$ -Wiener process exists and is unique. In our case of the problem (3) we have the following result.

**Theorem 1.** *Let  $\{W(t), t \geq 0\}$  be a  $Q$ -Wiener process in  $L_2^n(\mathbb{R})$  and  $A \left( i \frac{\partial}{\partial x} \right)$  be the generator of an  $R$ -semigroup  $\{S(t), t \in [0, \tau]\}$  in  $L_2^m(\mathbb{R})$  satisfying the condition*

$$\int_0^t \|S(\tau)B\|_{HS}^2 d\tau < \infty, \quad (9)$$

where  $\|\cdot\|_{HS}$  is the norm in the space of Hilbert-Schmidt operators acting from the space  $Q^{\frac{1}{2}}L_2^n(\mathbb{R})$  to  $L_2^m(\mathbb{R})$ . Then for each  $\mathcal{F}_0$ -measurable  $L_2^m(\mathbb{R})$ -valued random variable  $f$

$$X(t) = S(t)f + \int_0^t S(t-\tau)B dW(\tau), \quad t \in [0, T], \quad (10)$$

is the unique weak  $R$ -solution of (5).

We see in (10) that the main part of constructing an  $R$ -solution is constructing an  $R$ -semigroup generated by  $A$ . It is not an easy task to construct  $R$ -semigroups generated by given operators  $A$  in the general case. But for differential operators  $A \left( i \frac{\partial}{\partial x} \right)$  such semigroups can be constructed and we describe a way to do this in the present paper.

Our methods are based on investigations of the differential systems:

$$\frac{\partial u(t, x)}{\partial t} = A \left( i \frac{\partial}{\partial x} \right) u(t, x), \quad t \in [0, T], \quad x \in \mathbb{R}, \quad (11)$$

provided by the generalized Fourier transform technique in [3]. So, let us apply the Fourier transform to the system (11) and consider the dual one:

$$\frac{\partial \tilde{u}(t, s)}{\partial t} = A(s)\tilde{u}(t, s), \quad t \in [0, T], \quad s \in \mathbb{C}. \quad (12)$$

Let the functions  $\lambda_1(\cdot), \dots, \lambda_m(\cdot)$  be characteristic roots of the system (12) and  $\Lambda(s) := \max_{1 \leq k \leq m} \Re \lambda_k(s), s \in \mathbb{C}$ . Then solution operators of (12) have the following estimation

$$e^{tA(s)} \leq \left\| e^{tA(s)} \right\|_m \leq C(1 + |s|)^{p(m-1)} e^{t\Lambda(s)}, \quad t \geq 0, \quad s \in \mathbb{C}. \quad (13)$$



**Definition 4.** A system (11) is called

- 1) *correct by Petrovsky* if there exists such a  $C > 0$  that  $A(\sigma) \leq C$ ,  $\sigma \in \mathbb{R}$ ;
- 2) *conditionally-correct* if there exist such constants  $C > 0$ ,  $0 < h < 1$ ,  $C_1 > 0$  that  $A(\sigma) \leq C|\sigma|^h + C_1$ ,  $\sigma \in \mathbb{R}$ ;
- 3) *incorrect* if the function  $A(\cdot)$  grows for real  $s = \sigma$  in the same way as for complex ones:  $A(\sigma) \leq C|\sigma|^{p_0} + C_1$ ,  $\sigma \in \mathbb{R}$ .

Finally, note that the operator  $i \frac{\partial}{\partial x}$  is self-conjugate in  $L_2(\mathbb{R})$ :  $(i \frac{\partial}{\partial x})^* = i \frac{\partial}{\partial x}$ . Hence the differential operator of (1) has the following conjugate one

$$A^* \left( i \frac{\partial}{\partial x} \right) = \left\{ \overline{A_{kj}} \left( i \frac{\partial}{\partial x} \right) \right\}_{k,j=1}^m,$$

obtained of  $\{A_{jk} (i \frac{\partial}{\partial x})\}_{j,k=1}^m$  by replacing components with conjugate operators and by further transposition.

### 3 Construction of $R$ -semigroups generated by $A (i \frac{\partial}{\partial x})$

Since for the problem (12) solution operators of multiplication by  $e^{tA(\cdot)}$ ,  $t \geq 0$ , generally have an exponential growth (13), one can not obtain propagators of the problem (11) in the framework of the classical inverse Fourier transform. That is why we introduce an appropriate multiplier  $K(\cdot)$  into the inverse Fourier transform:

$$G_R(t, x) := \frac{1}{2\pi} \int_{-\infty}^{\infty} e^{i\sigma x} K(\sigma) e^{tA(\sigma)} d\sigma, \quad (14)$$

providing the uniform convergence of this integral with respect to  $t \in [0, T]$  in  $L_2^m(\mathbb{R}) \times L_2^m(\mathbb{R}) =: \mathbf{L}_2^m$ . For this purpose we require  $K(\cdot)e^{tA(\cdot)} \in \mathbf{L}_2^m$ .

The matrix-function  $G_R(t, x)$  obtained in (14) is a regularized Green function. If its convolution with  $f$  is well-defined, then the convolution gives a regularized solution of (11). In addition to the above condition, we introduce  $K(\cdot)$  providing

$$\int_{-\infty}^{\infty} e^{i\sigma x} K(\sigma) e^{tA(\sigma)} \tilde{f}(\sigma) d\sigma \in L_2^m(\mathbb{R}), \quad t \in [0, T], \quad (15)$$

for each  $\tilde{f} \in L_2^m(\mathbb{R})$ . These conditions hold, for example, if  $K(\cdot)e^{tA(\cdot)} \in \mathbf{L}_2^m$  and is bounded.

Now we show that the family of convolution operators with  $G_R(t, x)$ :

$$(S(t)f)(x) := G_R(t, x) * f(x), \quad t \in [0, \tau), \quad (16)$$

forms a local  $R$ -semigroup in  $L_2^m(\mathbb{R})$  for any  $\tau < \infty$ . To begin with, we verify the strong continuity property of the family  $\{S(t), t \in [0, T]\}$ ,  $T < \infty$ : for arbitrary  $f \in L_2^m(\mathbb{R})$  we show that  $\|S(t)f - S(t_0)f\|_{L_2^m(\mathbb{R})} \rightarrow 0$  as  $t \rightarrow t_0$ .

$$\|S(t)f - S(t_0)f\|_{L_2^m(\mathbb{R})}^2 =$$



$$= \int_{\mathbb{R}} \left( \frac{1}{2\pi} \int_{-\infty}^{\infty} e^{i\sigma x} K(\sigma) \left[ e^{tA(\sigma)} \tilde{f}(\sigma) - e^{t_0 A(\sigma)} \tilde{f}(\sigma) \right] d\sigma \right)^2 dx.$$

Let us split the inner integral into the three integrals:

$$\begin{aligned} & \int_{|\sigma| \geq N} e^{i\sigma x} K(\sigma) e^{tA(\sigma)} \tilde{f}(\sigma) d\sigma - \int_{|\sigma| \geq N} e^{i\sigma x} K(\sigma) e^{t_0 A(\sigma)} \tilde{f}(\sigma) d\sigma \\ & + \int_{|\sigma| \leq N} e^{i\sigma x} K(\sigma) \left[ e^{tA(\sigma)} - e^{t_0 A(\sigma)} \right] \tilde{f}(\sigma) d\sigma. \end{aligned} \quad (17)$$

Note that the functions  $h_N(x, t) := \int_{|\sigma| \geq N} e^{i\sigma x} K(\sigma) e^{tA(\sigma)} \tilde{f}(\sigma) d\sigma$  and

$$g_N(x, t) := \int_{|\sigma| \leq N} e^{i\sigma x} K(\sigma) \left[ e^{tA(\sigma)} - e^{t_0 A(\sigma)} \right] \tilde{f}(\sigma) d\sigma$$

are elements of  $L_2^m(\mathbb{R})$  for all  $t \in [0, T]$  as the inverse Fourier transform of the functions from  $L_2^m(\mathbb{R})$

$$\tilde{h}_N(\sigma, t) = \begin{cases} 0, & |\sigma| \leq N, \\ K(\sigma) e^{tA(\sigma)} \tilde{f}(\sigma), & |\sigma| > N, \end{cases}$$

and  $\tilde{g}_N(\sigma, t) = K(\sigma) e^{tA(\sigma)} \tilde{f}(\sigma) - \tilde{h}_N(\sigma, t)$ , respectively. Further, since  $K(\cdot) e^{tA(\cdot)} \in \mathbf{L}_2^m$  and  $\tilde{f}(\cdot) \in L_2^m(\mathbb{R})$ , the integral (15) is convergent uniformly with respect to  $x \in \mathbb{R}$  and  $t \in [0, T]$ , then for any  $\varepsilon > 0$

$$|h_N(x, t)| < \varepsilon/4, \quad x \in \mathbb{R}, \quad t \in [0, T],$$

by the choice of  $N$ . So, sum of absolute values of the first two integrals in (17) is less than  $\varepsilon/2$ . Now fix  $N$ . Since  $(e^{(t-t_0)A(\sigma)} - 1) \rightarrow 0$  as  $t \rightarrow t_0$  uniformly with respect to  $\sigma \in [-N, N]$ , we can take

$$|g_N(x, t)| < \varepsilon/2, \quad x \in \mathbb{R}, \quad t \in [0, T].$$

To obtain the estimate for

$$\|S(t)f - S(t_0)f\|_{L_2^m(\mathbb{R})}^2 = \frac{1}{4\pi^2} \int_{\mathbb{R}} (h_N(x, t) - h_N(x, t_0) + g_N(x, t))^2 dx$$

we consider the difference  $h_N(x, t) - h_N(x, t_0) =: \Delta_N(x, t, t_0)$ ,  $t, t_0 \in [0, T]$ , as a single function, then  $\Delta_N(\cdot, t, t_0) \in L_2^m(\mathbb{R})$  and for a fixed  $N$  by the choice of  $t_0$ ,  $|\Delta_N(x, t, t_0)| < \varepsilon/2$ ,  $x \in \mathbb{R}$ . In these notations we have:

$$\begin{aligned} & 4\pi^2 \|S(t)f - S(t_0)f\|_{L_2^m(\mathbb{R})}^2 = \\ & = \int_{\mathbb{R}} \Delta_N^2(x, t, t_0) dx + 2 \int_{\mathbb{R}} \Delta_N(x, t) g_N(x, t, t_0) dx + \int_{\mathbb{R}} g_N^2(x, t) dx. \end{aligned}$$

On the way described above one can show that every of these three integrals is an infinitesimal value. That is the integrals over the infinite intervals  $|x| > M$



are small by the choice of  $M$  because of their uniform convergence with respect to  $t \in [0, T]$ . Integrals on compacts  $[-M, M]$  are small because the integrands are small, that provided by the sequential choice of  $M$  and  $t \in [0, T]$ . This completes the proof that operators of the family (16) are strongly continuous.

Next, we show that the obtained operators commute with  $A\left(i\frac{\partial}{\partial x}\right)$  on  $f \in \text{dom}A\left(i\frac{\partial}{\partial x}\right)$ . By properties of convolution, a differential operator may be applied to any components of convolution, so we apply  $A\left(i\frac{\partial}{\partial x}\right)$  to  $f \in \text{dom}A\left(i\frac{\partial}{\partial x}\right)$ :

$$A\left(i\frac{\partial}{\partial x}\right)(S(t)f)(x) = G_R(t, x) * A\left(i\frac{\partial}{\partial x}\right)f(x) = S(t)A\left(i\frac{\partial}{\partial x}\right)f(x).$$

Hence, the equality (6) holds. In conclusion, we show the  $R$ -semigroup equation (7). For an arbitrary  $f \in \text{dom}A\left(i\frac{\partial}{\partial x}\right)$  consider the equality:

$$\frac{\partial}{\partial t}(S(t)f)(x) = \frac{\partial}{\partial t}[G_R(t, x) * f(x)] = \frac{1}{2\pi} \frac{\partial}{\partial t} \int_{-\infty}^{\infty} e^{i\sigma x} K(\sigma) e^{tA(\sigma)} \tilde{f}(\sigma) d\sigma.$$

Since the integral converges uniformly with respect to  $t \in [0, T]$ , we can differentiate under the integral sign:

$$\frac{\partial}{\partial t}(S(t)f)(x) = \frac{1}{2\pi} \int_{-\infty}^{\infty} e^{i\sigma x} K(\sigma) e^{tA(\sigma)} A(\sigma) \tilde{f}(\sigma) d\sigma.$$

The condition  $f \in \text{dom}A\left(i\frac{\partial}{\partial x}\right)$  provides  $A(\cdot)\tilde{f}(\cdot) \in L_2^m(\mathbb{R})$ , hence the inverse Fourier transform of  $A(\sigma)\tilde{f}(\sigma)$  is  $A\left(i\frac{\partial}{\partial x}\right)f(x)$  and

$$\begin{aligned} \frac{\partial}{\partial t}(S(t)f)(x) &= G_R(t, x) * A\left(i\frac{\partial}{\partial x}\right)f(x) = \\ &= A\left(i\frac{\partial}{\partial x}\right)[G_R(t, x) * f(x)] = A\left(i\frac{\partial}{\partial x}\right)(S(t)f)(x). \end{aligned}$$

Integration with respect to  $t$  gives the equality

$$(S(t)f)(x) - (S(0)f)(x) = \int_0^t A\left(i\frac{\partial}{\partial x}\right)(S(\tau)f)(x) d\tau.$$

Since  $A\left(i\frac{\partial}{\partial x}\right)$  is closed in  $L_2^m(\mathbb{R})$  and differentiable functions are dense there, this equality holds for any  $f \in L_2^m(\mathbb{R})$ :

$$(S(t)f)(x) - (S(0)f)(x) = A\left(i\frac{\partial}{\partial x}\right) \int_0^t (S(\tau)f)(x) d\tau, \quad t \in [0, T].$$

Put operator  $R$  in  $L_2^m(\mathbb{R})$  equal to  $S(0)$ , then by the strong continuity property,

$$Rf(x) = \frac{1}{2\pi} \int_{-\infty}^{\infty} e^{i\sigma x} K(\sigma) \tilde{f}(\sigma) d\sigma.$$

So, we have an  $R$ -semigroup generated by  $A\left(i\frac{\partial}{\partial x}\right)$  constructed in  $L_2^m(\mathbb{R})$ .

Now for all types of systems (11) – correct by Petrovsky, conditionally-correct and incorrect – we introduce appropriate correcting functions  $K(\sigma)$  as follows:



- for systems correct by Petrovsky we take  $K(\sigma) = \frac{1}{(1+\sigma^2)^{d/2+1}}$ , where  $d = p(m-1)$ ,
- for conditionally-correct systems we take  $K(\sigma) = e^{-a|\sigma|^h}$ , where  $a > \text{const} \cdot T$ ,
- for incorrect systems —  $K(\sigma) = e^{-a|\sigma|^{p_0}}$ , where  $a > \text{const} \cdot T$ .

#### 4 Some remarks on generalized solutions and solutions of quasi-linear equations

In the previous section we have studied  $R$ -solutions to the problem (5) with differential operators  $A(i\frac{\partial}{\partial x})$  that are generators of  $R$ -semigroups in  $H = L_2^m(\mathbb{R})$ , and we focused ourself on the construction of these  $R$ -semigroups. If not a regularized, but a genuine solution of the problem is needed, then we have to construct the solution in spaces, where operator  $R^{-1}$  is bounded.

How difficult it is to construct  $R$ -semigroups in general, we have noted. Constructing the required spaces in the general case, the same challenge. Nevertheless, in the case of the differential operators  $A(i\frac{\partial}{\partial x})$  suitable spaces can be chosen among those constructed by Gelfand[3] on the basis of the generalized Fourier transform technique. If to take  $f$  being an  $L_2^m(\mathbb{R})$ -valued random variable, for systems correct by Petrovsky we can construct a generalized solution  $X(t, \cdot, \omega) = (X_1(t, \cdot, \omega), \dots, X_m(t, \cdot, \omega))$ ,  $t \in [0, T]$ ,  $\omega \in \Omega$ , in  $\mathcal{S}' \times \dots \times \mathcal{S}'$ , where  $\mathcal{S}'$  is known as the space of distributions of slow growth. For conditionally-correct systems these are spaces  $(\mathcal{S}_{\beta, \mathcal{B}}^{\alpha, \mathcal{A}})'$  of distribution increasing exponentially with order  $1/\beta$  dual to  $\mathcal{S}_{\beta, \mathcal{B}}^{\alpha, \mathcal{A}}$  — the space of all infinitely differentiable functions satisfying the condition: for any  $\varepsilon > 0, \delta > 0$

$$|x^k \varphi^{(q)}(x)| \leq C_{\varepsilon, \delta} (\mathcal{A} + \varepsilon)^k (\mathcal{B} + \delta)^q k^{\alpha} q^{\beta}, \quad k, q \in \mathbb{N}_0, \quad x \in \mathbb{R},$$

with a constant  $C_{\varepsilon, \delta} = C_{\varepsilon, \delta}(\varphi)$ . And for incorrect systems the required space is  $\mathcal{Z}'$ , that is dual to the space  $\mathcal{Z}$  of all integer functions  $\varphi(\cdot)$  of argument  $z \in \mathbb{C}$ , satisfying the condition

$$|z^k \varphi(z)| \leq C_k e^{b|y|}, \quad k \in \mathbb{N}_0, \quad z = x + iy \in \mathbb{C},$$

with some constants  $b = b(\varphi)$ ,  $C_k = C_k(\varphi)$ .

Now consider the Cauchy problem for a quasi-linear equation:

$$dX(t) = AX(t)dt + F(t, X)dt + BdW(t), \quad t \in [0, T], \quad X(0) = f, \quad (18)$$

with  $A$  being the generator of an  $R$ -semigroup in a Hilbert space  $H$ , in particular with  $A = A(i\frac{\partial}{\partial x})$  generating one of the constructed  $R$ -semigroups in  $H = L_2^m(\mathbb{R})$ . Here  $F(t, X)$  is a nonlinear term satisfying the following conditions:

- (F1)  $\|F(t, y_1) - F(t, y_2)\|_H \leq C\|y_1 - y_2\|_H$ ,  $t \in [0, T]$ ,  $y_1, y_2 \in H$  (the Lipschitz condition);
- (F2)  $\|f(t, y)\|_H^2 \leq C\|1 + y\|_H^2$ ,  $t \in [0, T]$ ,  $y \in H$  (the growth condition).

Let us introduce a definition of a mild  $R$ -solution for the quasi-linear Cauchy problem (18). In the sense of this paper terminology it will be a strong solution.



**Definition 5.** An  $H$ -valued  $\mathcal{F}_t$ -measurable process  $\{X(t), t \in [0, T]\}$ ,  $X(t) = X(t, \omega), \omega \in \Omega$ , is called a *mild  $R$ -solution* of the problem (18) with  $A$  generating an  $R$ -semigroup  $S := \{S(t), t \in [0, \tau]\}$  if

- 1)  $\int_0^T \|X(\tau)\|_H d\tau < \infty$   $P_{\text{a.s.}}$ ;
- 2) for each  $t \in [0, T]$ ,  $X(t)$  satisfies the following equation

$$X(t) = S(t)f + \int_0^t S(t-s)F(s, X(s)) ds + \int_0^t S(t-s)B dW(s) ds \quad P_{\text{a.s.}} \quad (19)$$

A unique mild  $R$ -solution to (18), in particular to the problem with  $A = A(i \frac{\partial}{\partial x})$  and with  $F$  satisfying the conditions (F1)–(F2), can be constructed by the method of successive approximations, similarly to the case of strongly continuous semigroups considered by Da Prato[2] and Ogorodnikov[8].

As for mild solutions, they can be obtained only in spaces, where operator  $R^{-1}$  is defined, and similarly to the case of the linear problem above, these spaces must be special spaces of generalized functions or even more general spaces, where nonlinear operations on generalized functions are possible. That is the problem for further investigations. The beginning to the investigations of generalized solutions to quasi-linear problems

$$X'(t) = AX(t) + F(t, X) + BW(t), \quad t \geq 0, \quad X(0) = f,$$

was laid in the paper Melnikova and Alekseeva[7] due to construction of abstract stochastic Colombeau spaces.

## References

1. M. A. Alshanskiy and I. V. Melnikova. Regularized and generalized solutions of infinite-dimensional stochastic problems. *Math. sbornik* 202, 11:3–30, 2011.
2. G. Da Prato and J. Zabczyk. Stochastic equations in infinite dimensions. Cambridge Univ. Press, 1992 (454 pages).
3. I. M. Gel'fand and G. E. Shilov. Generalized functions, vol. 3: Some questions of the theory of differential equations (English translation). Academic Press, New York, 1968.
4. I. V. Melnikova and A. Filinkov. The Cauchy problem. Three approaches. Monographs and Surveys in Pure and Applied Mathematics, **120**. CRC / Chapman & Hall, 2001 (240 pages).
5. I. V. Melnikova, A. I. Filinkov and U. A. Anufrieva. Abstract stochastic equations I. Classical and Generalized Solutions. *Journal of Mathematical Sciences* 111, 2:3430–3475, 2002.
6. I. V. Melnikova and U. A. Anufrieva. Peculiarities and regularization of ill-posed Cauchy problems with differential operators. *J. of Math. Sciences* 148, 4:481–632, 2008.
7. I. V. Melnikova and U. A. Alekseeva. Quasilinear stochastic Cauchy problem in abstract Colombeau spaces. *Int. Journal of Mathematics and Mathematical Sciences*, 2012: Article ID 509026, 11 pages, 2012.
8. A. A. Ogorodnikov. Solution of nonlinear stochastic equations with a generator of a semigroup discontinuous at zero. *Russian Mathematics* 55, 6:76–84, 2011.





## The Fractional Laplacian as continuum limit of self-similar lattice models

Thomas M. Michelitsch, Gérard A. Maugin<sup>1</sup>, Shahram Derogar<sup>2</sup>, and Franck C.G.A Nicolleau<sup>3</sup>, Andrzej F. Nowakowski<sup>3</sup>

- <sup>1</sup> Institut Jean le Rond d'Alembert (Paris 6), CNRS UMR 7190 Paris, France  
(E-mail: michel@lmm.jussieu.fr)
- <sup>2</sup> Department of Architecture, Yeditepe University, Istanbul, Turkey  
(E-mail: derogar@yeditepe.edu.tr)
- <sup>3</sup> Sheffield Fluid Mechanics Group, Department of Mechanical Engineering,  
University of Sheffield, United Kingdom  
(E-mail: f.nicolleau@sheffield.ac.uk )

**Abstract.** We show that the fractional Laplacian (FL)  $-(-\Delta)^{\frac{\alpha}{2}}$  is the principal characteristic operator of harmonic systems with self-similar interparticle interactions. We demonstrate that the FL can be rigorously defined by Hamilton's variational principle as “*fractional continuum limit*” of a spring model with self-similar, in some cases fractal harmonic interactions which we introduced recently (Michelitsch *et al.*[5]). We generalize that approach to the multi-dimensional physical space of dimensions  $n = 1, 2, 3, \dots$ . In this way we demonstrate the interlink between fractal discrete behavior (discrete self-similar Laplacian) and its fractional continuum field counterpart (FL) and give the latter a physical justification. The dispersion relation of the discrete model is obtained as self-similar Weierstrass-Mandelbrot fractal function which takes in the fractional continuum limit the form of a smooth self-similar power law. The density of states (density of normal modes) takes the form of a characteristic scaling law which depends only on the scaling exponent of the FL and the dimension of the physical space. The approach has a wide range of interdisciplinary applications of self-similar dynamic problems such as anomalous diffusion (Levi flights), self-similar wave propagation, and may also be useful to model self-similar chaotic processes and dynamics in turbulence.

**Keywords:** Fractional Laplacian, fractional continuum limit, linear chain, Fractals, Weierstrass-Mandelbrot function, self-similarity, scaling laws.

### 1 Introduction

Despite fractional calculus has a long history, recently a new increasing interest has emerged to employ fractional operators and the so called *fractional Laplacian* (FL) (often also referred to as Riesz fractional derivative)  $-(-\Delta)^{\frac{\alpha}{2}}$  where  $\alpha$  indicates a fractional in general non-integer exponent. The reason for this new interest is the conclusion that the fractional approach is a highly powerful mathematical tool to model complex and chaotic phenomena in various disciplines.

The goal of this note is to demonstrate that the FL is the “natural” characteristic linear operator, in a sense most basic operator that can be generated from a physical “self-similar” spring model and its generalizations. Due to its non-local “long tail” and self-similar invariant characteristics of the FL we raise



the question what is the interlink of the FL with fractal and chaotic features often chosen in nature.

Recently many models were developed which employ the *FL* in various physical contexts, among them the description of “complex” dynamic phenomena including anomalous diffusion (Lévi flights) [1–3,8,10] and see also the numerous references therein.

This note is organized as follows: As point of departure we introduce a 1D harmonic spring model with harmonic elastic potential energy which describes *self-similar interparticle interactions* which we developed recently [5]. This discrete model leads to fractal dynamic vibrational characteristics such as a dispersion relation of the form of Weierstrass-Mandelbrot fractal functions. Application of Hamilton’s variational principle defines a discrete self-similar Laplacian with all good properties of a Laplacian: The self-similar Laplacian is self-adjoint, elliptic, negative (semi-) definite (indicating elastic stability), and translational invariant. We introduce a *fractional continuum limit* which yields in rigorous manner the FL. In this way the FL is physically justified being a continuum description of a self-similar spring model. The approach is generalized to  $n$  dimensions of the physical space.

## 2 Linear chain model with self-similar harmonic interactions

We consider an infinite sequence of points  $\{h_p\}$  generated by a non-linear mapping with (initial value  $h = h_0$ )

$$h_{p+1} = N(h_p) = N^p(h), \quad h_{p+1} = N^{-1}(h_p) = N^{-p}(h) \quad (1)$$

where we exclude for convenience periodic orbits and fixed points. All points of the sequence are assumed to fulfil  $h_p \neq h_q$  for  $p \neq q$  ( $-\infty < p < \infty$ ). Define a function  $\Phi$  for  $a$  arbitrary generated by the series

$$\Phi(h) = \sum_{s=-\infty}^{\infty} a^{-\delta s} f(h_s) \quad (2)$$

where the sum is performed over the infinite sequence of points  $h_s$  of (1).  $\Phi(h)$  is defined (convergent) for sufficiently good functions  $f$ . Function  $\Phi$  behaves self-similar under the (in general non-linear) transformation  $h \rightarrow N(h)$  of its argument, namely

$$\Phi(N(h)) = a^\delta \sum_{s=-\infty}^{\infty} a^{-\delta(s+1)} f(h_{s+1}) = a^\delta \Phi(h) \quad (3)$$

For the sake of simplicity but without loss of generality let us consider here a sequence generated by a linear mapping

$$N(h) = ah, \quad a > 1 \quad (4)$$



Then we introduce the self-similar elastic potential in the form of a self-similar function (3), namely

$$\mathcal{W}(x, h) = \frac{1}{4} \sum_{s=-\infty}^{\infty} a^{-\delta s} \{ (u(x + ha^s) - u(x))^2 + (u(x - ha^s) - u(x))^2 \} \quad (5)$$

which is self-similar in the sense of (3) with respect to  $h$ . The elastic potential describes a homogeneous mass distribution where each material point  $x$  is connected with other material points  $x \pm ha^s$  by a self-similar distribution of linear springs of spring constants  $\sim a^{-\delta s}$ . In general this potential can be defined also for nonlinear sequence  $h_s$  of (1). The notion of self-similarity at a point was coined by Peitgen *et al.*[9].

The total elastic energy of (5) is given by

$$V(h) = \int_{-\infty}^{\infty} \mathcal{W}(x, h) dx \quad (6)$$

A self-similar Laplacian is then defined by Hamilton's principle

$$\Delta_{\delta, h} u(x) = -\frac{\delta V}{\delta u(x)} \quad (7)$$

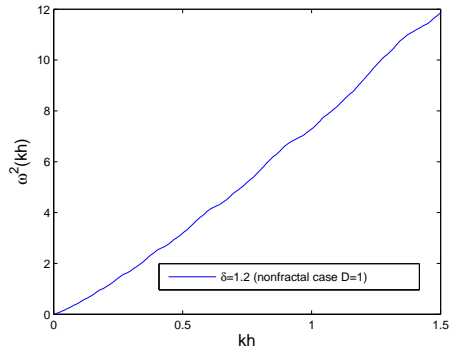
where  $\frac{\delta(\cdot)}{\delta u}$  stands for a functional derivative, and where

$$\Delta_{(\delta, a, h)} u(x) = \sum_{s=-\infty}^{\infty} a^{-\delta s} (u(x + ha^s) + u(x - ha^s) - 2u(x)), \quad 0 < \delta < 2 \quad (8)$$

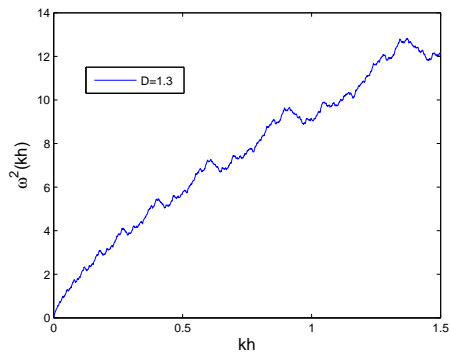
fulfilling self-similarity condition  $\Delta_{\delta, ah} = a^\delta \Delta_{\delta, h}$ . This Laplacian has all required good properties. The dispersion relation (negative eigenvalues) of this Laplacian are obtained in the form of Weierstrass-Mandelbrot functions

$$\omega_{(\delta, a)}^2(kh) = 4 \sum_{s=-\infty}^{\infty} a^{-\delta s} \sin^2\left(\frac{kha^s}{2}\right), \quad 0 < \delta < 2 \quad (9)$$

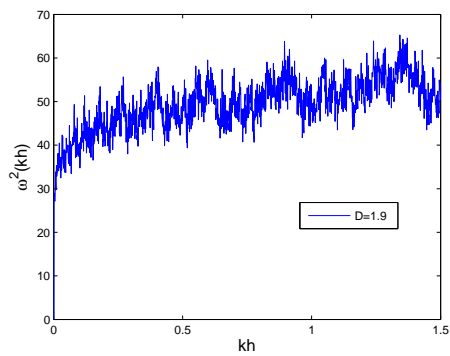
which are self-similar  $\omega_{(\delta, a)}^2(kah) = a^\delta \omega_{(\delta, a)}^2(kh)$  within its entire interval of existence  $0 < \delta < 2$ . The dispersion relation (9) is within  $0 < \delta < 1$  a nowhere differentiable fractal function of estimated Hausdorff dimension  $2 - \delta$  [4,5]. In figures 1-3 cases of increasing fractal dimension (decreasing  $\delta$ ) are plotted. Note that for  $1 \leq \delta < 2$  (9) is a non-fractal function of Hausdorff dimension  $D = 1$  (see figure 1). For increasing fractal dimension  $D$  (decreasing exponent  $\delta$ ) fractal dispersion curves have increasingly erratic characteristics. For more details we refer to our paper Michelitsch *et al.*[5].



**Fig. 1.** Dispersion relation (9) for a non-fractal case.



**Fig. 2.** Dispersion relation (9) for a non-fractal case.



**Fig. 3.** Dispersion relation (9) for a fractal case.



### 3 The FL as fractional continuum limit of the discrete chain Laplacian and its generalization to $n$ dimensions

Now we define the *fractional continuum limit* as follows [6,7]

$$A_a(h) = \lim_{a \rightarrow 1} \sum_{s=-\infty}^{\infty} a^{-\delta s} f(a^s h) \approx \frac{h^\delta}{\zeta} \int_0^\infty \frac{f(\tau)}{\tau^{\delta+1}} d\tau \quad (10)$$

where  $a = 1 + \zeta \rightarrow 1$  and  $0 < \zeta \ll 1$ . The *fractional continuum limit* of the elastic potential (5) takes then the form

$$\mathcal{W}(x, h) \approx \frac{h^\delta}{4\zeta} \int_0^\infty \frac{(u(x+\tau) - u(x))^2 + (u(x-\tau) - u(x))^2}{\tau^{\delta+1}} d\tau, \quad 0 < \delta < 2 \quad (11)$$

which can be generalized to  $n$  dimensions as

$$\mathcal{W}(\mathbf{x}, h, \alpha) \approx \frac{h^\alpha}{4\zeta} \int_0^\infty \frac{(u(\mathbf{x}+\mathbf{r}) - u(\mathbf{x}))^2 + (u(\mathbf{x}-\mathbf{r}) - u(\mathbf{x}))^2}{\tau^{\alpha+n}} d^n \mathbf{r} \quad (12)$$

where  $0 < \alpha < 2$ . Hamilton's principle yields from (12) the fractional continuum limit of the self-similar Laplacian in  $n$  dimensions

$$\Delta_{n,\alpha,h} u(x) =: -\frac{\delta V}{\delta u(x)} = \frac{h^\alpha}{2\zeta} \int_0^\infty \frac{(u(\mathbf{x}+\mathbf{r}) + u(\mathbf{x}-\mathbf{r}) - 2u(\mathbf{x}))}{\tau^{\alpha+n}} d^n \mathbf{r} \quad (13)$$

with  $0 < \alpha < 2$ . (13) recovers for  $n = 1$  also the fractional continuum limit of the self-similar Laplacian (8). The dispersion relation is obtained by  $\Delta_{n,\alpha,h} e^{ikx} = -\omega_{n,\alpha,h}^2(kh) e^{ikx}$  and yields [8] a power-law of the form

$$\omega_{n,\alpha,h}^2(kh) = \mathcal{A}_{n,\alpha} k^\alpha, \quad 0 < \alpha < 2 \quad (14)$$

with the positive constant [8]

$$\mathcal{A}_{n,\alpha} = \frac{h^\alpha}{\zeta} \frac{\pi^{\frac{n}{2}}}{2^{\alpha-1}\alpha} \frac{\Gamma(1 - \frac{\alpha}{2})}{\Gamma(\frac{\alpha+n}{2})} > 0, \quad 0 < \alpha < 2 \quad (15)$$

The positiveness of this constant is a consequence of the elastic stability.

The following observation is crucial: The fractional continuum limit Laplacian (13) coincides (up to a normalization factor) with the FL which is defined, e.g. [2,3,10]

$$\Delta_{n,\alpha,h} = -\mathcal{A}_{n,\alpha} (-\Delta)^{\frac{\alpha}{2}} \quad (16)$$

where the constant (15) is consistent with the normalization factor given by in the literature e.g. [2,3,10] and where (13) recovers with (16) and (15) the standard representation of the FL. Our self-similar chain model represents hence a discrete lattice counterpart which corresponds in the fractional continuum approximation the FL fractional approach.



With (15) it is straight-forward to obtain the density of normal modes (“density of states”)  $\mathcal{D}(\omega)$  where  $\mathcal{D}(\omega)d\omega$  measures the number of eigenmodes of frequency  $\omega$ . It is obtained as [8]

$$\mathcal{D}_{\alpha,n}(\omega) = B_{n,\alpha}\omega^{\frac{2n}{\alpha}-1}, \quad 0 < \alpha < 2 \quad (17)$$

with

$$B_{n,\alpha} = \frac{2^{2-n}}{\pi^{\frac{n}{2}} \Gamma(\frac{n}{2}) \alpha \mathcal{A}_{n,\alpha}^{\frac{n}{\alpha}}} \quad (18)$$

We observe that the state density  $\mathcal{D}_{\alpha,n}(\omega)$  scales as  $\sim \omega^{\frac{2n}{\alpha}-1}$  with a positive exponent where  $0 < n-1 < \frac{2n}{\alpha}-1$  depending only on physical dimension  $n$  and  $\alpha$ . Because of  $0 < \alpha < 2$  the scaling exponent of the self-similar density of states (17) is always greater than the exponent  $n-1$  of the standard Laplacian which is asymptotically approached by (17) when  $\alpha$  approaches the forbidden value  $\alpha \rightarrow 2$ .

## 4 Conclusions

We have demonstrated in this brief note that the fractional Laplacian can be rigorously defined as the fractional continuum limit by a self-similar linear spring model and its generalization to  $n = 1, 2, 3..$  dimensions. In this way a physical justification for the FL is introduced. The model also reveals the interlink between fractal vibrational Weierstrass-Mandelbrot characteristics and its smooth fractional continuum counterpart. The present approach allows to develop a smooth fractional field theory of phenomena with fractal and erratic - chaotic features [8]. Especially noteworthy is a vast potential of applications which include dynamic processes such as anomalous diffusion (Lévi flights), wave propagation and turbulence problems.

## References

- 1.D. Brockmann and L. Hufnagel, Front Propagation in Reaction-Superdiffusion Dynamics: Taming Levy Flights with Fluctuations, *Phys. Rev. Lett.* 98, 178301 (2007).
- 2.Z.-Q. Chen, P. Kim, R. Song, Heat kernel estimates for the Dirichlet FL, *J. Eur. Math. Soc.* 12, 1307-1329 (2008).
- 3.A. Hanyga, Multi-dimensional solutions of space-time fractional diffusion equations, *Proc. R. Soc. Lond. A*, 458, 429-450 (2002). doi: 10.1098/rspa.2001.0893
- 4.G.H. Hardy, Weierstrass's non-differentiable function. In: *Trans. Amer. Math. Soc.* Bd. 17, Nr. 3, 1916, S. 301-325, doi:10.1090/S0002-9947-1916-1501044-1.
- 5.T.M. Michelitsch, G.A. Maugin, F. C. G. A. Nicolleau, A. F. Nowakowski, S. Derogar. Dispersion relations and wave operators in self-similar quasicontinuous linear chains. *Physical Review E* 80, 011135, 2009.
- 6.T. M. Michelitsch, The self-similar field and its application to a diffusion problem, *J. Phys. A: Math. Theor.* 44 465206, 2011.



- 7.T.M. Michelitsch, G.A. Maugin, M. Rahman, S. Derogar, A.F. Nowakowski, F. C. G. A. Nicolleau, A continuum theory for one-dimensional self-similar elasticity and applications to wave propagation and diffusion, *European Journal of Applied Mathematics*, vol. 23, pp. 709-735, 2012).
- 8.T.M. Michelitsch, G.A. Maugin, A.F. Nowakowski, F. Nicolleau, The fractional Laplacian as a limiting case of a self-similar spring model and applications to n-dimensional anomalous diffusion. *Fractional Calculus and Applied Analysis*, in press.
- 9.H.O. Peitgen, H. Juergens, D. Saupe, *Fractals for the Classroom” Part Two*, Springer-Verlag, New York, und NCTM, 1992.
- 10.J. L. Vazquez (2010), *Nonlinear Diffusion with Fractional Laplacian Operators*. In *Nonlinear partial differential equations: the Abel Symposium 2010*; Holden, Helge & Karlsen, Kenneth H. eds., Springer, 2012. Pp. 271-298.







## Laceability in the Brick Product of Cycles

Dr. R.Murali<sup>\*</sup>, Shivaputra<sup>#</sup>, Chetan.S<sup>#</sup>

<sup>\*</sup>Department of Mathematics, Dr.Ambedkar Institute of Technology, India.

<sup>#</sup>Department of Electronics and Communication Engineering, Dr. Ambedkar Institute of Technology, India

E-mail: muralir2968@gmail.com

**Abstract:** B. Alspach, C.C. Chen and Kevin Mc Avaney [1] have discussed the Hamiltonian laceability of the Brick product  $C(2n, m, r)$  for even cycles. In [2], the authors have explored the Hamiltonian laceability properties of  $(m,r)$ -Brick Product  $C(2n+1, 1, r)$  for  $r=2,3$ . In [3] the authors have established Hamiltonian laceability properties of  $C(2n+1, 1, r)$  for  $r=3,4$ . In this paper we present the Hamiltonian laceability properties of  $C(2n+1, 1, r)$  for  $r=5,6$ , and 7.

**Keywords -** Brick product, Connected graph, Hamiltonian-t-laceable graph.

**2000 Mathematics subject classification:** 05C45, 05C99

### 1. INTRODUCTION

Let  $G$  be a finite, simple, connected and undirected graph. Let  $u$  and  $v$  be two vertices in  $G$ . The distance between  $u$  and  $v$  in  $G$ , denoted by  $d(u,v)$  is the length of a shortest  $u$ - $v$  path in  $G$ .  $G$  is Hamiltonian laceable if there exists in  $G$  a Hamiltonian path between every pair of distinct vertices in  $G$  at an odd distance.  $G$  is Hamiltonian- $t$ -laceable (Hamiltonian- $t^*$ -laceable) if there exists a Hamiltonian path between every pair of distinct vertices (at least one pair of distinct vertices)  $u$  and  $v$  in  $G$  with the property  $d(u,v)=t$ ,  $1 \leq t \leq \text{diam}G$ . Hamiltonian laceability in the Brick product of even cycles was studied by B.Alspace, C.C.Chen and Kevin McAvaney in [1]. In [2] and [3], the authors have discussed the Hamiltonian laceability properties of the  $(m,r)$ -Brick Product of odd cycles  $C(2n+1,m,r)$  for  $r=2,3$  and 4. In this paper we explore the Hamiltonian- $t$ -laceability of the  $(m,r)$ -Brick Product  $C(2n+1,1,r)$  for  $r=5,6$  and 7.

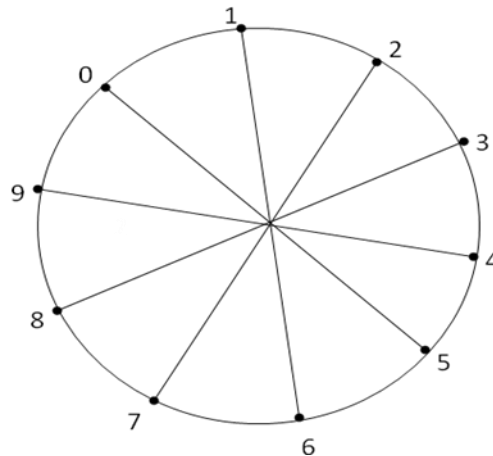
#### **Definition 1: (Brick Product of even cycles):**

Let  $m$ ,  $n$  and  $r$  be a positive integers. Let  $C_{2n} = a_0, a_1, a_2, a_3, \dots, a_{(2n-1)}, a_0$  denote a cycle of order  $2n$ . The  $(m,r)$ -brick product of  $C_{2n}$  denoted

by  $C(2n,m,r)$  is defined as follows. For  $m=1$ , we require that  $r$  be odd and greater than 1. Then,  $C(2n,m,r)$  is obtained from  $C_{2n}$  by adding chords  $a_{2k}(a_{2k+r})$ ,  $k=1,2,\dots,n$ , where the computation is performed under modulo  $2n$ .

From the definition above, it is clear that the Brick product of even cycles is a connected three regular graph.

The following figure 1 shows the Brick product of the cycle  $C_{10}$  for  $r = 5$ .



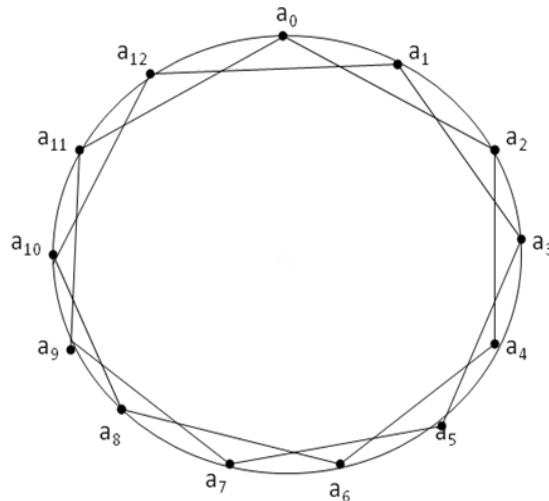
**Fig. 1: Brick product  $C(10,1,5)$**

**Definition 2: (Brick Product of odd cycles):**

Let  $m,n$  and  $r$  be positive integers. Let  $C_{2n+1}=a_0 a_1 a_2 a_3 \dots a_{2n} a_0$  denote a cycle of order  $2n+1$  ( $n>1$ ). The  $(m,r)$ -brick product of  $C_{2n+1}$ , denoted by  $C(2n+1,m,r)$  is defined as follows. For  $m=1$ , we require that  $1 < r < 2n$ . Then  $C(2n+1,m,r)$  is obtained from  $C_{2n+1}$  by adding chords  $a_k(a_{k+r})$ ,  $0 \leq k \leq 2n$  where the computation is performed under modulo  $2n+1$ .

From the definition above, it is clear that the Brick product of odd cycles is a connected four regular graph.

The following figure 2 shows the Brick product of the cycle  $C_{13}$  for  $r=2$ .



**Fig.2: The Brick product C (13, 1, 2)**

**Definition 3:** Let  $u$  and  $v$  be two distinct vertices in a connected graph  $G$ . Then  $u$  and  $v$  are attainable in  $G$  if there exists a Hamiltonian path in  $G$  between  $u$  and  $v$ .

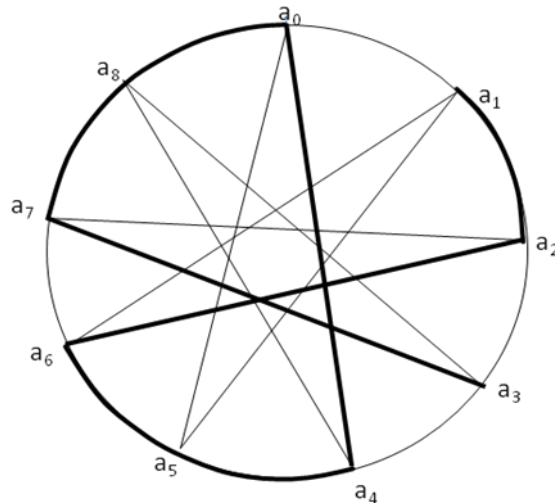
**Terminologies used in the Brick Product to determine the Hamiltonian path:**

For  $m=1$ , if  $a_i$  is any vertex of  $C(2n+1, m, r)$ , then the following are defined.

$$\begin{aligned}
 (a_i) P[m] &= (a_i)(a_{i+1})(a_{i+2}) \dots (a_{i+m-1}) & \forall i \in Z \\
 (a_i) P^{-1}[m] &= (a_i)(a_{i-1})(a_{i-2}) \dots (a_{i-m+1}) & \forall i \in Z \\
 (a_i) [J] &= (a_i)(a_{i+r}) \text{ and } (a_i)[J^{-1}] = (a_i)(a_{i-r}) & \forall i \in Z \\
 (a_i) [K] &= (a_i)(a_{i+2}) \text{ and } (a_i)[K^{-1}] = (a_i)(a_{i-2}) & \forall i \in Z
 \end{aligned}$$

**Example:** For  $n=4$ , consider the graph  $C(2n+1, 1, 4)$ . For the vertices  $a_i$  and  $a_j$  in  $G$ , we have  $d(a_i, a_j) = 2$  for  $i=1$  and  $j=3$ . Using the above notations, a Hamiltonian path in  $G$  between the vertices  $a_1$  and  $a_3$  is given by  $(a_i) P(2) J [P^{-1}(2)]^2 J^{-1} [P^{-1}(2)]^{2(n-3)} J^{-1} = a_1-a_2-a_6-a_5-a_4-a_0-a_8-a_7-a_3$  under modulo  $2n+1$ .

The following figure 3 shows the Hamiltonian path between the vertices  $a_1$  and  $a_3$ .



**Fig.3: Hamiltonian path from vertex  $a_1$  to  $a_3$  in the Brick Product  $C(9,1,4)$**

**Definition 4:** Let  $a_i$  and  $a_j$  be any two distinct vertices in a connected graph  $G$ . Let  $E'$  be a minimal set of edges not in  $G$  and  $P$  be a path in  $G$  such that  $P \cup E'$  is a Hamiltonian path in  $G$  from  $a_i$  to  $a_j$ . Then  $|E'|$  is called the **t-laceability number**  $\lambda_{(t)}$  of  $(a_i, a_j)$  and the edges in  $E'$  are called the t-laceability edges with respect to  $(a_i, a_j)$ .

## 2. RESULTS

In [2] the authors proved the following result:

**Theorem 5:** The graph  $G=C(2n+1, 1, 2)$  is Hamiltonian-t-laceable for  $1 \leq t \leq \text{diam}G$ .

In [3] the authors proved the following results:

**Theorem 6:** The graph  $C(2n+1, 1, 3)$  is Hamiltonian-t-laceable for  $t=1,2$  if  $n=3$  and is Hamiltonian-t-laceable for  $t=1,2,3$  if  $n \geq 6$  such that  $(2n+1) \equiv 1 \pmod{3}$ .



**Theorem 7:** The graph  $C(2n+1, 1, 3)$  is Hamiltonian- $t$ -laceable for  $t=1,2,3$ . Where  $n \geq 5$  such that  $(2n+1) \equiv 2 \pmod{3}$ .

**Theorem 8:** The graph  $C(2n+1, 1, 4)$  is Hamiltonian- $t$ -laceable for  $t=1,2$  if  $n = 4$  and is Hamiltonian- $t$ -laceable for  $t=1,2,3$  if  $n \geq 6$  such that  $(2n+1) \equiv 1 \pmod{4}$ .

**Theorem 9:** The graph  $C(2n+1, 1, 4)$  is Hamiltonian- $t$ -laceable for  $t=1,2,3$ . Where  $n \geq 5$  such that  $(2n+1) \equiv 3 \pmod{4}$ .

We now prove the following results:

**Theorem 10:** The graph  $G=C(2n+1,1,5)$  for  $n \geq 5$  and  $n \neq 7+5k$  is Hamiltonian- $t$ -laceable for  $t=1$ . For  $t=2$ ,  $G$  is Hamiltonian- $t$ -laceable with  $\lambda_{(t)}=1$ , where  $k$  is a non negative integer.

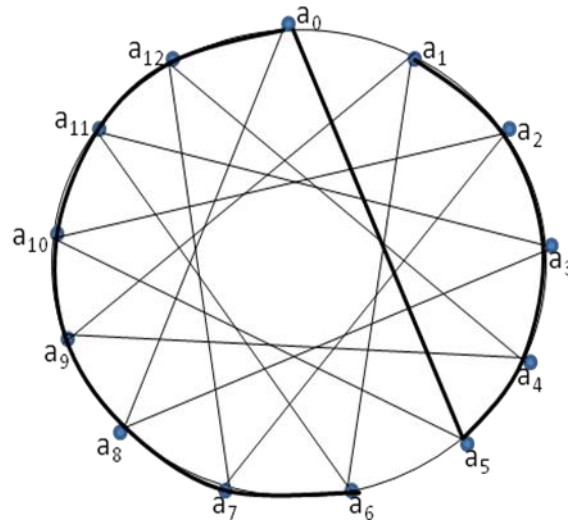
**Proof:** Consider the graph  $G= C(2n+1, 1, 5)$ .

Let  $d(a_i, a_j) = t$ , ( $0 \leq i < j \leq 2n$ ). For convenience we take  $j > i$ .

**Claim 1:**  $G$  is Hamiltonian- $t$ -laceable for  $t=1$

**Case (i):**  $j - i = 1$  or  $(2n+1)-(j-i) = 1$

If  $j - i = 1$  or  $(2n+1)-(j-i) = 1$  in  $C_{2n+1}$  then,  $a_i$  and  $a_j$  are attainable in  $G$ , since  $(a_i) [P^{-1}(2)]^{2n}$  is the Hamiltonian path.



**Fig.4: Hamiltonian path from vertex  $a_0$  to  $a_1$  in the Brick Product  $C(13,1,5)$**

**Case (ii):**  $j - i = 5$  or  $(2n+1)-(j - i) = 5$

If  $j - i = 5$  in  $C_{2n+1}$  then,  $a_i$  and  $a_j$  are attainable in  $G$ , since  $(a_i) [P(2)]^4 J^{-1} [P^{-1}(2)]^{2n-5}$  is the Hamiltonian path.

If  $(2n+1)-(j - i) = 5$  in  $C_{2n+1}$  then,  $a_i$  and  $a_j$  are attainable in  $G$ , since  $(a_i) [P^{-1}(2)]^4 J [P(2)]^{2n-5}$  is the Hamiltonian path.

**Claim 2:**  $G$  is Hamiltonian- $t$ -laceable for  $t=2$

**Case(i):**  $j - i = 2$  or  $(2n+1)-(j - i) = 2$

If  $j - i = 2$  or  $(2n+1)-(j - i) = 2$  in  $C_{2n+1}$  then,  $a_i$  and  $a_j$  are attainable in  $G$ , since  $(a_i) P(2) K^{-1} [P^{-1}(2)]^{2(n-1)}$  is a Hamiltonian path with  $t$ -laceability edge  $K^{-1}$ .

**Case(ii):**  $j - i = 6$  or  $(2n+1)-(j - i) = 6$

If  $j - i = 6$  or  $(2n+1)-(j - i) = 6$  in  $C_{2n+1}$  then,  $a_i$  and  $a_j$  are attainable in  $G$ , since  $(a_i) J [P^{-1}(2)]^4 K^{-1} [P^{-1}(2)]^{n+5}$  is the Hamiltonian path with  $t$ -laceability edge  $K^{-1}$ .

**Case(iii):** If  $j - i = 4$  or  $(2n+1)-(j - i) = 4$

If  $j - i = 4$  or  $(2n+1)-(j - i) = 4$  in  $C_{2n+1}$  then,  $a_i$  and  $a_j$  are attainable in  $G$ , since  $(a_i) J [P(2)]^{n+6} K [P(2)]^8$  is the Hamiltonian path with  $t$ -laceability edge  $K$ .



Hence the proof.

**Theorem 11:** The graph  $G=C(2n+1,1,6)$  for  $n \geq 6$  and  $n \neq 7+3k$  is Hamiltonian-t-laceable for  $t=1$ . For  $t=2$ ,  $G$  is Hamiltonian-t-laceable with  $\lambda_{(t)}=1$ , where  $k$  is a non negative integer.

**Proof:** Consider the graph  $G=C(2n+1, 1, 6)$ .  
Let  $d(a_i, a_j) = t$ , ( $0 \leq i < j \leq 2n$ ). For convenience we take  $j > i$ .

**Claim 1:**  $G$  is Hamiltonian-t-laceable for  $t=1$

**Case (i):**  $j - i = 1$  or  $(2n+1)-(j-i) = 1$

If  $j - i = 1$  or  $(2n+1)-(j-i) = 1$  in  $C_{2n+1}$  then,  $a_i$  and  $a_j$  are attainable in  $G$ , since  $(a_i) [P^{-1}(2)]^{2n}$  is the Hamiltonian path.

**Case (ii):**  $j - i = 6$  or  $(2n+1)-(j - i) = 6$

If  $j - i = 6$  in  $C_{2n+1}$  then,  $a_i$  and  $a_j$  are attainable in  $G$ , since  $(a_i) [P(2)]^5 J^{-1} [(P^{-1}(2)]^{2n-6}$  is the Hamiltonian path.

If  $(2n+1)-(j - i) = 6$  in  $C_{2n+1}$  then,  $a_i$  and  $a_j$  are attainable in  $G$ , since  $(a_i) [P^{-1}(2)]^5 J [P(2)]^{2n-6}$  is the Hamiltonian path.

**Claim 2:**  $G$  is Hamiltonian-t-laceable for  $t=2$

If  $n=6$  then  $(a_i) J [P(2)]^6 K [P(2)]^5$  is a Hamiltonian path with t-laceability edge  $K$ . If  $n \geq 7$  then

**Case(i):**  $j - i = 2$  or  $(2n+1)-(j - i) = 2$

If  $j - i = 2$  or  $(2n+1)-(j - i) = 2$  in  $C_{2n+1}$  then,  $a_i$  and  $a_j$  are attainable in  $G$ , since  $(a_i) P(2) K^{-1} [P^{-1}(2)]^{2(n-1)}$  is a Hamiltonian path with t-laceability edge  $K^{-1}$ .

**Case(ii):**  $j - i = 5$  or  $(2n+1)-(j - i) = 5$

If  $j - i = 5$  or  $(2n+1)-(j - i) = 5$  in  $C_{2n+1}$  then,  $a_i$  and  $a_j$  are attainable in  $G$ , since  $(a_i) J [P^{-1}(2)]^{n-7} K^{-1} [P^{-1}(2)]^{n+5}$  is the Hamiltonian path with t-laceability edge  $K^{-1}$ .

**Case(iii):** If  $j - i = 7$  or  $(2n+1)-(j - i) = 7$

If  $j - i = 7$  or  $(2n+1)-(j - i) = 7$  in  $C_{2n+1}$  then,  $a_i$  and  $a_j$  are attainable in  $G$ , since  $(a_i) J [P^{-1}(2)]^{2(n-3)} K [P^{-1}(2)]^{n-8}$  is the Hamiltonian path with t-laceability edge  $K$ .

Hence the proof.

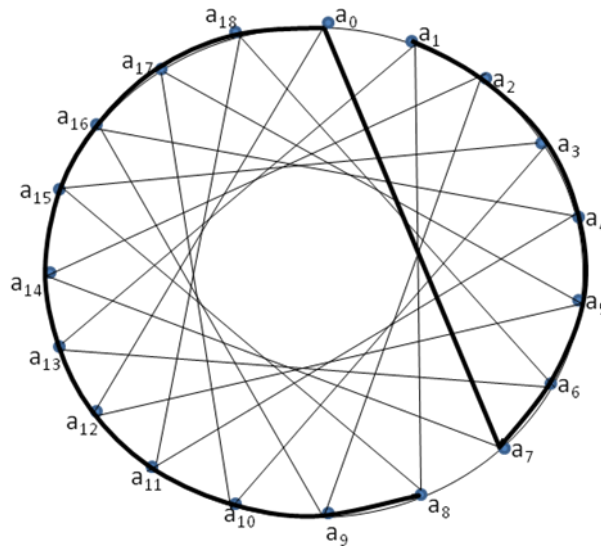
**Theorem 12:** The graph  $C(2n+1,1,7)$  is Hamiltonian-t-laceable for  $t=1$  if  $n \geq 7$  and  $n \neq 10+7k$  where  $k$  is a non negative integer.

**Proof:** Consider the graph  $G=C(2n+1, 1, 7)$ .

Let  $d(a_i, a_j) = t$ , ( $0 \leq i < j \leq 2n$ ). For convenience we take  $j>i$ .

**Case (i):**  $j - i = 1$  or  $(2n+1)-(j-i) = 1$

If  $j - i = 1$  or  $(2n+1)-(j-i) = 1$  in  $C_{2n+1}$  then,  $a_i$  and  $a_j$  are attainable in  $G$ , since  $(a_i) [P^{-1}(2)]^{2n}$  is the Hamiltonian path.



**Fig.5:** Hamiltonian path from vertex  $a_0$  to  $a_1$  in the Brick Product  $C(19,1,7)$

**Case (ii):**  $j - i = 7$  or  $(2n+1)-(j - i) = 7$

If  $j - i = 7$  in  $C_{2n+1}$  then,  $a_i$  and  $a_j$  are attainable in  $G$ , since  $(a_i) [P(2)]^6 J^{-1} [(P^{-1}(2))^{2n-7}]$  is the Hamiltonian path.

If  $(2n+1)-(j - i) = 7$  in  $C_{2n+1}$  then,  $a_i$  and  $a_j$  are attainable in  $G$ , since  $(a_i) [P^{-1}(2)]^6 J [P(2)]^{2n-7}$  is the Hamiltonian path.

Hence there exists Hamiltonian path between an every pair of vertices in  $G$  such that  $d(a_i,a_j)=1$ . Therefore  $G$  is Hamiltonian-t-laceable for  $t=1$ .

Hence the proof.





### 3. REFERENCES:

- [1] Brain Alspach, C.C. Chen and Kevin McAvaney, *On a class of Hamiltonian laceable 3-regular graphs*, Discrete Mathematics, 151(1996), pp. 19-38
- [2] Leena N. shenoy and R.Murali, *Laceability on a class of Regular Graphs*, International Journal of computational Science and Mathematics, volume 2, Number 3 (2010), pp. 397-406.
- [3] Girisha.A, H.Mariswamy, R.Murali and G.Rajendra, *Hamiltonian Laceability in a class of 4-Regular Graphs*, IOSR Journal of Mathematics, Volume 4, Issue 1 (Nov. - Dec. 2012), pp. 07-12.
- [4] Girisha.A and R.Murali, *Hamiltonian Laceability in cyclic product and brick product of cycles*, International Journal of Graph Theory, Volume 1, Issue 1, February 2013, pp. 32-40.
- [5] F. Harary, *Graph Theory*, Narosa Publishing House, Reprint, 1990.

\*\*\*\*\*





# Some aspects of stochastic calculus and approximation in chaotic systems analysis

Gabriel V. Orman and Irinel Radomir

Department of Mathematics and Computer Science  
"Transilvania" University of Braşov, 500091 Braşov, Romania.  
E-mail: ogabriel@unitbv.ro

**Abstract.** Frequently when we refer to *chaos* and *chaotic and complex systems* to describe the comportment of some natural phenomena, in fact we consider phenomena of the type of a *Brownian motion* which is a more realistic model of such phenomena. Thus one can talk about a passing *from chaotic and complex systems to Brownian motion*. Some aspects regardind the Brownian motion and its Markovian nature will be developed, in short, in this paper; we try also to emphasize their impact for some practical problems.

**Keywords:** stochastic differential equations, stochastic calculus, Markov processes, Brownian motion.

## 1 Introduction

It is known that a chaotic perpetual motion of a Brownian particle is the result of the collisions of particle with the molecules of the fluid in which there is.

But this particle is much bigger and also heavier than the molecules of the fluid which it collide, and then each collision has a negligible effect, while the superposition of many small interactions will produce an observable effect.

On the other hand, for a Brownian particle such molecular collisions appear in a very rapid succession, their number being enormous. For a so high frequency, evidently, the small changes in the particle's path, caused by each single impact, are too fine to be observable. For this reason the exact path of the particle can be described only by statistical methods.

We emphasize that L. Bachelier derived the law governing the position of a single grain performing a 1-dimensional Brownian motion starting at  $a \in R$  at time  $t = 0$ ; and A. Einstein also derived the same law from statistical mechanical considerations and applied it to the determination of molecular diameters.



Also Paul Lévy found a construction of the Brownian motion and given a profound description of the fine structure of the individual Brownian path. D. Ray obtained some results in the case when the motion is *strict Markov*; and W. Feller obtained that the generator of a strict Markovian motion with continuous paths (diffusion) can be expressed as a *differential operator*.

And in the last time we can speak about Markov processes from Kiyosi Itô's perspective (according to D.W. Stroock). The usual class of Markov processes which we consider has many times some restrictions which do not cover many interesting processes. This is the reason for which we try often to obtain some extensions of this notion.

Researches in this direction are due especially to K. Itô and in this context we shall refer below, in short, to some of them.

## 2 On Markov processes - an extended definition

Let  $S$  be a *state space* and consider a particle which moves in  $S$ . Also, suppose that the particle starting at  $x$  at the present moment will move into the set  $A \subset S$  with probability  $p_t(x, A)$  after  $t$  units of time, "irrespectively of its past motion", that is to say, this motion is considered to have a *Markovian character*.

The *transition probabilities* of this motion are  $\{p_t(x, A)\}_{t,x,A}$  and we considered that the time parameter  $t \in T = [0, +\infty)$ .

The state space  $S$  is assumed to be a *compact Hausdorff space with a countable open base*. The  $\sigma$ -field generated by the open sets (the topological  $\sigma$ -field on  $S$ ) is denoted by  $K(S)$ . Therefore, a *Borel set*  $A$  is a set in  $K(S)$  (i.e.  $A \in K(S)$ ).

The *mean value*

$$m = M(\mu) = \int_R x \mu(dx)$$

is used for the center and the scattering degree of a one-dimensional probability measure  $\mu$  having the second order moment finite, and the *variance* of  $\mu$  is defined by

$$\sigma^2 = \sigma^2(\mu) = \int_R (x - m)^2 \mu(dx).$$

On the other hand, from the Tchebychev's inequality, for any  $t > 0$ , we have

$$\mu(m - t\sigma, m + t\sigma) \leq \frac{1}{t^2},$$

so that several properties of 1-dimensional probability measures can be derived.



**Remark 2.1** *In the case when the considered probability measure has no finite second order moment,  $\sigma$  becomes useless. In such a case one can introduce the central value and the dispersion that will play similar roles as  $m$  and  $\sigma$  for general 1-dimensional probability measures.*

The *dispersion*  $\delta$  is defined as follows

$$\delta = \delta(\mu) = -\log \int \int_{\mathbb{R}^2} e^{-|x-y|} \mu(dx) \mu(dy).$$

Furthermore it is assumed that the following conditions are satisfied by the transition probabilities  $\{p_t(x, A)\}_{t \in T, x \in S, A \in K(S)}$ :

- 1 for  $t$  and  $A$  fixed,
  - a) the transition probabilities are Borel measurable in  $x$ ;
  - b)  $p_t(x, A)$  is a probability measure in  $A$ ;
- 2  $p_0(x, A) = \delta_x(A)$  (i.e. the  $\delta$ -measure concentrated at  $x$ );
- 3  $p_t(x, \cdot) \xrightarrow{\text{weak}} p_t(x_0, \cdot)$  as  $x \rightarrow x_0$  for any  $t$  fixed, that is

$$\lim_{x \rightarrow x_0} \int f(y) p_t(x, dy) = \int f(y) p_t(x_0, dy)$$

for all continuous functions  $f$  on  $S$ ;

- 4  $p_t(x, U(x)) \rightarrow 1$  as  $t \searrow 0$ , for any neighborhood  $U(x)$  of  $x$ ;
- 5 the Chapman-Kolmogorov equation holds:

$$p_{s+t}(x, A) = \int_S p_t(x, dy) p_s(y, A).$$

We can give now the definition of a Markov process as follows:

**Definition 2.1** *A "Markov process" is a system of stochastic processes*

$$\{X_t(\omega), t \in T, \omega \in (\Omega, K, P_a)\}_{a \in S},$$

*that is for each  $a \in S$ ,  $\{X_t\}_{t \in S}$  is a stochastic process defined on the probability space  $(\Omega, K, P_a)$ .*

It can be observed that a definition as it is given above not correspond to many processes that are of a real interest so that it is useful to obtain an extension of this notion. An extended notion has been proposed by K. Itô and it is given below.

Let  $E$  be a separable Banach space with real coefficients and norm  $\|\cdot\|$  and let also  $L(E, E)$  be the space of all bounded linear operators  $E \rightarrow E$ . It can be observed that  $L(E, E)$  is a linear space.



**Definition 2.2** *The collection of stochastic processes*

$$X = \{X_t(\omega) \equiv \omega(t) \in S, t \in T, \omega \in (\Omega, K, P_a)\}_{a \in S}$$

is called a "Markov process" if the following conditions are satisfied:

- 1) the "state space"  $S$  is a complete separable metric space and  $K(S)$  is a topological  $\sigma$ -algebra on  $S$ ;
- 2) the "time interval"  $T = [0, \infty)$ ;
- 3) the "space of paths"  $\Omega$  is the space of all right continuous functions  $T \rightarrow S$  and  $K$  is the  $\sigma$ -algebra  $K[X_t : t \in T]$  on  $\Omega$ ;
- 4) the probability law of the path starting at  $a$ ,  $P_a(H)$ , is a probability measure on  $(\Omega, K)$  for every  $a \in S$  which satisfy the following conditions:
  - 4a)  $P_a(H)$  is  $K(S)$ -measurable in  $a$  for every  $H \in K$ ;
  - 4b)  $P_a(X_0 = a) = 1$ ;
  - 4c)  $P_a(X_{t_1} \in E_1, \dots, X_{t_n} \in E_n) = \int \dots \int_{a_i \in E_i} P_a(X_{t_1} \in da_1) P_{a_1}(X_{t_2-t_1} \in da_2) \dots \dots P_{a_{n-1}}(X_{t_n-t_{n-1}} \in da_n) \quad \text{for } 0 < t_1 < t_2 < \dots < t_n.$

**Remark 2.2** *Evidently there are some differences between this definition and Definition 2.1 of a Markov process. Thus*

- i. *The space  $S$  is not necessary to be compact;*
- ii. *it is not assumed the existence of the left limits of the path;*
- iii. *the transition operator  $f \rightarrow G_t f(\cdot) = E.(f(X_t))$  do not necessarily carry  $C(S)$  into  $C(S)$  ( $C(S)$  being the space of all real-valued bounded continuous functions on  $S$ ).*

### 3 The Markovian nature of the Brownian path

In his study Bachelier found some solutions of the type  $\psi(x)$ . He derived<sup>1</sup> the law governing the position of a single grain performing a 1-dimensional Brownian motion starting at  $a \in \mathbf{R}^1$  at time  $t = 0$ :

$$P_a[x(t) \in db] = g(t, a, b)db \quad (t, a, b) \in (0, +\infty) \times \mathbf{R}^2, \quad (1)$$

<sup>1</sup>Bachelier, L. *Théorie de la spéculation*. Ann. Sci. École Norm. Sup., 17, 1900, 21-86.



where  $g$  is the source (Green) function

$$g(t, a, b) = \frac{e^{-\frac{(b-a)^2}{2t}}}{\sqrt{2\pi t}} \quad (2)$$

of the problem of heat flow:

$$\frac{\partial u}{\partial t} = \frac{1}{2} \frac{\partial^2 u}{\partial a^2} \quad (t > 0). \quad (3)$$

Bachelier also pointed out the Markovian nature of the Brownian path expressed in

$$\begin{aligned} P_a[a_1 \leq x(t_1) < b_1, a_2 \leq x(t_2) < b_2, \dots, a_n \leq x(t_n) < b_n] = \\ = \int_{a_1}^{b_1} \int_{a_2}^{b_2} \dots \int_{a_n}^{b_n} g(t_1, a, \xi_1) g(t_2 - t_1, \xi_1, \xi_2) \dots \\ \dots g(t_n - t_{n-1}, \xi_{n-1}, \xi_n) d\xi_1 d\xi_2 \dots d\xi_n, \quad 0 < t_1 < t_2 < \dots < t_n \end{aligned} \quad (4)$$

and used it to establish the law of maximum displacement

$$P_0 \left[ \max_{s \leq t} x(s) \leq b \right] = 2 \int_0^b \frac{e^{-\frac{a^2}{2t}}}{\sqrt{2\pi t}} da \quad t > 0, b \geq 0. \quad (5)$$

It is very interesting that A. Einstein, in 1905, also derived (1) from statistical mechanical considerations and applied it to the determination of molecular diameters.<sup>2</sup>

As we already emphasized, a rigorous definition and study of Brownian motion requires measure theory. Consider the space of *continuous* path  $w : t \in [0, +\infty) \rightarrow R$  with coordinates  $x(t) = w(t)$  and let  $\mathbf{B}$  be the smallest Borel algebra of subsets  $B$  of this path space which includes all the simple events  $B = (w : a \leq x(t) < b), (t \geq 0, a < b)$ . Wiener established the existence of nonnegative Borel measures  $P_a(B), (a \in R, B \in \mathbf{B})$  for which (4) holds<sup>3</sup>. Among other things, this result attaches a precise meaning to Bachelier's statement that *the Brownian path is continuous*.

Paul Lévy found another construction of the Brownian motion and gives a profound description of the fine structure of the individual Brownian path.

The standard Brownian motion can be now defined.

<sup>2</sup>see: A. Einstein, *Investigations on the theory of the Brownian movement*, New York, 1956.

<sup>3</sup>N. Wiener, *Differential space*, Math. Phys. 2, 1923, pp. 131-174



**Definition 3.1** A continuous-time stochastic process  $\{B_t | 0 \leq t \leq T\}$  is called a "standard Brownian motion" on  $[0, T)$  if it has the following four properties:

i  $B_0 = 0$ .

ii The increments of  $B_t$  are independent; that is, for any finite set of times  $0 \leq t_1 < t_2 < \dots < t_n < T$ , the random variables

$$B_{t_2} - B_{t_1}, B_{t_3} - B_{t_2}, \dots, B_{t_n} - B_{t_{n-1}}$$

are independent.

iii For any  $0 \leq s \leq t < T$  the increment  $B_t - B_s$  has the normal distribution with mean 0 and variance  $t - s$ .

iv For all  $\omega$  in a set of probability one,  $B_t(\omega)$  is a continuous function of  $t$ .

The Brownian motion can be represented as a random sum of integrals of orthogonal functions. Such a representation satisfies the theoretician's need to prove the existence of a process with the four defining properties of Brownian motion, but it also serves more concrete demands. Especially, the series re-representation can be used to derive almost all of the most important analytical properties of Brownian motion. It can also give a powerful numerical method for generating the Brownian motion paths that are required in computer simulation.

**Remark 3.1** Let us consider  $R \cup \{\infty\}$ . Then one can define

$$p_t(x, dy) = \frac{1}{t\sqrt{2\pi}} e^{-\frac{(y-x)^2}{2t^2}} dy \quad \text{in } R$$
$$p_t(\infty, A) = \delta_\infty A.$$

Let us observe that the conditions 1b) and 2-5 assumed on the transition probabilities  $\{p_t(x, A)\}_{t \in T, x \in S, A \in K(S)}$ , given in Section 2, are satisfied in this case for "Brownian transition probabilities" where  $R \cup \{\infty\}$  is considered as the one-point compactification of  $R$ .

Finally we shall give an interesting result regarding to a 3-dimensional Brownian motion.

Let  $X$  be a Markov process in a generalized sense as it is given in Definition 2.2. Let us denote by  $\mathbf{B}(S)$  the space of all bounded real  $K(S)$ -measurable functions and let us consider a function  $f \in \mathbf{B}(S)$ .





It is supposed that

$$E_a \left( \int_0^{\infty} |f(X_t)| dt \right) \quad (6)$$

is bounded in  $a$ . Then, the following

$$Uf(a) = E_a \left( \int_0^{\infty} f(X_t) dt \right) \quad (7)$$

is well-defined and is a bounded  $K(S)$ -measurable function of  $a \in S$ . The  $Uf$  is called *the potential* of  $f$  with respect to  $X$ . Having in view that  $Uf = \lim_{\alpha \downarrow 0} R_\alpha f$ , it is reasonable to write  $R_0$  instead of  $U$ . Based on this fact,  $R_\alpha f$  will be called *the potential of order  $\alpha$*  of  $f$ .

It is useful to retain that  $R_\alpha f \in \mathbf{B}(S)$  for  $\alpha > 0$ ; and generally  $f \in \mathbf{B}(S)$  while  $R_0 f (= Uf) \in \mathbf{B}(S)$  under the condition (6).

Now the name *potential* is justified by the following theorem on *the 3-dimensional Brownian motion*.

**Theorem 3.1** *Let  $X$  be the 3-dimensional Brownian motion. If  $f \in \mathbf{B}(S)$  has compact support, then  $f$  satisfies (6) and*

$$Uf(a) = \frac{1}{2\pi} \int_{R^3} \frac{f(b) db}{|b-a|} = \frac{1}{2\pi} \times \text{Newtonian potential of } t. \quad (8)$$

We do not insist on these aspects. But more details, proofs and related problems can be found in [1], [2], [3], [4], [14], [6], [13], [12].

**Conclusion 3.1** *As we have said at the beginning, we think that when, in various problems, we say "chaos" or "chaotic and complex systems" or we use another similar expression to define the comportment of some natural phenomena, in fact we imagine phenomena similarly to a Brownian motion which is a more realistic model of such phenomena. And this opinion lie at the basis of this paper.*

## References

- [1] A. T. Bharucha-Reid. Elements Of The Theory Of Markov Processes And Their Applications. Mineola, New York, 1997, Dover Publications, Inc.
- [2] K. Itô, *Selected Papers*, Springer, 1987.



- [3] K. Itô and H. P. McKean Jr. *Diffusion Processes and their Sample Paths*. Berlin Heidelberg, 1996, Springer-Verlag.
- [4] K. Itô. *Stochastic Processes*. Ole E. Barndorff-Nielsen, Ken-iti Sato, editors. Berlin Heidelberg, 2004, Springer-Verlag.
- [5] B. Øksendal. *Stochastic Differential Equations: An Introduction with Applications*. Sixth Edition, New York, 2003, Springer, Berlin-Heidelberg.
- [6] P. Olofsson, and M. Andersson. *Probability, Statistics and Stochastic Processes*, 2nd Edition. John Wiley & Sons, Inc., Publication, 2012.
- [7] G. V. Orman. *Lectures on Stochastic Approximation Algorithms. Theory and Applications*. Duisburg, 2001, Preprint, Univ. "Gerhard Mercator".
- [8] G. V. Orman. *Handbook Of Limit Theorems And Sochastic Approximation*. Brasov, 2003, Transilvania University Press.
- [9] G. V. Orman. *On Markov Processes: A Survey Of The Transition Probabilities And Markov Property*. In Christos H. Skiadas and Ioannis Dimotikalis, editors, *Chaotic Systems: Theory and Applications*. World Scientific Publishing Co Pte Ltd, 2010, 224-232.
- [10] G. V. Orman. *On a problem of approximation of Markov chains by a solution of a stochastic differential equation*. In Christos H. Skiadas, Ioannis Dimotikalis and Charilaos Skiadas, editors, *Chaos Theory: Modeling, Simulation and Applications*. World Scientific Publishing Co Pte Ltd, 2011, 30-40.
- [11] G. V. Orman and I. Radomir. *New Aspects in Approximation of a Markov Chain by a Solution of a Stochastic Differential Equation*. *Chaotic Modeling and Simulation (CMSIM) International Journal*, 2012, pp. 711-718.
- [12] G. V. Orman. *Aspects of convergence and approximation in random systems analysis*. LAMBERT Academic Publishing, Germany, 2012.
- [13] Z. Schuss. *Theory and Application of Stochastic Differential Equations*. New York, 1980, John Wiley & Sons.
- [14] D. W. Stroock, *Markov Processes from K. Itô Perspective*, Princeton Univ. Press, Princeton, 2003.



## Stabilization of an Inductorless Chua's Chaotic Circuit via Sliding Mode Control\*

Suphaphorn Panikhom, Wirote Sangtungong and Sarawut Sujitjorn

School of Electrical Engineering, Suranaree University of Technology,  
Nakhon Ratchasima, 30000, Thailand  
E-mail: suphaphorn.pa@rmuti.ac.th

**Abstract:** This article proposes stabilization of an inductorless Chua's chaotic circuit via sliding mode control (SMC). Modeling of the circuit and its electronic circuit design are presented. During controller design process, stability guarantee is required simultaneously. Since the second method of Lyapunov's is applied, coefficients of the Lyapunov function candidates and their derivatives are obtained via metaheuristic search. Adaptive tabu search (ATS) metaheuristic has been applied for the purposes, and the design is formulated as an optimization problem with nonlinear constraints. The paper gives details of algorithm implementation, control design, electronic circuit design and simulation results with discussions.

**Keywords:** Chua's Circuit, Stabilization, Sliding Mode Control.

### 1. Introduction

Research in chaos has been a very active topic in recently years. Leon O Chua introduced a chaotic circuit in 1983 [1] becoming a famous circuit nowadays. The circuit is a simple and typical third-order autonomous system that exhibits chaotic and bifurcation phenomena [2],[3]. Proper use for a chaotic system may need its chaotic behavior during a certain period of time alternating to well-behaved (or stabilized) dynamic. Therefore, stabilization techniques are needed for chaotic systems. Among those in literature, it has been possible to use traditional feedback control approach for the purpose [4]. Nonlinear feedback control approach has been proposed with stability analysis using Hurwitz matrix [5]. Another possibility for control and stabilization of a chaotic system is to use backstepping method [6, 7]. Recently, sliding mode control (SMC) has been successfully applied due to its robustness property [8-12]. The SMC forces a system under control to be on a sliding manifold, and remain there till its dynamic reaches an equilibrium. The method is applied to find controller parameters with stability simultaneously guaranteed, for instance the work reported by Wang (2009) [9]. Our proposed works employ the SMC together with a kind of metaheuristics namely adaptive tabu search (ATS) [13]. The ATS is an efficient intelligent search method which has been successfully applied to

---

\*Paper included in *Chaotic Systems: Theory and Applications*, C.H. Skiadas and I. Dimotikalis, Eds, World Scientific, pp 302—308, 2010.

various real-world problems [14],[15]. The simulation results from PSIM are provided to show the effectiveness of the proposed approach.

## 2. Mathematic Model of Chua's chaotic circuit

The standard form of Chua's circuit shown in Fig.1 consists of two main parts that are linear elements  $R, L$  and  $C$  and a nonlinear element  $g(V_{c_2})$  called Chua's diode. The piecewise-linear (PWL) function of Chua's diode is shown in Fig. 2(a). The double scroll chaotic behavior in Fig. 2(b) will be occurred when adjusting  $R$  into a suitable value.

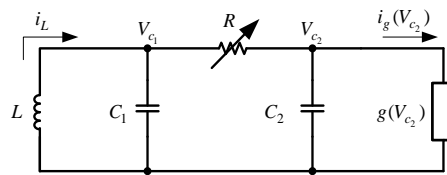


Fig.1 Standard unforced Chua's circuit.

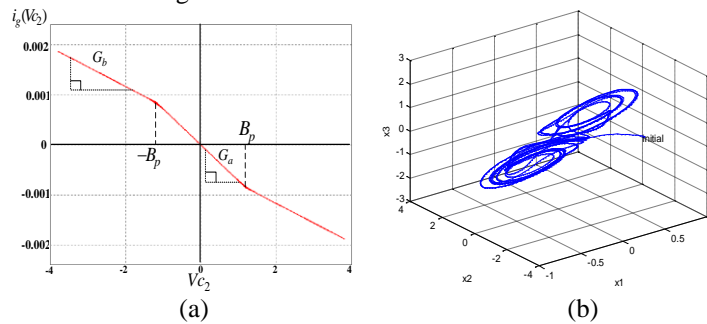


Fig.2 (a) Piecewise-linear function of the  $g(V_{c_2})$ ,

(b) Phase portrait of double scroll attractor in three dimensional view.

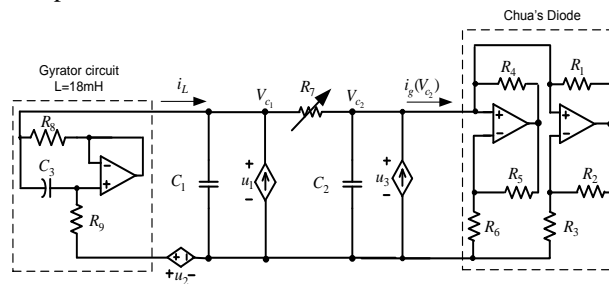


Fig.3 Inductorless Chua's chaotic circuit with controller input indicated.

The modified Chua's circuit is developed by changing the inductor to a Gyrator circuit composed of two resistors, a capacitor and an operational amplifier to compact the size of experimental circuit, and illuminate the noise voltage across the inductor. Likewise, Chua's diode can be realized by six resistors and two operational amplifiers [2]. Furthermore, the controller inputs

have been added into standard form in order to stabilize the chaotic Chua's circuit [3]. The schematic diagram of modified Chua's circuit with controller input indicated is illustrated in Fig.3.

By applying Kirchoff's laws to the circuit, the controlled Chua's circuit can be represented by

$$\left. \begin{aligned} \frac{dV_{c_1}}{dt} &= \frac{1}{R_7 C_1} (V_{c_2} - V_{c_1}) + \frac{i_L}{C_1} + \frac{u_1}{C_1} \\ \frac{di_L}{dt} &= -\frac{1}{L} (V_{c_1} - u_2) \\ \frac{dV_{c_2}}{dt} &= \frac{1}{R_7 C_2} (V_{c_1} - V_{c_2}) - \frac{i_g(V_{c_2})}{C_2} + \frac{u_3}{C_2} \end{aligned} \right\} \quad (1)$$

$$f(V_{c_2}) = R_7 [G_b V_{c_2} + (1/2)(G_a - G_b)(|V_{c_2} + B_p| - |V_{c_2} - B_p|)] \quad (2)$$

where  $V_{c_1}, V_{c_2}$  are the voltages across capacitors  $C_1$  and  $C_2$ , respectively,  $i_L$  is the current through inductor  $L$ , The nonlinearity function  $f(V_{c_2})$  is an I-V characteristic representing three segments PWL curve. The inner slopes  $G_a$ , the outer slope  $G_b$  and the breakpoint voltage  $B_p$  can be obtained from Fig.2(a).

Inputs  $u_1, u_2$  and  $u_3$  are sliding mode controllers.

To simplify (1) and (2), the circuit can be normalized by the following the new notation:

$$\begin{aligned} t' &= t/RC_1, & x_1 &= V_{c_1}, & x_2 &= i_L, & x_3 &= V_{c_2} \\ \tilde{x}_2 &= R_7 x_2 & \tilde{u}_1 &= R_7 u_1, & \tilde{u}_3 &= (1/C_2)(R_7 C_1) u_3 \\ f(x_3) &= R_7 i_g(V_{c_2}), & m &= R_7 G_a, & n &= R_7 G_b, \end{aligned} \quad (3)$$

Substitutes (3) into (1) and (2), so that the main bifurcation parameters of Chua's circuit can be obtained as  $\alpha = C_1/C_2$  and  $\beta = R^2 C_1/L$ . Normalized circuit can be reformulated as follows

$$\left. \begin{aligned} \frac{dx_1}{dt'} &= -x_1 + \tilde{x}_2 + x_3 + \tilde{u}_1 \\ \frac{d\tilde{x}_2}{dt'} &= -\beta(x_1 - u_2) \\ \frac{dx_3}{dt'} &= \alpha(x_1 - x_3 + f(x_3)) + \tilde{u}_3 \end{aligned} \right\} \quad (4)$$

$$f(x_3) = nx_3 + (1/2)(m-n)(|x_3 + B_p| - |x_3 - B_p|) \quad (5)$$

The schematic diagram in Fig.3 is overall an circuit of the proposed method. The value of electronic components are selected as  $C_1 = 90nF, C_2 = 10nF, C_3 = 0.01\mu F, R_1, R_2 = 220\Omega, R_3 = 2.4k\Omega, R_4, R_5 = 39k\Omega, R_6 = 3.3k\Omega, R_7 = 2K\Omega, R_8 = 1\Omega, R_9 = 1.8M\Omega$ . In this case, Chua's circuit will generate the double scroll



when  $R_7 = 1.6k\Omega$ . Parameters from PWL function can be obtained as,  $B_p = 1.16$ ,  $G_a = -7.22 \times 10^{-4}$  and  $G_b = -3.92 \times 10^{-4}$ . Therefore, the main bifurcation parameters of Chua's circuit are  $\alpha = 15.6$ ,  $\beta = 28$ ,  $m = -1.139$  and  $n = -0.711$ .

### 3. Sliding Mode Control of Chua's circuit

To stabilize a Chua's system by using SMC, there are two modes to be designed, reaching and sliding modes, respectively. As a result of the reaching mode, one obtains a switching function (or sliding surface) designated as an equivalent control,  $\mathbf{u}_{eq}$ . To achieve a total control requires the sliding mode design, which results in a complete control signal governing system's dynamic to reach the sliding surface, and then slide along the surface to an equilibrium point.

From last section, the controlled Chua's circuit represented by (3), (4) can be unified as

$$\dot{\mathbf{x}} = \mathbf{Ax} + \mathbf{f}(\mathbf{x}) + \mathbf{Bu} \quad (6)$$

$$\text{where } \mathbf{A} = \begin{bmatrix} -1 & 1 & 1 \\ -\beta & 0 & 0 \\ \alpha & 0 & -\alpha \end{bmatrix}, \mathbf{f}(x) = -\alpha \begin{bmatrix} 0 \\ 0 \\ f(x_3) \end{bmatrix}, \mathbf{B} = \begin{bmatrix} 0 & 0 & 0 \\ 0 & 1 & 0 \\ 0 & 0 & 1 \end{bmatrix}, \mathbf{x} = [x_1 \ \tilde{x}_2 \ x_3]^T$$

$$\text{and } \mathbf{u} = [\tilde{u}_1 \ u_2 \ \tilde{u}_3]^T$$

Since the controlled circuit is nonlinear, this work applies the direct method of Lyapunov's to guarantee stability. The system (6) is said to be globally asymptotically stable at origin if there exists a scalar function  $V(\mathbf{x})$ , such that  $V(\mathbf{x}) > 0, \forall \mathbf{x} \neq 0$ ,  $\dot{V}(\mathbf{x}) < 0, \forall \mathbf{x} \neq 0$  and  $V(\mathbf{x}) \rightarrow \infty$  for  $\|\mathbf{x}\| \rightarrow \infty$ . If Lyapunov function,  $V(\mathbf{x})$  is not known, stability cannot be concluded. Most works in literatures assume a quadratic form of Lyapunov function, i.e.  $V(\mathbf{x}) = \frac{1}{2}(\mathbf{x}^T \mathbf{x})$ . Its associative  $\dot{V}(\mathbf{x})$  along the solution trajectory is expressed by

$$\dot{V}(x) = \frac{1}{2}(\mathbf{x}^T \dot{\mathbf{x}} + \dot{\mathbf{x}}^T \mathbf{x}) \quad (7)$$

Although the forms of the functions are known, their coefficients are not. This has introduced difficulties in stability analysis because the parameters cannot be easily determined. Such circumstances are common when ones apply SMC because the reaching mode can be assumed via the above stability conditions as an alternative. In other words, the system dynamic is guaranteed to reach the sliding surface  $\mathbf{s} = 0$  according to the SMC method if there exists a Lyapunov function  $V(\mathbf{s}) = \frac{1}{2}(\mathbf{s}^T \mathbf{s})$ , and  $\dot{V}(\mathbf{s}) < 0, \forall \mathbf{s} \neq 0$ . The designed sliding surfaces further direct the system states to an equilibrium point.



Sliding surface or switching function is a desirable scheme to force the system dynamic to converge to an equilibrium point. A sliding surface with a compensator inclusive is represented by

$$\mathbf{s} = \mathbf{C}\mathbf{x} + \mathbf{z} \quad (8)$$

with its dynamic described by

$$\dot{\mathbf{s}} = \mathbf{C}\dot{\mathbf{x}} + \dot{\mathbf{z}} \quad (9)$$

in which the compensator dynamic [12] is described by  $\dot{\mathbf{z}} = \mathbf{K}\mathbf{x} + \mathbf{z}$ . For a design, the matrices  $\mathbf{C}$  and  $\mathbf{K}$  must be found to comply with the reaching condition,  $\dot{\mathbf{s}} = 0$ . Consequently, an equivalent control,  $\mathbf{u}_{eq}$ , is

$$\mathbf{u}_{eq} = -\mathbf{C}\mathbf{A}\mathbf{x} - \mathbf{C}\mathbf{f}(\mathbf{x}) - \mathbf{K}\mathbf{x} + \mathbf{z} \quad (10)$$

Replace  $\mathbf{u}$  in (6) by  $\mathbf{u}_{eq}$  in (10), the system under sliding mode control can be obtained as

$$\dot{\mathbf{x}}(t) = (\mathbf{A} - \mathbf{B}\mathbf{C}\mathbf{A} - \mathbf{B}\mathbf{K} - \mathbf{B}\mathbf{C})\mathbf{x}. \quad (11)$$

The derivative of Lyapunov function (7) can be expressed by

$$\dot{V}(x) = \frac{1}{2} \mathbf{x}^T \mathbf{Q} \mathbf{x} \quad (12)$$

where

$$\mathbf{Q} = \mathbf{A} - \mathbf{B}\mathbf{C}\mathbf{A} - \mathbf{B}\mathbf{K} - \mathbf{B}\mathbf{C} + \mathbf{A}^T - \mathbf{A}^T \mathbf{C}^T \mathbf{B}^T - \mathbf{K}^T \mathbf{B}^T - \mathbf{C}^T \mathbf{B}^T. \quad (13)$$

As a necessity, on the sliding surface  $\mathbf{C}$  and  $\mathbf{K}$  must satisfy the following conditions:  $\mathbf{Q} < 0 \Rightarrow \dot{V} < 0$  and  $\dot{\mathbf{s}} = 0$ . According to such conditions, the controlled system is asymptotically stable.

Reaching law is another necessary scheme of SMC since it governs the system state(s) to converge to the sliding surface. One basic form of the reaching law is constant plus proportional rate. Practically, the *sgn* function generates chattering. To avoid this, one can implement a boundary layer method, i.e.  $\|\mathbf{s}\| < \phi$ , where  $\phi$  represents the boundary width. This helps smooth the switching behavior. Therefore, the reaching law can be written a

$$\dot{\mathbf{s}} = -(q_1 + q_2 \phi^{-1})\mathbf{s} = -K_s \mathbf{s} \quad (14)$$

where  $q_1$  and  $q_2$  are positive constants,  $K_s > 0$ , representing total gain. The law (14) is much simpler than that proposed by [12]. To guarantee stability, we consider a Lyapunov function  $V(\mathbf{s}) = (1/2)(\mathbf{s}^T \mathbf{s})$ . Its derivative is obtained as



$$\dot{V}(\mathbf{s}) = \frac{1}{2} (\mathbf{s}^T \dot{\mathbf{s}} + \dot{\mathbf{s}}^T \mathbf{s}) = -K_s \|\mathbf{s}\|^2 \quad (15)$$

which is negative definite for  $K_s > 0$ . Equating (9) and (14), we obtain the following control signal

$$\mathbf{U} = -\mathbf{CAx} - \mathbf{Cf}(\mathbf{x}) - \mathbf{Kx} + \mathbf{Z} - K_s \mathbf{Cx} - K_s \mathbf{Z}. \quad (16)$$

From (16), one realizes that  $\mathbf{C}, \mathbf{K}$  and  $K_s$  must be found to satisfy asymptotically stable conditions. This requires an efficient computing method. Among many existing methods, metaheuristics called adaptive tabu search [13] is our choice, and described next.

### 3. Search for controller parameters

ATS is chosen as a tool to find suitable controller parameters. Since the algorithm has been known, we omit review of the ATS. Detailed explanation of the algorithm with applications can be found in [13-15]. We apply the ATS to search for the matrices  $\mathbf{C}$  and  $\mathbf{K}$  resulting in  $\mathbf{Q} < 0$  and  $\dot{V} < 0$ , as well as a positive constant  $K_s$ .

An important issue of algorithm implementation is objective function. Regarding this, the following procedures represent the objective function.

*Step1.* Receive parametric values of  $\mathbf{C}$ ,  $\mathbf{K}$  and  $K_s$  from ATS.

*Step2.* Assign parameters to the state equation in (6).

*Step3.* Calculate  $\mathbf{Q}$  using (13) and eigenvalues of  $\mathbf{Q}$ .

*Step4.* Based on obtained eigenvalues, determine the negative definiteness of  $\mathbf{Q}$ .

If ( $\mathbf{Q} < 0$ ) then (substitute  $\mathbf{C}$ ,  $\mathbf{K}$  and  $K_s$  in (16) by the current parameters).

- Solve the system model for the states  $x_1, x_2$  and  $x_3$  \*.

- Calculate cost value:  $f(s) = |x_{1i_{\max}}| + |x_{2i_{\max}}| + |x_{3i_{\max}}|$ .

If ( $\mathbf{Q} \geq 0$ ) then (set  $f(s) = 10^4$ ).

*Step5.* Return  $\mathbf{C}$ ,  $\mathbf{K}$ ,  $K_s$  and  $f(s)$  to ATS

\*Remarks: Forth-order Runge-Kutta method with  $\Delta t = 0.01s$  is used for solving equations. The maximum iteration is  $i_{\max} = 1,000$ .

The ATS repeatedly search for solutions. It stops when either  $f(s) \leq 10^{-3}$  or search iteration hits 1,000. Using Intel® core™ i7-2620M CPU 2.70 GHz, RAM 8 GB, the ATS coded in MATLAB spent 7 iterations, 411.52 seconds to

reach for  $\mathbf{C} = \begin{bmatrix} 0 & 0 & 0 \\ 10.667 & 1 & 0 \\ 16.422 & 0 & 1 \end{bmatrix}$ ,  $\mathbf{K} = \begin{bmatrix} 0 & 0 & 0 \\ 10.880 & 17.923 & 17.145 \\ 3.796 & -14.314 & 11.062 \end{bmatrix}$ ,  $K_s = 1.3631$  with

$f(s) = 44.53 \times 10^{-5}$ . The parameters  $\mathbf{C}$ ,  $\mathbf{K}$  and  $K_s$  can be substituted into  $\mathbf{U}$  in (2.16). This results in



$$\begin{bmatrix} \tilde{u}_1 \\ u_2 \\ \tilde{u}_3 \end{bmatrix} = \begin{bmatrix} 0 \\ -1.141x_1 - 29.953\tilde{x}_2 - 27.812x_3 - 0.363 \\ 9.0gx - 18.76x_1 - 2.108\tilde{x}_2 - 19.848x_3 + 0.726 \end{bmatrix} \quad (17)$$

#### 4 Simulation results

Both Chua system and controllers are realized as electronics circuit. The main electronic components are op-amps (LF351), analog multipliers (AD633), Rs and Cs. Fig.4 shows the schematic diagram of the controlled Chua's circuit. The diagram is used for simulation using PSIM. The sub circuit of the obtained controller u2 and u3 are electronically applied by using differential and inverting amplifier circuit based on equation (17). We are interested in the states  $x_1, x_2$  and  $x_3$ . PSIM provides the results as illustrated in Fig.5. The curves showing the states in figure 8 indicate that when the controller is switched on at  $t = 0.6s$  all the states are governed to the equilibrium nicely.

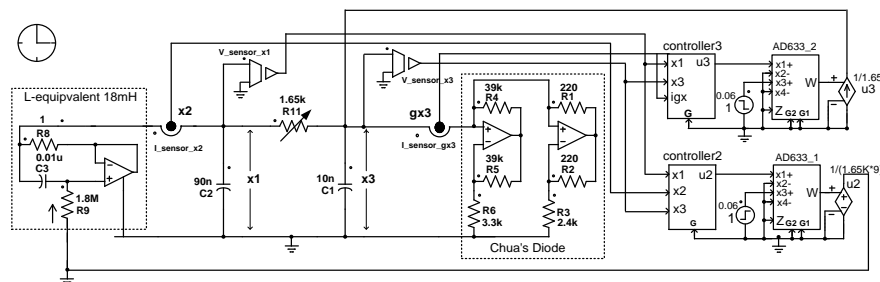


Fig.4 Schematic diagram of controlled Chua's circuit.

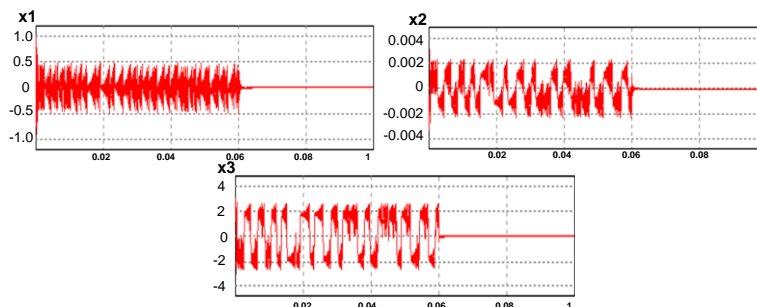


Fig.5 Time response of states (a)  $x_1$ , (b)  $x_2$  and (c)  $x_3$  in PSIM.

#### 5. Conclusion

Successful stabilization for a chaotic Chua's circuit has been presented by this article. The effective control utilizes sliding mode method. The article proposes simple reaching law which can completely avoid chattering has been proposed. To obtain controller parameters with stability guaranteed simultaneously requires complicated computing. Regarding this, the ATS has been applied to



search for the controller parameters as well as  $V(x)$  and  $\dot{V}(x)$  simultaneously. The theoretical approach has been tested using electronic circuit implementation. Simulation results agree very well indicating successful stabilization without drawing excessive control signals.

### Acknowledgement

The authors gratefully acknowledge the financial supports by Rajamangala University of Technology Isarn, Suranaree University of Technology, and the Office of the Higher Education Commission under NRU Project of Thailand.

### References

1. T. Matsumoto, A chaotic from Chua's circuit, IEEE Trans. Circuits Syst, vol. CAS-31, no. 12, 1055-1058, 1984.
2. K. S. Tang, K. F. Man, G. Q. Zhong, and G. Chen, Some New Circuit Design for Chaos Generation, in G. Chen and T. Ueta (Eds.) Chaos in Circuits and Systems, World Scientific, Singapore, 2002, 171-190.
3. L. A. B. Tôrres, L. A. Aguirre, R. M. Palhares, and E. M. A. M. Mendes, Chaos Control for Chua's Circuits. Control Of Chaos In Nonlinear Circuits And Systems: 97-164. 2008.
4. G. Chen and X. Dong, On feedback control of chaotic continuous-time systems, Circuits and Systems I: Fundamental Theory and Applications, IEEE Transactions on, vol. 40, 591-601, 1993.
5. M. Chen and Z. Han, Controlling and synchronizing chaotic Genesio system via nonlinear feedback control, Chaos, Solitons & Fractals, vol. 17, 709-716, 2003.
6. J. Lü and S. Zhang, Controlling Chen's chaotic attractor using backstepping design based on parameters identification, Physics Letters A, vol. 286, 148-152, 2001.
7. M. T. Yassen, Chaos control of chaotic dynamical systems using backstepping design, Chaos, Solitons & Fractals, vol. 27, 537-548, 2006.
8. J. Y. Hung, W. Gao, and J. C. Hung, Variable structure control: a survey, Industrial Electronics, IEEE Transactions on, vol. 40, 2-22, 1993.
9. G. Weibing and J. C. Hung, Variable structure control of nonlinear systems: a new approach, Industrial Electronics, IEEE Transactions on, vol. 40, 45-55, 1993.
10. T.-Y. Chiang, M.-L. Hung, J.-J. Yan, Y.-S. Yang, and J.-F. Chang, Sliding mode control for uncertain unified chaotic systems with input nonlinearity, Chaos, Solitons & Fractals, vol. 34, 437-442, 2007.
11. J. M. Nazzal and A. N. Natsheh, Chaos control using sliding-mode theory, Chaos, Solitons & Fractals, vol. 33, 695-702, 2007.
12. H. Wang, Z. Han, Q. Xie, and W. Zhang, Sliding mode control for chaotic systems based on LMI, Communications in Nonlinear Science and Numerical Simulation, vol. 14, 1410-1417, 2009.
13. D. Puangdownreong, S. Sujitjorn, and T. Kulworawanichpong, Convergence Analysis of Adaptive Tabu Search, ScienceAsia, vol. 30, 183-190, 2004.
14. D. Puangdownreong, K. N. Areerak, A. Srikaew, S. Sujitjorn, and P. Totarong, "System identification via Adaptive Tabu Search," In Proc. IEEE Int. Conf. on Industrial Technology (ICIT'02), Bangkok, Thailand, vol. 2, 915-920, 2002.
15. T. Kulworawanichpong, K-L. Areerak, K-N. Areerak, and S. Sujitjorn, Harmonic Identification for Active Power Filters Via Adaptive Tabu Search Method, Lecture Notes in Computer Science, Springer-Verlag Heidelberg, 2004, 687-694.



## Self-organization in the thin gas-sensitive Ag-containing polyacrylonitrile films

V. Petrov, N. Plugotarenko, T. Semenistaya

Southern Federal University, Rostov-on-Don, Russia  
E-mail: plugotarenkonk@sfedu.ru

**Abstract:** The surface of thin gas-sensitive Ag-containing polyacrylonitrile films is investigated by a method of atomic force microscopy. The assumption of existence in the studied spatial distributed system of signs of the determined chaos is confirmed with calculation of parameters of nonlinear dynamics. The interrelation between extent of self-organization in films of polyacrylonitrile and their gas-sensitive properties is found.

**Keywords:** electroconductive organic polymers, gas-sensitive materials, self-organization, theory of information, atomic force microscopy.

### 1. Introduction

Nanocomposite films of metallcontaining polyacrylonitrile (PAN), representing an organic matrix, which structure and properties change at influence of various temperatures, and the particles of a modifying additive dispersed in it, are a perspective material for microelectronics [1]. Ag-containing PAN films fabricated by pyrolysis method under the influence of incoherent IR-radiation from film-forming solutions, undergo transition from a liquid state of substance to the solid-state – this stage is process of self-organization of a material. The structure of the disorder material is formed in nonequilibrium conditions, the substance when hardening changes the properties in time and is distributed non-uniformly in space, and thus in the disorder environment occurs a spatial ordered structure [2]. Methods of nonlinear dynamics and theory of information are applied to the analysis of processes of self-organization in structure of materials: surface structure research of materials with various structural organization and revealing long-range correlations in these structures [3]. It is possible to investigate dynamics of system, measuring any of dynamic variables in one point at regular intervals. Thus the look and dimension of an attractor, number of degrees of freedom, correlation and fractal dimensions of a surface, Lyapunov exponents, average mutual information and other parameters of dynamics are defined. These methods which have been originally developed for research of behavior of systems, changing the condition in time, are adapted for studying of the spatial distributed systems what surfaces of the materials are.

### 2. Results and discussion

For carrying out researches a set of samples of Ag-containing PAN films using different technological regimes was fabricated.

Sensitivity of the films was evaluated using factor of gas-sensitivity  $S$ , which is calculated as:



$$S = (R_o - R_g)/R_o, R_o > R_g,$$

where  $R_o$  – value of resistance of a film on air,  $R_g$  – value of resistance of a film in the atmosphere of detected gas.

In view of the material surface is a fractal object general idea of fractal objects is used for its analysis [4].

Well-known in the theory of nonlinear systems Takens method is used to research the dynamics of formation of solid phase of gas-sensitive material of PAN films [2]. Patterns of self-organization processes at the formation of disordered materials, which the PAN films are, can be studied by means of the study of their surface, because their surface is a "snapshot" processes of solidification. Proceeding from this, the fractal dimension  $D_f$  of Ag-containing PAN films on the profile surface obtained with scanning probe microscope Solver P47 Pro (NT-MDT) in tapping mode on the air in the size of areas  $5 \times 5 \text{ mkm}^2$  was measured. Step of scanning determined the choice of the linear dimensions of the scanning area and used a number of steps. Surface scan carried out with a fixed number of points  $N = 256 \times 256$  regardless of the scanned area. Distribution function of the altitude profile of the surface  $\rho = f(h)$  of studied film, begins on some level  $h$ , taken as a zero. Using Image Analysis package processed 65536 points in a surface image of each sample for constructing this feature. This number of points is sufficient to identify the topology of attractor [2]. As a result of measurement of height profile for the samples, which were carried out along the surface through discrete intervals, get a three-dimensional image of the square surface. In the course of the processing of three-dimensional images of square surface areas by using the Image Analysis program received a graph of the distribution function of the height profile. For data processing Grassberger-Prokačičia algorithm was used [2].

The first Lyapunov exponent  $\lambda_1$  was calculated using Wolf's algorithm [5]. Lyapunov exponents are topological invariants that characterize the spatio-temporal evolution and stability of the system: dynamics of formation of solid-state is determined by the spatial-temporal chaos of a small dimension.

Calculation of the average mutual information  $I$  (AMI) was carried out by methods of the theory of information, described in [3]. AMI is the main characteristic of the correlations in nonlinear systems. AMI invariant relative to the different technologies and allows you to evaluate the impact of different technological factors on the structure of the material.

Studies have shown that application of different temperature and time regimes at forming the polymer nanocomposite films and modifying its transition metal with different percentage concentration lead to significant changes in the morphology of its surface.

Fig. 1 presents the image, obtained by AFM measurements of the surface morphology of a sample of Ag-containing PAN film. The distribution function of height profile  $h$  ( $\rho$  is the density of probability) (Fig.2) and the dependence of the correlation dimension  $D = f(\log_2 r)$  (Fig. 3) are given too.

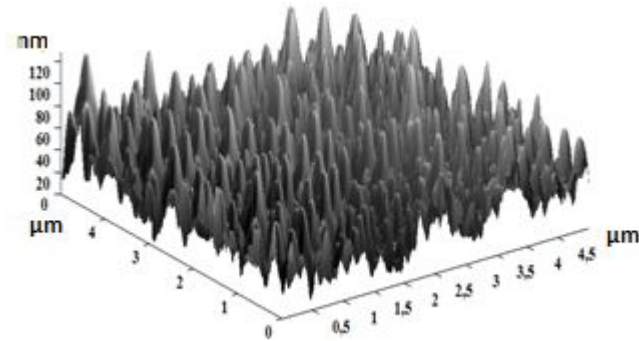


Fig. 1. AFM-image of the surface morphology of Ag-containing PAN film

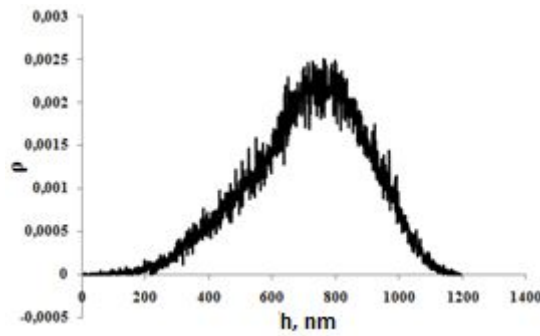


Fig. 2. Distribution function of height profile of Ag-containing PAN film

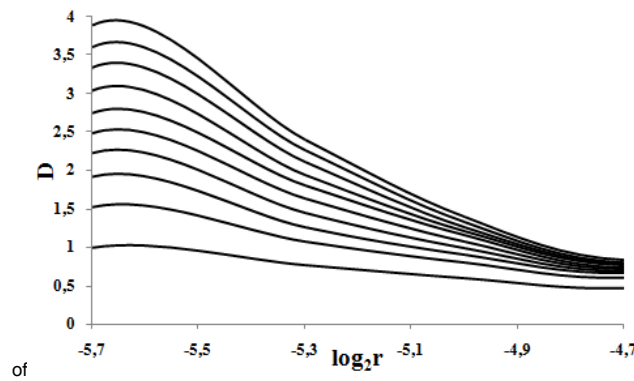


Fig. 3. Dependence  $D = f(\log_2 r)$  of Ag-containing PAN film

Dependence of correlation dimension  $D = f(\log_2 r)$  allows to testify the presence or absence of self-organizing structures in nanocomposite materials PAN/Ag. The analysis showed the presence of deterministic chaos in the system. It is

noted that the surface of the films with the best gas-sensing properties formed by three levels of self-similar structures.

Studies of the samples revealed that AMI has rather big range in values. AMI increases with increase of height of surface profile of films. Samples with disordered structure represent hundredths of units in AMI values that correspond to theoretical calculations for the amorphous material. Sufficiently high AMI values are observed in the samples with small value of the height of the surface profile (up to 30 nm) and good gas sensitivity ( $S = 0,46 \div 0,53$ ). High AMI values prove presence of long-range correlations in the system, which may be evidence of order as a result of self-organization processes [3].

Dependence of factor of gas-sensitivity on chlorine (107 ppm) and AMI value from silver content by weight in PAN films fabricated at the same technological regimes, is resulted on fig. 4. Character of the received dependences is similar. The maximal AMI value corresponds the maximal value of factor of gas-sensitivity.

Thus, the calculation of AMI allows to reveal correlations in disordered materials, which conclude a certain interrelation of electrophysical and gas-sensing properties of PAN/Ag films with its morphology of the surface.

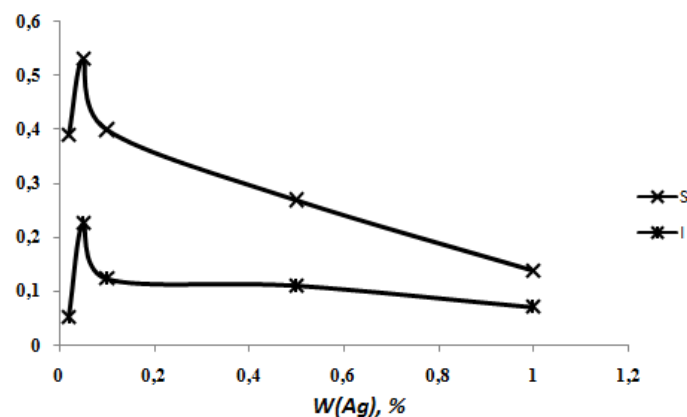


Fig. 4. Dependence of factor of gas-sensitivity (S) and AMI values (I) from silver content by weight in PAN films

For investigated samples Lyapunov first spatial exponent  $\lambda_r$ , which have appeared positive have been calculated. It means, that distribution of substance in space differs from equilibrium. The analysis of Lyapunov exponent testifies, that stability of structure of a material depends on technological parameters of its formation: higher values of temperature of second stage of IR-annealing tend to increase Lyapunov exponent. It is necessary to note absence of correlation between values of spatial Lyapunov exponent and percentage concentration of the modifying additive in samples.



### 3. Conclusions

The structure of the disorder materials is formed in strongly non-equilibrium conditions with violation of symmetry in the thermodynamically open, non-linear system. This is all the properties inherent in the self-organization. As a result of complex researches the presence of the spatially-ordered structures in the disorder amorphous organic matrix of polymer is confirmed.

During research it has been established, that greater value of the average mutual information and higher degree of self-organizing answers more ordered structure of the material and the highest values of factor of gas-sensitivity.

Thus, on the basis of knowledge of type of dynamics management of nonlinear system of synthesis of a material should be carried out coordinated with internal dynamic processes of substance. It will allow not only to operate effectively process of growth of the disorder materials, but also to program synthesis of materials for micro - and nanoelectronics with new unique properties.

### References

1. Korolev A. N., Semenistaya T.V., Al-Hadrami I. S., Loginova T. P., Bruns M. Nanocomposite copper-containing polyacrylonitrile films: composition, structure, morphology of the surface. // *Perspective materials*. 2010. №5. P. 52 – 56.
2. Vihrov S.P, Bodyagin N.V., Larina T.G., Mursalov S.M. Processes of height of unregulated semiconductors from positions of theory of self-organization. // *Physics and technique of semiconductors*. 2005. V. 39. №8. P. 953 – 959.
3. Avacheva T.G., Bodyagin N.V., Vihrov S.P, Mursalov S.M. Research of self-organization of unregulated materials with the use of theory of information. // *Physics and technique of semiconductors*. 2008. V. 42. №5. P. 513 – 518.
4. Douketis. C., Wang Z., Haslett T. L., Moskovits M. Fractal character of cold-deposited silver films determined by low-temperature scanning tunneling microscopy. // *Physical Review B*. 1995. V. 51. № 16. P. 11022 – 11031.
5. Wolf A., Swift J.B., Swinney H.L., Vastano J.A. Determining Lyapunov exponents from a time series. // *Physica D*. 1985. V. 16. P. 285 – 317.







# Exponential dichotomy and bounded solutions of the Schrödinger equation

Oleksander A. Pokutnyi<sup>1</sup>

Institute of mathematics of NAS of Ukraine, , 01601 Kiev, Ukraine  
(E-mail: lenasas@gmail.com)

**Abstract.** Necessary and sufficient conditions for existence of bounded on the entire real axis solutions of Schrödinger equation are obtained under assumption that the homogeneous equation admits an exponential dichotomy on the semi-axes. Bounded analytical solutions are represented using generalized Green's operator.

**Keywords:** exponential dichotomy, normally-resolvable operator, pseudoinverse Moore-Penrose operator.

Numerous papers deal with problems of the existence of bounded solutions of linear and nonlinear differential equations in Banach spaces and condition of exponential dichotomy on both semi-axes. We note the well-known paper [1], where such problems were considered in finite-dimensional spaces. Boundary value problems for linear differential equations in Banach spaces which admit exponential dichotomy on both semi-axes with bounded and unbounded operators in linear part was investigated in [2], [3]. The normal solvability of a differential operator was considered in [4]. The present paper dealt with the derivation of necessary and sufficient conditions for the existence of generalized bounded solutions of the Schrödinger equation in the Hilbert space.

## 1 Linear case

### 1.1 Statement of the Problem

Consider the next differential Schrödinger equation

$$\frac{d\varphi(t)}{dt} = -iH(t)\varphi(t) + f(t), t \in J \quad (1)$$

in a Hilbert space  $H$ , where, for each  $t \in J \subset R$ , the unbounded operator  $H(t)$  has the form  $H(t) = H_0 + V(t)$  ( here  $H_0 = H_0^*$  is unbounded self-adjoint operator with domain  $D = D(H_0) \subset H$ ), the mapping  $t \rightarrow V(t)$  is strongly continuous. Define as in [5] operator-valued function

$$\tilde{V}(t) = e^{itH_0} V(t) e^{-itH_0}.$$



In this case for  $\tilde{V}(t)$  Dyson's [5, p.311] representation is true and its propagator we define as  $\tilde{U}(t, s)$ . If  $U(t, s) = e^{-itH_0}\tilde{U}(t, s)e^{isH_0}$  then  $\psi_s(t) = U(t, s)\psi$  is a weak solution of (1) with condition  $\psi_s(s) = \psi$  in the sense that for any  $\eta \in D(H_0)$  function  $(\eta, \psi_s(t))$  is differentiable and

$$\frac{d}{dt}(\eta, \psi_s(t)) = -i(H_0\eta, \psi_s(t)) - i(V(t)\eta, \psi_s(t)), t \in J.$$

The present part dealt with the derivation of necessary and sufficient conditions for the existence of weak (in different senses) bounded solutions of the inhomogeneous equation (1) with  $f \in BC(J, H) = \{f : J \rightarrow H; \text{ the function } f \text{ is continuous and bounded}\}$ . Here the boundedness is treated in the sense that  $\|f\| = \sup_{t \in J} \|f(t)\| < \infty$ . For simplicity we suppose that  $D$  dense in  $H$ . The operator  $U(t, s)$  is a bounded linear operator for fixed  $t, s$ , and since the set  $D$  is dense in  $H$ , we find that it can be extended to the entire space  $H$  by continuity, which is assumed in forthcoming considerations. The extension of the family of evolution operators to the entire space is denoted in the same way.

## 1.2 Bounded solutions

Throughout the following, we use the notion of exponential dichotomy in the sense of [6]. It is of special interest to analyze the exponential dichotomy on the half-lines  $R_s^- = (-\infty, s]$  and  $R_s^+ = [s, \infty)$ . [In this case, the projection-valued functions defined on half-lines will be denoted by  $P_-(t)$  for all  $t \geq s$  and  $P_+(t)$  for all  $t < s$  with constants  $M_1, \alpha_1$  and  $M_2, \alpha_2$ , respectively ( $\alpha_1, \alpha_2$  - entropy or Lyapunov coefficients on the half-lines).] Most of the results obtained below follows directly from [3]. The main result of this section can be stated as follows.

**Theorem 1.** *Let  $\{U(t, s), t \geq s \in R\}$  be the family of strongly continuous evolution operators associated with equation (1). Suppose that the following conditions are satisfied.*

1. *The operator  $U(t, s)$  admits exponential dichotomy on the half-lines  $R_0^+$  and  $R_0^-$  with projection-valued operator-functions  $P_+(t)$  and  $P_-(t)$ , respectively.*

2. *The operator  $D = P_+(0) - (I - P_-(0))$  is generalized-invertible.*

*Then the following assertions hold.*

1. *There exist weak solutions of equation (1) bounded on the entire line if and only if the vector function  $f \in BC(R, H)$  satisfies the condition*

$$\int_{-\infty}^{+\infty} H(t)f(t)dt = 0, \quad (2)$$

where  $H(t) = \mathcal{P}_{N(D^*)}P_-(0)U(0, t)$ .

2. *Under condition (2), the weak solutions of (1) bounded on the entire line have the form*

$$\varphi_0(t, c) = U(t, 0)P_+(0)\mathcal{P}_{N(D)}c + (G[f])(t, 0)\forall c \in H, \quad (3)$$



where

$$(G[f])(t, s) = \begin{cases} \int_s^t U(t, \tau)P_+(\tau)f(\tau)d\tau - \int_t^{+\infty} U(t, \tau)(I - P_+(\tau))f(\tau)d\tau + \\ \quad + U(t, s)P_+(s)D^+[\int_s^{+\infty} U(s, \tau)(I - P_+(\tau))f(\tau)d\tau + \\ \quad + \int_{-\infty}^s U(s, \tau)P_-(\tau)f(\tau)d\tau], \quad t \geq s \\ \int_{-\infty}^t U(t, \tau)P_-(\tau)f(\tau)d\tau - \int_t^s U(t, \tau)(I - P_-(\tau))f(\tau)d\tau + \\ \quad + U(t, s)(I - P_-(s))D^+[\int_s^{+\infty} U(s, \tau)(I - P_+(\tau))f(\tau)d\tau + \\ \quad + \int_{-\infty}^s U(s, \tau)P_-(\tau)f(\tau)d\tau], \quad s \geq t \end{cases}$$

is the generalized Green operator of the problem on the bounded, on the entire line, solutions

$$(G[f])(0+, 0) - (G[f])(0-, 0) = - \int_{-\infty}^{+\infty} H(t)f(t)dt;$$

$$\mathcal{L}(G[f])(t, 0) = f(t), \quad t \in R$$

and

$$(\mathcal{L}x)(t) = \frac{dx}{dt} - iH(t)x(t),$$

$D^+$  is the Moore-Penrouse pseudoinverse operator to the operator  $D$ ;  $\mathcal{P}_{N(D)} = I - D^+D$  and  $\mathcal{P}_{N(D^*)} = I - DD^+$  are the projections [7] onto the kernel and cokernel of the operator  $D$ .

**Remark 1.** A similar theorem holds for the case in which the family of evolution operators  $U(t, s)$  admits exponential dichotomy on the half-lines  $R_s^+$  and  $R_s^-$ .

Now we show that condition 2 in theorem 1 can be omitted and in the different senses equation (1) is always resolvable. From the proof of the theorem 1 follows that equation (1) have bounded solutions if and only if the operator equation

$$D\xi = g, \tag{4}$$

$$g = \int_{-\infty}^0 U(0, \tau)P_-(\tau)f(\tau)d\tau + \int_0^{+\infty} U(0, \tau)(I - P_+(\tau))f(\tau)d\tau$$

is resolvable and its number depends from the dimension of  $N(D)$ .

Consider next 3 cases.

1) Classical strong generalized solutions.

Consider case when the operator  $D$  is normally-resolvable ( $R(D) = \overline{R(D)}$ ) is the set of values of  $D$ ). Then [7]  $g \in R(D)$  if and only if  $\mathcal{P}_{N(D^*)}g = 0$  and the set of solutions of (4) can be represented in the form [7]  $\xi = D^+g + \mathcal{P}_{N(D)}c, \forall c \in H$ .

2) Strong generalized solutions.

Consider the case when  $R(D) \neq \overline{R(D)}$ . We show that operator  $D$  may be extended to  $\overline{D}$  in such way that  $R(\overline{D})$  is closed.



Since the operator  $D$  is bounded the next representations of  $H$  in the direct sum are true

$$H = N(D) \oplus X, H = \overline{R(D)} \oplus Y,$$

with  $X = N(D)^\perp$  and  $Y = \overline{R(D)}^\perp$ . Let  $E = H/N(D)$  is quotient space of  $H$  and  $\mathcal{P}_{\overline{R(D)}}$  is orthoprojector, which projects onto  $\overline{R(D)}$ . Then operator

$$\mathcal{D} = \mathcal{P}_{\overline{R(D)}} D j^{-1} p : X \rightarrow R(D) \subset \overline{R(D)},$$

is linear, continuous and injective (here  $p : X \rightarrow E$  is continuous bijection and  $j : H \rightarrow E$  is a projection. The triple  $(H, E, j)$  is a locally trivial bundle with typical fiber  $\mathcal{P}_{N(L)}H$ ). In this case [8, p.26,29] we can define strong generalized solution of equation

$$\mathcal{D}\xi = g, \xi \in X.$$

We complete the space  $X$  with the norm  $\|\xi\|_{\overline{X}} = \|\mathcal{D}\xi\|_F$ , where  $F = \overline{R(D)}$  [8]. Then the extended operator

$$\overline{\mathcal{D}} : \overline{X} \rightarrow \overline{R(D)}, X \subset \overline{X}$$

is a homeomorphism of  $\overline{X}$  and  $\overline{R(D)}$ . Operator  $\overline{\mathcal{D}} := \overline{\mathcal{D}}\mathcal{P}_{\overline{X}} : \overline{H} \rightarrow H$  is normally-resolvable. By the construction of a strong generalized solution [8], the equation

$$\overline{\mathcal{D}} \overline{\xi} = g,$$

has a unique generalized solution, which we denote  $\overline{\mathcal{D}}^+ g$  which is called the strong generalized solution of (4). Then the set of strong generalized solutions of (4) has the form

$$\xi = \overline{\mathcal{D}}^+ g + \mathcal{P}_{N(D)}c, \forall c \in H.$$

3) Strong pseudosolutions.

Consider an element  $g \notin \overline{R(D)}$ . This condition is equivalent  $\mathcal{P}_{N(D^*)}g \neq 0$ . In this case there are elements from  $\overline{H}$  that minimize norm  $\|\overline{\mathcal{D}}\xi - g\|_{\overline{H}}$  for  $\xi \in \overline{H}$  :

$$\xi = \overline{\mathcal{D}}^+ g + \mathcal{P}_{N(D)}c, \forall c \in H.$$

These elements are called strong pseudosolutions by analogy of [7].

**Remark 2.** It should be noted that in each cases 1) - 3) the form of bounded solutions (4) isn't change.

**Remark 3.** As follows from 1) and 3) the notion of exponential dichotomy is equivalent of existence of bounded on the entire real axis solutions of (1).



## 2 Main result (Nonlinear case)

In the Hilbert space  $H$ , consider the differential equation

$$\frac{d\varphi(t)}{dt} = -iH(t)\varphi(t) + \varepsilon Z(\varphi, t, \varepsilon) + f(t). \quad (5)$$

We seek a bounded solution  $\varphi(t, \varepsilon)$  of equation (5) that becomes one of the solutions of the generating equation (1) for  $\varepsilon = 0$ .

To find a necessary condition on the operator function  $Z(\varphi, t, \varepsilon)$ , we impose the joint constraints

$$Z(\cdot, \cdot, \cdot) \in C[\|\varphi - \varphi_0\| \leq q] \times BC(R, H) \times C[0, \varepsilon_0],$$

where  $q$  is some positive constant.

Let us show that this problem can be solved with the use of the operator equation for generating constants

$$F(c) = \int_{-\infty}^{+\infty} H(t)Z(\varphi_0(t, c), t, 0) dt = 0. \quad (6)$$

**Theorem 2** (necessary condition). *Let the equation (1) admits exponential dichotomy on the half-lines  $R_0^+$  and  $R_0^-$  with projection-valued operator functions  $P_+(t)$  and  $P_-(t)$ , respectively, and let the nonlinear equation (5) have a bounded solution  $\varphi(\cdot, \varepsilon)$  that becomes one of the solutions of the generating equation (1) with constant  $c = c^0$ ,  $\varphi(t, 0) = \varphi_0(t, c^0)$  for  $\varepsilon = 0$ . Then this constant should satisfy the equation for generating constants (6).*

The proof of this theorem is the same as in [3, Theorem 1].

To find a sufficient condition for the existence of bounded solutions of (1), we additionally assume that the operator function  $Z(\varphi, t, \varepsilon)$  is strongly differentiable in a neighborhood of the generating solution ( $Z(\cdot, t, \varepsilon) \in C^1[\|\varphi - \varphi_0\| \leq q]$ ).

This problem can be solved with the use of the operator

$$B_0 = \int_{-\infty}^{+\infty} H(t)A_1(t)U(t, 0)P_+(0)\mathcal{P}_{N(D)}dt : H \rightarrow H,$$

where  $A_1(t) = Z^1(v, t, \varepsilon)|_{v=\varphi_0, \varepsilon=0}$  (the Fréchet derivative).

**Theorem 3** (sufficient condition). *Suppose that the equation (1) admits exponential dichotomy on the half-lines  $R_0^+$  and  $R_0^-$  with projection-valued functions  $P_+(t)$  and  $P_-(t)$ , respectively. In addition, let the operator  $B_0$  satisfy the following conditions.*

1. The operator  $B_0$  is Moore-Penrose pseudoinvertible.
2.  $\mathcal{P}_{N(B_0^*)}\mathcal{P}_{N(D^*)}P_-(0) = 0$ .

*Then for an arbitrary element of  $c = c^0 \in H$  satisfying the equation for generating constants (6), there is exists bounded solution. This solution can be found with the use of the iterative process*



$$\begin{aligned}\bar{y}_{k+1}(t, \varepsilon) &= \varepsilon G[Z(\varphi_0(\tau, c^0 + y_k, \tau, \varepsilon))](t, 0), \\ c_k &= -B_0^+ \int_{-\infty}^{+\infty} H(\tau) \{A_1(\tau) \bar{y}_k(\tau, \varepsilon) + \mathcal{R}(y_k(\tau, \varepsilon), \tau, \varepsilon)\} d\tau, \\ \mathcal{R}(y_k(t, \varepsilon)) &= Z(\varphi_0(t, c^0) + y_k(t, \varepsilon), t, \varepsilon) - Z(\varphi_0(t, c^0), t, 0) - A_1(t) y_k(t, \varepsilon), \\ \mathcal{R}(0, t, 0) &= 0, \quad \mathcal{R}_x^{(1)}(0, t, 0) = 0, \\ y_{k+1}(t, \varepsilon) &= U(t, 0) P_+(0) \mathcal{P}_{N(D)} c_k + \bar{y}_{k+1}(t, 0, \varepsilon), \\ \varphi_k(t, \varepsilon) &= \varphi_0(t, c^0) + y_k(t, \varepsilon), \quad k = 0, 1, 2, \dots, \quad y_0(t, \varepsilon) = 0, \quad \varphi(t, \varepsilon) = \lim_{k \rightarrow \infty} \varphi_k(t, \varepsilon).\end{aligned}$$

## 2.1 Relationship between necessary and sufficient conditions

First, we formulate the following assertion.

**Corollary.** *Let a functional  $F(c)$  have the Fréchet derivative  $F^{(1)}(c)$  for each element  $c^0$  of the Hilbert space  $H$  satisfying the equation for generating constants (6). If  $F^{(1)}(c)$  has a bounded inverse, then equation (5) has a unique bounded solution on the entire line for each  $c^0$ .*

**Remark 4.** If assumptions of the corollary are satisfied, then it follows from its proof that the operators  $B_0$  and  $F^{(1)}(c^0)$  are equal. Since the operator  $F^{(1)}(c)$  is invertible, it follows that assumptions 1 and 2 of Theorem 3 are necessarily satisfied for the operator  $B_0$ . In this case, equation (5) has a unique bounded solution for each  $c^0 \in H$ . Therefore, the invertibility condition for the operator  $F^{(1)}(c)$  relates the necessary and sufficient conditions. In the finite-dimensional case, the condition of invertibility of the operator  $F^{(1)}(c)$  is equivalent to the condition of simplicity of the root  $c^0$  of the equation for generating amplitudes [7].

In such way we obtain the modification of the well-known method of Lyapunov-Schmidt. It should be emphasized that theorem 2 and 3 give us possible condition of chaotic behavior of (5) [9].

## References

1. *K. J. Palmer.* Exponential dichotomies and transversal homoclinic points. *J. Differential Equat.* **55**.-1984. P. 225–256.
2. *Boichuk A.A., Pokutnyi O.A.* Dichotomy and boundary value problems on the whole line. - Proceedings, 5th Chaotic Modeling and Simulation International Conference, 12-15 June 2012, Athens Greece. - p.81-89.
3. *Pokutnyi A.A.* Bounded solutions of linear and weakly nonlinear differential equations in a Banach space with unbounded operator in the linear part. *Differential equations (in Russian)*, 2012, vol.48, No.6 - pp.803-813.



4. *A. A. Boichuk and A.A. Pokutnij*. Bounded solutions of linear differential equations in Banach space. *Nonlinear Oscillations*, **9**, no 1. - 2006. - P. 3-14; <http://www.springer.com/>.
5. *Reed M., Symon B.* Methods of modern mathematical physics: in 4 vol. - :World, 1978. - v.2: Harmonic analysis. Selfadjointness. - 1978. - 395p.(in Russian)
6. *Henry D.* Geometric theory of semilinear parabolic equations. - :Mir, 1985. - 376p.(in Russian)
7. *Boichuk A.A., Samoilenko A.M.* Generalized Inverse Operators and Fredholm Boundary Value Problems. - VSP, Utrecht-Boston, 2004. - 317 p.
8. *Klyushin D.A., Lyashko S.I., Nomirovskii D.A., Petunin Yu. I., Semenov V.V.* Generalized Solutions of Operator Equations and Extreme Elements. Springer, 2012. 202+xxi p.
9. *Chueshov I.D.* Introduction to the theory of infinite-dimensional dissipative systems. Acta, 2002. - 416p.







## Recovery of Coupling Architecture in Ensembles of Coupled Time-Delay Systems

Vladimir I. Ponomarenko, Mikhail D. Prokhorov and Ilya V. Sysoev

Saratov Branch of the Institute of Radio Engineering and Electronics of Russian Academy of Sciences, Saratov, Russia  
E-mail: [ponomarenkovi@gmail.com](mailto:ponomarenkovi@gmail.com)

**Abstract:** A method is proposed for the recovery of coupling architecture and coupling values in ensembles of interacting time-delay systems. The method is based on the reconstruction of the model equations for ensemble elements and diagnostics of significance of couplings from time series of elements oscillations.

**Keywords:** Dynamical modeling; Time series analysis; Time-delay systems; Ensembles of oscillators; Coupling detection.

### 1. Introduction

The behavior of complex systems composed of several interacting elements depends on not only the properties of the elements, but also on the character of their coupling. For example, the structure and intensity of couplings in an ensemble of oscillating systems determines the possibility of their synchronization and the formation of different spatial and temporal structures [1]. In recent years, much attention has been paid to the problem of revealing the presence of couplings in ensembles of multielement systems and determining their structure and characteristics from time series [2–4]. Usually this problem is solved using the methods based on the phase dynamics modeling. Here, we propose a method for reconstructing the coupling values and architecture in large ensembles of interacting systems based on a method for reconstructing the model equations of ensemble elements from time series of their oscillations. Using this method we reconstructed for the first time the a priori unknown architecture of couplings in an ensemble of chaotic time-delay systems with a complex coupling structure.

### 2. Method Description

Let us consider an ensemble composed of diffusively coupled time-delay systems, where each system is described by the equation:

$$\varepsilon_i \dot{x}_i(t) = -x_i(t) + f_i(x_i(t - \tau_i)) + \sum_{j=1(j \neq i)}^M k_{i,j} (x_j(t) - x_i(t)), \quad (1)$$



where  $i = 1, \dots, M$ ,  $M$  is the number of elements in the ensemble,  $\varepsilon_i$  is the parameter characterizing the inertial properties of the system,  $\tau_i$  is the delay time,  $f_i$  is a nonlinear function, and  $k_{i,j}$  are the coupling coefficients.

To determine all coupling coefficients in the ensemble we propose a method based on reconstructing model equation (1) for each element. First, we reconstruct the delay times. In [5] we have found out that there are practically no extrema separated by the delay time in time series of isolated ( $k_{i,j} = 0$ ) time-delay systems of type (1). Having determined, for different  $\tau$  values, number  $N_i$  of situations where the points of a chaotic time series, spaced by time interval  $\tau$ , are simultaneously extremal and having plotted dependence  $N_i(\tau)$ , we can find delay time  $\tau_i$  as a value at which this dependence exhibits an absolute minimum [5]. The validity of this method for reconstructing  $\tau_i$  in a chain of coupled time-delay systems was substantiated in [6]. According to our results, this method for determining the delay time remains efficient for ensembles of systems (1) with an arbitrary number of couplings between elements, provided that the interaction of systems does not induce a large number of additional extrema in chaotic time series of their oscillations. This assumption remains valid for weak coupling  $k_{i,j} \ll x_i$  even in the case of globally coupled systems (1). Note that the condition of weak coupling and the absence of synchronization between ensemble elements is necessary for almost all methods for revealing couplings [4].

Having determined  $\tau_i$ , one can reconstruct parameter  $\varepsilon_i$ , nonlinear function  $f_i$ , and the coupling coefficients  $k_{i,j}$  of the  $i$ th time-delay system (1), knowing the time series of oscillations of all ensemble elements. For that we propose the following approach. Let us write (1) in the form:

$$\varepsilon_i \dot{x}_i(t) + x_i(t) - \sum_{j=1(j \neq i)}^M k_{i,j} (x_j(t) - x_i(t)) = f_i(x_i(t - \tau_i)). \quad (2)$$

If one plots the dependence of the left-hand side of (2) on  $x_i(t - \tau_i)$ , it will coincide with the function  $f_i$ . Since  $\varepsilon_i$  and  $k_{i,j}$  are a priori unknown, we will search for them by minimizing the parameter:

$$L_i(\varepsilon_i, k_{i,j}) = \sum_{n=1}^{S-1} \left( (y_{i,n+1} - y_{i,n})^2 + (z_{i,n+1} - z_{i,n})^2 \right) \quad (3)$$

This parameter characterizes the distance between the points in the  $(y_i, z_i)$  plane, which are sorted with respect to the coordinate  $y_i$ . Here,  $y_i = x_i(t - \tau_i)$ ,



$$z_i = \varepsilon_i \dot{x}_i(t) + x_i(t) - \sum_{j=1(j \neq i)}^M k_{i,j} (x_j(t) - x_i(t)) \quad (4)$$

$n$  is the point number and  $S$  is the number of points. When the  $\varepsilon_i$  and  $k_{i,j}$  values are chosen incorrectly, the points in the  $(y_i, z_i)$  plane do not lie on one-dimensional curve  $f_i$ . Therefore, the  $L_i(\varepsilon_i, k_{i,j})$  value is larger than that for true  $\varepsilon_i$  and  $k_{i,j}$ .

For  $\varepsilon_i$  and  $k_{i,j}$  we set starting conjectures and then refine them by the simplex method with minimization of (3), which minimum is denoted as  $L_{i,M}$ . For  $M \leq 4$  and the absence of noise, all parameters are reconstructed with a high accuracy. However, at  $M > 4$  the situation in which the method does not allow one to reveal the absent couplings between ensemble elements becomes typical. These couplings are identified as weak because of the presence of indirect couplings via other elements.

Insignificant couplings can be rejected by the method of successive trial exclusion of the coefficients  $k_{i,j}$  from model (1). We hypothesize that the two elements are not coupled (by excluding the corresponding coupling coefficient  $k_{i,j}$ ) and reconstruct the other parameters of the model finding the minimum  $L_{i,j,M-1}$  of function (3). This procedure is then repeated by excluding another  $k_{i,j}$  at a fixed  $i$ , etc., for all  $j = 1, \dots, M$  ( $j \neq i$ ). Finally, we determine the exclusion of which  $k_{i,j}$  yields  $L_{i,M-1} = \min_j L_{i,j,M-1}$  and estimate the statistical significance

of the magnitude  $L = L_{i,M-1}/L_{i,M}$  based on the following considerations. At large  $S$ , the differences  $y_{i,n+1} - y_{i,n}$  and  $z_{i,n+1} - z_{i,n}$  in (3) are distributed according to the close to normal law, where  $S/2$  of these differences can be considered as independent because they have no common coordinates. In addition,  $L_{i,M}$  depends on  $M$  parameters of model (2), a fact that reduces the number of independent values in (3) to  $S/2 - M$ . Then, taking into account that the sum of squares of  $K$  independent normally distributed values obeys the chi-square law with  $K$  degrees of freedom [7], we find that the  $L_{i,M}$  values obtained at different parameters and/or in the presence of noise are distributed according to the chi-square law with  $S/2 - M$  degrees of freedom and the  $L_{i,M-1}$  values are distributed according to the chi-square law with  $S/2 - M + 1$  degrees of freedom. The parameter  $X$ , which is a ratio of two independent random values distributed according to the chi-square law with  $v$  and  $w$  degrees of freedom, is known to obey the Fisher-Snedecor distribution with the distribution function

$$F_{v,w}(X) = B_d \left( \frac{v}{2}, \frac{w}{2} \right) \quad (5)$$



where  $B$  is the incomplete  $\beta$  function and  $d = vX/(vX + w)$  [8]. Therefore, the magnitude  $L$  is described by distribution function (5) with  $X=L$ ,  $v=S/2 - M + 1$  and  $w = S/2 - M$ . We denote the  $L$  value at which  $F_{v,w}(L_{1-p}) = 1 - p$  as  $L_{1-p}$  ( $p$  is the statistical significance level). Then, if  $L > L_{1-p}$ , one can conclude at the significance level  $p$  that the elements are coupled and, therefore, all  $k_{ij} \neq 0$ . In the opposite case we conclude that the corresponding elements are not coupled and check the significance level for other couplings, successively excluding the remaining couplings of the  $i$ th element one by one. The procedure is repeated until all couplings become significant. This approach makes it possible to reconstruct the coupling architecture, parameters of all elements, and their nonlinear functions.

If the number of couplings between ensemble elements is known to be small, the method of successive trial addition of the coefficients  $k_{ij}$  to model (1) is preferred for reconstructing the coupling architecture and values. At first, we find the minimum  $L_{i,1}$  of function (3) under the assumption that all  $k_{ij}$  are absent in (1) (i.e., there are no couplings). Then we successively (one by one) introduce  $k_{ij}$  into (1) and find the minimum  $L_{i,j,2}$  of function (3). Running over all  $j \neq i$ , we find  $L_{i,2} = \min_j L_{i,j,2}$ . If  $L > L_{1-p}$ , where  $L = L_{i,1}/L_{i,2}$ , and  $F_{v,w}$  is plotted at  $v = S/2 - 1$  and  $w = S/2 - 2$ , the coupling introduced is nonzero at significance level  $p$ . This procedure is repeated until next coupling added to the model turns out to be insignificant.

### 3. Method Application

As an example, we consider the reconstruction of the coupling architecture in an ensemble of coupled Mackey-Glass systems described by (1) with the function

$$f_i(x_i(t - \tau_i)) = \frac{a_i x_i(t - \tau_i)}{b_i(1 + x_i^{10}(t - \tau_i))} \quad (6)$$

and  $\varepsilon_i = 1/b_i$ . These systems are affected by independent normal noises  $\zeta_i(t)$  with a zero mean and dispersion  $\sigma_i^2$ . The parameters of the elements were specified randomly: integer  $\tau_i \in [300, 400]$ ,  $\varepsilon_i \in [8, 12]$ ,  $a_i \in [0.2, 0.25]$ ,  $k_{ij} \in [0.08, 0.12]$  and  $\sigma_i^2 = 10^{-4}$ . At these parameter values all elements oscillate chaotically. The time series of each element contains 10 000 points with a sampling step of 1. Fig. 1 shows the architecture of randomly chosen couplings in an ensemble of  $M = 10$  elements.

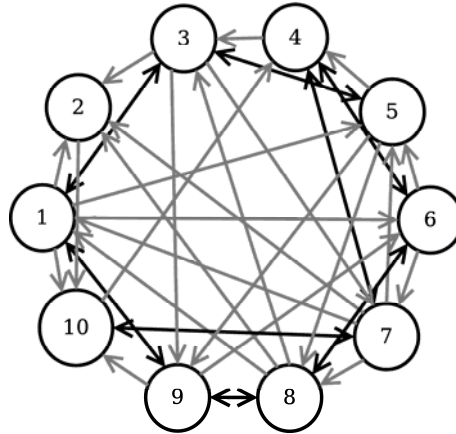


Fig. 1. Coupling architecture in an ensemble of ten elements. Forty of ninety possible couplings are present. Bidirectional and unidirectional couplings are shown in black and gray, respectively.

The results of reconstruction of one element with the parameters  $\tau_5 = 348$ ,  $\varepsilon_5 = 9.5$ ,  $k_{5,1} = 0.112$ ,  $k_{5,3} = 0.085$ ,  $k_{5,6} = 0.116$ ,  $k_{5,7} = 0.090$ , and  $k_{5,j} = 0$  ( $j = 2, 4, 5, 8, 9$ , and  $10$ ) are shown in Fig. 2. Having calculated number  $N_5$  of times when  $\dot{x}_5(t)$  and  $\dot{x}_5(t - \tau)$  simultaneously turn to zero for different  $\tau$ , taken with a step of 1, we plot the dependence  $N_5(\tau)$  (Fig. 2a). To estimate the time derivative from time series we used a local parabolic approximation. The minimum of  $N_5(\tau)$  is observed at the true delay time  $\tau = \tau_5 = 348$ .

Fig. 2b shows the nonlinear function  $f_5$  reconstructed in the  $(y_5, z_5)$  plane with  $y_5 = x_5(t - \tau'_5)$  and

$$z_5 = \varepsilon'_5 \dot{x}_5(t) + x_5(t) - \sum_{j=1(j \neq 5)}^{10} k'_{5,j} (x_j(t) - x_5(t)) \quad (7)$$

Function  $f_5$  obtained as the result of reconstruction of (1) under the assumption that all ensemble elements are uncoupled is shown with gray color. The function is plotted at the following parameters obtained during reconstruction:  $\tau'_5 = 348$ ,  $\varepsilon'_5 = 8.4$ , and  $k'_{5,j} = 0$  ( $j = 1, \dots, 10; j \neq 5$ ). Function  $f_5$  reconstructed using the method of successive trial addition of the coupling coefficients to the model at  $p = 0.05$  is shown with black color. It is plotted at the following parameters obtained during reconstruction:  $\tau'_5 = 348$ ,  $\varepsilon'_5 = 9.6$ ,  $k'_{5,1} = 0.111$ ,  $k'_{5,3} = 0.085$ ,  $k'_{5,6} = 0.105$ ,  $k'_{5,7} = 0.080$ , and  $k'_{5,j} = 0$  ( $j = 2, 4, 5, 8, 9$ , and  $10$ ).

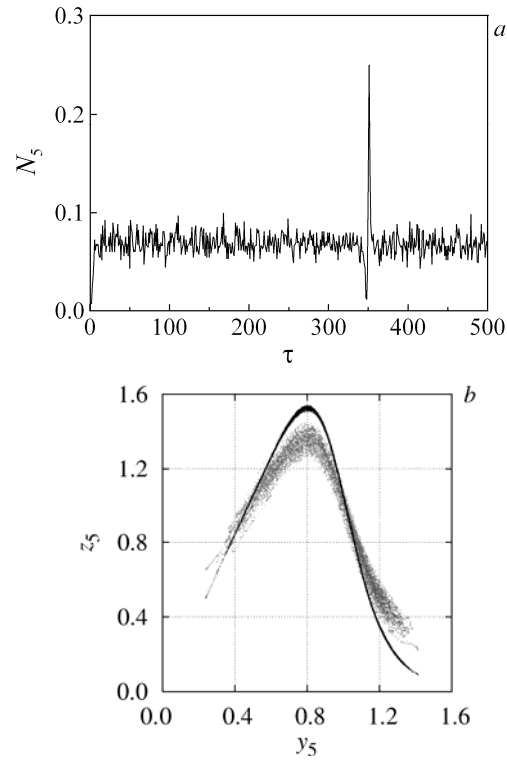


Fig. 2. (a) Number  $N_5$  of pairs of extrema in the time series of the variable  $x_5(t)$  (spaced by  $\tau$ ) normalized to the total number of extrema in the time series. (b) Reconstructed nonlinear function  $f_5$ .

Taking into account the coupling architecture significantly improves the quality of reconstruction of the nonlinear function and the accuracy of the model parameters estimation. The inaccuracy of the parameters recovery is mainly caused by the presence of noise.

The results of reconstructing the coupling architecture in the entire ensemble, obtained using the method of adding of couplings, are shown in Fig. 3. A square with the coordinates  $(j, i)$  illustrates the influence of the  $j$ th element on the  $i$ th element, except for the squares in the diagonal, which carry no information. At the significance level  $p = 0.05$  we found 39 of the 40 existing couplings (Fig. 1). Only one coupling was missed and spurious couplings were absent.

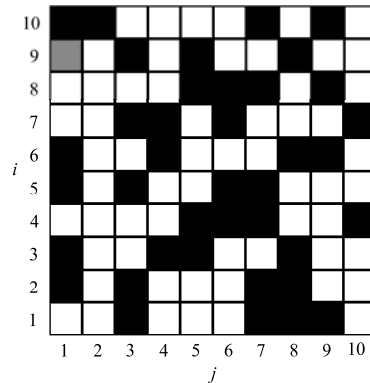


Fig.3. Diagram of the results of recovering the coupling architecture in an ensemble of ten Mackey–Glass systems obtained at the significance level  $p = 0.05$  using the method of successive trial addition of coupling coefficients to the model. Correctly recovered couplings, correctly found absent couplings, and missed couplings are shown in black, white, and gray, respectively.

Note that reconstructing the coupling architecture from the same time series using the method of excluding of couplings, we obtained many spurious couplings at the same  $p$ . The method of excluding of couplings is more efficient for reconstructing ensembles where the number of existing couplings is many times larger than the number of absent couplings. On the contrary, the method of adding of couplings is most efficient when the number of couplings in an ensemble is small. It works well even in the case of large ensembles ( $M = 50$ ). The case under consideration, in which the numbers of existing and absent couplings are comparable, is the most complicated for reconstruction. In these situations the method of adding of couplings is more efficient.

### 3. Conclusions

We have proposed the method for the reconstruction of coupling architecture in ensembles of interacting time-delay systems. Besides the coupling values, the method allows one to recover the delay times, parameters of inertia, and nonlinear functions of each element of the ensemble. For the diagnostics of significance of couplings we have used the method of successive trial addition of coupling terms to the model and the method of successive trial exclusion of coupling terms from the model. The method is successfully applied to the reconstruction of the coupling architecture in the ensemble of coupled nonidentical Mackey-Glass systems from chaotic time series of their oscillations.

### References

1. A. Pikovsky, M. Rosenblum, and J. Kurths. *Synchronization: A Universal Concept in Nonlinear Sciences*, Cambridge: Cambridge University Press, 2001.
2. M. Timme. Revealing network connectivity from response dynamics, *Phys. Rev. Lett.*, 98: 224101, 2007.



3. I. T. Tokuda, S. Jain, I. Z. Kiss, and J. L. Hudson. Inferring phase equations from multivariate time series, *Phys. Rev. Lett.* 99:064101, 2007.
4. D. A. Smirnov and B. P. Bezruchko. Detection of couplings in ensembles of stochastic oscillators, *Phys. Rev. E* 79: 046204, 2009.
5. M. D. Prokhorov, V. I. Ponomarenko, A. S. Karavaev, and B. P. Bezruchko. Reconstruction of time-delayed feedback systems from time series, *Physica D* 203:209–223, 2005.
6. V. I. Ponomarenko and M. D. Prokhorov. Estimating characteristics of ensemble of coupled delay-feedback systems from their experimental time series, *Tech. Phys. Lett.* 36:902–905, 2010.
7. M. Kendall and A. Stuart. *The Advanced Theory of Statistics*, New York: MacMillan, 1979.
8. N. L. Johnson, S. Kotz, and N. Balakrishnan. *Continuous Univariate Distributions*, vol. 2, New York: Wiley, 1995.





## Digital Secure Communication Using Chaotic Time-Delay Systems

Mikhail D. Prokhorov, Vladimir I. Ponomarenko, Danil D. Kulminskiy,  
Anatoly S. Karavaev

Saratov Branch of the Institute of Radio Engineering and Electronics of Russian  
Academy of Sciences, Saratov, Russia

E-mail: [mdprokhorov@yandex.ru](mailto:mdprokhorov@yandex.ru)

**Abstract:** We have developed an experimental system for secure communication with nonlinear mixing of information signal and chaotic signal of a time-delay system based on programmable microcontrollers with digital transmission line. The proposed scheme allows one to transmit and receive speech and musical signals in a real time without noticeable distortion.

**Keywords:** Chaotic communication, Time-delay systems, Chaotic synchronization.

### 1. Introduction

The development of communication systems employing the phenomenon of synchronization of chaotic oscillations has attracted a lot of attention [2, 4, 7, 8] due to the broadband power spectrum of chaotic signals, high speed of information transmission, and tolerance to sufficiently high levels of noise. Besides, many chaotic communication schemes are simply realized and demonstrate a rich variety of different oscillating regimes.

Different approaches for the transmission of information signals using chaotic dynamics have been proposed. Nonlinear mixing of information signal and chaotic signal is one of the most widespread among them [4]. However, one of the main disadvantages of communication systems with nonlinear mixing is their comparatively low interference immunity [4]. It is explained by the fact that, in order to ensure the security of transmitted data, the level of information signal must be significantly lower than that of the chaotic carrier. Under these conditions, the presence of noise in the communication channel leads to an appreciable distortion of the message signal at the scheme output.

We propose a scheme of data transmission with nonlinear mixing, in which the information signal is added to a chaotic signal that is formed as a result of digital calculations on a microcontroller. The receiver, whose parameters are identical with those of the transmitter, receives a digital signal from which the information component is extracted using again digital calculations. Such communication system exploits masking of the information signal by a chaotic signal and possesses sufficiently high stability to noise that is inherent in digital systems of data transmission.

In order to increase the level of security of hidden data transmission it has been proposed to employ time-delay systems, demonstrating chaotic dynamics of very high dimension, in private communication [5, 6, 9, 11]. For this reason, we

have considered in the present paper a communication scheme with nonlinear mixing based on chaotic oscillator with delayed feedback.

## 2. Communication Scheme

A block diagram of the communication system with nonlinear mixing is shown in Figure 1. A transmitter represents a ring system composed of a delay line, a nonlinear element, and a linear low-pass filter. The information signal  $m(t)$  is added to the chaotic signal  $f(x(t-\tau))$  with the help of a summator and the signal  $s(t)=f(x(t-\tau))+m(t)$  is transmitted into the communication channel and simultaneously injected into the feedback circuit of the transmitter whose dynamics is described by a first-order delay-differential equation

$$\varepsilon \dot{x}(t) = -x(t) + f(x(t-\tau)) + m(t), \quad (1)$$

where  $x(t)$  is the system state at time  $t$ ,  $f$  is a nonlinear function,  $\tau$  is the delay time, and  $\varepsilon$  is a parameter that characterizes the inertial properties of the system. With this nonlinear mixing the information signal is directly involved in the formation of a complicated dynamics of the chaotic system.

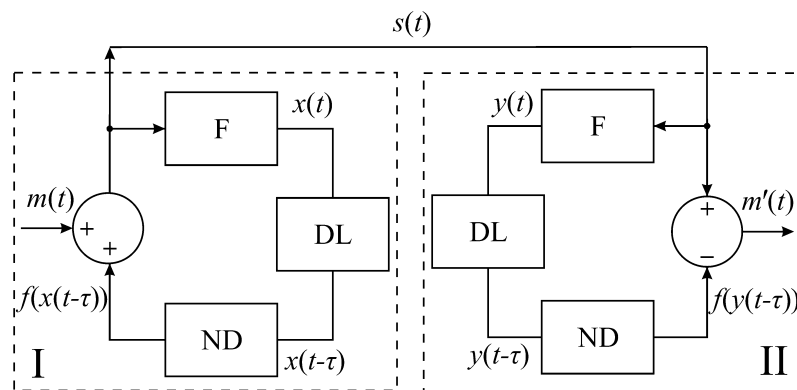


Fig. 1. Block diagram of the communication system with nonlinear mixing: (I) transmitter, (II) receiver, (DL) delay lines, (ND) nonlinear devices, and (F) filters.

A receiver is composed of the same elements as the transmitter, except for the summator that is replaced by a subtractor breaking the feedback circuit. The receiver equation is

$$\varepsilon \dot{y}(t) = -y(t) + f(x(t-\tau)) + m(t). \quad (2)$$

At the output of the subtractor we have the extracted information signal  $m'(t)=f(x(t-\tau))+m(t)-f(y(t-\tau))$ . If the transmitter and the receiver are



composed of identical elements, they become completely synchronized after the transient process. The difference between the oscillations of systems (1) and (2),  $\Delta(t) = x(t) - y(t)$ , decreases in time for any  $\varepsilon > 0$ , since  $\dot{\Delta}(t) = -\Delta(t)/\varepsilon$ . As the result of synchronization we have  $x(t) = y(t)$  and, hence,  $f(x(t-\tau)) = f(y(t-\tau))$  and  $m'(t) = m(t)$ . It should be noted, that the quality of the extraction of message  $m(t)$  does not depend on its amplitude and frequency characteristics. By this is meant that the considered communication scheme allows one to transmit complicated information signals without distortion. The nonlinear element in our scheme provides a quadratic transformation. In this case the transmitter equation takes the form

$$\varepsilon \dot{x}(t) = -x(t) + \lambda - (x(t-\tau))^2 + m(t), \quad (3)$$

where  $\lambda$  is the parameter of nonlinearity. The transmitter parameters were chosen to obtain a regime of developed chaotic oscillations.

We used a programmable microcontroller to implement the transmitter. Since this device has no built-in facilities supporting the floating-point operations, one should use integer calculations in microcontroller in order to increase the speed of response. For this purpose the variables and parameters of Eq. (3) were scaled as follows. For small  $\varepsilon$ , the allowable limits of variation of the parameter  $\lambda$  for which system (3) has a periodic or chaotic attractor are from 0 to 2. Within this range of  $\lambda$  variation the dynamical variable  $x(t)$  can take values from  $-2$  to  $+2$ . Let us pass to integer arithmetic and transform Eq. (3) in such a way that the dynamical variable would be placed in a 16-bit memory location, whereby its integer values vary between  $-2^{15}$  and  $2^{15}$ . It can be done by substituting variables as  $X(t) = 2^{14}x(t)$  and  $M(t) = 2^{14}m(t)$ . Then, Eq. (3) takes the following form:

$$\frac{\varepsilon \dot{X}(t)}{2^{14}} = -\frac{X(t)}{2^{14}} + \lambda - \left(\frac{X(t-\tau)}{2^{14}}\right)^2 + \frac{M(t)}{2^{14}}. \quad (4)$$

Multiplying both sides of Eq. (4) by  $2^{14}$  and introducing parameter  $\Lambda = 2^{14}\lambda$ , we obtain the following equation:

$$\varepsilon \dot{X}(t) = -X(t) + \Lambda - \frac{(X(t-\tau))^2}{2^{14}} + M(t). \quad (5)$$

This differential equation can be reduced to a difference equation, which is more convenient for program implementation on a microcontroller:

$$X_{n+1} = \left(1 - \frac{\Delta t}{\varepsilon}\right) X_n + \frac{\Delta t}{\varepsilon} (F(X_{n-k}) + M_n), \quad (6)$$

where  $n$  is the discrete time,  $\Delta t$  is the time step,  $k$  is the discrete delay time in units of sampling time  $\Delta t$ , and  $F(X_{n-k}) = \Lambda - X_{n-k}^2/2^{14}$ .

Figure 2 shows a block diagram of the transmitter based on a programmable microcontroller. At the first step of microcontroller program operation the circular buffer array (containing the values from  $X_{n-k}$  to  $X_n$ ) is initialized by a certain constant value as the initial condition. Then, the nonlinear function  $F(X_{n-k})$  is calculated and summed with the information signal  $M_n$ . After that, the obtained sum  $S_n$  is transmitted into the communication channel that is organized as a serial digital interface. The subsequent value of the discrete dynamic variable  $X_{n+1}$  is calculated in accordance with relation (6) and fed into the circular buffer. After  $k$  cycles the process of initialization is accomplished and the buffer is filled by actual values.

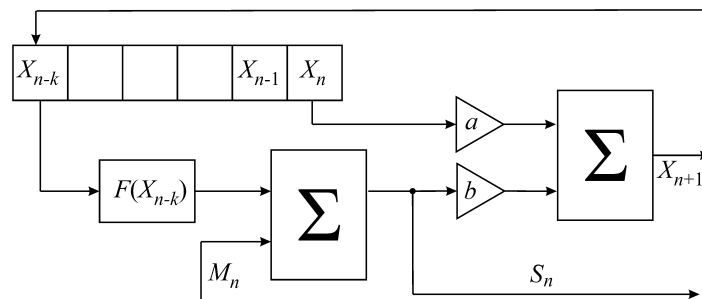


Fig. 2. Block diagram of the transmitter implemented on a microcontroller: ( $\Sigma$ ) summator,  $a$  and  $b$  are constant multipliers, where  $a = 1 - \Delta t/\varepsilon$  and  $b = \Delta t/\varepsilon$ .

The linear transformation of the signal in our scheme was performed using a digital low-pass first-order Butterworth filter. It should be noted that employment of high-order filters with an infinite or finite pulse characteristic usually allows one to increase the security of the communication scheme. The greater the number of coefficients in the equation that describes the filter, the greater the number of previous values of the variable involved in calculations of the next value and, hence, the higher the security level of transmitted data. The nonlinear transformation can also be of various types. For example, one can use a Bernoulli map, a tent map, or other maps with chaotic dynamics.

### 3. Extracting Information Signal Mixed with Chaotic Signal

In our scheme the transmitter was implemented on a programmable microcontroller of the Atmel megaAVR family. As the information signal we choose a musical information signal (a song). Part of the time series of this audio signal is presented in Figure 3(a). The analog information signal  $m(t)$  is fed to the input of an analog-to-digital converter (ADC) and the signal  $M_n$  from its output is mixed with the chaotic signal of the transmitter. The calculations are performed in terms of integer arithmetic, with the chaotic signal amplitude varying within 16 bits and the information signal within 12 bits.

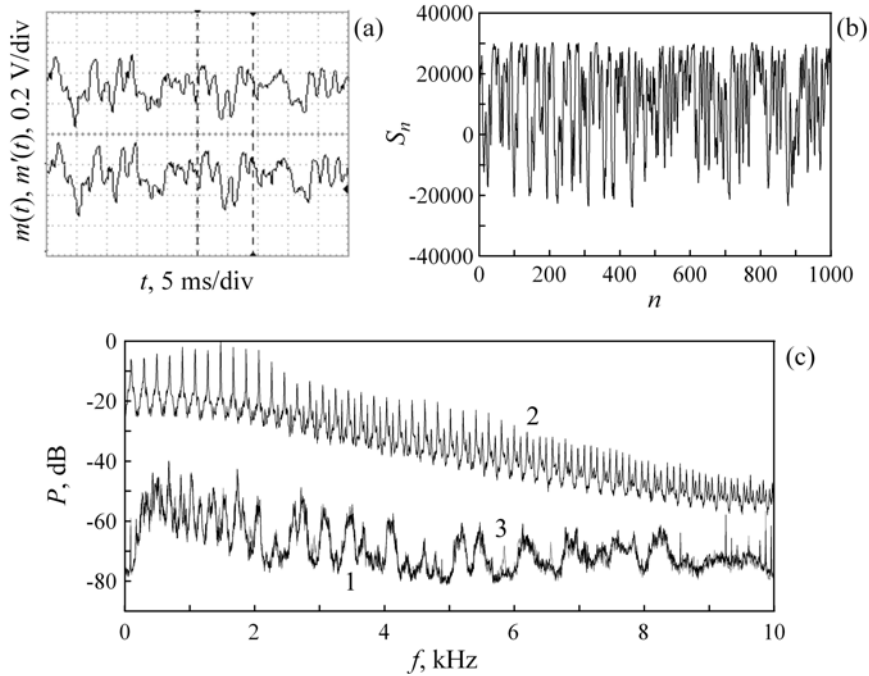


Fig. 3. (a) Oscillograms of temporal realizations of musical information signal  $m(t)$  at the transmitter input (on top) and the extracted information signal  $m'(t)$  at the receiver output (below). (b) Time series of chaotic signal  $S_n$ . (c) Power spectra of signals  $M_n$  (1),  $S_n$  (2), and  $M_n'$  (3). The spectrum of  $M_n'$  is shown by grey color.

Figure 3(b) shows a part of the time series of a chaotic signal  $S_n = F(X_{n-k}) + M_n$  generated by the oscillator with delayed feedback at  $\lambda = 1.9$ ,  $\Delta t/\varepsilon = 0.5$ , and  $k = 100$ . This signal had a digitization frequency of 20 kHz ( $\Delta t = 50$  mcs) and was transmitted over a digital communication channel at a rate of 115.2 kbit/s using RS-232 interface. If one passes this signal through a digital-to-analog converter (DAC) and reproduce, he will hear only noise without any signs of speech and music.

The receiver was implemented on the same programmable microcontroller as the transmitter. At the subtractor output of the receiver we have the extracted information signal  $M_n' = F(X_{n-k}) + M_n - F(Y_{n-k})$ . If the receiver parameters are identical with those of the transmitter and noise is absent, then  $F(Y_{n-k}) = F(X_{n-k})$  and  $M_n' = M_n$ . Passing the digital signal  $M_n'$  through a DAC we obtain the analog information signal  $m'(t)$  at its output. Part of the time series of  $m'(t)$  is also displayed in Figure 3(a). As it can be seen from Figure 3(a), the time series of the original and extracted information signals are very similar. Aurally the original musical signal  $m(t)$  and the signal  $m'(t)$  at the receiver output are indistinguishable.



Figure 4(c) shows the power spectra of the chaotic signal  $S_n$ , musical information signal  $M_n$ , and the signal  $M_n'$  extracted in the receiver. The amplitude of the musical information signal comprises about 25% of the amplitude of the chaotic carrier and the presence of audio signal is not noticeable in the power spectrum of the transmitted signal  $S_n$ . The power spectra of the signals  $M_n$  and  $M_n'$  are very close.

Thus, the quality of hidden information extraction at the receiver output is good enough in spite of the presence of noise inherent in a real system. The proposed scheme allows one to transmit and receive speech and musical signals in a real time without noticeable distortion.

#### **4. Extraction of Information Signal at the Mismatch of the Receiver and Transmitter Parameters**

In the example considered in the previous section the identity of the parameter values in the transmitter and receiver ensures the high quality of hidden message extraction for the authorized listener. The identity of the receiver and transmitter parameters is very important for communication schemes based on synchronization of chaotic systems. With the increase of mismatch of the receiver and transmitter parameters, the quality of chaotic synchronous response of the receiver deteriorates leading to a worse quality of the information signal extraction [4]. Beginning with a certain value of mismatch, the extraction of hidden message becomes impossible. The advantage of the proposed digital communication scheme is the employment of programmable microcontrollers that allows us to achieve the complete identity of the receiver and transmitter parameters, which is practically unattainable in the case of constructing the receiver and transmitter from analog elements.

For an eavesdropper the signal transmitted over the communication channel is perceived as noise. To extract a hidden message from the chaotic carrier the unauthorized listener must know the transmitter configuration, i.e. he must know that the transmitter is governed by the model time-delay equation (1) and he must know also the type of nonlinear function  $f$  and accurate values of the system parameters. For reconstruction of model equations of time-delay systems and estimation of their parameters from time series a number of methods has been proposed [1, 3, 10, 12]. In the absence of noise these methods allow one to recover the unknown parameters of time-delay systems with a good accuracy. However, in the presence of noise the parameter estimation is less accurate. Moreover, the error of parameter estimation increases with the increase of noise level.

The considered communication scheme employs nonlinear mixing of information signal and chaotic signal of a time-delay system. In this case the presence of information signal in the chaotic carrier inevitably decreases the accuracy of estimation of the system parameters just as in the case of noise presence. We have examined how accurately the transmitter parameters must be known for extracting a hidden information signal at the receiver output.

Let us choose the same transmitter parameters as in Section 3 and the same musical information signal. The receiver parameters are chosen the same as for

transmitter except for the discrete delay time  $k$ , which is varied in the vicinity of true value of  $k=100$ . Already for a minimal mismatch of  $k$  by unity ( $k=99$  or  $k=101$ ) we hear only noise at the receiver output. Thus, the information signal is completely masked in the case of a 1% mismatch of the delay time in the transmitter and receiver. Parts of the time series of the original musical signal  $m(t)$  and the signal  $m'(t)$  extracted in the receiver at  $k=99$  are presented in Figure 4. The amplitude of the signal  $m'(t)$  is significantly greater than the amplitude of  $m(t)$ . Besides, the signal  $m'(t)$  looks like a chaotic carrier.

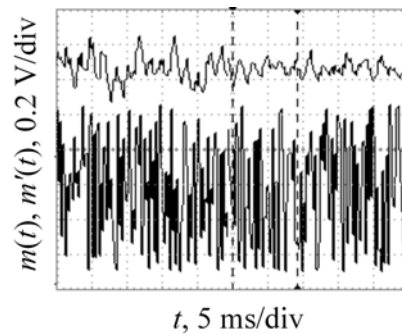


Fig. 4. Oscillograms of temporal realizations of the original information signal  $m(t)$  (on top) and the information signal  $m'(t)$  extracted in the receiver at the mismatch of parameter  $k$  ( $k=99$ ) (below).

We study also the influence of the parameter  $\varepsilon$  mismatch on the quality of the hidden message extraction. The receiver and transmitter parameters are chosen the same except for the parameter  $\varepsilon$ , which is varied in the vicinity of true value of  $\varepsilon=100$  mcs. It is found out that the information signal is not heard at the receiver output if a mismatch of  $\varepsilon$  is greater than 1.5%. In this case the time series and power spectra of  $m'(t)$  and  $m(t)$  are appreciably different. In the case of 0.1-1% mismatch by  $\varepsilon$ , the information signal is masked partially. We can distinguish several words and a musical background at the receiver output although the time series and power spectra of  $m'(t)$  and  $m(t)$  are appreciably different. If a mismatch of  $\varepsilon$  is 0.05%, the musical signal is extracted in the receiver with a small noise disturbance, which disappears under the further decrease of mismatch.

Thus, in order to extract a hidden message an authorized listener has to reconstruct the transmitter parameters with a high accuracy that is a very complicated problem for the proposed scheme.

## 5. Conclusion

We have developed the experimental digital communication system with nonlinear mixing of information signal and chaotic signal of time-delay system in which the transmitter and receiver are implemented on programmable microcontrollers. This system allows one to transmit and receive speech and



musical signals in a real time without noticeable distortion. The high quality of hidden message extraction is achieved due to the use of digital elements in the scheme, which ensure identity of the parameters and high stability to noise typical for digital communication systems.

We have studied a possibility of extraction of hidden information signal in the case of mismatch of the parameters of the receiver and transmitter in the proposed scheme. It is found out that for the hidden message extraction the parameter mismatch must be less than 1% that ensures the privacy of the proposed communication scheme.

### Acknowledgements

This work is supported by the Russian Foundation for Basic Research, Grant No. 13-02-00227 and by the grant of the president of Russian Federation, MK-4435.2012.8.

### References

1. M. J. Bünner, M. Ciofini, A. Giaquinta, R. Hegger, H. Kantz, R. Meucci and A. Politi. Reconstruction of systems with delayed feedback: (I) Theory. *Eur Phys J D* 10:165–176, 2000.
2. K. M. Cuomo and A. V. Oppenheim. Circuit implementation of synchronized chaos with applications to communications. *Phys Rev Lett* 71:65–68, 1993.
3. C. Dai, W. Chen, L. Li, Y. Zhu and Y. Yang. Seeker optimization algorithm for parameter estimation of time-delay chaotic systems. *Phys Rev E* 83:036203, 2011.
4. A. S. Dmitriev and A.I. Panas. *Dynamical Chaos: New Information Carriers for Communication Systems*. Fizmatlit, Moscow, 2002.
5. W.-H. Kye. Information transfer via implicit encoding with delay time modulation in a time-delay system. *Phys Lett A* 376:2663–2667, 2012.
6. R. M. Nguimdo, P. Colet, L. Larger and L. Pesquera. Digital key for chaos communication performing time delay concealment. *Phys Rev Lett* 107:034103, 2011.
7. U. Parlitz, L. O. Chua, L. Kocarev, K. S. Halle and A. Shang. Transmission of digital signals by chaotic synchronization. *Int J of Bifurcation and Chaos* 2:973–977, 1992.
8. L. M. Pecora, T. L. Carroll, G. A. Johnson, D. J. Mar and J. F. Heagy. Fundamentals of synchronization in chaotic systems, concepts, and applications. *Chaos* 7:520–543, 1997.
9. V. I. Ponomarenko and M. D. Prokhorov. Extracting information masked by the chaotic signal of a time-delay system. *Phys Rev E* 66:026215, 2002.
10. M. D. Prokhorov, V. I. Ponomarenko, A. S. Karavaev and B. P. Bezruchko. Reconstruction of time-delayed feedback systems from time series. *Physica D* 203:209–223, 2005.
11. K. Pyragas. Transmission of signals via synchronization of chaotic time-delay systems. *Int J of Bifurcation and Chaos* 8:1839–1842, 1998.
12. L. Zunino, M. C. Soriano, I. Fischer, O. A. Rosso and C. R. Mirasso. Permutation-information-theory approach to unveil delay dynamics from time-series analysis. *Phys Rev E* 82:046212, 2010.





## Acceleration Data Extraction Associating to the Peak-Valley Segmentation Approach Using the Morlet Wavelet Transform

S. Abdullah<sup>a1</sup>, T. E. Putra<sup>a2</sup>, D. Schramm<sup>b3</sup>, M. Z. Nuawi<sup>a4</sup>

<sup>a</sup>Department of Mechanical and Materials Engineering,  
Universiti Kebangsaan Malaysia  
43600 UKM Bangi Selangor, Malaysia

<sup>b</sup>Departmental Chair of Mechatronics, Universität Duisburg-Essen  
47057 Duisburg, Germany

E-mail: <sup>1</sup>[shahrum@eng.ukm.my](mailto:shahrum@eng.ukm.my), <sup>2</sup>[edi@eng.ukm.my](mailto:edi@eng.ukm.my),  
<sup>3</sup>[dieter.schramm@uni-due.de](mailto:dieter.schramm@uni-due.de), <sup>4</sup>[zaki@eng.ukm.my](mailto:zaki@eng.ukm.my)

**Abstract:** This paper presents a peak-valley segmentation procedure for the wavelet-based extraction of acceleration data. A 60-second acceleration signal was measured on a McPherson frontal coil spring of a 2000 cc Proton sedan car, and the data was used for the simulation. The Morlet wavelet-based analysis was used to extract higher amplitude segments in order to produce a shortened signal that has an equivalent behaviour. Using this process, it has been found that the Morlet wavelet was able to summarise the original data up to 49.45% with less than 10% difference with respect to statistical parameters. This clearly indicates that the Morlet wavelet can be successfully applied to compress the original signal without changing the main history as well. Finally, it has been proven that the Morlet wavelet successfully identified the higher amplitudes in the acceleration data.

**Keywords:** Acceleration data, Peak-valley extraction, Morlet wavelet, Modified data.

### 1. Introduction

Control and stability of a car entirely depend on the contact between the road surface and the tires [1]. The dynamic interaction between vehicle and road surface causes problems with respect to the vehicle structure and the ride quality. Collision between uneven road surfaces and tires gives a certain amount of vibration which contributes to mechanical failure of car components due to fatigue as the car structure was subjected to cyclic loading. This vibration also interfaces the function of the car suspension system and gives a great impact on the performance of the car [2-5].

According to Jinhee [6], car suspension systems experience vibration when is subjected to variable driving conditions leading to strain at this component. If this condition continues it will increase the probability of fatigue failure for the car suspension system. The problems arising have been solved by simulating the dynamic behaviour of a structural component on which the dynamic forces are acting. Measured road surface profiles are generally considered as external disturbances acting through the automotive suspension system onto the vehicle body. Road surface profiles are usually used to describe the bumpiness of the road. Because of weakness of measuring equipment used, there is noise in the



road surface profile data. Thus, the accuracy and reliability of the road surface profile is reduced. If the signal trends are not extracted from the input signal used, it will directly affect the test results, leading to inappropriate judgments and conclusions. Therefore, it is an important task that the signal trend is extracted and separated from the noise during road surface data processing [7]. Based on this background, methods for the signal trend extraction of road surface profile are introduced. At present, the popular methods for the signal trend extraction are: least-squares fitting, low-pass filtering, wavelet decomposition, empirical mode decomposition, etc., as reported in [7]. The objective of this work is to extract acceleration data in order to remove white noise in the data. In order to address the objective of the research, acceleration data is edited to produce shorter data while retaining its original characteristics. Therefore, a data editing technique is necessary for producing new modified signals as required. Continuous wavelet transform (CWT) has been applied to the digital signal processing algorithm. An algorithm for signal trend extraction of road surface profile has been developed by adopting a fatigue feature algorithm developed by Putra et al [8]. It is hypothesized that the pattern of an acceleration data is similar to the pattern of a fatigue signal.

## 2. Literature Overview

### 2.1. Global signal statistics

Statistical parameters are used for random signal classification and pattern monitoring. Common statistical parameters that are directly related to the observation of the data behaviour are the mean value, standard deviation (SD), the root-mean square (r.m.s.), skewness, kurtosis and the crest factor (CF). From these parameters, the r.m.s. and kurtosis give significant effects to evaluate the randomness of the data [9]. The r.m.s. calculates the energy distribution, wherein higher r.m.s. indicates a higher energy content, which in turn indicates higher fatigue damage in the signal. On the other hand, kurtosis represents the continuity of peaks in a time series loading. The peaks also reveal higher fatigue damage, suggesting that a higher kurtosis indicates higher fatigue damage.

The r.m.s. is the second statistical moment used for determining the total energy contained in a signal. The r.m.s. of signals with zero mean value is equal to the SD. The r.m.s. of discrete data can be calculated as follows:

$$r.m.s. = \left\{ \frac{1}{n} \sum_{j=1}^n x_j^2 \right\}^{1/2}$$

In addition, kurtosis is the fourth statistical moment that is very sensitive to spikes and it represents the continuation of peaks in a time series loading. The kurtosis value of a Gaussian normal distribution is close to 3.0. Higher kurtosis shows that the value is higher compared to the appropriate value in the Gaussian normal distribution, indicating that only a small proportion of data is closer to the mean value [10]. The kurtosis for a set of discrete data is formulated as:



$$K = \frac{1}{n(SD)^4} \sum_{j=1}^n (x_j - \bar{x})^4$$

## 2.2. Continuous Morlet Wavelet Transform

The continuous wavelet transform (CWT) is conducted on each reasonable scale, producing a lot of data and is used to determine the value of a continuous decomposition to reconstruct the signal accurately [11]. The Morlet wavelet is one of the mother wavelets that are involved in the CWT, and it can be described by the following equation:

$$\psi(t) = \exp(-\beta^2 t^2 / 2) \cos(\pi t)$$

By dilation with  $a$  (scale factor) and translation with  $b$  (position), a son wavelet can be acquired [12]:

$$\psi_{a,b}(t) = \exp\left[-\frac{\beta^2(t-b)^2}{a^2}\right] \cos\left[\frac{\pi(t-b)}{a}\right]$$

Wavelet decomposition calculates the resemblance index, also called the coefficient, between the signal being analyzed and the wavelet. Generally, the wavelet coefficient is expressed with the following integral [11]:

$$C_{a,b} = \int_{-\infty}^{+\infty} f(t) \psi_{(a,b)}(t) dt$$

The Morlet wavelet coefficient indicates the distribution of the internal energy of the signal in the time-frequency domain [13]. The signal internal energy  $e$  can be expressed as:

$$e_{(a,b)} = |C_{(a,b)}|^2$$

## 2.3. Peak-valley segmentation-based signal extraction

Fatigue damage is very sensitive to peak and valley in a time series loading. Thus, in the extraction, time series data needs to be converted in the form of peak-valley. For the development of the extraction algorithm, the input required was the distribution of the magnitude in the time domain obtained by the time-frequency method. The distribution was decomposed into the time domain spectrum by taking the magnitude cumulative value for an interval of time.

A gate value was used for the extraction of the damage feature. The gate value was the energy spectrum variable that maintains the minimum magnitude level. Segments with magnitudes exceeding the minimum magnitude value were maintained, whereas the segments with magnitudes less than the minimum

magnitude value were removed from the signal. The concept refers to the concept of the cut-off level used in the extraction in the time domain [14].

To obtain the optimum of the gate value, the maintained segments then were merged with each other to form a shorter modified signal, compared to the original signal. In the case of global signal statistical parameters, a difference of 10% is used considering that at least 10% of the original signal contains a lower amplitude cycle leading to the minimum structural damage to obtain a final signal corresponding to the original signal [15].

### 3. Methodology

Acceleration data measured at a McPherson frontal coil spring of a 2.000 cc Proton Wira sedan car was used for the current study. At the same time, strain data on the component was measured as well. The behaviour of both the acceleration and strain data was to be observed. According to Gillespie [16], the coil spring of a car at the similar brand of this research was made from SAE5160 alloy steel. Its properties are tabulated in Table 1 [17].

Table 1. The mechanical properties of the SAE5160 alloy steel.

Properties	Values
Modulus of elasticity, $E$ (GPa)	207
Density, $\rho$ ( $\text{kg/m}^3$ )	7.85
Poisson's ratio, $\nu$	0.27

An accelerometer was placed at the location of the coil spring showing the highest stress concentration which was obtained through finite element analysis. The car was driven on a highway road surface at a velocity of 70 km/h. The original signal produced by the accelerator was a variable amplitude load sampled at 500 Hz and recorded using a data acquisition setup, as shown in Figure 1.



Fig. 1. The data acquisition setup: (a) accelerometer, (b) PXI system.

## 4. Results and Discussion

### 4.1. Acceleration data

The collected data contained many small amplitudes and higher frequency patterns in the signal background. The data is a time domain signal measured at the coil spring sampled at 500 Hz for 30,000 data points. Therefore the total

record length was 60 seconds. Based on the acceleration obtained, the data obtained revealed parts with higher amplitudes because the vehicle was driven on a bumpy surface. The original acceleration data, the Morlet wavelet coefficient and the signal internal energy are shown in Figure 2.

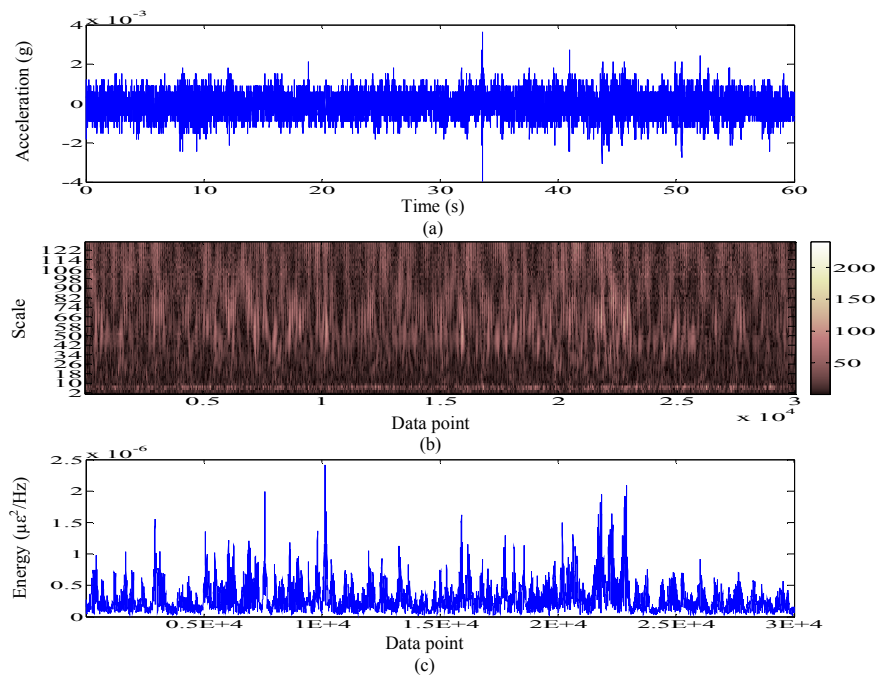


Fig. 2. (a) acceleration data, (b) wavelet coefficient, (c) internal energy.

#### 4.2. Acceleration data extraction

Various gate values were used in this extraction. The values were chosen because most of the magnitudes were below the gate value, whereas if the lower magnitude section was removed, it did not affect the damage relevance and the original properties of the signal. The gate values used were  $4 \times 10^{-7} \mu\epsilon^2/\text{Hz}$ ,  $5 \times 10^{-7} \mu\epsilon^2/\text{Hz}$  and  $6 \times 10^{-7} \mu\epsilon^2/\text{Hz}$ . After the data was extracted, the retained energy containing higher signal internal energy was obtained. Furthermore, based on the time positions of the retained energy and referring to the original signal before the extraction, maintained segments were obtained. The extractions produced segments that were not uniform in length because the Morlet wavelet algorithm extracted the time series based on the energy content of the signals.

For this purpose, the retained segments were reattached into a single load to validate if the process satisfied the requirements in data editing, i.e., maintaining 90% of the original statistical values. A verification process was done by comparing the statistical parameter values between the original and the modified signal. From the analysis of the modified signal, an optimal gate value was

determined based on the gate value ability (refer to the modified signal) to produce the shortest signal with the minimum signal statistical parameter deviation. Figure 3 shows the differences in the length of modified signals from the extraction at various gate values.

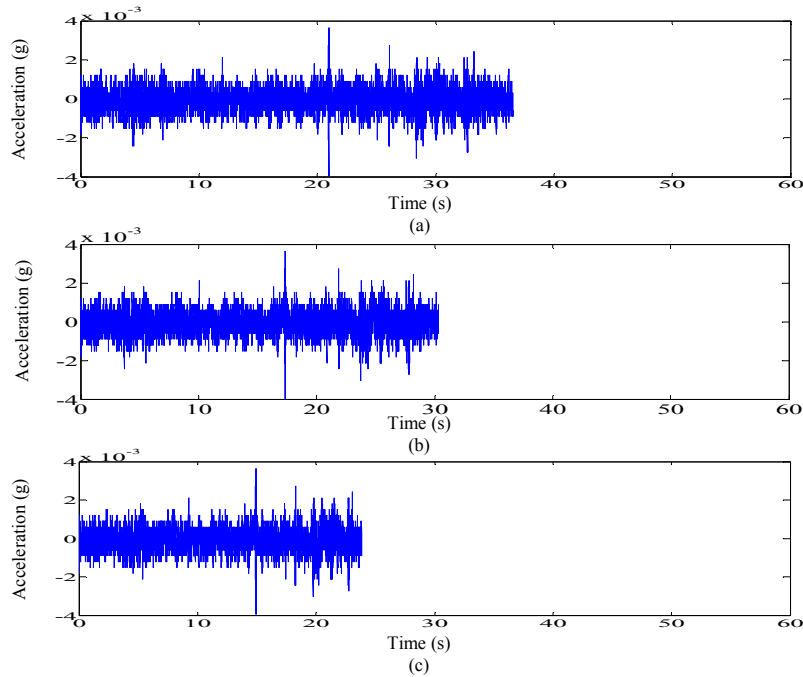


Fig. 3. Edited signals at: (a)  $4 \times 10^{-7} \mu\epsilon^2/\text{Hz}$ , (b)  $5 \times 10^{-7} \mu\epsilon^2/\text{Hz}$ , (c)  $6 \times 10^{-7} \mu\epsilon^2/\text{Hz}$ .

Based on Figure 3 above, at gate value of  $4 \times 10^{-7} \mu\epsilon^2/\text{Hz}$ , data of 36.57 seconds shortened only by 39.05% and its r.m.s. and kurtosis became 2.68% and 5.45%, respectively. For a gate value of  $5 \times 10^{-7} \mu\epsilon^2/\text{Hz}$ , the Morlet wavelet-based extraction resulted in a 30.33-second edited signal, which was 49.45% shorter than the original. The modified signal changed the r.m.s. and the kurtosis to 3.41% and 8.21%, respectively. For a gate value of  $6 \times 10^{-7} \mu\epsilon^2/\text{Hz}$ , the data was modified by 60.22% and changed the r.m.s. and kurtosis values became 5.14% and 10.98, respectively.

Based on the results,  $5 \times 10^{-7} \mu\epsilon^2/\text{Hz}$  was selected as the optimum gate value because at higher values, i.e.  $6 \times 10^{-7} \mu\epsilon^2/\text{Hz}$ , the change in kurtosis reached 10.98%. It was detrimental the original properties of the signal. The 30.33-second edited signal resulted at the optimum gate value experience increasing of the r.m.s. and kurtosis values. Increased r.m.s. indicated that the internal energy content of the signal also increased. Different kurtosis values showed the extraction method was capable of effectively removing lower amplitude while maintaining higher amplitude in the modified signal. In addition, at gate value of  $5 \times 10^{-7} \mu\epsilon^2/\text{Hz}$ , it gives similar distribution of frequency spectrum and power

spectral density, as shown in Figure 4. It shows the noise in the road surface profile had been removed. The data were successfully edited based on the relationship between the higher amplitude and the Morlet wavelet coefficients of the time-frequency domain obtained. This Morlet wavelet algorithm removed segments with magnitudes less than the gate value based on their positions on the time axis.

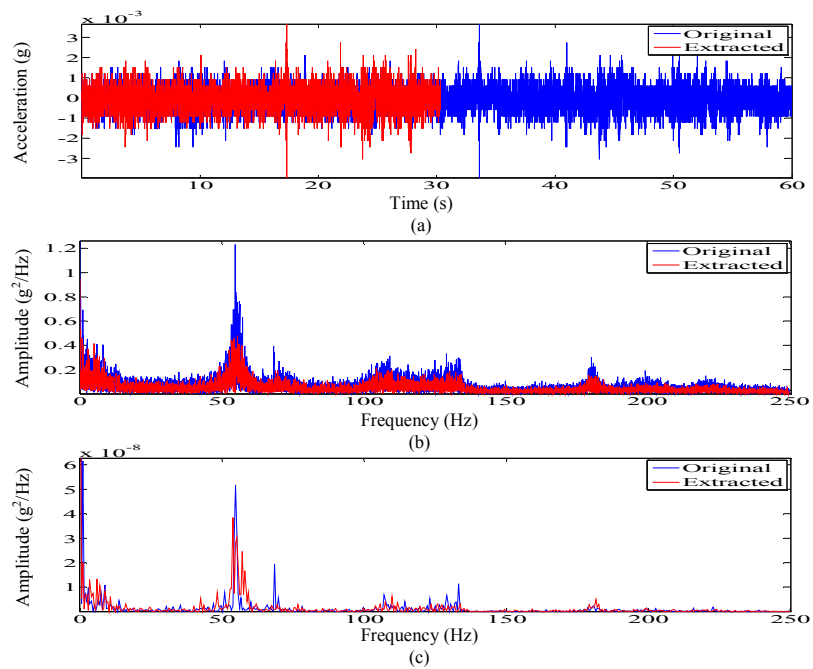


Fig. 4. Original and edited signals: (a) length, (b) frequency spectrum, (c) power spectral density.

## 5. Conclusion

In this study, an experiment was conducted to collect data for the purpose of obtaining acceleration data to simulate the extraction algorithm. The acceleration data causes vibration that will increase the probability to the fatigue failure at car components. The extraction process yielded data on the damaging segments by identifying and extracting segments based on the coefficient distribution of the Morlet wavelet transform. The damaging segments were combined to form shorter signals while maintaining original behaviours. Overall, the Morlet wavelet algorithm was able to shorten the signal up to 49.45% but maintained more than 90% of the statistical parameters and gave similar distribution of power spectral density as original data. The extraction method was able to identify the structural damage values of each segment. Finally, this study proved that the Morlet wavelet is an appropriate technique to extract acceleration data, especially for the automotive applications.



## References

1. C. Ferreira, P. Ventura, R. Morais, A. L. G. Valente, C. Neves and M. C. Reis, Sensing methodologies to determine automotive damper condition under vehicle normal operation, *Sensors and Actuators A: Physical* 156:237-244, 2009.
2. V. Yildirim, Free vibration characteristics of composite barrel and hyperboloidal coil springs, *Mechanics Composite Materials and Structures* 8:205-217, 2001.
3. V. Yildirim, A parametric study on the natural frequencies of unidirectional composite conical springs, *Communications in Numerical Methods in Engineering* 20:207-227, 2004.
4. S. Narayanan and S. Senthil, Stochastic optimal active control of a 2-dof quarter car model with non-linear passive suspension elements, *Journal of Sound and Vibration* 211:495-506, 1998.
5. L. Sun, Optimum design of "road-friendly" vehicle suspension systems subjected to rough pavement surfaces, *Applied Mathematical Modelling* 26:635-652, 2002.
6. L. Jinhee, Free vibration analysis of cylindrical helical springs by the pseudospectral method, *Journal of Sound and Vibration* 302:185-196, 2007.
7. D. Hu-ming, X. Fei, Z. Kaibin, M. Ying and S. Feng. Signal trend extraction of road surface profile measurement, *2<sup>nd</sup> International Conference on Signal Processing Systems (ICSPS)* 694-698, 2010.
8. T. E. Putra, S. Abdullah, M. Z. Nuawi and Z. M. Nopiah. Wavelet coefficient extraction algorithm for extracting fatigue features in variable amplitude loading, *Journal of Applied Sciences* 10:277-283, 2010.
9. V. Pakrashi, B. Basu, A. O' Connor, Structural damage detection and calibration using a wavelet-kurtosis technique, *Engineering Structures* 29:2097-2108, 2007.
10. C. Braccresi, F. Cianetti, G. Lori and D. Pioli. The frequency domain approach in virtual fatigue estimation of non-linear systems: the problem of non-Gaussian states of stress, *International Journal of Fatigue* 31:766-775, 2009.
11. M. Misiti, Y. Misiti, G. Oppenheim and J. M. Poggi. *Matlab User's Guide: Wavelet Toolbox<sup>TM</sup> 4*, The Math Works Inc., MA, 2008.
12. J. Lin and L. Qu. Feature extraction based on morlet wavelet and its application for mechanical fault diagnosis *Journal of Sound and Vibration*, 234:135-148, 2000.
13. A. K. Darpe. A novel way to detect transverse surface crack in a rotating shaft, *Journal of Sound and Vibration* 305:151-171, 2007.
14. R. I. Stephens, P. M. Dindinger and J. E. Gunger. Fatigue damage editing for accelerated durability testing using strain range and SWT parameter criteria, *International Journal of Fatigue* 19:599-606 1997.
15. J. Giacomini, A. Steinwolf and W. J. Staszewski. Application of Mildly Nonstationary Mission Synthesis (MNMS) to automotive road data, *ATA 7th Int. Conf. on the New Role of Experimentation in the Modern Automotive Product Development Process* 2001.
16. T. D. Gillespie. *Fundamental of Vehicle Dynamics*. SAE International, United Kingdom, 1992.
17. nCode. *Ice-Flow: Glyphworks 4.0 Tutorials*, nCode International Ltd., Sheffield, 2005.





# *Chaotic* Pattern Recognition Using the Adachi Neural Network Modified in a Random Manner

Ke Qin<sup>1</sup> and B. J. Oommen<sup>2,3</sup>

<sup>1</sup> University of Electronic Science & Technology of China, Chengdu, China. 611731  
(E-mail: qinke@uestc.edu.cn)

<sup>2</sup> Carleton University, Ottawa, ON, Canada. K1S 5B6

<sup>3</sup> University of Agder, Postboks 509, 4898 Grimstad, Norway.  
(E-mail: oommen@scs.carleton.ca)

**Abstract.** This paper deals with achieving *chaotic* Pattern Recognition (PR) using the Adachi Neural Network (AdNN), where the Neural Network (NN) has been modified in a random manner. The Adachi Neural Network is a fascinating NN which has been shown to possess chaotic properties, and to also demonstrate Associative Memory (AM) and Pattern Recognition (PR) characteristics. Variants of the AdNN have also been used to obtain other PR phenomena, and even blurring. An unsurmountable problem associated with the AdNN and the variants referred to above, is that all of them require a quadratic number of computations. Earlier, in [1], we managed to reduce the computational cost significantly by merely using a linear number of computations by enforcing a Maximum Spanning Tree topology, and a gradient search method. However, in the sense of a NNs structure, very few networks possess a linearly connected topology. Instead, most of the “*physical*” networks including biological NNs and Internet networks have the properties of a complex network such as a random network, small-world network or a scale-free network. In this paper, we mainly consider the issue of how the network topology can be modified by involving randomized connections so as to render the new network much closer to “*real*” NNs. On the other hand, the newly obtained network still possesses strong PR characteristics. To achieve this, we first construct a random network by means of the E-R model and then address the problem of computing the weights for the new network. This is done in such a manner that the modified random connection-based NN has approximately the same input-output characteristics, and thus the new weights are themselves calculated using a gradient-based algorithm. Through a detailed experimental analysis, we show that the new random AdNN-like network possesses PR properties for appropriate settings. As far as we know, such a random AdNN has not been reported, and our present results are novel.

**Keywords:** Chaotic Neural Networks, Chaotic Pattern Recognition, Adachi-like Neural Networks, Random Networks.

## 1 Introduction

The use of Artificial Neural Networks (ANNs) is one of the four best approaches for Pattern Recognition (PR). ANNs attempt to use some organizational principles such as learning, generalization, adaptivity, fault tolerance, distributed representation, and computation in order to achieve the recognition. One of the limitations of most ANN models is the dependency on an external stimulation. Once an output pattern has been identified, the ANN remains in that state



until the arrival of a new external input. This is in contrast to real biological NNs which exhibit sequential memory characteristics. To be more specific, once a pattern is recalled from a memory location, the brain is not “stuck” in it; it is also capable of recalling other associated memory patterns without being prompted by any additional external inputs. This ability to “jump” from one memory state to another *in the absence of a stimulus* is one of the hallmarks of the brain, which is *one phenomenon that a chaotic PR system has to emulate*.

The goal of the field of *Chaotic PR* systems can be summarized as follows: We do not intend a chaotic PR system to report the identity of a testing pattern with a “class proclamation”. Rather, what we want to achieve is to have the chaotic PR system give a strong *periodic* or *more frequent* signal when a pattern is recognized. Furthermore, between two consecutively recognized patterns, none of the trained patterns must be recalled. Finally, and most importantly, if an untrained pattern is presented, the system must give a chaotic signal.

This paper deals with the Adachi Neural Network AdNN [2], which possesses a spectrum of very interesting chaotic, AM and PR properties, as described in [1,3–11]. The fundamental problem associated with the AdNN and its variants are their quadratic computational requirements. We shall show that by using the E-R model and an effective gradient search strategy, this burden can be significantly reduced, and yet be almost as effective with regard to the chaotic and PR characteristics.

We are currently working on reducing the complexity of the AdNN and the associated computations by invoking the so-called “small-world” model.

## 2 Limitations of the Current Schemes

Although the works of Adachi *et al* and Calitoiu *et al* were ground-breaking, it turns out that, as stated in [3–5], the results claimed in the prior works were not as precise as stated. Apart from this limitation, the computational burden is excessive, rendering it impractical. Besides this, most of current NNs have a regular topology, e.g., a completely connected graph or a neighbor-coupled graph. This is in contrast with “real” NNs which usually have irregular topologies, e.g., a random graph, a small-world graph or even a scale-free graph. The contribution of this paper is to present a novel CNN which is connected in a randomized AdNN way. For brevity, we refer to the modified AdNN with random connections as the “Random-AdNN”.

## 3 Designing the Random-AdNN

### 3.1 The Topology of the Random-AdNN

To present the new characteristics of the Random-AdNN, we shall first arrive at a topology with randomly-chosen edges. Such a modified random AdNN is obtained in two steps. Firstly, we connect the neurons by using the E-R model. The second step involves the computation of the weights associated with this new structure, which we will address subsequently.




---

**Algorithm 1** Topology\_Random-AdNN

---

**Input:**  $N$ , the number of neurons in the network, and a set of  $P$  patterns which the network has to “memorize”.

**Output:** The topology and initial weights of the Random-AdNN.

**Method:**

- 1: Create a fully-connected graph  $\mathcal{G}$  with  $N$  vertexes which represents the AdNN.
- 2: For each edge, we delete it with a fixed probability,  $p_d$ .
- 3: Continue this process for all the  $\binom{N}{2}$  edges.
- 4: Compute the initial weights of the edges of  $\mathcal{G}$ ,  $\{w_{ij}\}$  as follows:  
 $w_{ij} = \frac{1}{P} \sum_{s=1}^P (2x_i^s - 1)(2x_j^s - 1)$ , where  $x_i^s$  is the  $i^{th}$  component of the  $s^{th}$  pattern.
- 5: If there is no edge between vertex  $i$  and  $j$ ,  $w_{ij} = 0$ ;

**End Algorithm** Topology\_Random-AdNN

---

### 3.2 The Weights of the Random-AdNN: Gradient Search

Since we have removed most of the “redundant” edges from the completely-connected graph by using the E-R model, it is clear that the NN at hand will not adequately compare with the original AdNN. Thus, our next task is to determine a new set of weights so as to force the Random-AdNN to retain some of its PR properties, namely those corresponding to the trained patterns. We briefly explain below (the details are omitted in the interest of space, and one can refer to [12] for more details) the process for achieving this.

The Random-AdNN is defined by the following equations:

$$x_i^R(t+1) = f(\eta_i^R(t+1) + \xi_i^R(t+1)), \quad (1)$$

$$\eta_i^R(t+1) = k_f \eta_i^R(t) + \sum_{e_{ij} \in T} w_{ij}^{R*} x_j^R(t), \quad (2)$$

$$\xi_i^R(t+1) = k_r \xi_i^R(t) - \alpha x_i^R(t) + a_i. \quad (3)$$

where  $\{w_{ij}^{R*}\}$ ,  $x_i^R$ ,  $\xi_i^R$  and  $\eta_i^R$  are the weights, outputs, and state variables of the Random-AdNN respectively, and have similar meanings to  $\{w_{ij}\}$ ,  $x_i$ ,  $\xi_i$  and  $\eta_i$  of the AdNN.

In order to find the optimal values of  $\{w_{ij}^{R*}\}$ , we define the square error between the original output of the AdNN and new output at the  $n^{th}$  step as:

$$E_p = \frac{1}{2} \sum_{i=1}^N (x_i^{A,p} - x_i^{R,p}(n))^2, \quad (4)$$

where  $x_i^{A,p}$  and  $x_i^{R,p}$  imply the outputs of the  $i^{th}$  neuron when the  $p^{th}$  pattern is presented to the AdNN network and the Random-AdNN network respectively. The overall global error is defined by  $E = \sum_{p=1}^P E_p$  where  $P$  is the number of trained patterns.

In order to adjust  $w_{ij}^R$  to obtain the smallest global error  $E$ , we consider the gradient,  $\Delta w_{ij}^R$ , and move  $w_{ij}^R$  by an amount which equals  $\Delta w_{ij}^R$  in the direction



where the error is minimized. This can be formalized as follows:

$$\begin{aligned} \Delta w_{ij}^R &= -\beta \frac{\partial E}{\partial w_{ij}^R} = -\beta \frac{\partial \sum_{p=1}^P E_p}{\partial w_{ij}^R} = -\beta \sum_{p=1}^P \frac{\partial E_p}{\partial x_i^{R,p}(n)} \cdot \frac{\partial x_i^{R,p}(n)}{\partial w_{ij}^R} \\ &= \beta \sum_{p=1}^P (x_i^{A,p} - x_i^{R,p}(n)) \cdot \frac{1}{\varepsilon} \cdot x_i^{R,p}(n) \cdot (1 - x_i^{R,p}(n)) \cdot x_j^{R,p}(n), \quad (5) \end{aligned}$$

where  $\beta$  is the learning rate of the gradient search. The formal algorithm which achieves the update is given in Algorithm 2.

---

**Algorithm 2** Weights\_Random-AdNN

---

**Input:** The number of neurons,  $N$ , a set of  $P$  patterns, and the initial weights  $\{w_{ij}^R\}$  of the Random-AdNN. These initial weights are  $\{w_{ij}^A\}$  for the edges in the random graph, and are set to *zero* otherwise. The parameters and settings which we have used are the learning rate  $\beta = 0.05$ ,  $\varepsilon = 0.015$ ,  $\alpha = 10$ ,  $k_f = 0.2$  and  $k_r = 1.02$ .

**Output:** The weights  $\{w_{ij}^{R*}\}$  of the Random-AdNN.

**Method:**

- 1: Compute the outputs of the Random-AdNN corresponding to the  $P$  trained inputs.
- 2: For all edges of the Random-AdNN, compute  $\Delta w_{ij}^R$  as per Equation (5). Otherwise, set  $\Delta w_{ij}^R = 0$ .
- 3:  $w_{ij}^R \leftarrow w_{ij}^R + \Delta w_{ij}^R$ .
- 4: Go to Step 1 until  $E$  is less than a given value or  $\Delta w_{ij}^R \approx 0$ .

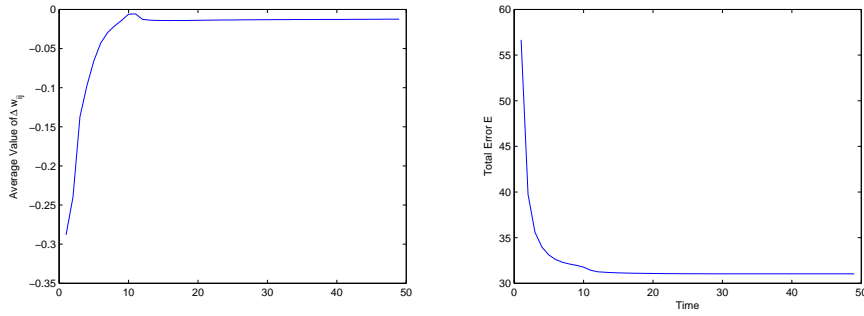
**End Algorithm** Weights\_Random-AdNN

---

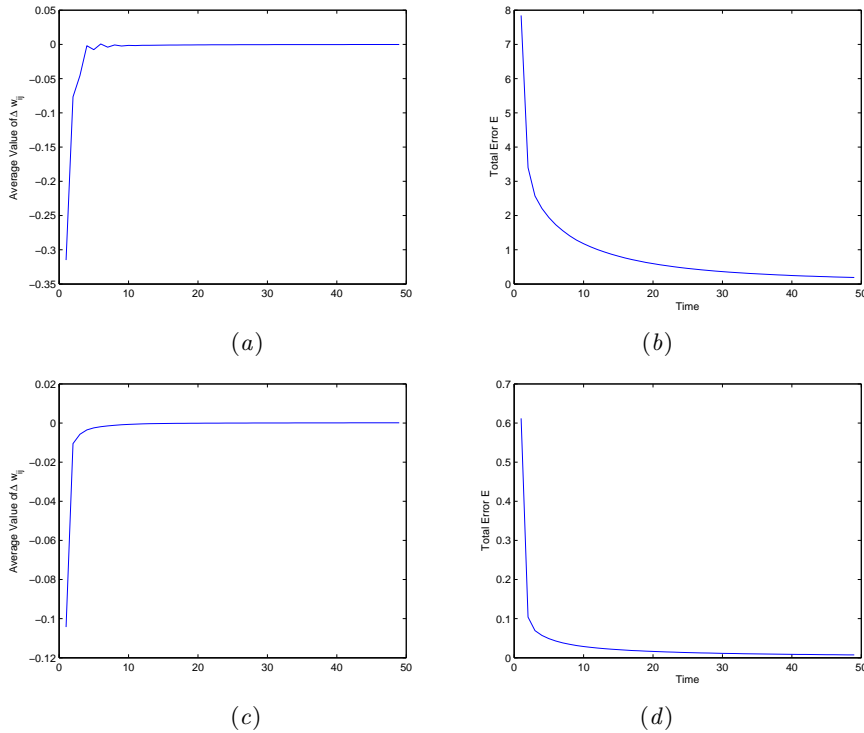
The results of a typical numerical experiment which proceeds along the above gradient search are shown in Fig. 1 and 2. In these simulations, we have chosen the learning rate  $\beta$  to be 0.05. To clarify issues, we catalogue our experiments for three specific cases, namely when the probability  $p_d$  for deleting an edge is 0.9, 0.5 and 0.1 respectively.

If  $p_d$  is 0.9, the total error  $E$  and average values of  $\Delta w_{ij}^R$  do not converge to 0, as shown in Fig. 1. However, as  $p_d$  decreases, e.g., 0.5, then  $E$  and  $\Delta w_{ij}^R$  converge to 0, as shown in Fig. 2 (a) and (b). If  $p_d$  is even less,  $E$  and  $\Delta w_{ij}^R$  also converge to 0 but with a faster rate, as shown in Fig. 2 (c) and (d). This phenomenon can be easily explained: The larger the value of  $p_d$ , the smaller is the number of edges and vice versa. Thus, if  $p_d = 0$ , it means that the Random-AdNN is exactly the same as the original AdNN. On the other hand, if  $p_d = 1$ , it means that all the vertexes are isolated and remain as disconnected units. Of course, the “fitting” effect that we obtain by the approximate graph, the Random-AdNN, is more precise as the number of edges increases.

The Lyapunov analysis of the Random-AdNN is also available, but omitted here in the interest of space. It can be found in [12].



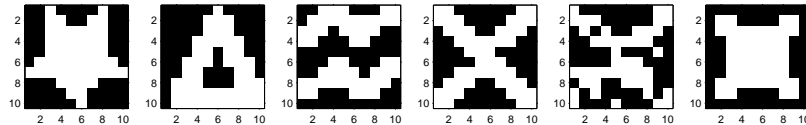
**Fig. 1.** The figure on the left shows the variation of the average of  $\Delta w_{ij}^L$  (averaged over all values of  $i$  and  $j$ ) over the first 50 iterations of the gradient search scheme. The average converges to a value arbitrarily close to zero after 12 time steps. The figure on the right shows the variation of the global error over the same time frame. Observe that this quantity does not converge to *zero*.



**Fig. 2.** The figures show the variation of the average of  $\Delta w_{ij}^L$  and the global error over the same time frame. The probability of edge deletion is  $p_d = 0.5$  (for (a) and (b)) and  $p_d = 0.1$  (for (c) and (d)) respectively.

## 4 Chaotic and PR Properties of the Random-AdNN

We now briefly report the PR properties of the Random-AdNN. These properties have been discovered as a result of examining the Hamming distance between the input pattern and the patterns that appear in the output. The experiments were conducted using the Adachi data set described below.



**Fig. 3.** The  $10 \times 10$  patterns used by Adachi *et al.* The first four patterns are used to train the network. The fifth pattern is obtained from the fourth pattern by including 15% noise. The sixth pattern is the untrained pattern.

In the ideal setting we would have preferred the Random-AdNN to be chaotic when exposed to untrained patterns, and the output to appear periodically or more frequently when exposed to trained patterns. Besides yielding this phenomenon, the Random-AdNN also goes through a chaotic phase and a PR phase as some of its parameters change.

We summarize the results for the Random-AdNN, obtained by using different settings of  $p_d$ . The others parameters are:  $k_f = 0.2$ ,  $k_r = 1.02$ ,  $\alpha = 10$ ,  $\varepsilon = 0.015$ ,  $\beta = 0.05$ .

From these tables we see clearly that, the Random-AdNN is able to “resonate” the input patterns with the corresponding output patterns. Consider Table 1 (a) as an example. If the input is P1, then the network outputs P1 accordingly, and at the same time, no other trained patterns appear in the output sequence. Even when a noisy pattern is presented to the system, e.g., P5, which is a noisy pattern of P4 with 15% noise, the network still “resonates” P4 instead of P5 in the output sequence. Furthermore, if the input is an untrained pattern, e.g., P6, then none of the trained patterns will be recalled. Observe that even the input pattern P6, will itself be retrieved only a few times, which is much less than the other diagonal entries in the table, i.e., when the inputs are P1 – P4. The difference between (a) – (c) is that in Table (c), the network “resonates” the input patterns more frequently than in (a) and (b). This is because when  $p_d = 0.1$ , the Random-AdNN is almost the same as the original AdNN since the Random-AdNN has most of the edges of the AdNN. However, in this case, the Random-AdNN also needs a quadratic number of computations, which is computationally much more intensive than for the case when  $p_d = 0.9$ . In this regard, we comment that  $p_d = 0.9$  is good enough for PR, which has only a very small computational burden. By a simple computation we can see that the expected degree for each vertex of the Random-AdNN is only  $N(1 - p_d) = 10$  for the Adachi data set, which implies that the compu-



**Table 1.** The frequency of the Hamming distance between the input and the output patterns for the Random-AdNN. The probability  $p_d$  is 0.9, 0.5, 0.1 for (a), (b), (c) respectively.

$p_d = 0.9$		Input Patterns					
		P1	P2	P3	P4	P5	P6
<b>Retrieved Patterns</b>	P1	151	0	0	0	0	0
	P2	0	422	0	0	0	0
	P3	0	0	161	0	0	0
	P4	0	0	0	106	177	0
	P5	0	0	0	10	2	0
	P6	0	0	0	0	0	46

(a)

$p_d = 0.5$		Input Patterns					
		P1	P2	P3	P4	P5	P6
<b>Retrieved Patterns</b>	P1	202	0	0	0	0	0
	P2	0	285	0	0	0	0
	P3	0	0	234	0	0	0
	P4	0	0	0	211	206	0
	P5	0	0	0	4	3	0
	P6	0	0	0	0	0	33

(b)

$p_d = 0.1$		Input Patterns					
		P1	P2	P3	P4	P5	P6
<b>Retrieved Patterns</b>	P1	238	0	0	0	0	0
	P2	0	331	0	0	0	0
	P3	0	0	258	0	0	0
	P4	0	0	0	237	189	0
	P5	0	0	0	9	20	0
	P6	0	0	0	0	0	34

(c)

tational load has been greatly reduced when compared to the original AdNN, which has a vertex degree of 99.

## 5 Conclusions

In this paper we have concentrated on the field of Chaotic Pattern Recognition (PR), which is a relatively new sub-field of PR. Such systems, which have only recently been investigated, demonstrate chaotic behavior under normal conditions, and resonate when it is presented with a pattern that it is trained with. The network that we have investigated is the Adachi Neural Network (AdNN) [2], which has been shown to possess chaotic properties, and to also demonstrate Associative Memory (AM) and Pattern Recognition (PR) characteristics. In this paper we have considered how the topology can be modified so as to render the network much closer to “real” neural networks. To achieve this, we have changed the network structure to be a random graph, and then computed the best weights for the new graph by using a gradient-based algorithm. By a detailed experimental suite, we showed that the new Random-AdNN possesses chaotic and PR properties for different settings.

**Acknowledgements:** The first author would like to thank the Ministry of Science and Technology of Sichuan Province, China, for its financial support (Grant Nos. 2012HH0003 and 9140A17060411DZ02) for this research.



## References

1. Qin, K., Oommen, B.J.: Adachi-like chaotic neural networks requiring linear-time computations by enforcing a tree-shaped topology. *IEEE Transactions on Neural Networks* **20**(11) (2009) 1797–1809
2. Adachi, M., Aihara, K.: Associative dynamics in a chaotic neural network. *Neural Networks* **10**(1) (1997) 83–98
3. Calitoiu, D., Oommen, B.J., Nussbaum, D.: Desynchronizing a chaotic pattern recognition neural network to model inaccurate perception. *Ieee Transactions on Systems Man and Cybernetics Part B-Cybernetics* **37**(3) (2007) 692–704
4. Calitoiu, D., Oommen, B.J., Nussbaum, D.: Periodicity and stability issues of a chaotic pattern recognition neural network. *Pattern Analysis and Applications* **10**(3) (2007) 175–188
5. Qin, K., Oommen, B.J.: Chaotic pattern recognition: The spectrum of properties of the adachi neural network. In: *Lecture Notes in Computer Science*. Volume 5342., Florida, USA (2008) 540–550
6. Chen, L., Aihara, K.: Global searching ability of chaotic neural networks. *IEEE Transactions on Circuits and Systems I: Fundamental Theory and Applications* **46**(8) (1999) 974–993
7. Qin, K., Oommen, B.J.: An enhanced tree-shaped adachi-like chaotic neural network requiring linear-time computations. In: *The 2nd International Conference on Chaotic Modeling, Simulation and Applications*, Chania, Greece (2009) 284–293
8. Luo, G.C., Ren, J.S., Qin, K.: Dynamical associative memory: The properties of the new weighted chaotic adachi neural network. *IEICE TRANSACTIONS on Information and Systems* **E95d**(8) (2012) 2158–2162
9. Qin, K., Oommen, B.J.: Networking logistic neurons can yield chaotic and pattern recognition properties. In: *IEEE International Conference on Computational Intelligence for Measure Systems and Applications*, Ottawa, Ontario, Canada (2011) 134–139
10. Hiura, E., Tanaka, T.: A chaotic neural network with duffing's equation. In: *Proceedings of International Joint Conference on Neural Networks*, Orlando, Florida, USA (2007) 997–1001
11. Qin, K., Oommen, B.J.: The entire range of chaotic pattern recognition properties possessed by the adachi neural network. *Intelligent Decision Technologies* **6**(1) (2012) 27–41
12. Qin, K.: *Generic Analysis of Chaotic Neural Networks and Their Applications in Pattern Recognition and Crypto-systems*. PhD thesis. (2010) University of Electronic Science and Technology of China, Chengdu, China.





# Stochastic Model Reduction for Polynomial Chaos Expansion Using Proper Orthogonal Decomposition

Mehrdad Raisee<sup>1</sup>, Dinesh Kumar<sup>2</sup> and Chris Lacor<sup>2\*</sup>

<sup>1</sup> Center of Excellence in Design and Optimization of Energy Systems (CEDOES)  
School of Mechanical Engineering, College of Engineering, University of Tehran,  
P.O.Box: 11155-4563, Tehran, IRAN

(E-mail: [mraisee@ut.ac.ir](mailto:mraisee@ut.ac.ir))

<sup>2</sup> Fluid Mechanics and Thermodynamics Research Group, Department of  
Mechanical Engineering, Vrije Universiteit Brussel, Pleinlaan 2, 1050 Brussels,  
BELGIUM

(E-mail: [dkumar@vub.ac.be](mailto:dkumar@vub.ac.be), [chris.lacor@vub.ac.be](mailto:chris.lacor@vub.ac.be))

**Abstract.** In this paper, a non-intrusive stochastic model reduction scheme is developed for polynomial chaos representation using proper orthogonal decomposition. The main idea is to extract the optimal orthogonal basis via inexpensive calculations on a coarse mesh and then use them for the fine discretization analysis. The developed reduced-order model is implemented to the stochastic steady-state heat diffusion equation. The random conductivity field is approximated via the Karhunen-Loeve (KL) expansion. Input random variables are uniformly distributed so that the Gauss-Legendre quadrature scheme is utilized for the numerical integration. The numerical results showed that the non-intrusive model reduction scheme is able to accurately reproduce mean and variance fields. It is found that the computation-time of the reduced-order model is lower than that of the full-order model.

**Keywords:** Uncertainty Quantification, Polynomial Chaos, Reduced-order Model.

## 1 Introduction

In many engineering applications, uncertainty in physical properties, input data and model parameters result in uncertainties in the system output. A representative practical example is design of turbomachineries where uncertainties in flow conditions and small variations in structural parameters of components (e.g. blade profile) can have a significant impact on the performance. For design refinement of such complex mechanical devices, it is necessary to include all uncertainty information in the output results using uncertainty quantification (UQ) schemes. However, many complex applications require a fine 3D computational mesh, small time-step and high-dimensional space for stochastic analysis. This dramatically increases the computational cost which is not desirable for design proposes. Thus, it is necessary to employ efficient numerical schemes for stochastic analysis of complex industrial flows. A variety of different uncertainty quantification methods such as Monte Carlo approach, sensitivity method, perturbation method, regression method and polynomial chaos

---

\* Corresponding Author



have been proposed for uncertainty quantification. All of these techniques have positive and negative features, and no single technique is optimum for all situations. Following our previous work on UQ (Dinescu *et al.*[1] and Wang *et al.* [7]), here we employed Polynomial Chaos (PC) approach to model uncertainty propagation. Polynomial chaos methods have been successfully applied to solid mechanics problems by several researches (See for example Ghanem and Spanos [3] and Doostan *et al.* [2]). PC schemes have also been employed for a number of fluid mechanics problems by a number of researchers such as: Walters and Huyse [6], Mathelin *et al.* [4] and Dinescu *et al.* [1]. The polynomial chaos representation can be used for different Probability Density Functions (PDFs) and can be implemented through either intrusive or non-intrusive methods. The intrusive approach requires the modification of the CFD codes and this may be difficult, expensive, and time consuming for many CFD problems. Moreover, the source codes of most commercial CFD softwares are not accessible and thus it is impossible to implement the intrusive PC approach to such softwares. For these reasons, here we focused on non-intrusive PC methodology with uniform PDF for uncertainty quantification. The main shortcoming of all PC methods is the *curse of dimensionality*. Developing efficient reduced-order models for shortening the computational cost associated with the stochastic analysis is of great interest for prediction of complex industrial flows with large number of uncertain parameters. In recent years, several model reduction techniques have been proposed for uncertainty quantification. Two informative examples of such works are: Nouy [5] and Doostan *et al.* [2]. In Nouy [5] a Generalize Spectral Decomposition (GSD) was proposed that gives the reduced basis independent of the stochastic discretization scheme. The GSD implementation to a class of Stochastic Partial Differential Equations (SPDE) leads to drastic computational saving though does not circumvent the curse of dimensionality. Doostan *et al.* [2] proposed an intrusive model reduction technique for chaos representation of a SPDE to tackle the curse of dimensionality. A 2D test case from solid mechanics is chosen to illustrate the accuracy and convergence of the model.

In this work, a non-intrusive reduced-order technique is developed and applied to the 2D steady-state stochastic heat diffusion equation. This paper is organized as follows. In Section 2 we present the details of mathematical formulation and problem under investigation. In Section 3, the model reduction methodology is described. Finally, in Section 4 the numerical results are presented and discussed.

## 2 Mathematical Formulation

To demonstrate the non-intrusive stochastic model reduction algorithm, 2D steady-state stochastic heat conduction in a square plate of side  $2a$  is considered (see Figure 1). The 2D heat diffusion with random thermal conductivity is described by the following SPDE:

$$\frac{\partial}{\partial x}(k(x, y; \zeta) \frac{\partial T}{\partial x}) + \frac{\partial}{\partial y}(k(x, y; \zeta) \frac{\partial T}{\partial y}) = 0 \quad (1)$$

As shown in Figure (1), the top boundary of the plate is at hot temperature

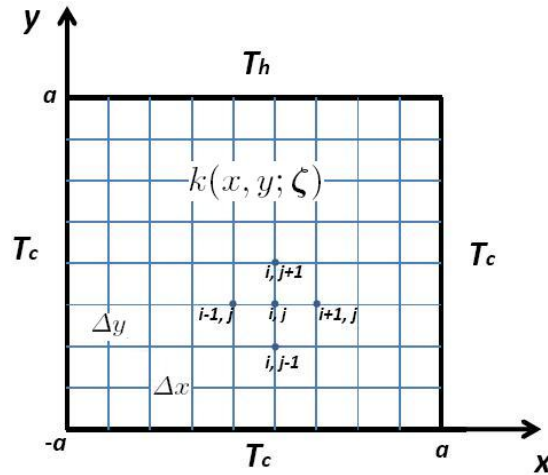


Fig. 1. Schematic of computational domain.

$T_h$  whilst the side and bottom boundaries of the plate are at cold temperature  $T_c$ . The thermal conductivity of the plate,  $k(x, y; \zeta)$ , is assumed to be a two-dimensional homogeneous random process with known mean  $\bar{k}(x, y)$  and known covariance function:

$$R(x_1, y_1; x_2, y_2) = \sigma_k^2 e^{-|x_1-x_2|/b_x - |y_1-y_2|/b_y} \quad (2)$$

where  $b_x$  and  $b_y$  are the correlation lengths in  $x$  and  $y$  directions, respectively, and  $\sigma_k$  is the standard deviation on the thermal conductivity.

A key ingredient here is the representation of stochastic thermal conductivity field as a Karhunen-Loeve (KL) expansion, a type of Fourier expansion for random functions, which amounts to a discretization in the space of random events. According to the KL expansion, the eigenvalues and eigenfunctions are obtained by solving the following 2D integral equation:

$$\int_D R(x_1, y_1; x_2, y_2) \phi_n(x_2, y_2) dx_2 dy_2 = \lambda_n \phi_n(x_1, y_1) \quad (3)$$

Separation of kernel (2) as  $R(x_1, y_1; x_2, y_2) = \sigma_k^2 e^{-|x_1-x_2|/b_x} \cdot e^{-|y_1-y_2|/b_y}$  and substitution in (3) leads to two identical 1D integral eigenvalue equations in  $x$  and  $y$  directions. Solution of the integral equations give eigenvalues (i.e.  $\lambda_i^{(x)}$  and  $\lambda_j^{(y)}$ ) and their corresponding eigenfunctions (i.e.  $\phi_i^{(x)}$  and  $\phi_j^{(y)}$ ). As described in Ghanem and Spanos [3], the complete form of KL expansion for random process  $k(x, y; \zeta)$  is:

$$k(x, y; \zeta) = \bar{k}(x, y) + \sum_{i=1}^{\infty} \sum_{j=1}^{\infty} \left\{ \sqrt{\lambda_i^{(x)} \lambda_j^{(y)}} \zeta_{i,j} \frac{1}{\sqrt{2}} [\phi_i^{(x)}(x) \phi_j^{(y)}(y) + \phi_j^{(x)}(x) \phi_i^{(y)}(y)] \right\} \quad (4)$$



Having obtained an analytical expression for the thermal conductivity, the SPDE (Equation (1)) is discretized using an explicit central differencing scheme in a uniform grid ( $\Delta x = \Delta y$ ), see Figure 1. Thus, for any set of  $\zeta \equiv \{\zeta_i\}_{i=1}^n$ , first thermal conductivity is calculated in the computational domain using KL expression (Equation (4)). Then, the new temperature  $T^{n+1}$  at grid node  $(i, j)$  is obtained from old nodal temperature  $T^n$  of neighbouring nodes. The solution is converged when the maximum error between the old and new temperature values is sufficiently small ( $\epsilon \simeq 10^{-9}$ ).

### 3 Model Reduction Methodology

In the classical polynomial chaos expansion, the random temperature field  $T(x, y; \zeta)$  can be decomposed into deterministic and stochastic components. The PC representation of temperature field of order  $p$  for  $n$  random variable  $\zeta \equiv \{\zeta_i\}_{i=1}^n$  can be written as:

$$T(x, y; \zeta) - \langle T(x, y) \rangle = \sum_{i=1}^P T^i(x, y) \psi_i(\zeta) \quad (5)$$

where the total number of terms are  $P + 1 = (p + n)!/p!n!$  and the mean value of  $T(x, y; \zeta)$  is expressed as:

$$\langle T(x, y) \rangle = \int_{\omega} T(x, y; \zeta) f(\zeta) d\zeta \quad (6)$$

In the above equation,  $f$  is Probability Density Function (PDF). Here we assumed random variables are uniformly distributed over interval  $[-1, 1]$  and thus the PDF is  $f = 1/2^n$  for  $n$  random variables  $\{\zeta_i\}_{i=1}^n$ . The non-intrusive method uses spectral projection to find the PC expansion coefficients  $T^i(x, y)$  in Equation (5). Projecting Equation (5) onto the  $k^{th}$  basis and use of orthogonality gives:

$$T^i(x, y) = \frac{1}{\langle \psi_i^2(\zeta) \rangle} \int_{\omega} T(x, y; \zeta) \psi_i(\zeta) f(\zeta) d\zeta \quad (7)$$

The objective of the spectral projection method is to compute the polynomial coefficients by evaluating numerator in Equation (7) numerically, while the denominator can be computed analytically for multi-variant orthogonal polynomials. Here we used the  $n$ -dimensional *Gauss-Legendre quadrature* to compute the projection integrals in Equation (7) as:

$$T^i(x, y) = \frac{1}{\langle \psi_i^2(\zeta) \rangle} \sum_{i_1=1}^q \dots \sum_{i_n=1}^q (w_1^{i_1} \otimes \dots \otimes w_n^{i_n}) T(x, y; \zeta_1^{i_1}, \dots, \zeta_n^{i_n}) f(\zeta_1^{i_1}, \dots, \zeta_n^{i_n}) \quad (8)$$

where  $(\zeta^k, w^k)$ ,  $k = 1, 2, \dots, q$  are the one-dimensional (1D) Gauss-Legendre integration points and weights.



The above classical expansion dose not represent an optimal PC representation of  $T(x, y, \zeta)$ . To find the optimal PC expansion one can consider the fact that spatial discretization errors and random discretization errors may be decoupled. Therefore, one can minimize the random discretization errors on the coarse grid and then solve the real physical problem on a fine mesh by using limited number of optimal random basis  $\{z_i\}_{i=1}^m$  (obtained in the coarse grid analysis) where  $m$  is the number of dominated eigenvalues. The first step in the model reduction scheme is to find optimal PC basis using POD; a well-known procedure for extracting a basis for a model decomposition from an ensemble of realizations. To this end, suppose in a coarse grid, expression (9) represents an optimal PC expansion of the stochastic temperature field  $T(x, y, \zeta)$ ;

$$T(x, y; \zeta) - \langle T(x, y) \rangle = \sum_{i=1}^m T^i(x, y) z_i(\zeta) \quad (9)$$

Now in the coarse grid, the covariance function  $C(x_1, y_1; x_2, y_2)$  of temperature field can be obtained from:

$$C(x_1, y_1; x_2, y_2) = \sum_{i=1}^P T^i(x_1, y_1) T^i(x_2, y_2) \langle \psi_i^2 \rangle \quad (10)$$

The corresponding eigenvalues  $\nu_i$  and eigenfunctions  $\phi_i(x, y)$  are the solution of the following eigenvalue problem:

$$\int_D C(x_1, y_1; x_2, y_2) \phi_i(x_2, y_2) dx_2 dy_2 = \nu_i \phi_i(x_1, y_1) \quad (11)$$

The upper limit  $m$  in the Equation (9) can be found by the size of dominant eigenspace (10) such that  $\sum_{i=1}^m \nu_i / \sum_i \nu_i \geq 0.99$ .

Having obtained  $T^i(x, y)$  from classical PC on the coarse grid and eigenfunctions  $\phi_i(x, y)$  from the solution of eigenvalue problem (11), the set of optimal basis  $\{z_i\}_{i=1}^m$  can be now represented as a linear combination of the set of classical polynomial chaos;  $\{\psi_i\}_{i=1}^P$  using the following scalar product<sup>1</sup>:

$$z_i(\zeta) = [T(x, y; \zeta) - \langle T(x, y) \rangle, \phi_i(x, y)] = \sum_{j=1}^P \alpha_{ij} \psi_j(\zeta) \quad (12)$$

where coefficient  $\alpha_{ij}$  are obtained via the scalar product:

$$\alpha_{ij} = \int_R T^j(x, y) \phi_i(x, y) d\vec{x} d\vec{y} \quad (13)$$

One now dose the classical polynomial chaos on a fine mesh, where  $z_i$  are used instead of  $\psi_i$ . For  $1 \leq i \leq m$ , the coefficients in expansion (9) are obtained from:

$$T^i(x, y) = \frac{\langle T(x, y; \zeta), z_i \rangle}{\langle z_i, z_i \rangle} = \frac{1}{\nu_i} \sum_{j=1}^P \alpha_{ij} \langle T(x, y; \zeta), \psi_j \rangle \quad (14)$$

<sup>1</sup> The scalar product of functions  $v$  and  $w$  is defined as:  $[v, w] = \int_x v \cdot w dx$ .



## 4 Results and Discussion

We now examine the performance of the reduced-order model by analyzing the 2D steady-state heat conduction equation. It is assumed that the top wall is at  $T_h = 300^\circ C$  and side and bottom walls at  $T_c = 100^\circ C$ . First, a 2D KL expansion is performed using the exponential kernel with a standard deviation of  $\sigma_k = 1.0 W/m.K$  and correlation lengths of  $b_x = b_y = 10.0 m$ . The mean thermal conductivity is assumed to be  $\bar{k} = 5.0 W/m.K$ . The first six largest terms in the KL expansions are chosen for further analysis.

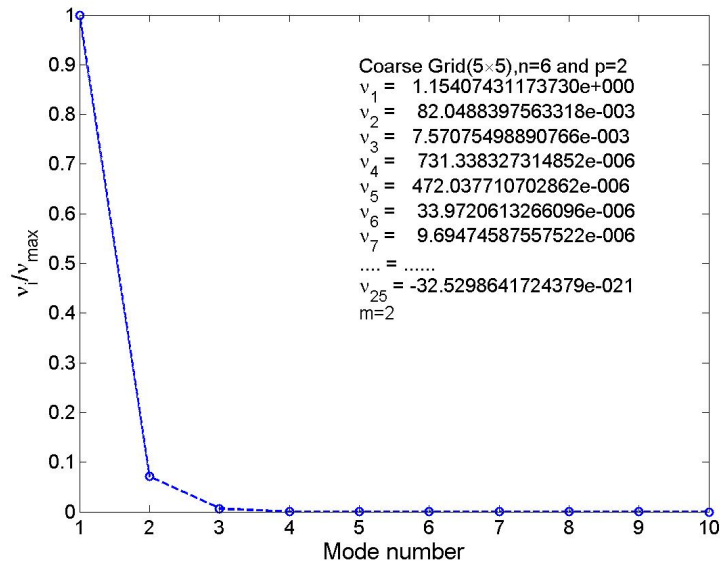


Fig. 2. Computed eigenvalues using coarse discretization analysis.

Figures 2 and 3 respectively show the distributions of eigenvalues and  $|\alpha_{ij}|$  coefficients obtained from the coarse discretization analysis on a  $5 \times 5$  mesh when a second-order Legendre polynomial ( $p = 2$ ) is employed. From these figures it can be concluded that only two ( $m = 2$ ) basis functions (i.e.  $z_1$  and  $z_2$ ) are adequate for the fine discretization analysis. Thus, fine discretization analysis is performed using the new  $z_1$  and  $z_2$  basis functions on a  $40 \times 40$  mesh. The computed mean and variance fields using full- and reduced-order models are compared in Figure 4. It is visible the fine grid computations via reduced- and full-order models resulted in identical results for the mean temperature. Moreover, full- and reduced-order analysis on the fine mesh produced very similar variance fields. The order of maximum difference in variance fields is  $10^{-3}$ . The ratio of computation-time for the reduced-order analysis to the time needed for the full-order calculation using three fine meshes of  $30 \times 30$ ,  $40 \times 40$  and  $50 \times 50$  is shown in Figure 5. While reduced-order computations on the  $30 \times 30$  results to about 10% saving in the computation-time, more than 50% saving in computation-time is obtained when a finer  $50 \times 50$  mesh is employed.

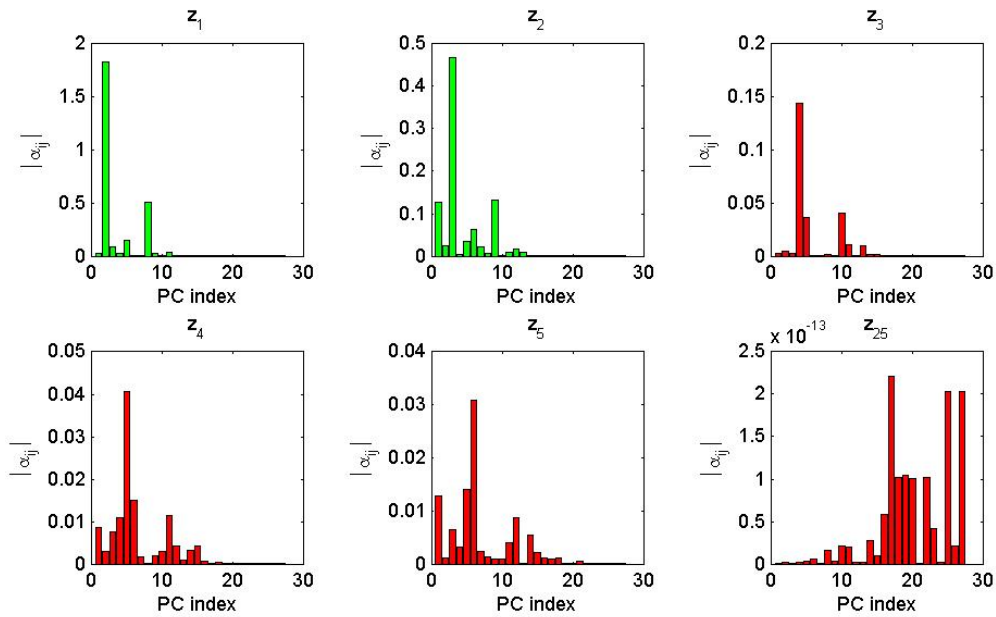


Fig. 3. Computed  $|\alpha_{ij}|$  using coarse discretization analysis.

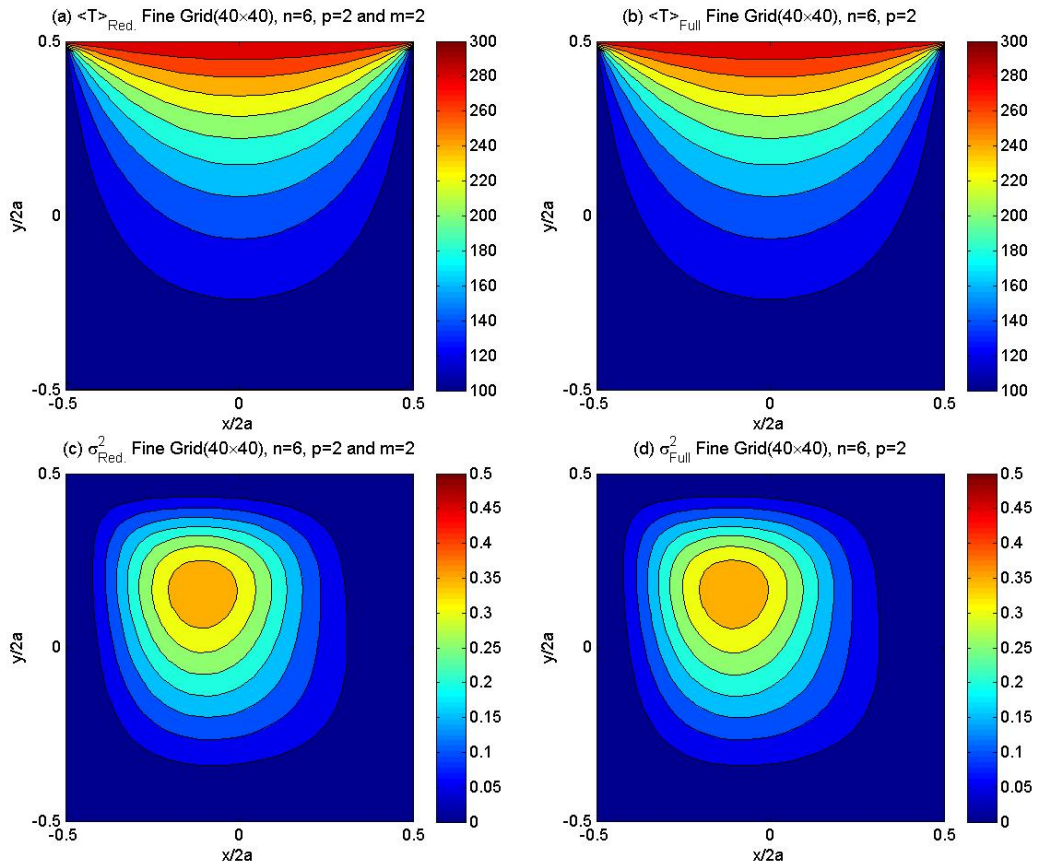


Fig. 4. Comparison of mean and variance fields.

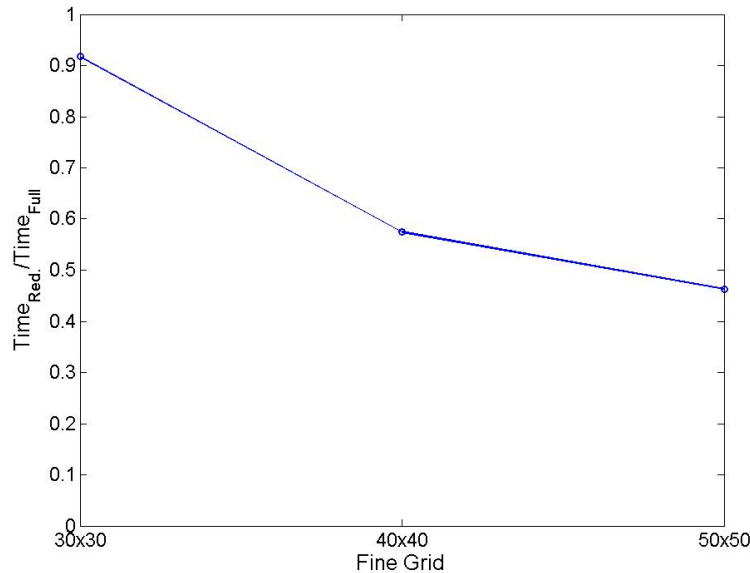


Fig. 5. Ratio of reduced-order computation-time to the full-order computation-time.

## Conclusion

In this paper, a non-intrusive model reduction technique for PC expansion is presented and discussed. The reduced-order model is applied to the 2D steady-state heat diffusion equation. Distributions of mean and variance obtained from the reduced-order model are compared with those of full-order model. The numerical results show that the developed reduced-order model is able to produce acceptable results for such statistical quantities. Computation-time of the reduced-order model is found to be lower than that of the full-order model.

## References

- 1.C. Dinescu, S. Smirnov, Ch. Hirsch, and C. Lacor. Assessment of intrusive and non-intrusive non-deterministic CFD methodologies based on polynomial chaos expansions. *Int. J. of Eng. Systems Modeling and Simulation*, 2:87-98, 2010.
- 2.A. Doostan, R. Ghanem, and J. Red-Horse. Stochastic model reduction for chaos representations. *Comp. Meth. in Appl. Mech. and Eng.*, 196:3951-3966, 2007.
- 3.R. Ghanem, and O. Spanos. *Stochastic Finite Elements: A Spectral Approach*, 1991, Springer Verlag.
- 4.L. Mathelin, M. Y. Hussaini, and T. A. Zang. Stochastic approaches to uncertainty quantification in CFD simulations. *Numer. Algorithms*, 38:209-236, 2007.
- 5.A. Nouy. A generalized spectral decomposition technique to solve a class of linear stochastic partial differential equations. *Comp. Meth. in Appl. Mech. and Eng.*, 196:4521-4537, 2007.
- 6.R. W. Walters, and L. Huyse. *Uncertainty analysis for fluid mechanics with applications*. NASA/CR 2002-211449.
- 7.X. Wang, Ch. Hirsch, Z. Liu, S. Kang, and C. Lacor. Uncertainty-based robust aerodynamic optimization of rotor blades. *Int. J. Numer. Meth. Engng*, DOI: 10.1002/nme.4438, 2012.





## The profile of temperature in the dissipative over-dense plasma layer

L. Rajaei<sup>1\*</sup>, S. Miraboutalebi<sup>2</sup>

<sup>1</sup> Physics Department, Qom University, Qom, Iran  
(E-mail: [rajaeel@yahoo.com](mailto:rajaeel@yahoo.com))

<sup>2</sup> Physics Department, Islamic Azad University, North Tehran Branch, Tehran,  
1651153311, Iran  
(E-mail: [smirabotalebi@gmail.com](mailto:smirabotalebi@gmail.com))

**Abstract.** An investigation is undertaken to introduce an effective mechanism of plasma heating which significantly enhances and facilitates the heating of a dense plasma layer. This mechanism directly related to the phenomena of anomalous transparency of a dense plasma layer through the resonant excitation of the coupled surface waves. It is shown that the collisional effects reduce the rate of the energy transmission through the plasma layer under resonant conditions. This dissipative effects cause heating of the plasma layer to a considerable amount of temperature. The temperature distribution in the plasma layer during the transmission of the electromagnetic waves is studied.

**Keywords:** Microwave, Dissipation, Incident wave, Over-dense plasma, Surface plasma, Transparency.

### 1 Introduction

The investigations of circumstances and important factors in the plasma heating is the subject of relevance for many fields of plasma physics ranging from laboratory experiments to astrophysics [1]. The heat flow and temperature gradient in plasma are fundamental process that take place during plasma phenomena and are of great importance effects. These process in some situations, have inevitable destructive effects. One of the challenges of embedding plasma in electric field is the appearance of high temperature electrons which acts like an internal transport barrier. The three well known heating mechanisms of plasma are ohmic heating, neutral beam injection and high frequency electromagnetic waves. In the high frequency electromagnetic waves mechanism of plasma heating, the energy of waves is converted into thermal electron motion through electron-ion collisions [2,3]. Also the interaction of the electromagnetic waves with plasma may lead to the resonant excitation of the electrostatic waves which subsequently decays generating energetic electrons [4].

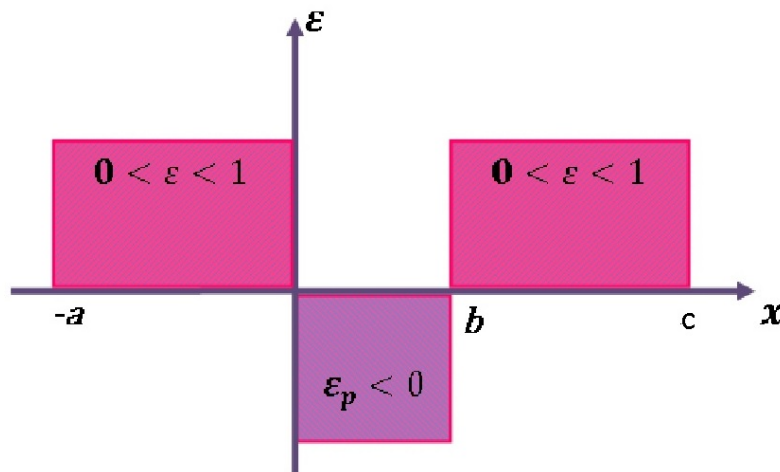
In our previous works we studied the total transparency conditions of an overdense plasma layer due to the resonant excitation of the coupled surface modes, [5]-[9]. In the present paper we demonstrate another mechanism of plasma heating that significantly enhances and facilitates the heating of the dense plasma. We will show that for a collisional plasma under resonant conditions, the dissipative effects cause heating of the dense plasma to a considerable

\* Corresponding author: Tel +98-25-32854972. E-mail address: [rajaeel@yahoo.com](mailto:rajaeel@yahoo.com)

amount of temperature. Hence the process of resonant excitation of the coupled plasmons can be considered as an effective mechanism of plasma heating. In fact this process has a dual acting effect, it cause the transparency of the plasma slab and at the same time it gives rise to plasma heating.

This paper is organized as follows: In section two the geometrical construction of the problem and the transmission of the electromagnetic waves through the considered structure. In section three the solutions of the heat equations at steady states condition is given and the temperature is predicted. Finally, section four presents the results.

## 2 the model



**Fig. 1.** Schematic diagram showing the spatial distribution of the effective electric permittivity.

Let us consider a geometrical structure fulfills the conditions under which the high transparency of a normally reflected overdense plasma can be observed , [7]. The system is modeled as an overdense plasma layer with length  $b$  placed between two equal ordinary dielectrics or equivalently cold plasma layer (see Fig. 1). In order to examine the resonant conditions of the excitation of the surface modes let us consider a p-polarize wave specified by the magnetic field component  $\mathbf{B} = (0, 0, B_z)$  and the electric field in the plane of incidence  $(x, y)$ , namely  $\mathbf{E} = (E_x, E_y, 0)$ . Considering the geometrical structure of Fig. (1), the spatial part of the electric and the magnetic fields must be proportional to  $exp(iky)$  and the waves amplitudes become functions only of the variable  $x$ . In this case the magnetic field and temperature at the steady state, obtain the following forms:



$$\kappa \frac{\partial^2 T}{\partial^2 x} + Q = 0. \quad (1)$$

$$\epsilon \frac{\partial}{\partial x} \frac{1}{\epsilon} \frac{\partial B_z}{\partial x} + (\epsilon - k_y^2) B_z = 0. \quad (2)$$

where  $\kappa$  refers to the thermal conductivity. Also,

$$Q = \frac{\epsilon_0}{2} \epsilon'' \omega E_0^2 |\mathbf{E}|, \quad (3)$$

where  $\epsilon''$  is the imaginary part of the permittivity. Here  $\epsilon = (1 - \frac{\omega_p^2}{\omega^2 s})$ ,  $s = (1 + i\nu/\omega)$ , also  $k_0 = \frac{\omega}{c}$  and  $\omega_p = \frac{4\pi n_0 e^2}{m}$ . In these equations, all field quantities have become dimensionless and redefined as follows:

$$(\tilde{\mathbf{r}} = k_0 \mathbf{r}, \tilde{t} = \omega t), \tilde{\mathbf{E}} = \frac{\mathbf{E}}{E_0}, \tilde{\nu} = \frac{\nu}{\omega}, \tilde{T} = \frac{T}{T_0}, \quad (4)$$

where the tilde quantities are dimensionless, but for simplicity, we ignore the tilde sign of our field quantities in equations. Likewise, the temperature should satisfy the surface heat balances. where  $k_y = \sin\theta$ . Analytical solutions of Eqs.(2) gives the magnetic field in the both dielectrics and the over dense plasma mediums, and are obtained in the following forms:

$$B_z = (A_1 e^{\alpha x} + A_2 e^{-\alpha x}), \quad (5)$$

where  $\alpha = \sqrt{k_y^2 - \epsilon}$ . The electromagnetic fields in the vacuum regions,  $x < -a$  and  $x > b$ , have the following forms:

$$B_z = E_0 e^{i \cos \theta x} + R e^{-i \cos \theta x} \quad x < -a, \quad (6)$$

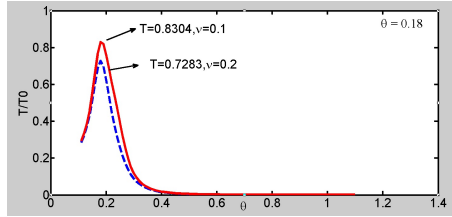
$$B_z = T_r e^{i \cos \theta x} \quad x > b, \quad (7)$$

where  $E_0$ ,  $R$  and  $T$  respectively assign the field components for the incident, reflected and transmitted waves.

These field solutions should satisfy the conditions of continuity of  $dB_z/dx$  and  $B_z$ , on all the boundaries and as a result, one achieve eight equations for the unknown coefficients, specifically the coefficient  $R$  and  $T_r$  are obtained. For resonant values of the incident angle  $\theta$ , we should expect anomalous transmission of the electromagnetic waves.

Fig. (2) shows the transmission curve  $T_r$  and  $R$  as a function of the incidence angle  $\theta$  for two different values of the collisional frequencies, namely for  $\nu = 0.1$  and  $\nu = 0.2$ . Two important results are obtained from these plots. As the first result, there is an acute increase in the transmission properties of the system, when the angle of incidence reaches to one of its resonant values. According to the figure.(2), the maximum of the transmission coefficient  $T$  occurs about  $\theta = 0.18 \text{ rad}$  for two different value of collisional frequencies.

As the second result, comparing the two maximums indicates that, with the increase of the collisional frequency  $\nu$ , the maximum rate of the electromagnetic



**Fig. 2.** The transmission coefficients vs incident angel for two different value of collisional frequency

waves decreases. In order to investigate the effect of this dissipated energy on the increase of the plasma temperature, the electric field amplitude in the over-dense plasma at the maximum points is needed. To provide this we note that for the case  $\nu = 0.1$ , the deficiency at the maximum point is about  $1 - (|R|^2 + |T_r|^2) = 0.3071$ , while For the case  $\nu = 0.2$  the deficiency is about  $1 - (R^2 + T_r^2) = 0.4373$ .

### 3 The heat equation

In order to investigate the temperature variations or the increase of the temperature degree of the over-dense plasma due to passing of the electromagnetic waves one should consider the solutions of the heat equation (1). The factor  $Q$  that is given in Eq.(3) can be considered as a thermal source for the heat equation. The imaginary part of the permittivity explicitly appears in the heat source and hence is vitally important to produce heat. Also the heat source  $Q$  depends on the amplitude of the passing electric field in the over-dense plasma layer. The electric field amplitudes, obtained in previous section, in the over-dense plasma layer under the resonant transmission of waves. Substituting them in Eq. (3) for each value of the collisional frequency  $\nu$ , the heating source  $Q$  would be obtained. Subsequently one can study the temperature variations and the key factors of these variations by solving the corresponding heat equation via Eq.(1).

Here we follow the above procedure and analyze the temperature variations from Eq.1 in steady state both numerically and analytically.

we require only the boundary condition which includes convection relation on both boundaries of the plasma.

$$T(x) = 1, x = 0, \quad \frac{\partial T}{\partial x} = 0, x = b.$$

It should be noticed that the sample or the plasma will be kept in room temperature, therefore,  $T_0$  is the room temperature also here  $T$  is dimensionless and equals to  $T/T_0$ . Heat equation will be solved through analytic as well as the numerical method and, subsequently, compare the data obtained. The analytical answers of this equation are as follows:

$$T(x) = -\frac{1}{\kappa} \int \int Q(x) dx dx + C_1 x + C_2, \quad (8)$$

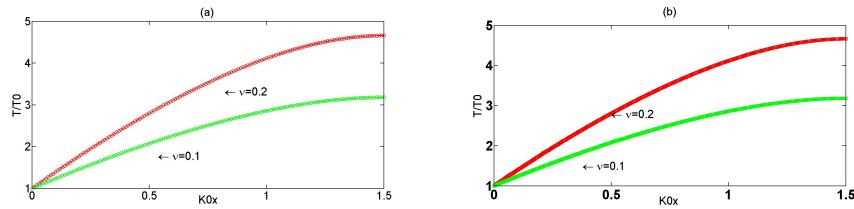
where  $C_1$  and  $C_2$  are calculated by boundary conditions. Also Eq. 8 can be written in the following form

$$T(x) = -F_1(x) + F_2(0)x + F_1(0), \quad (9)$$

where  $F_1(x) = \int \int Q(x)dx$ ,  $F_2(x) = \int Q(x)dx$ ,

The above relation demonstrates that the curve of temperature is an ascending function of space. To investigate this more closely, the analytical solutions of the temperature functions obtained from Eq.1 are plotted in Fig. (3a). This figure contains two different curves corresponding to two different values of the collisional frequencies  $\nu$ . As it is shown in the figure, the plasma temperature increases as one move away from the plasma fronting edge. It should be noticed that this temperature rising takes place due to the collisional effects which appears in the form of the thermal source term  $Q$ .

It is also plotted the temperature curve by using a numerical method and the results are given in Fig. (3b). To solve the heat equation (1) numerically, the finite difference method has been employed. These numerical results are in a good agreement with the analytical results and show an ascending function of space for the temperature function.



**Fig. 3.** The profile of temperature for analytic and numeric solutions.

## 4 Conclusions

It has been shown here that the coupled resonant excitation of the surface modes could create a condition for suitably heating of a dense collisional plasma layer. To provide the resonant conditions, the plasma layer was considered between two dielectric layers. The slab then was supposed to be subjected to the electromagnetic waves. After solving the equation of the wave for a cold plasma, the electric field in all mediums was obtained. Eventually, the energy transmission on the rear side of the dielectric layer was examined. Here, the important issue is the effect of the collision on the amount of energy transmission which, as researchers have shown, diminishes as the collisional effects increase. Equally the important issue is the way in which the dissipative energy in the plasma appears. The results indicate that the dissipated energy in the plasma led to the heating of the particles and the increasing of the plasma temperature.



## References

- 1.J. C. Metcalfe, and M. B. C. Quigley, Heat transfer in plasma-arc welding, *Welding Journal* 54,3 (1975) 99s-103s.
- 2.J. M. Dawson and J. Oberman. High frequency conductivity and the emission and absorption coefficients of a fully ionized plasma. *Phys. Fluids*, 5 (1962)517.
- 3.A. B. Langdon. Nonlinear inverse bremsstrahlung and heated electron distributions. *Phys. Rev. Lett.*, 44 (1980)575 .
- 4.D. Forslund, J. Kindel, K. Lee, E. Lindman, and R. Morse. Theory and simulation of resonant absorption in a hot plasma. *Phys. Rev. A*, 11 (1975)679.
- 5.Yu. P. Bilokh, Plasmon mechanism of light transmission through a metal film or a plasma layer, *Optics comm.* 259(2006)436-444.
- 6.R. Dragila, B. Luther-Davies and S. Vukovic 1985 High transparency of classically opaque metallic films, *Physics Review Letter.* **55**, 1117–1120.
- 7.L. Rajaei, S. Miraboutalebi and B. Shokri 2011 Transmission of Electromagnetic wave Through a Warm Over-dense Plasma layer with dissipative factor, *Phys Scr.* **84**, 8949.
- 8.S. Miraboutalebi, L. Rajaei, and M. K. KhadiviBorogeni, Plasmon resonance coupling in cold overdense dissipative plasma, *Journal of Theoretical and Applied Physics* 7.1 (2013)1-9.
- 9.S. Miraboutalebi, L. Rajaei, and L. FarhangMatin, Surface wave excitations on magnetized over-dense plasma, *Journal of Theoretical and Applied Physics* 6.1 (2012)1-8.



## Delay-dependent output feedback guaranteed cost control for Hopfield neural networks

G. Rajchakit

Major of Mathematics, Faculty of Science, Maejo University, Chiangmai, 50290,  
Thailand  
(E-mail: [griengkrai@yahoo.com](mailto:griengkrai@yahoo.com))

**Abstract.** This paper studies the problem of guaranteed cost control for a class of Hopfield delayed neural networks. The time delay is a continuous function belonging to a given interval, but not necessary to be differentiable. A cost function is considered as a nonlinear performance measure for the closed-loop system. The stabilizing controllers to be designed must satisfy some exponential stability constraints on the closed-loop poles. By constructing a set of augmented Lyapunov-Krasovskii functionals combined with Newton-Leibniz formula, a guaranteed cost controller is designed via memoryless state feedback control and new sufficient conditions for the existence of the guaranteed cost state-feedback for the system are given in terms of linear matrix inequalities (LMIs).

*Keywords:* Neural networks, guaranteed cost control, stabilization, interval time-varying delays, Lyapunov function, linear matrix inequalities

### 1 Introduction

Stability and control of Hopfield neural networks with time delay has been attracted considerable attention in recent years [1-8]. In many practical systems, it is desirable to design neural networks which are not only asymptotically or exponentially stable but can also guarantee an adequate level of system performance. In the area of control, signal processing, pattern recognition and image processing, delayed neural networks have many useful applications. Some of these applications require that the equilibrium points of the designed network be stable. In both biological and artificial neural systems, time delays due to integration and communication are ubiquitous and often become a source of instability. The time delays in electronic neural networks are usually time-varying, and sometimes vary violently with respect to time due to the finite switching speed of amplifiers and faults in the electrical circuitry. Guaranteed cost control problem [9-12] has the advantage of providing an upper bound on a given system performance index and thus the system performance degradation incurred by the uncertainties or time delays is guaranteed to be less than this bound. The Lyapunov-Krasovskii functional technique has been among the popular and effective tool in the design of guaranteed cost controls for neural networks with time delay. Nevertheless, despite such diversity of results available, most existing work either assumed that the time delays are constant or differentiable [13-16]. Although, in some cases, delay-dependent guaranteed cost control for systems with time-varying delays were considered



2 G. Rajchakit

in [12, 13, 15], the approach used there can not be applied to systems with interval, non-differentiable time-varying delays. To the best of our knowledge, the guaranteed cost control and state feedback stabilization for Hopfield neural networks with interval, non-differentiable time-varying delays have not been fully studied yet, which are important in both theories and applications. This motivates our research.

In this paper, we investigate the guaranteed cost control for Hopfield delayed neural networks problem. The novel features here are that the delayed neural network under consideration is with various globally Lipschitz continuous activation functions, and the time-varying delay function is interval, non-differentiable. A nonlinear cost function is considered as a performance measure for the closed-loop system. The stabilizing controllers to be designed must satisfy some exponential stability constraints on the closed-loop poles. Based on constructing a set of augmented Lyapunov-Krasovskii functionals combined with Newton-Leibniz formula, new delay-dependent criteria for guaranteed cost control via memoryless feedback control is established in terms of LMIs.

The outline of the paper is as follows. Section 2 presents definitions and some well-known technical propositions needed for the proof of the main result. LMI delay-dependent criteria for guaranteed cost control is presented in Section 3. The paper ends with conclusions and cited references.

## 2 Preliminaries

The following notation will be used in this paper.  $\mathbb{R}^+$  denotes the set of all real non-negative numbers;  $\mathbb{R}^n$  denotes the  $n$ -dimensional space with the scalar product  $\langle x, y \rangle$  or  $x^T y$  of two vectors  $x, y$ , and the vector norm  $\| \cdot \|$ ;  $M^{n \times r}$  denotes the space of all matrices of  $(n \times r)$ -dimensions.  $A^T$  denotes the transpose of matrix  $A$ ;  $A$  is symmetric if  $A = A^T$ ;  $I$  denotes the identity matrix;  $\lambda(A)$  denotes the set of all eigenvalues of  $A$ ;  $\lambda_{\max}(A) = \max\{\text{Re}\lambda; \lambda \in \lambda(A)\}$ .  $x_t := \{x(t+s) : s \in [-h, 0]\}$ ,  $\|x_t\| = \sup_{s \in [-h, 0]} \|x(t+s)\|$ ;  $C^1([0, t], \mathbb{R}^n)$  denotes the set of all  $\mathbb{R}^n$ -valued continuously differentiable functions on  $[0, t]$ ;  $L_2([0, t], \mathbb{R}^m)$  denotes the set of all the  $\mathbb{R}^m$ -valued square integrable functions on  $[0, t]$ ;

Matrix  $A$  is called semi-positive definite ( $A \geq 0$ ) if  $\langle Ax, x \rangle \geq 0$ , for all  $x \in \mathbb{R}^n$ ;  $A$  is positive definite ( $A > 0$ ) if  $\langle Ax, x \rangle > 0$  for all  $x \neq 0$ ;  $A > B$  means  $A - B > 0$ . The notation  $\text{diag}\{\dots\}$  stands for a block-diagonal matrix. The symmetric term in a matrix is denoted by  $*$ .

Consider the following Hopfield neural networks with interval time-varying delay:

$$\begin{aligned} \dot{x}(t) &= -Ax(t) + W_0 f(x(t)) + W_1 g(x(t-h(t))) + Bu(t), \quad t \geq 0, \\ x(t) &= \phi(t), t \in [-h_1, 0], \end{aligned} \quad (1)$$

where  $x(t) = [x_1(t), x_2(t), \dots, x_n(t)]^T \in \mathbb{R}^n$  is the state of the neural,  $u(\cdot) \in L_2([0, t], \mathbb{R}^m)$  is the control;  $n$  is the number of neurals, and

$$f(x(t)) = [f_1(x_1(t)), f_2(x_2(t)), \dots, f_n(x_n(t))]^T,$$





Guaranteed cost control for Hopfield neural networks 3

$$g(x(t)) = [g_1(x_1(t)), g_2(x_2(t)), \dots, g_n(x_n(t))]^T,$$

are the activation functions;  $A = \text{diag}(\bar{a}_1, \bar{a}_2, \dots, \bar{a}_n)$ ,  $\bar{a}_i > 0$  represents the self-feedback term;  $B \in R^{n \times m}$  is control input matrix;  $W_0, W_1$  denote the connection weights, the discretely delayed connection weights and the distributively delayed connection weight, respectively; The time-varying delay function  $h(t)$  satisfies the condition

$$0 \leq h_0 \leq h(t) \leq h_1,$$

The initial functions  $\phi(t) \in C^1([-h_1, 0], R^n)$ , with the norm

$$\|\phi\| = \sup_{t \in [-h_1, 0]} \sqrt{\|\phi(t)\|^2 + \|\dot{\phi}(t)\|^2}.$$

In this paper we consider various activation functions and assume that the activation functions  $f(\cdot), g(\cdot)$  are Lipschitzian with the Lipschitz constants  $f_i, e_i > 0$ :

$$\begin{aligned} |f_i(\xi_1) - f_i(\xi_2)| &\leq f_i |\xi_1 - \xi_2|, \quad i = 1, 2, \dots, n, \forall \xi_1, \xi_2 \in \mathbb{R}, \\ |g_i(\xi_1) - g_i(\xi_2)| &\leq e_i |\xi_1 - \xi_2|, \quad i = 1, 2, \dots, n, \forall \xi_1, \xi_2 \in \mathbb{R}, \end{aligned} \quad (2)$$

The performance index associate with the system (2.1) is the following function

$$J = \int_0^\infty f^0(t, x(t), x(t-h(t)), u(t)) dt, \quad (3)$$

where  $f^0(t, x(t), x(t-h(t)), u(t)) : R^+ \times R^n \times R^n \times R^m \rightarrow R^+$ , is a nonlinear cost function satisfies

$$\exists Q_1, Q_2, R : f^0(t, x, y, u) \leq \langle Q_1 x, x \rangle + \langle Q_2 y, y \rangle + \langle Ru, u \rangle, \quad (4)$$

for all  $(t, x, u) \in R^+ \times R^n \times R^m$  and  $Q_1, Q_2 \in R^{n \times n}$ ,  $R \in R^{m \times m}$ , are given symmetric positive definite matrices. The objective of this paper is to design a memoryless state feedback controller  $u(t) = Kx(t)$  for system (2.1) and the cost function (2.3) such that the resulting closed-loop system

$$\dot{x}(t) = (A + BK)x(t) + W_0 f(x(t)) + W_1 g(x(t-h(t))), \quad (5)$$

is exponentially stable and the closed-loop value of the cost function (2.3) is minimized.

*Definition 2.1* Given  $\alpha > 0$ . The zero solution of closed-loop system (2.5) is  $\alpha$ -exponentially stabilizable if there exist a positive number  $N > 0$  such that every solution  $x(t, \phi)$  satisfies the following condition:

$$\|x(t, \phi)\| \leq N e^{-\alpha t} \|\phi\|, \quad \forall t \geq 0.$$

*Definition 2.2* Consider the control system (1). If there exist a memoryless state feedback control law  $u^*(t) = Kx(t)$  and a positive number  $J^*$  such that the zero solution of the closed-loop system (2.5) is exponentially stable and the cost function (2.3) satisfies  $J \leq J^*$ , then the value  $J^*$  is a guaranteed costant and  $u^*(t)$  is a guaranteed cost control law of the system and its corresponding cost function.

We introduce the following technical well-known propositions, which will be used in the proof of our results.



4 G. Rajchakit

*Proposition 2.1.* (Schur complement lemma [17]). Given constant matrices  $X, Y, Z$  with appropriate dimensions satisfying  $X = X^T, Y = Y^T > 0$ . Then  $X + Z^T Y^{-1} Z < 0$  if and only if

$$\begin{pmatrix} X & Z^T \\ Z & -Y \end{pmatrix} < 0.$$

*Proposition 2.2.* (Integral matrix inequality [18]). For any symmetric positive definite matrix  $M > 0$ , scalar  $\gamma > 0$  and vector function  $\omega : [0, \gamma] \rightarrow \mathbb{R}^n$  such that the integrations concerned are well defined, the following inequality holds

$$\left( \int_0^\gamma \omega(s) ds \right)^T M \left( \int_0^\gamma \omega(s) ds \right) \leq \gamma \left( \int_0^\gamma \omega^T(s) M \omega(s) ds \right)$$

### 3 Design of guaranteed cost controller

In this section, we give a design of memoryless guaranteed feedback cost control for neural networks (2.1). Let us set

$$\begin{aligned} W_{11} &= -[P + \alpha I]A - A^T[P + \alpha I] - 2BB^T + 0.25BRB^T + \sum_{i=0}^1 G_i, \\ W_{12} &= P + AP + 0.5BB^T, \\ W_{13} &= e^{-2\alpha h_0} H_0 + 0.5BB^T + AP, \\ W_{14} &= 2e^{-2\alpha h_1} H_1 + 0.5BB^T + AP, \\ W_{15} &= P + 0.5BB^T + AP, \\ W_{22} &= \sum_{i=0}^1 W_i D_i W_i^T + \sum_{i=0}^1 h_i^2 H_i + (h_1 - h_0)U - 2P - BB^T, \\ W_{23} &= P, \quad W_{24} = P, \quad W_{25} = P, \\ W_{33} &= -e^{-2\alpha h_0} G_0 - e^{-2\alpha h_0} H_0 - e^{-2\alpha h_1} U + \sum_{i=0}^1 W_i D_i W_i^T, \\ W_{34} &= 0, \quad W_{35} = -2\alpha h_1 U, \\ W_{44} &= \sum_{i=0}^1 W_i D_i W_i^T - e^{-2\alpha h_1} U - e^{-2\alpha h_1} G_1 - e^{-2\alpha h_1} H_1, \quad W_{45} = e^{-2\alpha h_1} U, \\ W_{55} &= -e^{-2\alpha h_1} U + W_0 D_0 W_0^T, \\ E &= \text{diag}\{e_i, i = 1, \dots, n\}, \quad F = \text{diag}\{f_i, i = 1, \dots, n\}, \\ \lambda_1 &= \lambda_{\min}(P^{-1}), \\ \lambda_2 &= \lambda_{\max}(P^{-1}) + h_0 \lambda_{\max}[P^{-1}(\sum_{i=0}^1 G_i)P^{-1}] \\ &\quad + h_1^2 \lambda_{\max}[P^{-1}(\sum_{i=0}^1 H_i)P^{-1}] + (h_1 - h_0) \lambda_{\max}(P^{-1} U P^{-1}). \end{aligned}$$



Guaranteed cost control for Hopfield neural networks 5

**Theorem 3.1.** Consider control system (2.1) and the cost function (2.3). If there exist symmetric positive definite matrices  $P, U, G_0, G_1, H_0, H_1$ , and diagonal positive definite matrices  $D_i, i = 0, 1$  satisfying the following LMIs

$$\begin{bmatrix} W_{11} & W_{12} & W_{13} & W_{14} & W_{15} \\ * & W_{22} & W_{23} & W_{24} & W_{25} \\ * & * & W_{33} & W_{34} & W_{35} \\ * & * & * & W_{44} & W_{45} \\ * & * & * & * & W_{55} \end{bmatrix} < 0, \quad (6)$$

$$\begin{bmatrix} -PA - A^T P - \sum_{i=0}^1 e^{-2\alpha h_i} H_i & 2PF & PQ_1 \\ * & -D_0 & 0 \\ * & * & -Q_1^{-1} \end{bmatrix} < 0, \quad (7)$$

$$\begin{bmatrix} W_1 D_1 W_1^T - e^{-2\alpha h_1} U & 2PE & PQ_2 \\ * & -D_1 & 0 \\ * & * & -Q_2^{-1} \end{bmatrix} < 0, \quad (8)$$

then

$$u(t) = -\frac{1}{2} B^T P^{-1} x(t), \quad t \geq 0. \quad (9)$$

is a guaranteed cost control and the guaranteed cost value is given by

$$J^* = \lambda_2 \|\phi\|^2.$$

Moreover, the solution  $x(t, \phi)$  of the system satisfies

$$\|x(t, \phi)\| \leq \sqrt{\frac{\lambda_1}{\lambda_2}} e^{-\alpha t} \|\phi\|, \quad \forall t \geq 0.$$

*Proof.* Let  $Y = P^{-1}$ ,  $y(t) = Yx(t)$ . Using the feedback control (2.5) we consider the following Lyapunov-Krasovskii functional

$$V(t, x_t) = \sum_{i=1}^6 V_i(t, x_t),$$

$$V_1 = x^T(t) Y x(t),$$

$$V_2 = \int_{t-h_0}^t e^{2\alpha(s-t)} x^T(s) Y G_0 Y x(s) ds,$$

$$V_3 = \int_{t-h_1}^t e^{2\alpha(s-t)} x^T(s) Y G_1 Y x(s) ds,$$

$$V_4 = h_0 \int_{-h_0}^0 \int_{t+s}^t e^{2\alpha(\tau-t)} \dot{x}^T(\tau) Y H_0 Y \dot{x}(\tau) d\tau ds,$$

$$V_5 = h_1 \int_{-h_1}^0 \int_{t+s}^t e^{2\alpha(\tau-t)} \dot{x}^T(\tau) Y H_1 Y \dot{x}(\tau) d\tau ds,$$

$$V_6 = (h_1 - h_0) \int_{t-h_1}^{t-h_0} \int_{t+s}^t e^{2\alpha(\tau-t)} \dot{x}^T(\tau) Y U Y \dot{x}(\tau) d\tau ds.$$



6 G. Rajchakit  
It easy to check that

$$\lambda_1 \|x(t)\|^2 \leq V(t, x_t) \leq \lambda_2 \|x_t\|^2, \quad \forall t \geq 0, \quad (10)$$

Taking the derivative of  $V_1$  we have

$$\begin{aligned} \dot{V}_1 &= 2x^T(t)Y\dot{x}(t) \\ &= y^T(t)[-PA^T - AP]y(t) - y^T(t)BB^T y(t) \\ &\quad + 2y^T(t)W_0f(\cdot)y(t) + 2y^T(t)W_1g(\cdot)y(t) \\ \dot{V}_2 &= y^T(t)G_0y(t) - e^{-2\alpha h_0}y^T(t-h_0)G_0y(t-h_0) - 2\alpha V_2; \\ \dot{V}_3 &= y^T(t)G_1y(t) - e^{-2\alpha h_1}y^T(t-h_1)G_1y(t-h_1) - 2\alpha V_3; \\ \dot{V}_4 &= h_0^2\dot{y}^T(t)H_0\dot{y}(t) - h_1e^{-2\alpha h_0} \int_{t-h_0}^t \dot{x}^T(s)H_0\dot{x}(s) ds - 2\alpha V_4; \\ \dot{V}_5 &= h_1^2\dot{y}^T(t)H_1\dot{y}(t) - h_1e^{-2\alpha h_1} \int_{t-h_1}^t \dot{y}^T(s)H_1\dot{y}(s) ds - 2\alpha V_4; \\ \dot{V}_6 &= (h_1-h_0)^2\dot{y}^T(t)U\dot{y}(t) - (h_1-h_0)e^{-2\alpha h_1} \int_{t-h_1}^{t-h_0} \dot{y}^T(s)U\dot{y}(s) ds - 2\alpha V_6. \end{aligned}$$

Applying Proposition 2.2 and the Leibniz - Newton formula

$$\int_s^t \dot{y}(\tau)d\tau = y(t) - y(s),$$

we have for  $j = 1, 2, i = 0, 1$  :

$$\begin{aligned} -h_i \int_{t-h_i}^t \dot{y}^T(s)H_j\dot{y}(s) ds &\leq -\left[\int_{t-h_i}^t \dot{y}(s) ds\right]^T H_j \left[\int_{t-h_i}^t \dot{y}(s) ds\right] \\ &\leq -[y(t) - y(t-h(t))]^T H_j [y(t) - y(t-h(t))] \quad (11) \\ &= -y^T(t)H_i y(t) + 2x^T(t)H_j y(t-h(t)) \\ &\quad - y^T(t-h_i)H_j y(t-h_i); \end{aligned}$$

Note that

$$\int_{t-h_1}^{t-h_0} \dot{y}^T(s)U\dot{y}(s) ds = \int_{t-h_1}^{t-h(t)} \dot{y}^T(s)U\dot{y}(s) ds + \int_{t-h(t)}^{t-h_0} \dot{y}^T(s)U\dot{y}(s) ds.$$

Applying Proposition 2.2 gives

$$\begin{aligned} [h_1-h(t)] \int_{t-h_1}^{t-h(t)} \dot{y}^T(s)U\dot{y}(s) ds &\geq \left[\int_{t-h_1}^{t-h(t)} \dot{y}(s) ds\right]^T U \left[\int_{t-h_1}^{t-h(t)} \dot{y}(s) ds\right] \\ &\geq [y(t-h(t)) - y(t-h_1)]^T U [y(t-h(t)) - y(t-h_1)] \end{aligned}$$

Since  $h_1 - h(t) \leq h_1 - h_0$ , we have

$$[h_1-h_0] \int_{t-h_1}^{t-h(t)} \dot{y}^T(s)U\dot{y}(s) ds \geq [y(t-h(t)) - y(t-h_1)]^T U [y(t-h(t)) - y(t-h_1)],$$



then

$$-[h_1-h_0] \int_{t-h_1}^{t-h(t)} \dot{y}^T(s)U\dot{y}(s)ds \leq -[y(t-h(t))-y(t-h_1)]^T U[y(t-h(t))-y(t-h_1)].$$

Similarly, we have

$$-(h_1-h_0) \int_{t-h(t)}^{t-h_0} \dot{y}^T(s)U\dot{y}(s) ds \leq -[y(t-h_0)-y(t-h(t))]^T U[y(t-h_0)-y(t-h(t))].$$

Then, we have

$$\begin{aligned} \dot{V}(\cdot) + 2\alpha V(\cdot) &\leq y^T(t)[-PA^T - AP]y(t) - y^T(t)BB^T y(t) + 2y^T(t)W_0f(\cdot) \\ &\quad + 2y^T(t)W_1g(\cdot) + y^T(t)\left(\sum_{i=0}^1 G_i\right)y(t) + 2\alpha\langle Py(t), y(t)\rangle \\ &\quad + \dot{y}^T(t)\left(\sum_{i=0}^1 h_i^2 H_i\right)\dot{y}(t) + (h_1 - h_0)\dot{y}^T(t)U\dot{y}(t) \\ &\quad - \sum_{i=0}^1 e^{-2\alpha h_i} y^T(t - h_i)G_i y(t - h_i) \\ &\quad - e^{-2\alpha h_0} [y(t) - y(t - h_0)]^T H_0 [y(t) - y(t - h_0)] \\ &\quad - e^{-2\alpha h_1} [y(t) - y(t - h_1)]^T H_1 [y(t) - y(t - h_1)] \\ &\quad - e^{-2\alpha h_1} [y(t - h(t)) - y(t - h_1)]^T U [y(t - h(t)) - y(t - h_1)] \\ &\quad - e^{-2\alpha h_1} [y(t - h_0) - y(t - h(t))]^T U [y(t - h_0) - y(t - h(t))]. \end{aligned} \tag{12}$$

Using the equation (1)

$$P\dot{y}(t) + APy(t) - W_0f(\cdot) - W_1g(\cdot) + 0.5BB^T y(t) = 0,$$

and multiplying both sides with  $[2y(t), -2\dot{y}(t), 2y(t - h_0), 2y(t - h_1), y(t - h(t))]^T$ , we have

$$\begin{aligned} 2y^T(t)P\dot{y}(t) + 2y^T(t)APy(t) - 2y^T(t)W_0f(\cdot) - 2y^T(t)W_1g(\cdot) \\ \quad + y^T(t)BB^T y(t) = 0, \\ -2\dot{y}^T(t)P\dot{y}(t) - 2\dot{y}^T(t)APy(t) + 2\dot{y}^T(t)W_0f(\cdot) \\ \quad + 2\dot{y}^T(t)W_1g(\cdot) - \dot{y}^T(t)BB^T y(t) = 0, \\ 2y^T(t-h_0)P\dot{y}(t) + 2y^T(t-h_0)APy(t) - 2y^T(t-h_0)W_0f(\cdot) \\ \quad - 2y^T(t-h_0)W_1g(\cdot) + y^T(t-h_0)BB^T y(t) = 0, \\ 2y^T(t-h_1)P\dot{y}(t) + 2y^T(t-h_1)APy(t) - 2y^T(t-h_1)W_0f(\cdot) \\ \quad - 2y^T(t-h_1)W_1g(\cdot) + y^T(t-h_1)BB^T y(t) = 0, \\ 2y^T(t-h(t))P\dot{y}(t) + 2y^T(t-h(t))APy(t) - 2y^T(t-h(t))W_0f(\cdot) \\ \quad - 2y^T(t-h(t))W_1g(\cdot) + y^T(t-h(t))BB^T y(t) = 0. \end{aligned} \tag{13}$$



8 G. Rajchakit

Adding all the zero items of (13) and  $f^0(t, x(t), x(t-h(t)), u(t)) - f^0(t, x(t), x(t-h(t)), u(t)) = 0$ , respectively into (12) and using the condition (4) for the following estimations

$$\begin{aligned} f^0(t, x(t), x(t-h(t)), u(t)) &\leq \langle Q_1 x(t), x(t) \rangle + \langle Q_2 x(t-h(t)), x(t-h(t)) \rangle \\ &\quad + \langle Ru(t), u(t) \rangle \\ &= \langle PQ_1 P y(t), y(t) \rangle + \langle PQ_2 P y(t-h(t)), y(t-h(t)) \rangle \\ &\quad + 0.25 \langle BRB^T y(t), y(t) \rangle \\ 2 \langle W_0 f(x), y \rangle &\leq \langle W_0 D_0 W_0^T y, y \rangle + \langle D_0^{-1} f(x), f(x) \rangle, \\ 2 \langle W_1 g(z), y \rangle &\leq \langle W_1 D_1 W_1^T y, y \rangle + \langle D_1^{-1} g(z), g(z) \rangle, \\ 2 \langle D_0^{-1} f(x), f(x) \rangle &\leq \langle F D_0^{-1} F x, x \rangle, \\ 2 \langle D_1^{-1} g(z), g(z) \rangle &\leq \langle E D_1^{-1} E z, z \rangle, \end{aligned}$$

we obtain

$$\begin{aligned} \dot{V}(\cdot) + 2\alpha V(\cdot) &\leq \zeta^T(t) \mathcal{E} \zeta(t) + y^T(t) S_1 y(t) + y^T(t-h(t)) S_2 y(t-h(t)) \\ &\quad - f^0(t, x(t), x(t-h(t)), u(t)) \end{aligned} \quad (14)$$

where  $\zeta(t) = [y(t), \dot{y}(t), y(t-h_0), y(t-h_1), y(t-h(t)), f(\cdot), g(\cdot)]$ , and

$$\mathcal{E} = \begin{bmatrix} W_{11} & W_{12} & W_{13} & W_{14} & W_{15} \\ * & W_{22} & W_{23} & W_{24} & W_{25} \\ * & * & W_{33} & W_{34} & W_{35} \\ * & * & * & W_{44} & W_{45} \\ * & * & * & * & W_{55} \end{bmatrix}$$

$$S_1 = -PA - A^T P - \sum_{i=0}^1 e^{-2\alpha h_i} H_i + 4PF D_0^{-1} F P + P Q_1 P,$$

$$S_2 = W_1 D_1 W_1^T - e^{-2\alpha h_2} U + 4PE D_1^{-1} E P + P Q_2 P.$$

Note that by the Schur complement lemma, Proposition 2.1, the conditions  $S_1 < 0$  and  $S_2 < 0$  are equivalent to the conditions (7) and (8), respectively. Therefore, by condition (6), (7), (8), we obtain from (14) that

$$\dot{V}(t, x_t) \leq -2\alpha V(t, x_t), \quad \forall t \geq 0. \quad (15)$$

Integrating both sides of (15) from 0 to  $t$ , we obtain

$$V(t, x_t) \leq V(\phi) e^{-2\alpha t}, \quad \forall t \geq 0.$$

Furthermore, taking condition (3.5) into account, we have

$$\lambda_1 \|x(t, \phi)\|^2 \leq V(x_t) \leq V(\phi) e^{-2\alpha t} \leq \lambda_2 e^{-2\alpha t} \|\phi\|^2,$$

then

$$\|x(t, \phi)\| \leq \sqrt{\frac{\lambda_2}{\lambda_1}} e^{-\alpha t} \|\phi\|, \quad t \geq 0,$$



Guaranteed cost control for Hopfield neural networks 9  
which concludes the exponential stability of the closed-loop system (5). To prove the optimal level of the cost function (3), we derive from (14) and (6) - (8) that

$$\dot{V}(t, z_t) \leq -f^0(t, x(t), x(t-h(t)), u(t)), \quad t \geq 0. \quad (16)$$

Integrating both sides of (16) from 0 to  $t$  leads to

$$\int_0^t f^0(t, x(t), x(t-h(t)), u(t))dt \leq V(0, z_0) - V(t, z_t) \leq V(0, z_0),$$

due to  $V(t, z_t) \geq 0$ . Hence, letting  $t \rightarrow +\infty$ , we have

$$J = \int_0^\infty f^0(t, x(t), x(t-h(t)), u(t))dt \leq V(0, z_0) \leq \lambda_2 \|\phi\|^2 = J^*.$$

This completes the proof of the theorem.

## 4 Conclusions

In this paper, the problem of guaranteed cost control for Hopfield neural networks with interval nondifferentiable time-varying delay has been studied. A nonlinear quadratic cost function is considered as a performance measure for the closed-loop system. The stabilizing controllers to be designed must satisfy some exponential stability constraints on the closed-loop poles. By constructing a set of time-varying Lyapunov-Krasovskii functional combined with Newton-Leibniz formula, a memoryless state feedback guaranteed cost controller design has been presented and sufficient conditions for the existence of the guaranteed cost state-feedback for the system have been derived in terms of LMIs.

**Acknowledgements.** This work was supported by the National Foundation for Science and Technology Development, Vietnam and the Thailand Research Fund Grant.

## References

- 1.Hopfield J.J., "Neural networks and physical systems with emergent collective computational abilities," *Proc. Natl. Acad. Sci. USA*, **79**(1982), 2554-2558.
2. Kevin G., *An Introduction to Neural Networks*, CRC Press, 1997.
3. Wu M., He Y., She J.H., *Stability Analysis and Robust Control of Time-Delay Systems*, Springer, 2010.
4. Arik S., An improved global stability result for delayed cellular neural networks, *IEEE Trans. Circ. Syst.* **499**(2002), 1211-1218.
5. He Y., Wang Q.G., M. Wu, LMI-based stability criteria for neural networks with multiple time-varying delays, *Physica D*, **112**(2005), 126-131.
6. Kwon O.M., J.H. Park, Exponential stability analysis for uncertain neural networks with interval time-varying delays. *Appl. Math. Comput.*, **212**(2009), 530541.
7. Phat V.N., Trinh H. , Exponential stabilization of neural networks with various activation functions and mixed time-varying delays, *IEEE Trans. Neural Networks*, **21**(2010), 1180-1185.



- 10 G. Rajchakit
8. Botmart T. and P. Niamsup, Robust exponential stability and stabilizability of linear parameter dependent systems with delays, *Appl. Math. Comput.*, **217**(2010), 2551-2566.
9. W.H. Chen W.H., Guan Z.H., Lua X., Delay-dependent output feedback guaranteed cost control for uncertain time-delay systems, *Automatica*, **40**(2004), 1263 - 1268.
10. Palarkci M.N., Robust delay-dependent guaranteed cost controller design for uncertain neutral systems, *Appl. Math. Computations*, **215**(2009), 2939-2946.
11. Park J.H., Kwon O.M., On guaranteed cost control of neutral systems by retarded integral state feedback, *Applied Mathematics and Computation*, **165**(2005), 393-404.
12. Park J.H., Choi K., Guaranteed cost control of nonlinear neutral systems via memory state feedback, *Chaos, Fractals and Solitons*, **24**(2005), 183-190.
13. Fridman E., Orlov Y., Exponential stability of linear distributed parameter systems with time-varying delays. *Automatica*, **45**(2009), 194201.
14. Xu S., Lam J., A survey of linear matrix inequality techniques in stability analysis of delay systems. *Int. J. Syst. Sci.*, **39**(2008), 12, 10951113.
15. Xie J.S., Fan B.Q., Young S.L., Yang J., Guaranteed cost controller design of networked control systems with state delay, *Acta Automatica Sinica*, **33**(2007), 170-174.
16. Yu L., Gao F., Optimal guaranteed cost control of discrete-time uncertain systems with both state and input delays, *Journal of the Franklin Institute*, **338**(2001), 101-110.
17. Boyd S., Ghaoui L. El, Feron E., and V. Balakrishnan, *Linear Matrix Inequalities in System and Control Theory*, Philadelphia: SIAM, 1994.
18. Gu K., Kharitonov V., Chen J., *Stability of Time-delay Systems*, Birkhauser, Berlin, 2003.





# Delay-dependent optimal guaranteed cost control of stochastic neural networks with interval nondifferentiable time-varying delays

M. Rajchakit

Major of Statistics, Faculty of Science, Maejo University, Chiangmai, 50290,  
Thailand  
(E-mail: manlika@mju.ac.th)

**Abstract.** This paper studies the problem of guaranteed cost control for a class of stochastic delayed neural networks. The time delay is a continuous function belonging to a given interval, but not necessary to be differentiable. A cost function is considered as a nonlinear performance measure for the closed-loop system. The stabilizing controllers to be designed must satisfy some mean square exponential stability constraints on the closed-loop poles. By constructing a set of argumented Lyapunov-Krasovskii functionals combined with Newton-Leibniz formula, a guaranteed cost controller is designed via memoryless state feedback control and new sufficient conditions for the existence of the guaranteed cost state-feedback for the system are given in terms of linear matrix inequalities (LMIs). A numerical example is given to illustrate the effectiveness of the obtained result.

*Keywords:* stochastic neural networks, guaranteed cost control, mean square stabilization, interval time-varying delays, Lyapunov function, linear matrix inequalities

## 1 Introduction

Stability and control of neural networks with time delay has been attracted considerable attention in recent years [1-8]. In many practical systems, it is desirable to design neural networks which are not only asymptotically or exponentially stable but can also guarantee an adequate level of system performance. In the area of control, signal processing, pattern recognition and image processing, delayed neural networks have many useful applications. Some of these applications require that the equilibrium points of the designed network be stable. In both biological and artificial neural systems, time delays due to integration and communication are ubiquitous and often become a source of instability. The time delays in electronic neural networks are usually time-varying, and sometimes vary violently with respect to time due to the finite switching speed of amplifiers and faults in the electrical circuitry. Guaranteed cost control problem [9-12] has the advantage of providing an upper bound on a given system performance index and thus the system performance degradation incurred by the uncertainties or time delays is guaranteed to be less than this bound. The Lyapunov-Krasovskii functional technique has been among the popular and effective tool in the design of guaranteed cost controls for neural networks with time delay. Nevertheless, despite such diversity of results available, most existing work either assumed that the time delays are constant



2 M. Rajchakit

or differentiable [13-16]. Although, in some cases, delay-dependent guaranteed cost control for systems with time-varying delays were considered in [12, 13, 15], the approach used there can not be applied to systems with interval, non-differentiable time-varying delays. To the best of our knowledge, the guaranteed cost control and state feedback stabilization for stochastic neural networks with interval, non-differentiable time-varying delays have not been fully studied yet (see, e.g., [4-16] and the references therein), which are important in both theories and applications. This motivates our research.

In this paper, we investigate the guaranteed cost control for stochastic delayed neural networks problem. The novel features here are that the delayed neural network under consideration is with various globally Lipschitz continuous activation functions, and the time-varying delay function is interval, non-differentiable. A nonlinear cost function is considered as a performance measure for the closed-loop system. The stabilizing controllers to be designed must satisfy some mean square exponential stability constraints on the closed-loop poles. Based on constructing a set of augmented Lyapunov-Krasovskii functionals combined with Newton-Leibniz formula, new delay-dependent criteria for guaranteed cost control via memoryless feedback control is established in terms of LMIs, which allow simultaneous computation of two bounds that characterize the mean square exponential stability rate of the solution and can be easily determined by utilizing MATLABs LMI Control Toolbox.

The outline of the paper is as follows. Section 2 presents definitions and some well-known technical propositions needed for the proof of the main result. LMI delay-dependent criteria for guaranteed cost control and a numerical example showing the effectiveness of the result are presented in Section 3. The paper ends with conclusions and cited references.

## 2 Preliminaries

The following notation will be used in this paper.  $\mathbb{R}^+$  denotes the set of all real non-negative numbers;  $\mathbb{R}^n$  denotes the  $n$ -dimensional space with the scalar product  $\langle x, y \rangle$  or  $x^T y$  of two vectors  $x, y$ , and the vector norm  $\| \cdot \|$ ;  $M^{n \times r}$  denotes the space of all matrices of  $(n \times r)$ -dimensions.  $A^T$  denotes the transpose of matrix  $A$ ;  $A$  is symmetric if  $A = A^T$ ;  $I$  denotes the identity matrix;  $\lambda(A)$  denotes the set of all eigenvalues of  $A$ ;  $\lambda_{\max}(A) = \max\{\text{Re}\lambda; \lambda \in \lambda(A)\}$ .  $x_t := \{x(t+s) : s \in [-h, 0]\}$ ,  $\|x_t\| = \sup_{s \in [-h, 0]} \|x(t+s)\|$ ;  $C^1([0, t], \mathbb{R}^n)$  denotes the set of all  $\mathbb{R}^n$ -valued continuously differentiable functions on  $[0, t]$ ;  $L_2([0, t], \mathbb{R}^m)$  denotes the set of all the  $\mathbb{R}^m$ -valued square integrable functions on  $[0, t]$ ;

Matrix  $A$  is called semi-positive definite ( $A \geq 0$ ) if  $\langle Ax, x \rangle \geq 0$ , for all  $x \in \mathbb{R}^n$ ;  $A$  is positive definite ( $A > 0$ ) if  $\langle Ax, x \rangle > 0$  for all  $x \neq 0$ ;  $A > B$  means  $A - B > 0$ . The notation  $\text{diag}\{\dots\}$  stands for a block-diagonal matrix. The symmetric term in a matrix is denoted by  $*$ .



Consider the following stochastic neural networks with interval time-varying delay:

$$\begin{aligned} \dot{x}(t) &= -Ax(t) + W_0f(x(t)) + W_1g(x(t-h(t))) + Bu(t) + \sigma(x(t), x(t-h(t)), t)\omega(t), \quad t \geq 0, \\ x(t) &= \phi(t), t \in [-h_1, 0], \end{aligned} \quad (1)$$

where  $x(t) = [x_1(t), x_2(t), \dots, x_n(t)]^T \in \mathbb{R}^n$  is the state of the neural,  $u(\cdot) \in L_2([0, t], \mathbb{R}^m)$  is the control;  $n$  is the number of neurals, and

$$\begin{aligned} f(x(t)) &= [f_1(x_1(t)), f_2(x_2(t)), \dots, f_n(x_n(t))]^T, \\ g(x(t)) &= [g_1(x_1(t)), g_2(x_2(t)), \dots, g_n(x_n(t))]^T, \end{aligned}$$

are the activation functions;  $A = \text{diag}(\bar{a}_1, \bar{a}_2, \dots, \bar{a}_n)$ ,  $\bar{a}_i > 0$  represents the self-feedback term;  $B \in \mathbb{R}^{n \times m}$  is control input matrix;  $W_0, W_1$  denote the connection weights, the discretely delayed connection weights and the distributively delayed connection weight.

$\omega(t)$  is a scalar Wiener process (Brownian Motion) on  $(\Omega, \mathcal{F}, \mathcal{P})$  with

$$E\{\omega(t)\} = 0, \quad E\{\omega^2(t)\} = t, \quad E\{\omega(i)\omega(j)\} = 0 (i \neq j), \quad (2)$$

and  $\sigma: \mathbb{R}^n \times \mathbb{R}^n \times \mathbb{R} \rightarrow \mathbb{R}^n$  is the continuous function, and is assumed to satisfy that

$$\begin{aligned} \sigma^T(x(t), x(t-h(t)), t)\sigma(x(t), x(t-h(t)), t) &\leq \rho_1 x^T(t)x(t) + \rho_2 x^T(t-h(t))x(t-h(t)), \\ x(t), x(t-h(t)) &\in \mathbb{R}^n, \end{aligned} \quad (3)$$

where  $\rho_1 > 0$  and  $\rho_2 > 0$  are known constant scalars. For simplicity, we denote  $\sigma(x(t), x(t-h(t)), t)$  by  $\sigma$ , respectively.

The time-varying delay function  $h(t)$  satisfies the condition

$$0 \leq h_0 \leq h(t) \leq h_1.$$

The initial functions  $\phi(t) \in C^1([-h_1, 0], \mathbb{R}^n)$ , with the norm

$$\|\phi\| = \sup_{t \in [-h_1, 0]} \sqrt{\|\phi(t)\|^2 + \|\dot{\phi}(t)\|^2}.$$

In this paper, we consider various activation functions and assume that the activation functions  $f(\cdot), g(\cdot)$  are Lipschitzian with the Lipschitz constants  $f_i, e_i > 0$ :

$$\begin{aligned} |f_i(\xi_1) - f_i(\xi_2)| &\leq f_i |\xi_1 - \xi_2|, \quad i = 1, 2, \dots, n, \forall \xi_1, \xi_2 \in \mathbb{R}, \\ |g_i(\xi_1) - g_i(\xi_2)| &\leq e_i |\xi_1 - \xi_2|, \quad i = 1, 2, \dots, n, \forall \xi_1, \xi_2 \in \mathbb{R}. \end{aligned} \quad (4)$$

The performance index associate with the system (1) is the following function

$$J = \int_0^\infty f^0(t, x(t), x(t-h(t)), u(t)) dt, \quad (5)$$



4 M. Rajchakit  
where  $f^0(t, x(t), x(t-h(t)), u(t)) : R^+ \times R^n \times R^n \times R^m \rightarrow R^+$ , is a nonlinear cost function satisfies

$$\exists Q_1, Q_2, R : f^0(t, x, y, u) \leq \langle Q_1 x, x \rangle + \langle Q_2 y, y \rangle + \langle Ru, u \rangle, \quad (6)$$

for all  $(t, x, u) \in R^+ \times R^n \times R^m$  and  $Q_1, Q_2 \in R^{n \times n}$ ,  $R \in R^{m \times m}$ , are given symmetric positive definite matrices. The objective of this paper is to design a memoryless state feedback controller  $u(t) = Kx(t)$  for system (1) and the cost function (5) such that the resulting closed-loop system

$$\dot{x}(t) = -(A-BK)x(t) + W_0 f(x(t)) + W_1 g(x(t-h(t))) + \sigma(x(t), x(t-h(t)), t) \omega(t), \quad (7)$$

is mean square exponentially stable and the closed-loop value of the cost function (5) is minimized.

*Definition 2.1* Given  $\alpha > 0$ . The zero solution of closed-loop system (7) is  $\alpha$ -exponentially stabilizable in the mean square if there exist a positive number  $N > 0$  such that every solution  $x(t, \phi)$  satisfies the following condition:

$$E \{ \| x(t, \phi) \| \} \leq E \{ N e^{-\alpha t} \| \phi \| \}, \quad \forall t \geq 0.$$

*Definition 2.2* Consider the control system (1). If there exist a memoryless state feedback control law  $u^*(t) = Kx(t)$  and a positive number  $J^*$  such that the zero solution of the closed-loop system (7) is mean square exponentially stable and the cost function (5) satisfies  $J \leq J^*$ , then the value  $J^*$  is a guaranteed constant and  $u^*(t)$  is a guaranteed cost control law of the system and its corresponding cost function.

We introduce the following technical well-known propositions, which will be used in the proof of our results.

*Proposition 2.1.* (Integral matrix inequality [17]). For any symmetric positive definite matrix  $M > 0$ , scalar  $\gamma > 0$  and vector function  $\omega : [0, \gamma] \rightarrow \mathbb{R}^n$  such that the integrations concerned are well defined, the following inequality holds

$$\left( \int_0^\gamma \omega(s) ds \right)^T M \left( \int_0^\gamma \omega(s) ds \right) \leq \gamma \left( \int_0^\gamma \omega^T(s) M \omega(s) ds \right)$$



### 3 Design of guaranteed cost controller

In this section, we give a design of memoryless guaranteed feedback cost control for stochastic neural networks (1). Let us set

$$\begin{aligned}
 W_{11} &= -AP - PA^T - 2\alpha P - BB^T + 0.25BBB^T + \sum_{i=0}^1 G_i - \sum_{i=0}^1 e^{-2\alpha h_i} H_i \\
 &\quad + 4PFD_0^{-1}FP + PQ_1P + 2\rho_1PP, \\
 W_{12} &= P + AP + 0.5BB^T, \\
 W_{13} &= e^{-2\alpha h_0} H_0 + 0.5BB^T + AP, \\
 W_{14} &= 2e^{-2\alpha h_1} H_1 + 0.5BB^T + AP, \\
 W_{15} &= P0.5BB^T + AP, \\
 W_{22} &= \sum_{i=0}^1 W_i D_i W_i^T + \sum_{i=0}^1 h_i^2 H_i + (h_1 - h_0)U - 2P - BB^T, \\
 W_{23} &= P, \quad W_{24} = P, \quad W_{25} = P, \\
 W_{33} &= -e^{-2\alpha h_0} G_0 - e^{-2\alpha h_0} H_0 - e^{-2\alpha h_1} U + \sum_{i=0}^1 W_i D_i W_i^T, \\
 W_{34} &= 0, \quad W_{35} = e^{-2\alpha h_1} U, \\
 W_{44} &= \sum_{i=0}^1 W_i D_i W_i^T - e^{-2\alpha h_1} U - e^{-2\alpha h_1} G_1 - e^{-2\alpha h_1} H_1, \quad W_{45} = e^{-2\alpha h_1} U, \\
 W_{55} &= -e^{-2\alpha h_1} U + \sum_{i=0}^1 W_i D_i W_i^T - e^{-2\alpha h_2} U + 4PED_1^{-1}EP + PQ_2P + 2\rho_2PP, \\
 E &= \text{diag}\{e_i, i = 1, \dots, n\}, \quad F = \text{diag}\{f_i, i = 1, \dots, n\}, \\
 \lambda_1 &= \lambda_{\min}(P^{-1}), \\
 \lambda_2 &= \lambda_{\max}(P^{-1}) + h_0 \lambda_{\max}[P^{-1}(\sum_{i=0}^1 G_i)P^{-1}] \\
 &\quad + h_1^2 \lambda_{\max}[P^{-1}(\sum_{i=0}^1 H_i)P^{-1}] + (h_1 - h_0) \lambda_{\max}(P^{-1}UP^{-1}).
 \end{aligned}$$

**Theorem 3.1.** Consider control system (1) and the cost function (5). If there exist symmetric positive definite matrices  $P, U, G_0, G_1, H_0, H_1$ , and diagonal positive definite matrices  $D_i, i = 0, 1$  satisfying the following LMIs

$$\begin{bmatrix}
 W_{11} & W_{12} & W_{13} & W_{14} & W_{15} \\
 * & W_{22} & W_{23} & W_{24} & W_{25} \\
 * & * & W_{33} & W_{34} & W_{35} \\
 * & * & * & W_{44} & W_{45} \\
 * & * & * & * & W_{55}
 \end{bmatrix} < 0, \quad (8)$$



6 M. Rajchakit  
then

$$u(t) = -\frac{1}{2}B^T P^{-1}x(t), \quad t \geq 0. \quad (9)$$

is a guaranteed cost control and the guaranteed cost value is given by

$$J^* = E \{ \lambda_2 \|\phi\|^2 \}.$$

Moreover, the solution  $x(t, \phi)$  of the system satisfies

$$E \{ \|x(t, \phi)\| \} \leq E \left\{ \sqrt{\frac{\lambda_2}{\lambda_1}} e^{-\alpha t} \|\phi\| \right\}, \quad \forall t \geq 0.$$

*Proof.* Let  $Y = P^{-1}$ ,  $y(t) = Yx(t)$ . Using the feedback control (7) we consider the following Lyapunov-Krasovskii functional and taking the mathematical expectation

$$E \{ V(t, x_t) \} = E \left\{ \sum_{i=1}^6 V_i(t, x_t) \right\},$$

$$E \{ V_1 \} = E \{ x^T(t) Y x(t) \},$$

$$E \{ V_2 \} = E \left\{ \int_{t-h_0}^t e^{2\alpha(s-t)} x^T(s) Y G_0 Y x(s) ds \right\},$$

$$E \{ V_3 \} = E \left\{ \int_{t-h_1}^t e^{2\alpha(s-t)} x^T(s) Y G_1 Y x(s) ds \right\},$$

$$E \{ V_4 \} = E \left\{ h_0 \int_{-h_0}^0 \int_{t+s}^t e^{2\alpha(\tau-t)} \dot{x}^T(\tau) Y H_0 Y \dot{x}(\tau) d\tau ds \right\},$$

$$E \{ V_5 \} = E \left\{ h_1 \int_{-h_1}^0 \int_{t+s}^t e^{2\alpha(\tau-t)} \dot{x}^T(\tau) Y H_1 Y \dot{x}(\tau) d\tau ds \right\},$$

$$E \{ V_6 \} = E \left\{ (h_1 - h_0) \int_{t-h_1}^{t-h_0} \int_{t+s}^t e^{2\alpha(\tau-t)} \dot{x}^T(\tau) Y U Y \dot{x}(\tau) d\tau ds \right\}.$$

It easy to check that

$$E \{ \lambda_1 \|x(t)\|^2 \} \leq E \{ V(t, x_t) \} \leq E \{ \lambda_2 \|x_t\|^2 \}, \quad \forall t \geq 0, \quad (10)$$



Taking the derivative of  $V_i, i = 1, 2, \dots, 6$  and taking the mathematical expectation, we have

$$\begin{aligned}
 E \left\{ \dot{V}_1 \right\} &= E \left\{ 2x^T(t)Y\dot{x}(t) \right\} \\
 &= E \left\{ y^T(t)[-PA^T - AP]y(t) - y^T(t)BB^T y(t) \right\} \\
 &\quad + E \left\{ 2y^T(t)W_0f(\cdot) + 2y^T(t)W_1g(\cdot) + 2y^T(t)\sigma\omega(t) \right\}; \\
 E \left\{ \dot{V}_2 \right\} &= E \left\{ E \left\{ y^T(t)G_0y(t) - e^{-2\alpha h_0}y^T(t-h_0)G_0y(t-h_0) - 2\alpha V_2 \right\} \right\}; \\
 E \left\{ \dot{V}_3 \right\} &= E \left\{ y^T(t)G_1y(t) - e^{-2\alpha h_1}y^T(t-h_1)G_1y(t-h_1) - 2\alpha V_3 \right\}; \\
 E \left\{ \dot{V}_4 \right\} &= E \left\{ h_0^2\dot{y}^T(t)H_0\dot{y}(t) - h_1e^{-2\alpha h_0} \int_{t-h_0}^t \dot{x}^T(s)H_0\dot{x}(s) ds - 2\alpha V_4 \right\}; \\
 E \left\{ \dot{V}_5 \right\} &= E \left\{ h_1^2\dot{y}^T(t)H_1\dot{y}(t) - h_1e^{-2\alpha h_1} \int_{t-h_1}^t \dot{y}^T(s)H_1\dot{y}(s) ds - 2\alpha V_4 \right\}; \\
 E \left\{ \dot{V}_6 \right\} &= E \left\{ (h_1 - h_0)^2\dot{y}^T(t)U\dot{y}(t) - (h_1 - h_0)e^{-2\alpha h_1} \int_{t-h_1}^{t-h_0} \dot{y}^T(s)U\dot{y}(s) ds - 2\alpha V_6 \right\}.
 \end{aligned}$$

Applying Proposition 2.1 and the Leibniz - Newton formula

$$\int_s^t \dot{y}(\tau)d\tau = y(t) - y(s),$$

we have for  $i, j = 0, 1, :$

$$\begin{aligned}
 -E \left\{ h_i \int_{t-h_i}^t \dot{y}^T(s)H_j\dot{y}(s) ds \right\} &\leq -E \left\{ \left[ \int_{t-h_i}^t \dot{y}(s) ds \right]^T H_j \left[ \int_{t-h_i}^t \dot{y}(s) ds \right] \right\} \\
 &\leq -E \left\{ [y(t) - y(t-h(t))]^T H_j [y(t) - y(t-h(t))] \right\} \\
 &= -E \left\{ y^T(t)H_j y(t) + 2x^T(t)H_j y(t-h(t)) \right\} \\
 &\quad - E \left\{ y^T(t-h_i)H_j y(t-h_i) \right\}.
 \end{aligned} \tag{11}$$

Note that

$$E \left\{ \int_{t-h_1}^{t-h_0} \dot{y}^T(s)U\dot{y}(s) ds \right\} = E \left\{ \int_{t-h_1}^{t-h(t)} \dot{y}^T(s)U\dot{y}(s) ds \right\} + E \left\{ \int_{t-h(t)}^{t-h_0} \dot{y}^T(s)U\dot{y}(s) ds \right\}.$$

Applying Proposition 2.1 gives

$$\begin{aligned}
 E \left\{ [h_1 - h(t)] \int_{t-h_1}^{t-h(t)} \dot{y}^T(s)U\dot{y}(s) ds \right\} &\geq E \left\{ \left[ \int_{t-h_1}^{t-h(t)} \dot{y}(s) ds \right]^T U \left[ \int_{t-h_1}^{t-h(t)} \dot{y}(s) ds \right] \right\} \\
 &\geq E \left\{ [y(t-h(t)) - y(t-h_1)]^T U [y(t-h(t)) - y(t-h_1)] \right\}.
 \end{aligned}$$

Since  $h_1 - h(t) \leq h_1 - h_0$ , we have

$$E \left\{ [h_1 - h_0] \int_{t-h_1}^{t-h(t)} \dot{y}^T(s)U\dot{y}(s) ds \right\} \geq E \left\{ [y(t-h(t)) - y(t-h_1)]^T U [y(t-h(t)) - y(t-h_1)] \right\},$$



8 M. Rajchakit  
then

$$-E \left\{ [h_1 - h_0] \int_{t-h_1}^{t-h(t)} \dot{y}^T(s) U \dot{y}(s) ds \right\} \leq -E \{ [y(t-h(t)) - y(t-h_1)]^T U [y(t-h(t)) - y(t-h_1)] \}.$$

Similarly, we have

$$-E \left\{ (h_1 - h_0) \int_{t-h(t)}^{t-h_0} \dot{y}^T(s) U \dot{y}(s) ds \right\} \leq -E \{ [y(t-h_0) - y(t-h(t))]^T U [y(t-h_0) - y(t-h(t))] \}.$$

Then, we have

$$\begin{aligned} E \{ \dot{V}(\cdot) + 2\alpha V(\cdot) \} &\leq E \{ y^T(t) [-PA^T - AP] y(t) - y^T(t) BB^T y(t) + 2y^T(t) W_0 f(\cdot) \} \\ &+ E \left\{ 2y^T(t) W_1 g(\cdot) + 2y^T(t) \sigma \omega(t) + y^T(t) \left( \sum_{i=0}^1 G_i \right) y(t) + 2\alpha \langle Py(t), y(t) \rangle \right\} \\ &+ E \left\{ \dot{y}^T(t) \left( \sum_{i=0}^1 h_i^2 H_i \right) \dot{y}(t) + (h_1 - h_0) \dot{y}^T(t) U \dot{y}(t) \right\} \\ &- E \left\{ \sum_{i=0}^1 e^{-2\alpha h_i} y^T(t-h_i) G_i y(t-h_i) \right\} \\ &- E \{ e^{-2\alpha h_0} [y(t) - y(t-h_0)]^T H_0 [y(t) - y(t-h_0)] \} \\ &- E \{ e^{-2\alpha h_1} [y(t) - y(t-h_1)]^T H_1 [y(t) - y(t-h_1)] \} \\ &- E \{ e^{-2\alpha h_1} [y(t-h(t)) - y(t-h_1)]^T U [y(t-h(t)) - y(t-h_1)] \} \\ &- E \{ e^{-2\alpha h_1} [y(t-h_0) - y(t-h(t))]^T U [y(t-h_0) - y(t-h(t))] \}. \end{aligned} \tag{12}$$

Using the equation (7)

$$P\dot{y}(t) + APy(t) - W_0 f(\cdot) - W_1 g(\cdot) + 0.5BB^T y(t) - \sigma \omega(t) = 0,$$

and multiplying both sides with  $[2y(t), -2\dot{y}(t), 2y(t-h_0), 2y(t-h_1), 2y(t-h(t)), 2\sigma \omega(t)]^T$ , and taking the mathematical expectation, we have

$$\begin{aligned} E \{ 2y^T(t) P\dot{y}(t) + 2y^T(t) APy(t) - 2y^T(t) W_0 f(\cdot) - 2y^T(t) W_1 g(\cdot) \} \\ + E \{ y^T(t) BB^T y(t) - 2y^T(t) \sigma \omega(t) \} &= 0, \\ -E \{ 2\dot{y}^T(t) P\dot{y}(t) - 2\dot{y}^T(t) APy(t) + 2\dot{y}^T(t) W_0 f(\cdot) \} \\ + E \{ 2\dot{y}^T(t) W_1 g(\cdot) - \dot{y}^T(t) BB^T y(t) + 2\dot{y}^T(t) \sigma \omega(t) \} &= 0, \\ E \{ 2y^T(t-h_0) P\dot{y}(t) + 2y^T(t-h_0) APy(t) - 2y^T(t-h_0) W_0 f(\cdot) \} \\ - E \{ 2y^T(t-h_0) W_1 g(\cdot) + y^T(t-h_0) BB^T y(t) - 2y^T(t-h_0) \sigma \omega(t) \} &= 0, \\ E \{ 2y^T(t-h_1) P\dot{y}(t) + 2y^T(t-h_1) APy(t) - 2y^T(t-h_1) W_0 f(\cdot) \} \\ - E \{ 2y^T(t-h_1) W_1 g(\cdot) + y^T(t-h_1) BB^T y(t) - 2y^T(t-h_1) \sigma \omega(t) \} &= 0, \end{aligned}$$





$$\begin{aligned}
 & E \{ 2y^T(t-h(t))Py(t) + 2y^T(t-h(t))APy(t) - 2y^T(t-h(t))W_0f(\cdot) \} \\
 & \quad - E \{ 2y^T(t-h(t))W_1g(\cdot) + y^T(t-h(t))BB^Ty(t) - 2y^T(t-h(t))\sigma\omega(t) \} = 0, \\
 & E \{ 2\omega^T(t)\sigma^TP\dot{y}(t) + 2\omega^T(t)\sigma^TAPy(t) - 2\omega^T(t)\sigma^TW_0f(\cdot) \} \\
 & \quad - E \{ 2\omega^T(t)\sigma^TW_1g(\cdot) + \omega^T(t)\sigma^TBB^Ty(t) - 2\omega^T(t)\sigma^T\sigma\omega(t) \} = 0.
 \end{aligned} \tag{13}$$

Adding all the zero items of (13) and  $f^0(t, x(t), x(t-h(t)), u(t)) - f^0(t, x(t), x(t-h(t)), u(t)) = 0$ , respectively into (12), applying assumption (2), (3), using the condition (6) for the following estimations and taking the mathematical expectation

$$\begin{aligned}
 E \{ f^0(t, x(t), x(t-h(t)), u(t)) \} & \leq E \{ \langle Q_1x(t), x(t) \rangle + \langle Q_2x(t-h(t)), x(t-h(t)) \rangle \} \\
 & \quad + E \{ \langle Ru(t), u(t) \rangle \} \\
 & = E \{ \langle PQ_1Py(t), y(t) \rangle + \langle PQ_2Py(t-h(t)), y(t-h(t)) \rangle \} \\
 & \quad + E \{ 0.25 \langle BRB^Ty(t), y(t) \rangle \}, \\
 E \{ 2 \langle W_0f(x), y \rangle \} & \leq E \{ \langle W_0D_0W_0^Ty, y \rangle + \langle D_0^{-1}f(x), f(x) \rangle \}, \\
 E \{ 2 \langle W_1g(z), y \rangle \} & \leq E \{ \langle W_1D_1W_1^Ty, y \rangle + \langle D_1^{-1}g(z), g(z) \rangle \}, \\
 E \{ 2 \langle D_0^{-1}f(x), f(x) \rangle \} & \leq E \{ \langle FD_0^{-1}Fx, x \rangle \}, \\
 E \{ 2 \langle D_1^{-1}g(z), g(z) \rangle \} & \leq E \{ \langle ED_1^{-1}Ez, z \rangle \},
 \end{aligned}$$

we obtain

$$E \{ \dot{V}(\cdot) + 2\alpha V(\cdot) \} \leq E \{ \zeta^T(t) \mathcal{E} \zeta(t) - f^0(t, x(t), x(t-h(t)), u(t)) \}, \tag{14}$$

where  $\zeta(t) = [y(t), \dot{y}(t), y(t-h_0), y(t-h_1), y(t-h(t))]$ , and

$$\mathcal{E} = \begin{bmatrix} W_{11} & W_{12} & W_{13} & W_{14} & W_{15} \\ * & W_{22} & W_{23} & W_{24} & W_{25} \\ * & * & W_{33} & W_{34} & W_{35} \\ * & * & * & W_{44} & W_{45} \\ * & * & * & * & W_{55} \end{bmatrix}.$$

Therefore, by condition (8), we obtain from (14) that

$$E \{ \dot{V}(t, x_t) \} \leq -E \{ 2\alpha V(t, x_t) \}, \quad \forall t \geq 0. \tag{15}$$

Integrating both sides of (15) from 0 to  $t$ , we obtain

$$E \{ V(t, x_t) \} \leq E \{ V(\phi) e^{-2\alpha t} \}, \quad \forall t \geq 0.$$

Furthermore, taking condition (10) into account, we have

$$E \{ \lambda_1 \| x(t, \phi) \|^2 \} \leq E \{ V(x_t) \} \leq E \{ V(\phi) e^{-2\alpha t} \} \leq E \{ \lambda_2 e^{-2\alpha t} \| \phi \|^2 \},$$

then

$$E \{ \| x(t, \phi) \| \} \leq E \left\{ \sqrt{\frac{\lambda_2}{\lambda_1}} e^{-\alpha t} \| \phi \| \right\}, \quad t \geq 0,$$



10 M. Rajchakit

which concludes the mean square exponential stability of the closed-loop system (2.7). To prove the optimal level of the cost function (5), we derive from (14) and (8) that

$$E \left\{ \dot{V}(t, z_t) \right\} \leq -E \left\{ f^0(t, x(t), x(t-h(t)), u(t)) \right\}, \quad t \geq 0. \quad (16)$$

Integrating both sides of (18) from 0 to  $t$  leads to

$$E \left\{ \int_0^t f^0(t, x(t), x(t-h(t)), u(t)) dt \right\} \leq E \{ V(0, z_0) - V(t, z_t) \} \leq E \{ V(0, z_0) \},$$

due to  $E \{ V(t, z_t) \} \geq 0$ . Hence, letting  $t \rightarrow +\infty$ , we have

$$J = E \left\{ \int_0^\infty f^0(t, x(t), x(t-h(t)), u(t)) dt \right\} \leq E \{ V(0, z_0) \} \leq E \{ \lambda_2 \|\phi\|^2 \} = J^*.$$

This completes the proof of the theorem.

**Example 3.1.** Consider the stochastic neural networks with interval time-varying delays (2.1), where

$$A = \begin{bmatrix} 0.2 & 0 \\ 0 & 0.2 \end{bmatrix}, W_0 = \begin{bmatrix} -0.3 & 0.1 \\ 0.1 & -0.3 \end{bmatrix}, W_1 = \begin{bmatrix} -0.4 & 0.3 \\ 0.3 & -0.9 \end{bmatrix}, B = \begin{bmatrix} 0.5 \\ 0.4 \end{bmatrix},$$

$$E = \begin{bmatrix} 0.7 & 0 \\ 0 & 0.9 \end{bmatrix}, F = \begin{bmatrix} 0.7 & 0 \\ 0 & 0.8 \end{bmatrix}, Q_1 = \begin{bmatrix} 0.7 & 0.2 \\ 0.2 & 0.6 \end{bmatrix}, Q_2 = \begin{bmatrix} 0.2 & 0.3 \\ 0.3 & 0.3 \end{bmatrix}, R = \begin{bmatrix} 0.9 & 0.5 \\ 0.5 & 0.8 \end{bmatrix},$$

$$\begin{cases} h(t) = 0.1 + 2.0297 \sin^2 t & \text{if } t \in \mathcal{I} = \cup_{k \geq 0} [2k\pi, (2k+1)\pi] \\ h(t) = 0 & \text{if } t \in R^+ \setminus \mathcal{I}, \end{cases}$$

Note that  $h(t)$  is non-differentiable, therefore, the stability criteria proposed in [5, 6, 7, 12, 15] are not applicable to this system. Given  $\alpha = 1.1, \rho_1 = 0.5, \rho_2 = 0.8, h_0 = 0.1, h_1 = 2.1297$ , by using the Matlab LMI toolbox, we can solve for  $P, U, G_0, G_1, H_0, H_1, D_0$ , and  $D_1$  which satisfy the condition (3.1) in Theorem 3.1. A set of solutions are

$$P = \begin{bmatrix} 3.1297 & 0.4831 \\ 0.4831 & 1.1970 \end{bmatrix}, \quad U = \begin{bmatrix} 2.0912 & 0.1291 \\ 0.1291 & 3.0017 \end{bmatrix},$$

$$G_0 = \begin{bmatrix} 0.1473 & 0.0113 \\ 0.0113 & 0.8931 \end{bmatrix}, \quad G_1 = \begin{bmatrix} 0.6179 & 0.1197 \\ 0.1197 & 1.0273 \end{bmatrix},$$

$$H_0 = \begin{bmatrix} 1.0387 & 0.3970 \\ 0.3970 & 2.2207 \end{bmatrix}, \quad H_1 = \begin{bmatrix} 0.9712 & 0.0012 \\ 0.0012 & 0.7219 \end{bmatrix},$$

$$D_0 = \begin{bmatrix} 0.2189 & 0 \\ 0 & 0.2189 \end{bmatrix}, \quad D_1 = \begin{bmatrix} 0.1249 & 0 \\ 0 & 0.1249 \end{bmatrix}.$$

Then

$$u(t) = -1.7196x_1(t) - 1.2551x_2(t), t \geq 0$$



is a guaranteed cost control law and the cost given by

$$J^* = E \left\{ 11.3271 \|\phi\|^2 \right\}.$$

Moreover, the solution  $x(t, \phi)$  of the system satisfies

$$E \{ \|x(t, \phi)\| \} \leq E \{ 0.7315e^{-1.1t} \|\phi\| \}, \forall t \geq 0.$$

## 4 Conclusions

In this paper, the problem of guaranteed cost control for stochastic neural networks with interval nondifferentiable time-varying delay has been studied. A nonlinear quadratic cost function is considered as a performance measure for the closed-loop system. The stabilizing controllers to be designed must satisfy some mean square exponential stability constraints on the closed-loop poles. By constructing a set of time-varying Lyapunov-Krasovskii functional combined with Newton-Leibniz formula, a memoryless state feedback guaranteed cost controller design has been presented and sufficient conditions for the existence of the guaranteed cost state-feedback for the system have been derived in terms of LMIs.

**Acknowledgements.** This work was supported by the Thai Research Fund Grant, the Higher Education Commission and Faculty of Science, Maejo University, Thailand.

## References

- 1.Hopfield J.J., "Neural networks and physical systems with emergent collective computational abilities," *Proc. Natl. Acad. Sci. USA*, **79**(1982), 2554-2558.
2. Kevin G., *An Introduction to Neural Networks*, CRC Press, 1997.
- 3.Wu M., He Y., She J.H., *Stability Analysis and Robust Control of Time-Delay Systems*, Springer, 2010.
- 4.Arik S., An improved global stability result for delayed cellular neural networks, *IEEE Trans. Circ. Syst.* **499**(2002), 1211-1218.
- 5.He Y., Wang Q.G., M. Wu, LMI-based stability criteria for neural networks with multiple time-varying delays, *Physica D*, **112**(2005), 126-131.
- 6.Kwon O.M., J.H. Park, Exponential stability analysis for uncertain neural networks with interval time-varying delays. *Appl. Math. Comput.*, **212**(2009), 530541.
- 7.Phat V.N., Trinh H. , Exponential stabilization of neural networks with various activation functions and mixed time-varying delays, *IEEE Trans. Neural Networks*, **21**(2010), 1180-1185.
- 8.Botmart T.and P. Niamsup, Robust exponential stability and stabilizability of linear parameter dependent systems with delays, *Appl. Math. Comput.*, **217**(2010), 2551-2566.
- 9.W.H. Chen W.H., Guan Z.H., Lua X., Delay-dependent output feedback guaranteed cost control for uncertain time-delay systems, *Automatica*, **40**(2004), 1263 - 1268.



- 12 M. Rajchakit
10. Palarkci M.N., Robust delay-dependent guaranteed cost controller design for uncertain neutral systems, *Appl. Math. Computations*, **215**(2009), 2939-2946.
11. Park J.H., Kwon O.M., On guaranteed cost control of neutral systems by retarded integral state feedback, *Applied Mathematics and Computation*, **165**(2005), 393-404.
12. Park J.H., Choi K., Guaranteed cost control of nonlinear neutral systems via memory state feedback, *Chaos, Fractals and Solitons*, **24**(2005), 183-190.
13. Fridman E., Orlov Y., Exponential stability of linear distributed parameter systems with time-varying delays. *Automatica*, **45**(2009), 194201.
14. Xu S., Lam J., A survey of linear matrix inequality techniques in stability analysis of delay systems. *Int. J. Syst. Sci.*, **39**(2008), 12, 10951113.
15. Xie J.S., Fan B.Q., Young S.L., Yang J., Guaranteed cost controller design of networked control systems with state delay, *Acta Automatica Sinica*, **33**(2007), 170-174.
16. Yu L., Gao F., Optimal guaranteed cost control of discrete-time uncertain systems with both state and input delays, *Journal of the Franklin Institute*, **338**(2001), 101-110.
17. Gu K., Kharitonov V., Chen J., Stability of Time-delay Systems, Birkhauser, Berlin, 2003.



## Two-Side Confidence Intervals for the Poisson Means

**Manlika Rajchakit**

Major of Statistics, Faculty of Science, Maejo University, Chiang Mai 50290,  
Thailand.

E-mail: manlika@mju.ac.th.

**Abstract:** In this paper we consider interval estimation for the Poisson means. The following confidence intervals are considered: Wald CI, Score CI, Score continuity correction CI, Agresti and Coull CI, Bayes Wald CI, Bayes Score CI, and Bayes Score continuity correction CI. Each interval is examined for its coverage probability and its expected lengths. Based on this simulation; we recommend Score CI and the Wald CI for the small  $n$  and the larger  $n$  respectively.

**Keywords:** Bayes Estimators; Poisson distribution; Interval Estimation.

### 1. Introduction

Estimation is one of the main branches of statistics. They refer to the process by which one makes inference about a population, based on information obtained from a sample. Statisticians use sample statistics to estimate population parameter. For example; sample means are used to estimate population mean; sample proportions, and to estimate proportions. An estimate of population parameters may be expressed in two ways; point and interval estimate. A point estimate of a population parameter is a single value of a statistic, for example, the sample mean  $\bar{x}$  is a point estimate of the population mean  $\mu$ . Similarly, the sample proportion  $p$  is a point estimate of the population proportion  $P$ . An interval estimate is defined by two numbers, between which a population parameter is to lie, for example,  $a < \bar{x} < b$  is an interval estimate of the population mean  $\mu$ . It indicates that the population mean is greater than a bit less than  $b$ . Statisticians use a confidence interval to express the precision and uncertainty associated with a particular sampling method, for example, we might say that we are 95% confidence that the true population mean falls within a specified range. This statement is a confidence interval. It mean that if we used the same sampling method to select different samples and compute different interval estimates, the true population mean would fall within a range defined by the sample statistic  $\pm$  margin of error 95% of the time.

In this paper, we are compare seven method confidence interval (CIs) for the Poisson means, Poisson distribution is a discrete probability distribution. A Poisson random variable ( $X$ ) representing the number of successes occurring in a given time interval or a specified region of space.

The probability distribution is

$$P(X) = \frac{e^{-\lambda} \lambda^x}{x!}.$$



Where  $x=0, 1, 2, \dots, e=2.71828$  (but use your calculator's e button), and  $\lambda$  =mean number of successes in the given time interval or region of space.

Confidence interval (CI) of Poisson means that popular is

$$\hat{\lambda} \pm z_{\frac{\alpha}{2}} \sqrt{\hat{\lambda}/n},$$

and  $z_{\alpha/2}$  is the  $100(1-\alpha/2)$  percentile of the standard normal distribution. This formula, we call Wald method, it is easy to present and compute but it has poor coverage properties for small n. Brown, Cai and das Gupta [2] showed that Wald CI is actually far too poor and unreliable and the problem are not just for small n. Cai [1] showed that Wald CI suffers from a series systematic bias in the coverage. Therefore, the other researcher are present any method for solve this problem; see Manlika [3], Ross [4], Stamey [5] and Wardell [7]. We have known that common method used maximum likelihood estimator. So, we require to developed the CIs by Bayes estimator with Wald CI, Score CI and Score continuity correction CI which the prior distribution of  $\lambda$  is assumed to be gamma distribution with  $\alpha$  and  $\beta$  parameters. Wararit [6] showed that the optimal values of  $\alpha$  and  $\beta$  are their value provide  $\alpha\beta$  closed to the  $\lambda$  parameter. The  $\alpha$  value is always higher than the  $\beta$  value, the  $\alpha$  lies between 4.0 and 5.0.

## 2. The confidence interval

1. Create random variable that has Poisson distribution.
2. Compute interval estimation for a Poisson distribution seven methods:

### 2.1 Wald CI

$$\hat{\lambda} \pm Z \sqrt{\frac{\hat{\lambda}}{n}}. \quad (a)$$

### 2.2 Score CI

$$\frac{(n\hat{\lambda} + z^2/2)}{n} \pm zn^{-1/2} \left( \hat{\lambda} + \frac{z^2}{4n} \right)^{1/2}. \quad (b)$$



### 2.3 Score continuity correction CI

$$\frac{(2n\hat{\lambda} + Z^2 - 1)mZ\sqrt{Z^2 + 4n\hat{\lambda}m^2}}{2n} \quad (c)$$

### 2.4 Agresti and Coull CI

$$\frac{X + z^2/2}{n} \pm z \left( \frac{X + z^2/2}{n} \right)^{1/2} \quad (d)$$

### 2.5 Bayes Wald CI

$$\hat{\lambda}'_{\alpha} \pm Z \sqrt{\frac{\hat{\lambda}'_{\alpha}}{n}} \quad (e)$$

### 2.6 Bayes Score CI

$$\frac{(\hat{\lambda}'_{\alpha} + z^2/2)}{\hat{\lambda}'_{\alpha}} \pm z \hat{\lambda}'_{\alpha}^{1/2} \left( \frac{\hat{\lambda}'_{\alpha} + z^2/2}{4\hat{\lambda}'_{\alpha}} \right)^{1/2} \quad (f)$$

### 2.7 Bayes Score continuity correction CI

$$\frac{(2\hat{\lambda}'_{\alpha} + Z^2 - 1)mZ\sqrt{Z^2 + 4\hat{\lambda}'_{\alpha}m^2}}{2\hat{\lambda}'_{\alpha}} \quad (g)$$

Note that for (a)-(c)  $\hat{\lambda} = \bar{x}$ ;  $\hat{\lambda}$  is well known to be the MLE of  $\lambda$  and  $z$  is the  $100(1 - \alpha/2)$  percentile of the standard normal distribution

$$\text{For (e)-(g)} \quad \hat{\lambda}'_{\alpha} = \frac{(\alpha + X)\beta}{n\beta + 1} \quad \text{and} \quad \hat{\lambda}'_{\alpha} = n\beta + 1.$$

$\hat{\lambda}'_{\alpha}$  is Bayes' estimator of Poisson mean, and  
X is number of successes occurring in a given time interval  
or a specified region of space.

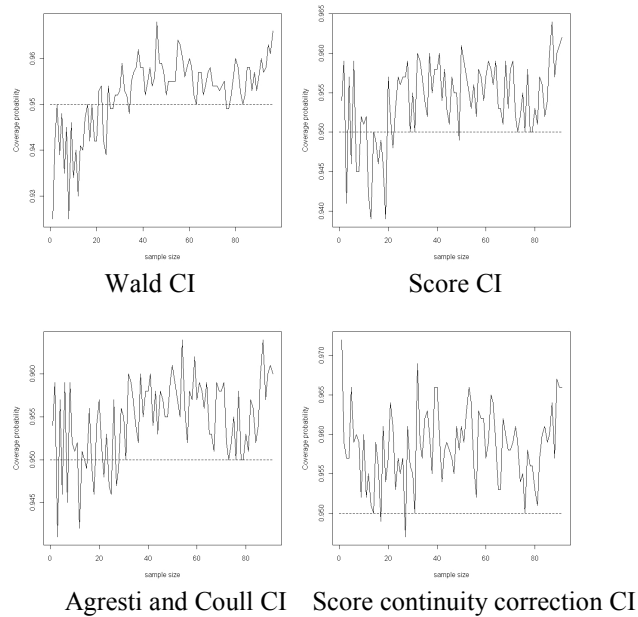
## 3. Simulation results

The performance of the estimated coverage probabilities of the confidence interval (a)-(f) and their expected lengths were examined via Monte Carlo simulation. Data were generate from Poisson distribution with  $\lambda = 1, 2, 3, 4, 5$  and sample size  $n=10$  to 100. All simulations were performed using programs



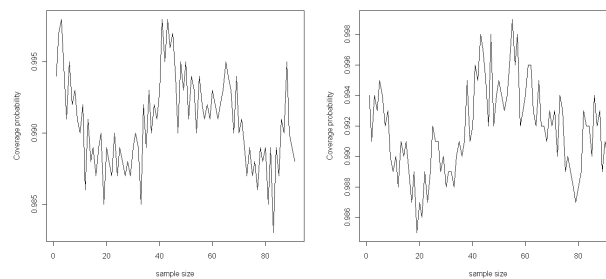
written in the R Statistical software, repeated 1,000 times in each case at level of significance  $\alpha = 0.01, 0.05$ , and  $0.10$ . The simulation results are shown in Figure 1-2 and Table 1.

Figure 1 show that the coverage probability of the Wald CI, Score CI, Agresti and Coull CI, and Score continuity correction CI for fixed  $\lambda = 3$  and variable  $n$  from 10 to 100. Naively, one may expect that the coverage probability gets systematically near the nominal level as the sample size  $n$  increases.



**Figure1** Coverage probability of four intervals for a Poisson mean with  $\alpha = 0.05$  and  $n = 10$  to  $100$ .

Figure2. Show that the coverage probability of the alternative intervals with Bayes estimator gives the coverage probability upper nominal level.

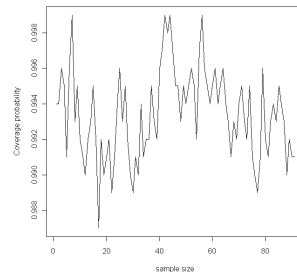






Bayes Wald CI

Bayes Score CI



Bayes Score continuity correction CI

**Figure2** Coverage probability of three intervals for a Poisson mean with  $\alpha = 0.05$  and  $n = 10$  to  $100$ .

In addition, the expected lengths of the score CI and the Wald CI are much shorter than the other CIs when  $n$  are small and larger respectively. The expected length increase as the value  $\lambda$  gets larger (e.g. For Score CI,  $n=10$  and  $\alpha = 0.05$ ; 0.23284 for  $\lambda = 1$ ; 0.327333 for  $\lambda = 3$ ; and 0.482786 for  $\lambda = 5$ ). Moreover, when the sample size increase, the expected length is shorter (e.g. For Score CI,  $\lambda = 1$  and; 0.23284 for  $n=10$ ; 0.102252 for  $n=50$ ; and 0.072279 for  $n=100$ ).

#### 4. Conclusions

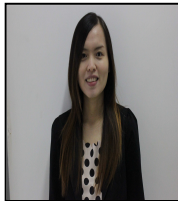
Our main objective is to compare the CIs under different situation; we compare the performance of all the CIs described above under various situations and three different confidence levels  $\alpha = 0.05, 0.01, 0.10$ . We found that, Wald CI is below the nominal level, but it has smallest expected length for  $n$  are small ( $n < 30$ ), Score CI, Score corrected continuity CI, Agresti and Coull CI are above the nominal level and they have expected length slightly higher Wald CI. Three alternatives with Bayes estimator have a higher CI and they are similar with each other and do a good job, so, we recommend Score CI and the Wald CI for the small  $n$  and the larger  $n$  respectively.

#### References

- [1] T. T. Cai, "One-sided confidence intervals in discrete distributions", *J. of Statistical planning and inference*, 131 (2005) 63-88.
- [2] D. B. Lawrence, T. T. Cai, and A. Dasgupta, "Interval estimation for a binomial Proportion", *Statistica Sinica*, 16 (2003):101-133.
- [3] M. Tanusit, "A Comparative Study of Parameter Inference Methods for Poisson distribution: Small Sample Size", *Advance and Applications in Statistics*, 14 (2010):49-55.
- [4] T. D. Ross, "Accurate confidence intervals for binomial proportion and Poisson rate estimation", *Comput. Biol. Med.*, 33 (2003) : 509-531.



- [5] J. D. Stamey, J. W. Seaman, and D. M. Young, "Bayesian analysis of complementary Poisson rate parameters with data subject to misclassification", *Statist. Plann. Inference*, 134 (2005), 36-48.
- [6] W. Panichkitkosolkul, "The Optimal Parameters of Prior Distribution for Bayes' Estimator of Poisson Mean", *SWU Sci. J.*, 23 No. 1 (2007) 23-31.
- [7] G. D. Wardell, "Small Sample Interval Estimation of Bernoulli and Poisson Parameters", *The American Statistician*, 51 (1997) : 321-325



**Manlika Tanusit** received the B.S. degree in Statistics from Kasetsart University, Bangkok City, Thailand, in 2008. Currently, she is a lecturer at the Department of Statistics, Maejo University, Chiang Mai, Thailand. His research interests include stability and stabilization of dynamical systems, qualitative theory of differential/discrete-time systems.  
Email: manlika@mju.ac.th



## Correlation and Randomness Properties of Binary Sequences Generated Using Matrix Recurrence Relation Defined over $Z_8$

Ramesh S<sup>\*</sup>, Dileep D<sup>#</sup>

<sup>\*</sup>Department of Electronics & Communication Engineering,  
Dr Ambedkar Institute of Technology, Bangalore, India

<sup>#</sup>Istrac, ISRO, Bangalore

E-mail: [rameshs.hullepura@gmail.com](mailto:rameshs.hullepura@gmail.com)

**Abstract:** *This article describes an approach to the generation of key sequence based on matrix recurrence relation defined over  $Z_8$ . The generated sequence is subjected to FIPS 140-1 test suite and Hamming Autocorrelation test. The generated sequence passes the FIPS 140-1 test suite and also exhibits good Hamming autocorrelation properties. The results of these tests are analyzed.*

**Keywords:** Random number, pseudo random number, Recurrence relation over  $Z_8$ , Auto correlation

### 1. Introduction

Good Cryptography requires good random numbers. Security of these protocols relies on the unpredictability of the key they use. Almost all cryptographic protocols require the generation and use of secret value that must be unknown to attacker. Random number generators used to generate key sequence must satisfy stringent requirements like unpredictability, uniform distribution, long period, and good statistical properties. Pierre L'Ecuyer[1,2,3,4] discusses the most widely used random number generators based on linear recurrence models such as Multiple recurrence generators, Multiple recurrence generators with carry, the Linear feedback shift registers etc., The authors proposed the [5,6,7] random number generator based on the matrix recurrence relation defined over  $Z_8$ . In this paper the generation of sequence of random number defined over  $z_8$  based on matrix recurrence relation, the FIPS 140-1 tests performed on the proposed generator and the Hamming auto correlation properties of the sequence so generated are also discussed.



## 2. Organization of the paper

The rest of this article is organized as follow. In Section II, we present a proposed a random number generator defined over  $Z_8$  using matrix recurrence relation. In Section III, we discuss briefly the FIPS 140-1 tests and Normalized Hamming autocorrelation test, which are used to test the proposed random number generator.

## 3. The Proposed Random Number Generator defined over $Z_8$ Based on matrix recurrence relation [5, 6]

The following matrix recurrence relation defines the proposed random number generator over  $Z_8$  [5, 6, and 7]

$$X_j = \sum_{i=0}^{k-1} C_i X_{j-i-1}, \quad j \geq k+1 \text{ arithmetic modulo } 8 \quad (1)$$

Where  $X$  is an  $n$ -tuple ( $n \times 1$ ) over  $Z_8$  and coefficients

$C_i$ ,  $i = 0$  to  $k-1$  and can be

- a)  $n \times n$  non-singular matrix over  $Z_8$  or
- b) Any  $n \times n$  arbitrary matrix over  $Z_8$

When  $m$  is prime  $X$  is a vector otherwise it is an element of module over  $Z_8$ .

Output is concatenated sequence  $\{ x_i^T \}$  where  $x_i^T$  is transpose of  $x_i$ ,  $i = 0, 1, 2, \dots$

## 4. Testing of Random Numbers

The evaluations of the quality of the random number generators are very difficulty problem, which has no unique solution. On the other hand there is no single practical tests that can realize the randomness in a given sequence of random numbers. Since all the



pseudorandom sequence generators are based on deterministic rules, there exist always tests in which a given generator will fail. A large number of statistical tests have been proposed, such as DIEHARD specification FIPS 140-1 and Knuth's test, Autocorrelation test, Crypt -XS. In this paper we compute the FIPS 140-1 test statistics for a binary sequence generated by the equation (1) and also the autocorrelation test is performed on the sequence generated by the equation (1).

The Frequency test, serial test (two-bit test), Poker test, runs test, autocorrelation test are the five statistical tests that are commonly used for determining whether the binary sequence  $s$  possesses some specific characteristics that a truly random sequence would be likely to exhibit [5]. These tests are discussed in detail in papers [Knuth] [Menezes] [5, 6, 11, and 12]

#### **4.1. FIPS 140-1 Statistical Tests for Randomness**

The second and following pages should begin 1.0 inch (2.54 cm) from the top edge. On all pages, the bottom margin should be 1-1/8 inches (2.86 cm) from the bottom edge of the page for 8.5 x 11-inch paper; for A4 paper, approximately 1-5/8 inches (4.13 cm) from the bottom edge of the page.

Federal Information Processing Standard FIPS- 140-1 specifies monobit test. Poker test runs test and long run test for computing the statistics for randomness also provide the explicit bounds that the computed value of a statistic must satisfy. A single bit string  $s$  of length 20000 bits, output from a generator, is subjected to each of the above tests. If any of the tests fail, then the generator fails the test.[ 5,6,7,8, 12].

##### **4.1.1. Monobit test**

The number  $n_1$  of 1's in sequence  $s$  should satisfy  $9654 < n_1 < 10346$ .

##### **4.1.2. Poker test**

Let  $q$  be a positive integer such that  $\lfloor n/q \rfloor \geq 5$ . ( $2^q$ ), and let  $k = \lfloor n/q \rfloor$ . Divide the sequence  $s$  into  $k$  non-overlapping parts each of



length  $q$ , and let  $n_i$  be the number of occurrences of the  $i^{\text{th}}$  type of sequence of length  $q$ ,  $1 \leq i \leq 2^q$ .

$$X_2 = \frac{2^q}{k} \left( \sum_{i=1}^{2^q} n_i^2 \right) - k$$

The statistic  $X_2$  defined by equation (2) is computed for  $m = 4$ . The poker test is passed if  $1.03 < X_2 < 57.4$ .

#### 4.1.3. Runs test

The number  $B_i$  and  $G_i$  of blocks and gaps, respectively, of length  $i$  in sequence  $s$  are counted for each  $i$ ,  $1 \leq i \leq 6$ . (For the purpose of this test, runs of length greater than 6 are considered to be of length 6.) The runs test is passed if the 12 counts  $B_i$  and  $G_i$ ,  $1 \leq i \leq 6$ , are each within the corresponding interval specified by the table 1

Table 1. Interval specified for Run test

Length of run	Required interval
1	2267 – 2733
2	1079 – 1421
3	502 – 748
4	223 – 402
5	90 – 223
6	90 – 223

#### 4.1.4. Long run test

The long run test is passed if there are no runs of length 34 or more. FIPS 140-1 allows these tests to be substituted by alternative tests, which provide equivalent or superior randomness checking.

#### 4.2. Hamming Auto Correlation Test

One of the desirable properties of sequence of random numbers is that, the elements of the sequence must not be clustered [5-7, 12].



This property can be verified by computing normalized Hamming correlation of the sequence  $R_h(\tau)$  which is given by equation (3).

$$R_h(\tau) = (a-d)/(a+d) \quad (3)$$

Where  $a$  = agreements,  $d$  = disagreements between bits of sequence and its shifted version and  $\tau$  is time shift.  $R_h(\tau)$  is computed by counting the number of agreements and disagreements for different time shifts. The value of  $R_h(\tau)$  ranges between  $+1$  and  $-1$ . For  $\tau = 0$ ,  $R_h(\tau) = 1$ , since there is no disagreements.

Table 2. Matrix used for computing recurrence equation (1)

$C_0$	$C_1$	$C_2$	$C_3$	$C_4$
7 0	5 0	6 1	3 1	5 2
0 1	1 1	1 1	1 2	1 1
$C_5$	$C_6$	$C_7$	$C_8$	$C_9$
3 3	4 3	7 5	5 4	0 7
3 4	3 5	1 2	1 3	1 5
$C_{10}$	$C_{11}$	$C_{12}$	$C_{13}$	$C_{14}$
3 4	6 5	4 5	5 7	1 4
5 7	1 3	1 3	1 4	1 7
$C_{15}$	$C_{16}$	$C_{17}$	$C_{18}$	$C_{19}$
2 1	3 2	6 3	7 1	5 5
1 1	1 1	1 1	4 1	3 2

Table 3 .Initial vectors used for computing recurrence equation (1)

$X_1$	$X_2$	$X_3$	$X_4$	$X_5$	$X_6$	$X_7$
1	3	4	6	3	5	7
2	1	5	1	7	1	0
$X_8$	$X_9$	$X_{10}$	$X_{11}$	$X_{12}$	$X_{13}$	$X_{14}$
		0	1			
5	5	3	2	7	1	4
2	4	2	3	3	3	4
$X_{15}$	$X_{16}$	$X_{17}$	$X_{18}$	$X_{19}$	$X_{20}$	
5	6	7	8			
3	5	1	6	5	4	
3	0	5	2	6	6	



## 5 Results and discussion

### 5.1. FIPS-140-1 Tests Results

The sequence of length 20000 consecutive binary mapped bits generated using equation (1) is subjected to FIPS 140-1 statistical test to determine the randomness property. Table 2 gives an array of 20 arbitrary  $2 \times 2$  matrix over  $Z_8$  and the sequence is generated by using these matrices as coefficient matrix in the equation (1) for different stages  $k = 3$  to 20. Table 3 gives corresponding initial vectors used for the generation of the sequence. The results are tabulated in Table 4 for different stages  $k = 3$  to 20.

Results show that, the sequences passes FIPS 140-1 tests for stages  $k > 4$  for the given matrices and initial vector. However for the stages  $k \leq 4$  the sequence doesn't pass all the tests but few. The algorithm is tested for different sets of  $2 \times 2$  matrices

Table 4. Results of FIPS 140-1 tests carried out on the recurrence equation (1)

Randomness test	Case 1 3 stages		Case 2 4 stages	
	$n_1$	$n_0$	$n_1$	$n_0$
Mono bit Test	10220	9798	9992	10008
Poker Test	265.88		171.75	
Run Test	Run 1	Run 0	Run 1	Run 0
1	2259	2420	2384	2400
2	1395	1399	1311	1274
3	564	537	701	693
4	377	322	278	286
5	216	162	134	190
6	135	102	166	130
Long run test	Passes Long run test			





Randomness test	Case 3 5 stages		Case 4 6 stages	
Mono-bit Test	$n_1$	$n_0$	$n_1$	$n_1$
	9988	1001 2	9930	9988
Poker Test	7.6544		12.768	
Run Test	Run 1	Run 0	Run Test	Run 1
1	2500	2433	1	2500
2	1214	1273	2	1214
3	627	662	3	627
4	311	299	4	311
5	168	161	5	168
6	159	151	6	159
Long run test	Passes Long run test			

and initial vectors and it is found that for  $k > 4$  the sequence generated pass FIPS 140-1 tests.

### 5.2 Hamming Autocorrelation Test Results

Sequence  $\{x_i^T\}$  is over  $Z_8$  and is converted into a binary sequence where 0,1,2,3,4,5,6,7 are replaced by binary 3-tuples 000,001,010,011,100,101,110, 111 respectively.

Hamming correlation  $R_h(\tau)$  is computed using equation (3) by considering

i) Sequence of 10,000 consecutive output integer of the recurrence equation (1) which is right circularly shifted by  $\tau$  shifts,  $\tau = 0,1,\dots, 9999$ ,and

ii) Sequence of 20,000 consecutive output bits of the recurrence equation (1) which is right circularly shifted by  $\tau$  shifts,  $\tau = 0,1,\dots, 19999$



Plots of Normalized Hamming autocorrelation test are shown in Figure 1 to 6

Rando mness test	Case 5 7 stages		Case 6 8 stages	
	n <sub>1</sub>	n <sub>0</sub>	n <sub>1</sub>	n <sub>0</sub>
Mono bit Test	9887	1011 3	991 8	10082
Poker Test	21.9328		16.5952	
Run Test	Run 1	Run 0	Run 1	Run 0
1	2569	2507	257 7	2499
2	1254	1304	115 8	1217
3	621	602	630	626
4	321	312	328	332
5	108	133	152	163
6	163	180	150	159
Long run test	Passes Long run test			

Rando mness test	Case 7 9 stages		Case 8 10stages	
	n <sub>1</sub>	n <sub>0</sub>	n <sub>1</sub>	n <sub>1</sub>
Mono- bit Test	9945	10055	999 0	10010
Poker Test	13.9072		11.2384	
Run Test	Run 1	Run 0	Run Test	Run 1
1	2482	2433	254 2	2538
2	1212	1252	122 2	1217



3	611	641	630	641
4	322	262	315	320
5	158	177	170	154
6	161	181	144	152
Long run test	Passes Long run test			

Randomness test	Case 9 11 stages		Case 10 12 stages	
Mono-bit Test	n <sub>1</sub>	n <sub>0</sub>	n <sub>1</sub>	n <sub>0</sub>
	10118	9882	10118	9882
Poker Test	11.5648		12.9728	
Run Test	Run 1	Run 0	Run 1	Run 0
1	2391	2534	2391	2534
2	1292	1219	1292	1219
3	643	577	643	577
4	301	297	301	297
5	153	173	153	173
6	182	162	182	162
Long run test	Passes Long run test			

Randomness test	Case 11 13 stages		Case 12 14 stages	
Mono-bit Test	n <sub>1</sub>	n <sub>0</sub>	n <sub>1</sub>	n <sub>0</sub>
	10076	9924	10076	9924
Poker Test	19.9232		13.952	



Run Test	Run 1	Run 0	Run 1	Run 0
1	2503	2573	2503	2573
2	1265	1220	1265	1220
3	645	644	645	644
4	296	277	296	277
5	158	167	158	167
6	162	147	162	147
Long run test	Passes Long run test			

Randomness test	Case 13 15 stages		Case 14 16 stages	
Mono bit Test	n <sub>1</sub>	n <sub>0</sub>	n <sub>1</sub>	n <sub>0</sub>
	9988	10012	9988	10012
Poker Test	7.6544			
Run Test	Run 1	Run 0	Run 1	Run 0
1	2500	2433	2500	2433
2	1214	1273	1214	1273
3	627	662	627	662
4	311	299	311	299
5	168	161	168	161
6	159	161	159	161
Long run test	Passes Long run test			

Table 5. Results of Hamming autocorrelation

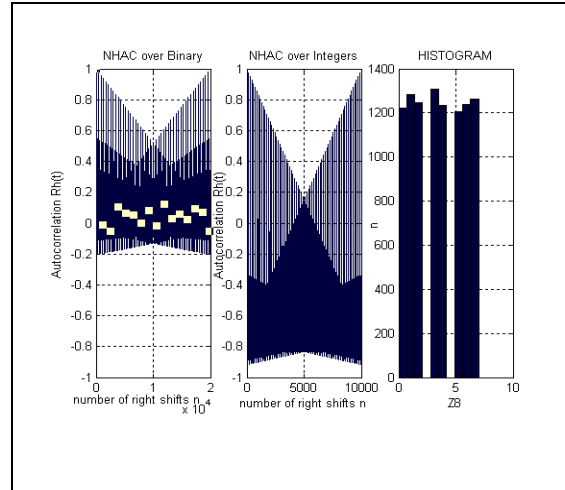


Figure1. Normalized Hamming auto correlation (NHAC) over integers, binary and its histogram

Number of stages = 5

$C_i$ 's are non -singular matrix ( $C_0$  to  $C_4$ ) and  $X_i$ 's are ( $X_1$  to  $X_5$ )

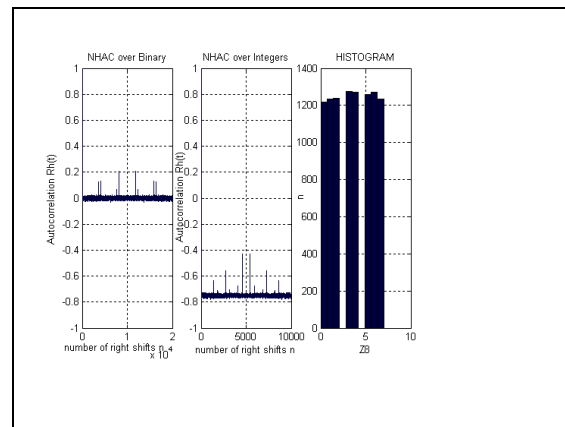


Figure 2. Normalized Hamming auto correlation (NHAC) over integers, binary and its histogram

Number of stages = 6

$C_i$ 's are non -singular matrix ( $C_0$  to  $C_5$ ) and  $X_i$ 's are ( $X_1$  to  $X_6$ )

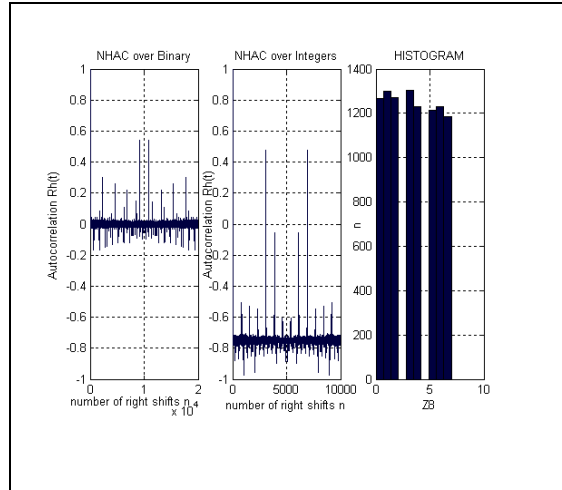


Figure3. Normalized Hamming auto correlation (NHAC) over integers, binary and its histogram

Number of stages = 7

$C_i$ 's are non -singular matrix ( $C_0$  to  $C_6$ ) and  $X_i$ 's are ( $X_1$  to  $X_7$ )

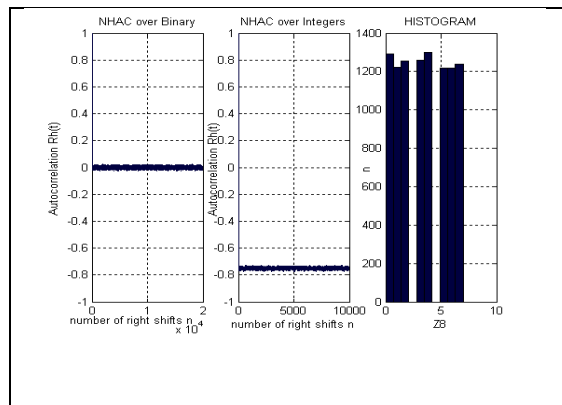


Figure 4. Normalized Hamming auto correlation (NHAC) over integers, binary and its histogram

Number of stages = 8

$C_i$ 's are non -singular matrix ( $C_0$  to  $C_7$ ) and  $X_i$ 's are ( $X_1$  to  $X_8$ )

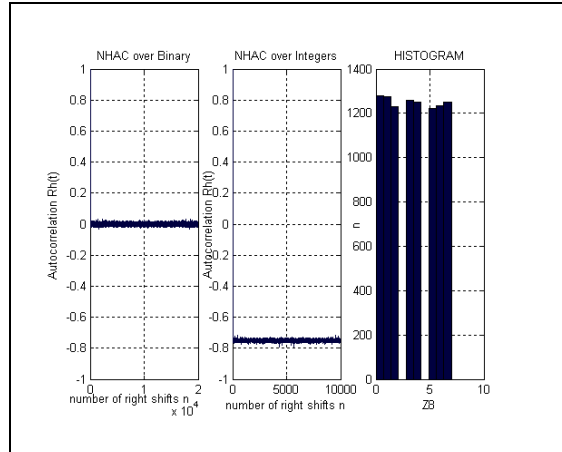


Figure 5. Normalized Hamming auto correlation (NHAC) over integers, binary and its histogram

Number of stages = 9

$C_i$ 's are non-singular matrix ( $C_0$  to  $C_8$ ) and  $X_i$ 's are ( $X_1$  to  $X_9$ )

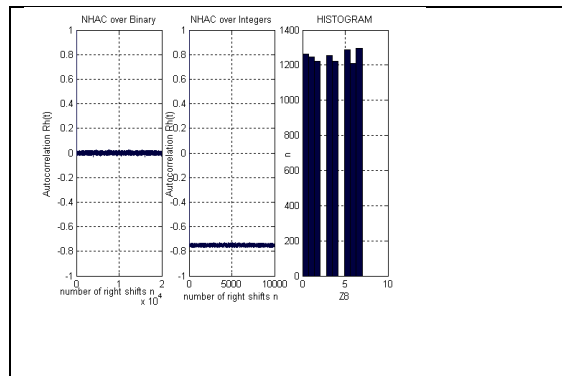


Figure 6. Normalized Hamming auto correlation (NHAC) over integers, binary and its histogram

Number of stages = 10

$C_i$ 's are non-singular matrix ( $C_0$  to  $C_9$ ) and  $X_i$ 's are ( $X_1$  to  $X_{10}$ )



## 5. Conclusions

Use of matrix recurrence relation defined over  $Z_8$  for the generation of sequence of random numbers with desirable statistical properties suitable for cryptographic application has been discussed. The generated sequence passes the FIPS 140-1 test suite for stages  $k > 4$ . Normalized Hamming Auto Correlation test performed on the sequence generated using recurrence (1) relation exhibits good correlation properties for number of stages  $k > 5$  for the given matrix and initial vector.

## References

1. Kencheng Zeng et al. , “Pseudorandom bit generators in stream-cipher cryptography”, IEEE, 1991.
2. Pierre L’Ecuyer, “Random number generation”, <http://www.iro.umontreal.ca/~lecuyer>, 2004
3. Francois Panneton and Pierre L’Ecuyer, “Random number generators based on linear recurrences in  $Z^2$ ”, <http://www.iro.umontreal.ca/~lecuyer>, 2004.
4. Francois Panneton and Pierre L’Ecuyer, “On the xorshift random number generators”, ACM journal, vol.V, no. N, month 20YY, Pages 1–16.
5. Ramesh S, K.N.Haribhat,and Murali R, “Generation of random number sequences: A literature review”, proceedings of national conference on signal processing and communication ,J.N.N.College of Engineering,Shimoga,India,pp.61-62,July 2006
6. Ramesh S, K.N.Haribhat,and Murali R, “Generation of random number sequences defined over  $Z_4$  and their properties”, proceedings of international conference on communication technology IEEE ICCT2006 Gulin,China,Nov 27-30, 2006
7. Ramesh S, K.N.Haribhat,and Murali R, “Generation of sequence of random numbers defined over  $Z_4$  and their applications in stream cipher system”, accepted for proceedings of Sonata international conference on communication, computers and controls,RVCE,Bangalore-India,Nov-23 to25,2006
8. Alfred J. Menezes,P.Van Oorschot and S.Vanstone, “Hand book of applied cryptography”,CRC Press,1996.
9. Benjamin jun, Paul koche, The Intel random number generator, “Cryptography research,Inc,white paper prepared for the Intel corporation,1999
10. Knuth, D. E, “The art of computer programming”, volume 2: semi numerical algorithms, third edition. Pearson education,.1998
11. Bruce Schneier, “Applied cryptography”, second edition, John wiley and sons, 1996.
12. Sathyanarayana S V,M.Ashwatha Kumar ,K.N Haribhat, “study of elliptical curve pseudorandom sequence generator”, proceedings of 5<sup>th</sup> national workshop on cryptology ,J.N.N.College of engineering,Shimoga,India,2005





## Synchronization in von Bertalanffy's models

J. Leonel Rocha<sup>1</sup>, Sandra M. Aleixo<sup>1</sup> and Acilina Caneco<sup>2</sup>

<sup>1</sup> Instituto Superior de Engenharia de Lisboa - ISEL, ADM and CEAUL, Rua  
Conselheiro Emídio Navarro, 1, 1959-007 Lisboa, Portugal  
(E-mail: [jrocha@adm.isel.pt](mailto:jrocha@adm.isel.pt), [sandra.aleixo@adm.isel.pt](mailto:sandra.aleixo@adm.isel.pt)),

<sup>2</sup> Instituto Superior de Engenharia de Lisboa - ISEL, ADM and CIMA-UE, Rua  
Conselheiro Emídio Navarro, 1, 1959-007 Lisboa, Portugal  
(E-mail: [acilina@adm.isel.pt](mailto:acilina@adm.isel.pt))

**Abstract.** Many data have been useful to describe the growth of marine mammals, invertebrates and reptiles, seabirds, sea turtles and fishes, using the logistic, the Gompertz and von Bertalanffy's growth models. A generalized family of von Bertalanffy's maps, which is proportional to the right hand side of von Bertalanffy's growth equation, is studied and its dynamical approach is proposed. The system complexity is measured using Lyapunov exponents, which depend on two biological parameters: von Bertalanffy's growth rate constant and the asymptotic weight.

Applications of synchronization in real world is of current interest. The behaviour of birds flocks, schools of fish and other animals is an important phenomenon characterized by synchronized motion of individuals. In this work, we consider networks having in each node a von Bertalanffy's model and we study the synchronization interval of these networks, as a function of those two biological parameters. Numerical simulation are also presented to support our approaches.

**Keywords:** Von Bertalanffy's models, synchronization, Lyapunov exponents.

### 1 Introduction and motivation

Several mathematical equations have been used to describe the growth of marine populations, namely fishes, seabirds, marine mammals, invertebrates, reptiles and sea turtles. Among these equations, three of the most familiar are the logistics, the Gompertz and the von Bertalanffy models, see [5] and references therein. For a certain population, the growth of an individual, regarded as an increase in its length or weight with increasing age, is commonly modeled by a mathematical equation that represents the growth of an "average" individual in the population. One of the most popular functions that have been used to analyze the increase in average length or weight of fish is von Bertalanffy's model, see for example [1] and [3].

Synchronization is a fundamental nonlinear phenomenon, which can be observed in many real systems, in physics, chemistry, mechanics, engineering, secure communications or biology, see for example [13]. It can be observed in living beings, on the level of single cells, physiological subsystems, organisms and even on the level of large populations. Sometimes, this phenomenon is essential for a normal functioning of a system, e.g. for the performance of a pacemaker, where the synchronization of many cells produce a macroscopic rhythm that governs respiration and heart contraction. Sometimes, the synchrony leads to a severe pathology, e.g. in case of the Parkinson's disease, when



locking of many neurons leads to the tremor activity. Biological systems use internal circadian clocks to efficiently organize physiological and behavioral activity within the 24-hour time domain. For some species, social cues can serve to synchronize biological rhythms. Social influences on circadian timing might function to tightly organize the social group, thereby decreasing the chances of predation and increasing the likelihood of mating, see [14]. Almost all seabirds breed in colonies; colonial and synchronized breeding is hypothesized to reduce predation risk and increases social interactions, thereby reducing the costs of breeding. On the other hand, it is believed that synchronization may promote extinctions of some species. Full synchronism may have a deleterious effect on population survival because it may lead to the impossibility of a recolonization in case of a large global disturbance, see [15]. Understand the aggregate motions in the natural world, such as bird flocks, fish schools, animal herds, or bee swarms, for instance, would greatly help in achieving desired collective behaviors of artificial multi-agent systems, such as vehicles with distributed cooperative control rules.

The layout of this paper is as follows. In Sec.2, we present a new dynamical approach to von Bertalanffy's growth equation, a family of unimodal maps, designated by von Bertalanffy's maps. In Sec.3, we present the network model having in each node a von Bertalanffy's model. The synchronization interval is presented in terms of the network connection topology, expressed by its Laplacian matrix and of the Lyapunov exponent of the network's nodes. In Sec.4, we give numerical simulations on some kinds of lattices, evaluating its synchronization interval. We present some discussion on how this interval changes with the increasing of the number of neighbors of each node, with the increasing of the total number of nodes and with the intrinsic growth rate. We also observe and discuss some desynchronization phenomenon.

## 2 Von Bertalanffy's growth dynamics approach

An usual form of von Bertalanffy's growth function, one of the most frequently used to describe chick growth in marine birds and in general marine growths, is given by

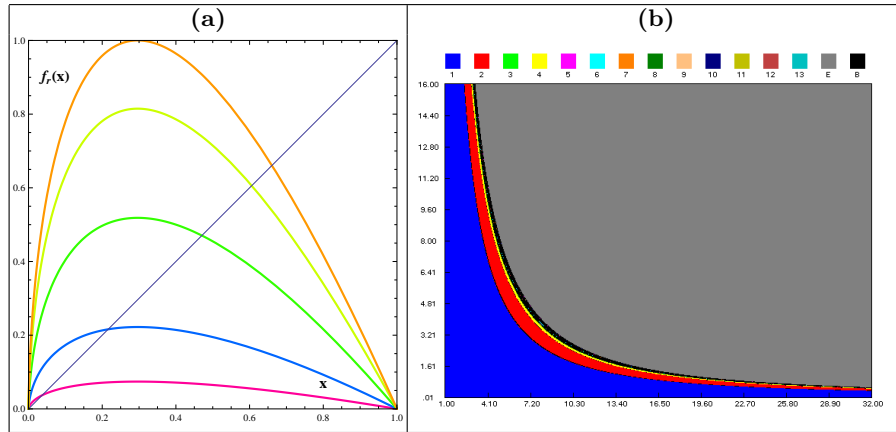
$$W_t = W_\infty \left(1 - e^{-\frac{K}{3}(t-t_0)}\right)^3, \quad (1)$$

where  $W_t$  is the weight at age  $t$ ,  $W_\infty$  is the asymptotic weight,  $K$  is von Bertalanffy's growth rate constant and  $t_0$  is the theoretical age the chick would have at weight zero. The growth function, Eq.(1), is solution of the von Bertalanffy's growth equation,

$$g(W_t) = \frac{dW_t}{dt} = \frac{K}{3} W_t^{\frac{2}{3}} \left(1 - \left(\frac{W_t}{W_\infty}\right)^{\frac{1}{3}}\right), \quad (2)$$

introduced by von Bertalanffy to model fish weight growth, see [11] and [12]. The *per capita* growth rate, associated to this growth model, is given by

$$h(W_t) = \frac{g(W_t)}{W_t} = \frac{K}{3} W_t^{-\frac{1}{3}} \left(1 - \left(\frac{W_t}{W_\infty}\right)^{\frac{1}{3}}\right). \quad (3)$$



**Fig. 1.** (a) Graphics of von Bertalanffy's maps  $f_r(x)$ , Eq.(4), for several values of intrinsic growth rate  $r$  (0.5 (magenta), 1.5, 3.5, 5.5 and 6.75 (orange)); (b) Bifurcation diagram of von Bertalanffy's maps  $f_r(x)$  in the  $(K, W_\infty)$  parameter plane. The blue region is the stability region. The period doubling and chaotic regions correspond to the cycles shown on top of figure. The gray region is the inadmissible region.

In this paper, we consider a family of unimodal maps, the von Bertalanffy maps, which is proportional to the right hand side of von Bertalanffy's equation, Eq.(2),  $f_r : [0, 1] \rightarrow [0, 1]$ , defined by

$$f_r(x) = r x^{\frac{2}{3}} \left(1 - x^{\frac{1}{3}}\right), \quad (4)$$

with  $x = \frac{W_i}{W_\infty} \in [0, 1]$  the normalized weight and  $r = r(K, W_\infty) = \frac{K}{3} \times W_\infty^{\frac{2}{3}} > 0$  an intrinsic growth rate of the individual weight, see Fig.1(a).

Remark that, the family of maps that we will study depends on two biological parameters: von Bertalanffy's growth rate constant  $K$  and the asymptotic weight  $W_\infty$ . The following conditions are satisfied:

- (A1)  $f_r$  is continuous on  $[0, 1]$ ;
- (A2)  $f_r$  has an unique critical point  $c \in ]0, 1[$ ;
- (A3)  $f'_r(x) \neq 0, \forall x \in ]0, 1[ \setminus \{c\}$ ,  $f'_r(c) = 0$  and  $f''_r(c) < 0$ ;
- (A4)  $f_r \in C^3(]0, 1[)$  and the Schwarzian derivative of  $f_r$ , denoted by  $S(f_r(x))$ , verifies  $S(f_r(x)) < 0, \forall x \in ]0, 1[ \setminus \{c\}$  and  $S(f_r(c)) = -\infty$ .

Conditions (A1)–(A4) are essential to prove the stability of the only positive fixed point, [10]. In particular, the negative Schwarzian derivative ensures a “good” dynamic behavior of the models. In general, the growth models studied have negative Schwarzian derivative and the use of unimodal maps is usual, see for example [8] and [9].

The dynamical complexity of the proposed models is displayed at  $(K, W_\infty)$  parameter plane, depending on the variation of the intrinsic growth rate  $r$ . The analysis of their bifurcations structure is done based on the bifurcation diagram, see Fig.1(b). For these models, the extinction region and the semistability



curve have no expressive meaning. Because it is difficult to identify *per capita* growth rates, Eq.(3), less than one for all densities, to the extinction case, and *per capita* growth rates strictly less than one for all densities, except at one population density, to the semistability case, except at most a set of measure zero. We verify that,  $\lim_{x \rightarrow 0^+} f_r'(x) > 1$  and the origin's basin of attraction is empty, except at most a set of measure zero. The fixed point 0 is unstable.

A behavior of stability is defined when a population persists for intermediate initial densities and otherwise goes extinct. The *per capita* growth rate of the population, Eq.(3), is greater than one for an interval of population densities. The lower limit of these densities correspond to the positive fixed point  $A_{K, W_\infty} \equiv A_r$ , of each function  $f_r$ , Eq.(4), see Fig.1(a). Furthermore, attending to (A2) and (A3) we have that  $f_r^2(c) > 0$ , then there is a linearly stable fixed point  $A_r \in ]0, 1[$ , whose basin of attraction is  $]0, 1[$ , for more details see [10].

The symbolic dynamics techniques prove to be a good method to determine a numerical approximation to the stability region (in blue), see Fig.1(b). For more details about symbolic dynamics techniques see for example [8]. In the  $(K, W_\infty)$  parameter plane, this region is characterized by the critical point iterates that are always attracted to the fixed point sufficiently near of the super stable or super attractive point  $\tilde{A}_r$ , defined by  $f_r(c) = c$ . Let  $\bar{A}_r \in ]0, 1[$  be the fixed points sufficiently near of  $\tilde{A}_r$ , then

$$\lim_{n \rightarrow \infty} f_r^n(c) = \bar{A}_r, \text{ for } \left( 3K^{-1}A_r^{\frac{1}{3}} \left( 1 - A_r^{\frac{1}{3}} \right) \right)^{\frac{3}{2}} < W_\infty(K) < \hat{W}_\infty(K)$$

where  $\hat{W}_\infty(K)$  represents the super stable curve of the cycle of order 2, given in implicit form by  $f_r^2(c) = c$ . In this parameter plane, the set of the super stable or super attractive points  $\tilde{A}_r$  defines the super stable curve of the fixed point. In the region before reaching the super stable curve, the symbolic sequences associated to the critical points orbits are of the type  $CL^\infty$ . After this super stable curve, the symbolic sequences are of the type  $CR^\infty$ . In this parameter region, the topological entropy is null, [6].

The period doubling region corresponds to the parameters values, to which the population weight oscillates asymptotically between  $2^n$  states, with  $n \in \mathbb{N}$ . In period-doubling cascade, the symbolic sequences correspondent to the iterates of the critical points are determined by the iterations  $f_r^{2^n}(c) = c$ . Analytically, these equations define the super-stability curves of the cycle of order  $2^n$ . The period doubling region is bounded below by the curve of the intrinsic growth rate values where the period doubling starts,  $\hat{W}_\infty(K)$ , correspondent to the 2-period symbolic sequences  $(CR)^\infty$ . Usually, the upper limit of this region is determined using values of intrinsic growth rate  $r$ , corresponding to the first symbolic sequence with non null topological entropy. Commonly, the symbolic sequence that identifies the beginning of chaos is  $(CRLR^3)^\infty$ , a 6-periodic orbit, see for example [8] and [9]. The unimodal maps in this region, also have null topological entropy, [6].

In the chaotic region of the  $(K, W_\infty)$  parameter plane, the evolution of the population size is *a priori* unpredictable. The maps are continuous on the interval with positive topological entropy whence they are chaotic and



the Sharkovsky ordering is verified. The symbolic dynamics are characterized by iterates of the functions  $f_r$  that originate orbits of several types, which already present chaotic patterns of behavior. The topological entropy is a non-decreasing function in order to the parameter  $r$ , until reaches the maximum value  $\ln 2$  (consequence of the negative Schwartzian derivative). In [8] and [9] can be seen a topological order with several symbolic sequences and their topological entropies, which confirm this result to others growth models. This region is bounded below by the curve of the intrinsic growth rate values where the chaos starts. The upper limit is the *fullshift* curve, defined by  $f_r(c) = 1$ . This curve characterizes the transition between the chaotic region and the inadmissible region. In the inadmissible region, the graphic of any function  $f_r$  is no longer totally in the invariant set  $[0, 1]$ . The maps under these conditions not already belong to the studied familie functions and are not good models for populations dynamics.

### 3 Synchronization and Lyapunov exponents

Consider a general network of  $N$  identical coupled dynamical systems, described by a connected, undirected graph, with no loops and no multiple edges. In each node the dynamics of the system is defined by the maps  $f_r$  given by Eq.(4). The state equations of this network, in the discretized form, are

$$x_i(k+1) = f_r(x_i(k)) + c \sum_{j=1}^N l_{ij} f_r(x_j(k)), \text{ with } i = 1, 2, \dots, N \quad (5)$$

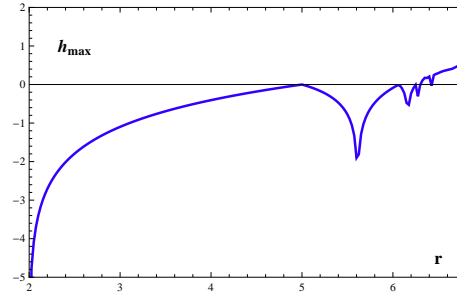
where  $c$  is the coupling parameter and  $L = (l_{ij})$  is the Laplacian matrix or coupling configuration of the network. The Laplacian matrix is given by  $L = D - A$ , where  $A$  is the adjacency matrix and  $D = (d_{ij})$  is a diagonal matrix, with  $d_{ii} = k_i$ , being  $k_i$  the degree of node  $i$ . The eigenvalues of  $L$  are all real and non negatives and are contained in the interval  $[0, \min \{N, 2\Delta\}]$ , where  $\Delta$  is the maximum degree of the vertices. The spectrum of  $L$  may be ordered,  $\lambda_1 = 0 \leq \lambda_2 \leq \dots \leq \lambda_N$ . The network (5) achieves asymptotical synchronization if

$$x_1(t) = x_2(t) = \dots = x_N(t) \xrightarrow[t \rightarrow \infty]{} e(t),$$

where  $e(t)$  is a solution of an isolated node (equilibrium point, periodic orbit or chaotic attractor), satisfying  $\dot{e}(t) = f(e(t))$ .

One of the most important properties of a chaotic system is the sensitivity to initial conditions. A way to measure the sensitivity with respect to initial conditions is to compute the average rate at which nearby trajectories diverge from each other. Consider the trajectories  $x_k$  and  $y_k$ , starting, respectively, from  $x_0$  and  $y_0$ . If both trajectories are, until time  $k$ , always in the same linear region, we can write

$$|x_k - y_k| = e^{\lambda k} |x_0 - y_0|, \text{ where } \lambda = \frac{1}{k} \sum_{j=0}^{k-1} \ln |f'_r(x_j)|.$$



**Fig. 2.** Lyapunov exponents estimates for von Bertalanffy's maps Eq.(4), as a function of the intrinsic growth rate  $r$ .

The Lyapunov exponents of a trajectory  $x_k$  is defined by

$$h_{\max} = \lim_{k \rightarrow +\infty} \frac{1}{k} \sum_{j=0}^{k-1} \ln |f'_r(x_j)| \quad (6)$$

whenever it exists. The computation of the Lyapunov exponent  $h_{\max}$  gives the average rate of divergence (if  $h_{\max} > 0$ ), or convergence (if  $h_{\max} < 0$ ) of the two trajectories from each other, during the time interval  $[0, k]$ , see for example [16]. We note that, the Lyapunov exponents depend on two biological parameters: von Bertalanffy's growth rate constant and the asymptotic weight. See in Fig.2 the Lyapunov exponents estimate for von Bertalanffy's maps Eq.(4).

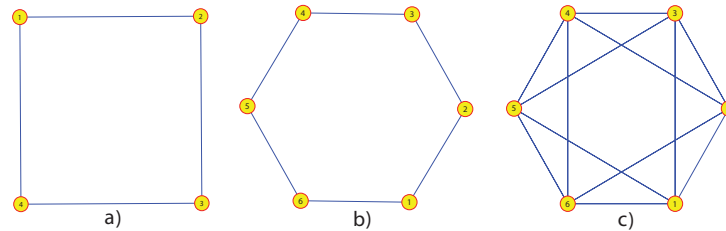
If the coupling parameter  $c$  belongs to the synchronization interval

$$\left] \frac{1 - e^{-h_{\max}}}{\lambda_2}, \frac{1 + e^{-h_{\max}}}{\lambda_N} \right[ \quad (7)$$

then the synchronized states  $x_i(t)$ , ( $i = 1, \dots, N$ ) are exponentially stable, [17]. The second eigenvalue  $\lambda_2$  is known as the algebraic connectivity or Fiedler value and plays a special role in the graph theory. As bigger is  $\lambda_2$ , more easily the network synchronizes. As much larger  $\lambda_2$  is, more difficult is to separate the graph in disconnected parts. The graph is connected if and only if  $\lambda_2 \neq 0$ . In fact, the multiplicity of the null eigenvalue  $\lambda_1$  is equal to the number of connected components of the graph. Fixing the topology of the network, the eigenvalues of the Laplacian  $\lambda_2$  and  $\lambda_N$  are fixed, so the synchronization only depends on the Lyapunov exponent of each node,  $h_{\max}$ . Remark that the synchronization interval also depends on two biological parameters: von Bertalanffy's growth rate constant and the asymptotic weight.

## 4 Numerical simulation and conclusions

To support our approaches, we consider a regular ring lattice, a graph with  $N$  nodes, each one connected to  $k$  neighbors,  $\frac{k}{2}$  on each side, having in each node the same model, the von Bertalanffy maps  $f_r$  given by Eq.(4). See in Fig.3



**Fig. 3.** Lattices. In a) with  $N = 4$  nodes and  $k = 2$ , in b) with  $N = 6$  nodes and  $k = 2$  and in c) with  $N = 6$  nodes and  $k = 4$ . From (a) to (b) the total number of vertices of the network increases maintaining the number of neighbors of each node, and from (b) to (c) increases the number of neighbors of each node, but the total number of vertices of the network remains the same.

some example of lattices. If, for instance,  $N = 6$  and  $K = 4$ , see Fig.3c), the adjacency matrix  $A$  and the Laplacian matrix  $L$  are

$$A = \begin{bmatrix} 0 & 1 & 1 & 0 & 1 & 1 \\ 1 & 0 & 1 & 1 & 0 & 1 \\ 1 & 1 & 0 & 1 & 1 & 0 \\ 0 & 1 & 1 & 0 & 1 & 1 \\ 1 & 0 & 1 & 1 & 0 & 1 \\ 1 & 1 & 0 & 1 & 1 & 0 \end{bmatrix} \quad \text{and} \quad L = D - A = \begin{bmatrix} 4 & -1 & -1 & 0 & -1 & -1 \\ -1 & 4 & -1 & -1 & 0 & -1 \\ -1 & -1 & 4 & -1 & -1 & 0 \\ 0 & -1 & -1 & 4 & -1 & -1 \\ -1 & 0 & -1 & -1 & 4 & -1 \\ -1 & -1 & 0 & -1 & -1 & 4 \end{bmatrix}.$$

So, the network correspondent to the graph in Fig.3 c) is defined by the system,

$$\begin{cases} \dot{x}_1 = f_r(x_1) + c(4x_1 - x_2 - x_3 - x_5 - x_6) \\ \dot{x}_2 = f_r(x_2) + c(-x_1 + 4x_2 - x_3 - x_4 - x_6) \\ \dot{x}_3 = f_r(x_3) + c(-x_1 - x_2 + 4x_3 - x_4 - x_5) \\ \dot{x}_4 = f_r(x_4) + c(-x_2 - x_3 + 4x_4 - x_5 - x_6) \\ \dot{x}_5 = f_r(x_5) + c(-x_1 - x_3 - x_4 + 4x_5 - x_6) \\ \dot{x}_6 = f_r(x_6) + c(-x_1 - x_2 - x_4 - x_5 + 4x_6) \end{cases}.$$

For this lattice the eigenvalues of the Laplacian matrix are  $\lambda_1 = 0$ ,  $\lambda_2 = \lambda_3 = \lambda_4 = 4$  and  $\lambda_5 = \lambda_6 = 6$ . If we consider, for instance,  $r = 6.60$ , the Lyapunov exponent of  $f_r(x)$  is 0.377, Eq.(6). Then, attending to Eq.(7), this lattice synchronizes if  $\frac{1-e^{-0.377}}{2} < c < \frac{1+e^{-0.377}}{6} \Leftrightarrow 0.079 < c < 0.281$  and the amplitude of the synchronization interval is 0.202. For more examples see Table 1. The lattice correspondent to the Fig.3 b) has eigenvalues of the Laplacian matrix  $\lambda_1 = 0$ ,  $\lambda_2 = \lambda_3 = 1$ ,  $\lambda_4 = \lambda_5 = 3$  and  $\lambda_6 = 4$ . Thus, for the same  $r = 6.60$ , the lattice synchronizes if  $0.313 < c < 0.421$  and the amplitude of this interval is 0.107. Moreover, to the lattice in Fig.3 a), the eigenvalues of the Laplacian matrix are  $\lambda_1 = 0$ ,  $\lambda_2 = \lambda_3 = 2$  and  $\lambda_4 = 4$ . For the same  $r = 6.60$ , the lattice synchronizes if  $0.157 < c < 0.421$  and the amplitude of this interval is 0.264. In Table 1 are presented more examples, where we computed the synchronization interval for several values of the intrinsic growth rate  $r$ , for all these lattices a), b) and c) of Fig.3. The results of Table 1 allow us to claim:

- (C1) From the lattice a) to lattice b) in Fig.3, the total number of vertices of the network increases maintaining the number of neighbors of each node.



$r$	$h_{max}$	Synchronization Interval			Amplitude		
		Lattice a)	Lattice b)	Lattice c)	Lattice a)	Lattice b)	Lattice c)
6.50	0.297	]0.128, 0.436[	]0.257, 0.436[	]0.064, 0.291[	0.308	0.179	0.226
6.55	0.347	]0.147, 0.427[	]0.293, 0.427[	]0.073, 0.285[	0.280	0.134	0.211
6.60	0.377	]0.157, 0.421[	]0.313, 0.421[	]0.079, 0.281[	0.264	0.107	0.202
6.65	0.406	]0.167, 0.417[	]0.334, 0.417[	]0.083, 0.278[	0.250	0.083	0.194
6.70	0.463	]0.185, 0.407[	]0.371, 0.407[	]0.093, 0.272[	0.222	0.037	0.179
6.73	0.506	]0.199, 0.401[	]0.397, 0.401[	]0.099, 0.267[	0.202	0.003	0.168
6.74	0.533	]0.207, 0.397[	(*)	]0.103, 0.265[	0.190	(*)	0.161
6.75	0.598	]0.225, 0.388[	(*)	]0.112, 0.258[	0.163	(*)	0.146

**Table 1.** Lyapunov exponent,  $h_{max}$ , synchronization interval,  $\left] \frac{1-e^{-h_{max}}}{\lambda_2}, \frac{1+e^{-h_{max}}}{\lambda_N} \right[$ , and amplitude of this interval,  $\frac{1+e^{-h_{max}}}{\lambda_N} - \frac{1-e^{-h_{max}}}{\lambda_2}$ , for several intrinsic growth rates  $r$ , for the lattices a), b) and c) of Fig.3. (\*) In this case, the desynchronization phenomenon occurs, see (C4).

We verify that the synchronization is worse, not only because it begins to synchronize at a higher value of the coupling parameter  $c$ , but also, because the synchronization interval is shorter.

- (C2) Comparing the results for the lattices b) and c) in Fig.3, we may conclude that maintaining the total number of vertices of the network, but increasing the number of neighbors of each node, the synchronization is better, not only because it begins to synchronize at a lower value of the coupling parameter  $c$ , but also, because the synchronization interval is larger.
- (C3) Observing the columns of Table 1, we verify that, as the intrinsic growth rate  $r$  increases, the synchronization is worse, not just because it begins to synchronize at a higher value of the coupling parameter  $c$ , but also, because the synchronization interval is shorter.
- (C4) Note that, for the intrinsic growth rate  $r = 6.74$  and  $r = 6.75$ , for the lattice b), the upper bound of the synchronization interval is lower than the lower bound. This means that, there is no synchronization for any value of the coupling parameter  $c$ . This desynchronization phenomenon was expected because the network (5) synchronizes only if  $h_{max} < \ln(2R + 1)$ , where  $R = \frac{\lambda_1 - \lambda_2}{\lambda_2 - \lambda_N}$ , see [17]. In the case of lattice b), we have  $\ln(2R + 1) = 0.511$ , so there is synchronization only if  $h_{max} < 0.511$ , which do not happens for  $r = 6.74$  and  $r = 6.75$ . In all the other studied cases, the Lyapunov exponent verifies  $h_{max} < \ln(2R + 1)$ , so we have a non empty synchronization interval.





## Acknowledgment

Research partially sponsored by national funds through the Foundation for Science and Technology, Portugal - FCT under the project PEst-OE/MAT/UI0006/2011, CEAUL, CIMA-UE and ISEL. The authors are grateful to Prof. Danièle Fournier-Prunaret for having made the image of Fig.1(b).

## References

- 1.G.M. Cailliet, W.D. Smith, H.F. Mollet and K.J. Goldman. Age and growth studies of chondrichthyan fishes: the need for consistency in terminology, verification, validation, and growth function fitting. *Environ. Biol. Fish.*, 77: 211–228, 2006.
- 2.A.B. Cooper. A Guide to Fisheries Stock Assessment. From Data to Recommendations. New Hampshire Sea Grant, 2006.
- 3.T.E. Essington, J.F. Kitchell and C.J. Walters. The von Bertalanffy growth function, bioenergetics, and the consumption rates of fish. *Can. J. Fish. Aquat. Sci.*, 58: 2129–2138, 2001.
- 4.J.A. Hutchings and J.D. Reynolds. Marine fish population collapses: consequences for recovery and extinction risk. *BioSci.*, 54: 297–309, 2004.
- 5.V.S. Karpouzi and D. Pauly. Life-History Patterns in Marine Birds. In M.L.D. Palomares and D. Pauly, editors, *Fisheries Centre Research Reports 16 (10), Von Bertalanffy Growth Parameters of Non-Fish Marine Organisms*, pages 27–43, Canada, 2008. The Fisheries Centre, University of British Columbia.
- 6.D. Lind and B. Marcus. An Introduction to Symbolic Dynamics and Codings. 2<sup>nd</sup> edition, Cambridge University Press, Cambridge, 1999.
- 7.J.A. Musick. Criteria to define extinction risk in marine fishes. *Fisheries*, 24: 6–14, 1999.
- 8.J.L. Rocha and S.M. Aleixo. An extension of gompertzian growth dynamics: Weibull and Fréchet models. *Math. Biosci. Eng.*, 10: 379–398, 2013.
- 9.J.L. Rocha and S.M. Aleixo. Dynamical analysis in growth models: Blumberg's equation. *Discrete Contin. Dyn. Syst.-Ser.B*, 18: 783–795, 2013.
- 10.S.J. Schreiber. Chaos and population disappearances in simple ecological models. *J. Math. Biol.*, 42: 239–260, 2001.
- 11.L. Von Bertalanffy. A quantitative theory of organic growth. *Human Biology*, 10: 181–213, 1938.
- 12.L. Von Bertalanffy. Quantitative laws in metabolism and Growth. *The Quarterly Review of Biology*, 32: 217–231, 1957.
- 13.A. Balanov, N. Janson, D. Postnov and O. Sosnovtseva. Synchronization: From Simple to Complex, Springer, 2009.
- 14.A.J. Davidson and M. Menaker, Birds of a feather clock together sometimes: social synchronization of circadian rhythms. *Curr. Opin. Neurobiol.*, 13 (6): 765–769, 2003.
- 15.J.A.L. Silva and F.T. Giordani, Density-dependent migration and synchronism in metapopulations. *Bull. of Math. Bio-*, 68: 451–465, 2006.
- 16.M.Hasler and Y.L. Maistrenko, An introduction to the synchronization of chaotic systems: coupled skew tent maps. *IEEE Trans. on Circ. Syst. - I*, 44 (10): 856–866, 1987.
- 17.X. Li and G. Chen, Synchronization and desynchronization of complex dynamical networks: An engineering viewpoint. *IEEE Trans. on Circ. Syst. -I*, 50 (11): 1381–1390, 2003.





## Mutual information rate and topological order in networks

J. Leonel Rocha<sup>1</sup> and Acilina Caneco<sup>2</sup>

<sup>1</sup> Instituto Superior de Engenharia de Lisboa - ISEL, ADM and CEAUL, Rua  
Conselheiro Emídio Navarro, 1, 1959-007 Lisboa, Portugal  
(E-mail: [jrocha@adm.isel.pt](mailto:jrocha@adm.isel.pt)),

<sup>2</sup> Instituto Superior de Engenharia de Lisboa - ISEL, ADM and CIMA-UE, Rua  
Conselheiro Emídio Navarro, 1, 1959-007 Lisboa, Portugal  
(E-mail: [acilina@adm.isel.pt](mailto:acilina@adm.isel.pt))

**Abstract.** In this paper we study the evolution of the information flow associated with a topological order in networks. The amount of information produced by a network may be measure by the mutual information rate. This measure and the synchronization interval are expressed in terms of the transversal Lyapunov exponents. The networks are constructed by successively joining one edge, maintaining the same number of nodes, and the topological order is described by the monotonicity of the network topological entropy. The network topological entropy measures the complexity of the network topology and it is expressed by the Perron value of the adjacency matrix. We conclude that, as larger the network topological entropy, the larger is the rate with which information is exchanged between nodes of such networks. To illustrate our ideas we present numerical simulations for several networks with a topological order established.

**Keywords:** Mutual information rate, topological entropy, networks.

### 1 Introduction and motivation

Information theory is an area of mathematics and engineering, concerning the quantification of information and it benefits of matters like mathematics, statistics, computer science, physics, neurobiology and electrical engineering. Information theory and synchronization are directly related in a network. The entropy is a fundamental measure of information content and the topological entropy can describe the character of complexity of a network, see for example [10]. In [6], using the mutual information rate to measure the information flow, we have proved that the larger the synchronization is, the larger is the rate with which information is exchanged between nodes in the network. Although the important growth in the field of complex networks, it is still not clear which conditions for synchronization implies information transmission and it is still not known which topology is suitable for the flowing of information. Nevertheless, we conclude with this study that, the more complex is a network, expressed by its topological entropy, the larger is the flux of information.

In this work we study the relationship between the topological order in networks and the transmission of information. The topological order in networks is described by the monotonicity of the network topological entropy. The concept of the network topological entropy was previously introduced in [10]. However,



there are several concepts of network entropy, see [7]. We will use the one based on symbolic dynamics. In Sec.2, we present some preliminaries concepts to be used in the following, such as: fundamental notions of graphs theory, conditions for complete synchronization, communication channel and mutual information rate. Sec.3 is devoted to the study of topological order in networks, using the definition of the network topological entropy. In Sec.4, numerical simulations are presented for several networks with a topological order established. Finally, in Sec.5, we discuss our study and provide some relevant conclusions.

## 2 Preliminaries concepts

In this section, we introduce some notions and basic results on graphs and networks theory. Mathematically, networks are described by graphs (directed or undirected) and the theory of dynamical networks is a combination of graph theory and nonlinear dynamics. From the point of view of dynamical systems, we have a global dynamical system emerging from the interactions between the local dynamics of the individual elements. The tool of graph theory allows us to analyze the coupling structure between them.

A graph  $G$  is an ordered pair  $G = (V, E)$ , where  $V$  is a nonempty set of  $N$  vertices or nodes  $v_i$  and  $E$  is a set of edges or links,  $e_{ij}$ , that connect two vertices  $v_i$  and  $v_j$ . We will only consider the case of undirected graphs, that means that the edge  $e_{ij}$  is the same as the edge  $e_{ji}$ . If the graph  $G$  is not weighted, the adjacency matrix  $A = A(G) = [a_{ij}]$  is defined as follows:

$$a_{ij} = \begin{cases} 1, & \text{if } v_i \text{ and } v_j \text{ are connected} \\ 0, & \text{if } v_i \text{ and } v_j \text{ are not connected} \end{cases} .$$

The degree of a node  $v_i$  is the number of edges incident on it and is denoted by  $k_i$ . For more details in graph theory see [4].

Consider a network of  $N$  identical chaotic dynamical oscillators, described by a connected and undirected graph, with no loops and no multiple edges. In each node the dynamics of the oscillators is defined by  $\dot{x}_i = f(x_i)$ , with  $f : \mathbb{R}^n \rightarrow \mathbb{R}^n$  and  $x_i \in \mathbb{R}^n$  is the state variables of the node  $i$ . The state equations of this network are

$$\dot{x}_i = f(x_i) + \sigma \sum_{j=1}^N l_{ij} x_j, \quad \text{with } i = 1, 2, \dots, N \quad (1)$$

where  $\sigma > 0$  is the coupling parameter,  $L = [l_{ij}] = A - D$  is the Laplacian matrix or coupling configuration of the network. One of the most important subjects under investigation is the network synchronizability, fixing the connection topology and varying the local dynamics or fixing the local dynamic and varying the connection topology [5]. In [9] it was establish that complete synchronization can be achieved provided that all the conditional Lyapunov exponents are negative. In Sec.4, we use this result to determine the synchronization interval. The negativity of the conditional Lyapunov exponents is a necessary condition for the stability of the synchronized state, [3]. It is also a mathematical expression of the decreasing to zero of the logarithm average of



the distance of the solutions on the transverse manifold to the solutions on the synchronization manifold.

A communication channel represents a pathway through which information is exchanged. In this work, a communication channel is considered to be formed by a transmitter  $S_i$  and a receiver  $S_j$ , where the information about the transmitter can be measured. In a network, each one of the links between them, i.e., each one of the edges of the corresponding graph, represents a communication channel. In [1], it is defined the mutual information rate (MIR) between one transmitter  $S_i$  and one receiver  $S_j$ , denoted by  $I_C(S_i, S_j)$ , by

$$I_C(S_i, S_j) = \begin{cases} \lambda_{\parallel} - \lambda_{\perp}, & \text{if } \lambda_{\perp} > 0 \\ \lambda_{\parallel} & , \text{ if } \lambda_{\perp} \leq 0 \end{cases}, \quad (2)$$

where  $\lambda_{\parallel}$  denotes the positive Lyapunov exponents associated to the synchronization manifold and  $\lambda_{\perp}$  denotes the positive Lyapunov exponents associated to the transversal manifold, between  $S_i$  and  $S_j$ .  $\lambda_{\parallel}$  represents the information (entropy production per time unit) produced by the synchronous trajectories and corresponds to the amount of information transmitted. On the other hand,  $\lambda_{\perp}$  represents the information produced by the nonsynchronous trajectories and corresponds to the information lost in the transmission, the information that is erroneously retrieved in the receiver. For more details and references see for example [1] and [2]. In [6], we prove that as the coupling parameter increases, the mutual information rate increases to a maximum at the synchronization interval and then decreases.

### 3 Topological order in networks

In this section we study a topological order in networks, which are constructed by successively joining one edge, maintaining the same number of nodes. This topological order is described by the monotonicity of the network topological entropy. The introduction of the network topological entropy concept was made in [10], which requires a strict and long construction, using tools of symbolic dynamics and algebraic graph theory. However, we present some basic aspects of this definition. The topological entropy  $h_{top}(X)$  of a shift dynamical system  $(X, \sigma)$  over some finite alphabet  $\mathcal{A}$  is defined by

$$h_{top}(X) = \lim_{n \rightarrow \infty} \frac{\log Tr(A^n(X))}{n}$$

and  $h_{top}(X) = 0$  if  $X = \emptyset$ , where  $A(X)$  is the transition matrix of  $X$ , [8]. We remark that the transition matrix  $A(X)$  describes the dynamics between the nodes of the network, which is represented by a graph  $G$ . The Perron-Frobenius Theorem states that, if the adjacency matrix  $A \neq 0$  is irreducible and  $\lambda_A$  is the Perron value of  $A$ , then  $h_{top}(X) = \log \lambda_A$ . We calculate the topological entropy of the associated dynamical system, which is equal to the logarithm of the growth rate of the number of admissible words, [8]. If we have a network associated to a graph  $G$ , which determine the shift space  $X$ , we will call network topological entropy of  $G$  the quantity  $h_{top}(X)$ , i.e.,

$$h_{top}(G) = h_{top}(X) = \log \lambda_A. \quad (3)$$



The following result establishes a topological order in networks.

**Proposition 1.** *Let  $G_1$  and  $G_2$  be two undirected graphs, with the same number of vertices  $N$ , and  $G_1$  be a not complete graph. If the graph  $G_2$  is obtained from the graph  $G_1$  by joining an edge, then  $h_{top}(G_2) > h_{top}(G_1)$ .*

*Proof.* Let  $A = [a_{ij}]$  and  $B = [b_{ij}]$  be the adjacency matrices of the graphs  $G_1$  and  $G_2$ , respectively. If the graph  $G_2$  is obtained from the graph  $G_1$  by joining an edge, then the adjacency matrix  $B$  is obtained from the adjacency matrix  $A$  by replacing some entry  $a_{ij} = 0$  by  $b_{ij} = 1$ . As the graphs  $G_1$  and  $G_2$  are not directed, then the matrices  $A$  and  $B$  are symmetric, and  $b_{ji} = 1$ . Thus, the matrix  $B$  is equal to the matrix  $A$  plus some matrix with non negative entries. For any power  $n$ , we have  $B^n = A^n + C$ , for some matrix  $C$  whose entries are all non negative. As  $Tr(C) \geq 0$  and  $Tr(B^n) = Tr(A^n) + Tr(C)$ , then  $Tr(B^n) > Tr(A^n)$ . Consequently, we obtain  $\frac{\log Tr(B^n)}{n} > \frac{\log Tr(A^n)}{n}$ , for all integers  $n$ . From the definition of network topological entropy, Eq.(3), we have  $h_{top}(G_2) > h_{top}(G_1)$ .

#### 4 Numerical simulations

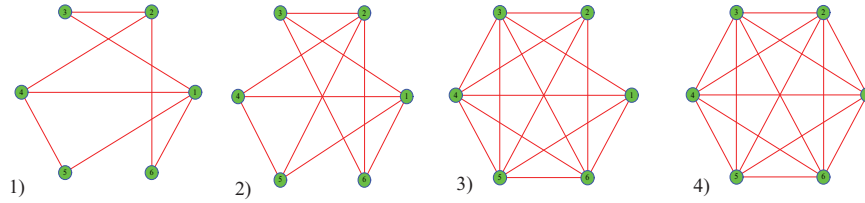
In this section we will consider, as an example, a network with  $N = 6$  nodes, having in each node the same skew-tent map,  $f : [0, 1] \rightarrow [0, 1]$ , defined by

$$f(x) = \begin{cases} \frac{x}{a} & , \text{ if } 0 \leq x \leq a \\ \frac{1-x}{1-a} & , \text{ if } a < x \leq 1 \end{cases}, \quad (4)$$

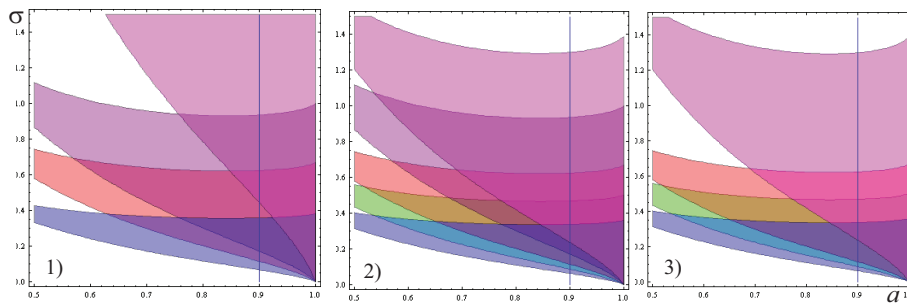
with  $0.5 \leq a < 1$ , see [6]. See Fig.1 where we present some examples of these networks. We start with a network of 7 edges, without the edges 1 - 2, 3 - 5, 5 - 6, 3 - 4, 4 - 6, 2 - 5, 3 - 6 and 2 - 4, and each time we add one edge, the last one of this list. We evaluate the eigenvalues of the Jacobian matrix, the Lyapunov exponents, the region where all transversal Lyapunov exponents are negatives, the synchronization interval and the mutual information rate for all communication channels of these networks. In order to compare the results, as we add one edge, we consider for all studied cases the same value  $a = 0.9$  of the skew-tent map parameter. For this network, the region where all transversal Lyapunov exponents are negatives do not intersect the line  $a = 0.9$ . So, for this value of  $a$  there is no synchronization interval, see 1) of Fig.2, and we do not evaluate the mutual information rate in this case.

We present the details for the network with 8 edges shown in 1) of Fig.1. The adjacency matrix  $A$  and the Laplacian matrix  $L$  of this network are:

$$A = \begin{bmatrix} 0 & 0 & 1 & 1 & 1 & 1 \\ 0 & 0 & 1 & 1 & 0 & 1 \\ 1 & 1 & 0 & 0 & 0 & 0 \\ 1 & 1 & 0 & 0 & 1 & 0 \\ 1 & 0 & 0 & 1 & 0 & 0 \\ 1 & 1 & 0 & 0 & 0 & 0 \end{bmatrix} \quad \text{and} \quad L = A - D = \begin{bmatrix} -4 & 0 & 1 & 1 & 1 & 1 \\ 0 & -3 & 1 & 1 & 0 & 1 \\ 1 & 1 & -2 & 0 & 0 & 0 \\ 1 & 1 & 0 & -3 & 1 & 0 \\ 1 & 0 & 0 & 1 & -2 & 0 \\ 1 & 1 & 0 & 0 & 0 & -2 \end{bmatrix},$$



**Fig. 1.** Construction of networks by successively joining one edge, with 8, 10, 14 and 15 edges and  $N = 6$  nodes.



**Fig. 2.** Regions where the transversal Lyapunov exponents are negatives. The synchronization region is the intersection of these regions. In the vertical axis is the coupling parameter  $\sigma$  and in the horizontal axis is the tent map parameter  $a$ . In 1) is the network with 7 edges, in 2) with 8 edges, and in 3) with 9 edges. The image in 1) shows that for  $a = 0.9$  there is no synchronization interval because the intersection of the regions where all transversal Lyapunov exponents are negatives does not occur for  $a = 0.9$ .

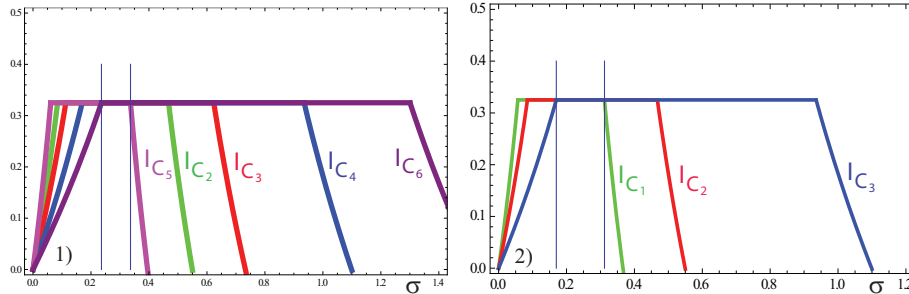
where  $D$  is the diagonal matrix with entries  $d_{ii} = k_i$ , being  $k_i$  the degree of each node  $i$ . This network is defined by the following system,

$$\begin{cases} \dot{x}_1 = f(x_1) + \sigma(-4x_1 + x_3 + x_4 + x_5 + x_6) \\ \dot{x}_2 = f(x_2) + \sigma(-3x_2 + x_3 + x_4 + x_6) \\ \dot{x}_3 = f(x_3) + \sigma(x_1 + x_2 - 2x_3) \\ \dot{x}_4 = f(x_4) + \sigma(x_1 + x_2 - 3x_4 + x_5) \\ \dot{x}_5 = f(x_5) + \sigma(x_1 + x_4 - 2x_5) \\ \dot{x}_6 = f(x_6) + \sigma(x_1 + x_2 - 2x_6) \end{cases},$$

where  $\sigma$  is the coupling parameter. The Jacobian matrix is given by,

$$J = \begin{bmatrix} c - 4\sigma & 0 & \sigma & \sigma & \sigma & \sigma \\ 0 & c - 3\sigma & \sigma & \sigma & 0 & \sigma \\ \sigma & \sigma & c - 2\sigma & 0 & 0 & 0 \\ \sigma & \sigma & 0 & c - 3\sigma & \sigma & 0 \\ \sigma & 0 & 0 & \sigma & c - 2\sigma & 0 \\ \sigma & \sigma & 0 & 0 & 0 & c - 2\sigma \end{bmatrix},$$

being  $c = c(x)$  the slope of  $f$ , Eq.(4), given by  $c(x) = \frac{1}{a}$ , if  $x \leq a$  and  $c(x) = -\frac{1}{1-a}$  if  $x > a$ . The eigenvalues of the Jacobian are  $\mu_1 = c$ ,  $\mu_2 = c - 4\sigma$ ,  $\mu_3 = c - 3\sigma$ ,  $\mu_4 = c - 2\sigma$ ,  $\mu_5 = c - \frac{7}{2}\sigma - \frac{\sqrt{17}}{2}$  and  $\mu_6 = c - \frac{7}{2}\sigma - \frac{\sqrt{17}}{2}$ . The



**Fig. 3.**  $I_{C_i}$  for the network with 8 edges in 1) of Fig.1 and with 10 edges in 2) of Fig.1.

first eigenvector is  $(1, 1, 1, 1, 1, 1)$  and it corresponds to the parallel Lyapunov exponent  $\lambda_{\parallel}$ . The others eigenvectors correspond to the transversal Lyapunov exponents  $\lambda_{\perp_i}$ , with  $i = 2, 3, 4, 5, 6$ . So, the parallel Lyapunov exponent is

$$\lambda_{\parallel} = \int \ln |\mu_1| = \int_0^a \ln \frac{1}{a} + \int_a^1 \ln \left| \frac{-1}{1-a} \right| = -a \ln a - (1-a) \ln(1-a) \quad (5)$$

and the transversal Lyapunov exponents are

$$\lambda_{\perp_i} = a \ln \left| \frac{1}{a} - \nu_i \sigma \right| + (1-a) \ln \left| -\frac{1}{1-a} - \nu_i \sigma \right|, \quad \text{with } i = 2, 3, 4, 5, 6$$

where  $\nu_2 = 4$ ,  $\nu_3 = 3$ ,  $\nu_4 = 2$ ,  $\nu_5 = \frac{7}{2}\sigma + \frac{\sqrt{17}}{2}$  and  $\nu_6 = \frac{7}{2}\sigma - \frac{\sqrt{17}}{2}$ . In order to have synchronization, all transversal Lyapunov exponents must be negatives, see 2) in Fig.2. In this figure, each color corresponds to a region where one of the transversal Lyapunov exponents is negative. For example, if  $a = 0.9$ , then the synchronization interval is  $]0.236, 0.336[$ , where all the transversal Lyapunov exponents  $\lambda_{\perp_i}$  are negative. See also 3) in Fig.2 for the network with 9 edges. To evaluate the mutual information rate (MIR), according to Eq.(2), for each  $\lambda_{\perp_i}$  we obtain the interval  $]a_i, b_i[$  where  $\lambda_{\perp_i} < 0$ , thus

$$I_{C_i} = \begin{cases} -a \ln a - (1-a) \ln(1-a) - a \ln \left| \frac{1}{a} - \nu_i \sigma \right| - (1-a) \ln \left| -\frac{1}{1-a} - \nu_i \sigma \right|, & \text{if } \sigma < a_i \text{ or } \sigma > b_i \\ -a \ln a - (1-a) \ln(1-a), & \text{if } a_i < \sigma < b_i \end{cases}$$

with  $a = 0.9$  and  $i = 2, 3, 4, 5, 6$ . See in 1) of Fig.3 the plots of these  $I_{C_i}$ . The MIR attains its maximum  $0.325\dots$ , in an interval of length  $1.028$  and the network topological entropy, given by Eq.(3), is  $\log \lambda_A = 1.02835\dots$

The second case that we study in detail is the network with 10 edges and without the edges, see 2) of Fig.1. The adjacency matrix  $A$  and the Laplacian matrix  $L$  are given by,

$$A = \begin{bmatrix} 0 & 0 & 1 & 1 & 1 & 1 \\ 0 & 0 & 1 & 1 & 1 & 1 \\ 1 & 1 & 0 & 0 & 0 & 1 \\ 1 & 1 & 0 & 0 & 1 & 0 \\ 1 & 1 & 0 & 1 & 0 & 0 \\ 1 & 1 & 1 & 0 & 0 & 0 \end{bmatrix} \quad \text{and} \quad L = A - D = \begin{bmatrix} -4 & 0 & 1 & 1 & 1 & 1 \\ 0 & -4 & 1 & 1 & 1 & 1 \\ 1 & 1 & -3 & 0 & 0 & 1 \\ 1 & 1 & 0 & -3 & 1 & 0 \\ 1 & 1 & 0 & 1 & -3 & 0 \\ 1 & 1 & 1 & 0 & 0 & -3 \end{bmatrix}.$$





This network is defined by the system,

$$\begin{cases} \dot{x}_1 = f(x_1) + \sigma(-4x_1 + x_3 + x_4 + x_5 + x_6) \\ \dot{x}_2 = f(x_2) + \sigma(-4x_2 + x_3 + x_4 + x_5 + x_6) \\ \dot{x}_3 = f(x_3) + \sigma(x_1 + x_2 - 3x_3 + x_4) \\ \dot{x}_4 = f(x_4) + \sigma(x_1 + x_2 - 3x_4 + x_5) \\ \dot{x}_5 = f(x_5) + \sigma(x_1 + x_2 + x_4 - 3x_5) \\ \dot{x}_6 = f(x_6) + \sigma(x_1 + x_2 + x_3 - 3x_6) \end{cases},$$

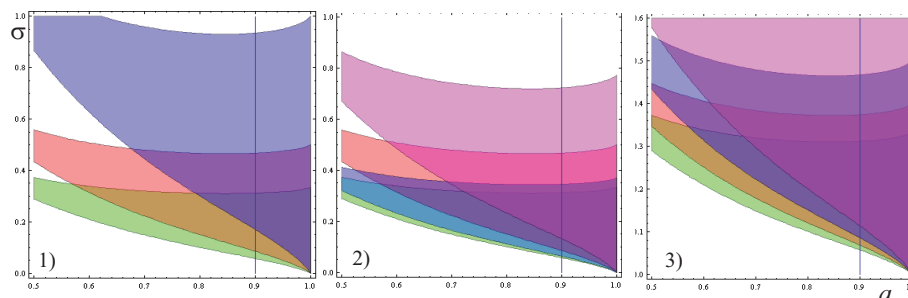
and the Jacobian matrix is given by

$$J = \begin{bmatrix} c-4\sigma & 0 & \sigma & \sigma & \sigma & \sigma \\ 0 & c-4\sigma & \sigma & \sigma & \sigma & \sigma \\ \sigma & \sigma & c-3\sigma & \sigma & 0 & 0 \\ \sigma & \sigma & \sigma & c-3\sigma & \sigma & 0 \\ \sigma & \sigma & 0 & \sigma & c-3\sigma & 0 \\ \sigma & \sigma & \sigma & 0 & 0 & c-3\sigma \end{bmatrix}.$$

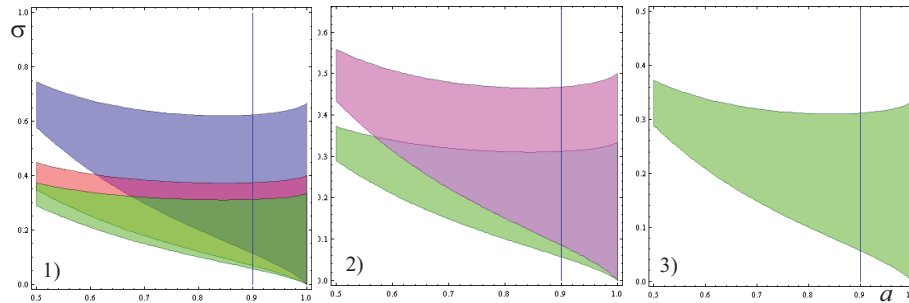
The eigenvalues of the Jacobian matrix are  $\mu_1 = c$ ,  $\mu_2 = c - 6\sigma$ ,  $\mu_3 = \mu_4 = \mu_5 = c - 4\sigma$  and  $\mu_6 = c - 2\sigma$ . Thus, the parallel Lyapunov exponent is identical to the previous case, Eq.(5), and the transversal Lyapunov exponents are

$$\lambda_{\perp_i} = a \ln \left| \frac{1}{a} - \nu_i \sigma \right| + (1-a) \ln \left| -\frac{1}{1-a} - \nu_i \sigma \right|, \quad \text{with } i = 2, 3, 4$$

where  $\nu_2 = 6$ ,  $\nu_3 = 4$  and  $\nu_4 = 2$ . See 1) in Fig.4 the regions where these transversal Lyapunov exponents are negatives. For  $a = 0.9$ , this network synchronizes if  $\sigma \in ]0.170, 0.312[$ . We compute the  $I_{C_i}$  like in the previous case and we plot its graphics in 2) of Fig.3. The MIR attains its maximum 0.325..., in an interval of length 1.216 and the network topological entropy is  $\log \lambda_A = 1.21559...$  Figs.4, 5 and Table 1 contain information similar to the other cases analyzed in this topological order.



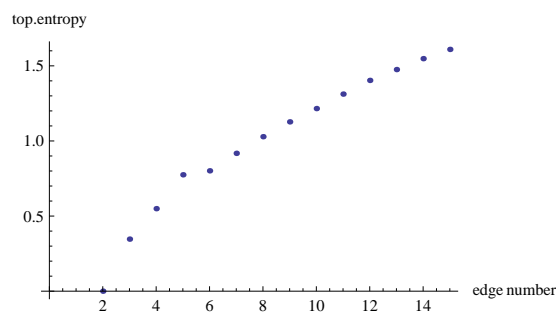
**Fig. 4.** Regions where the transversal Lyapunov exponents are negatives. The synchronization region is the intersection of these regions. In 1) is the network with 10 edges, in 2) with 11 edges, and in 3) with 12 edges. For the same value of  $a$ , the amplitude of the synchronization interval increases.



**Fig. 5.** Regions where the transversal Lyapunov exponents are negative. The synchronization region is the intersection of these regions. In 1) is the network with 13 edges, in 2) with 14 edges and in 3) with 15 edges (complete network). For the same value of  $a$ , the amplitude of the synchronization interval increases.

Edges	$\mu_i = c - \nu_i \sigma$ ( $i = 2, 3, 4, 5, 6$ )	Sync. interv.	Ampl.	$\log \lambda_A$
8	$\nu_2 = 4, \nu_3 = 3, \nu_4 = 2, \nu_5 = \frac{7+\sqrt{17}}{2}, \nu_6 = \frac{7-\sqrt{17}}{2}$	]0.236,0.336[	0.100	1.028
9	$\nu_2 = \nu_3 = 4, \nu_4 = 3, \nu_5 = \frac{7+\sqrt{17}}{2}, \nu_6 = \frac{7-\sqrt{17}}{2}$	]0.236,0.336[	0.100	1.127
10	$\nu_2 = 6, \nu_3 = \nu_4 = \nu_5 = 4, \nu_6 = 2$	]0.170,0.312[	0.142	1.216
11	$\nu_2 = 6, \nu_3 = \nu_4 = 4, \nu_5 = 4 + \sqrt{2}, \nu_6 = 4 - \sqrt{2}$	]0.131,0.312[	0.181	1.312
12	$\nu_2 = \nu_3 = 6, \nu_4 = 5, \nu_5 = 4, \nu_6 = 3$	]0.113,0.312[	0.199	1.403
13	$\nu_2 = \nu_3 = \nu_4 = 6, \nu_5 = \nu_6 = 4$	]0.085,0.312[	0.227	1.475
14	$\nu_2 = \nu_3 = \nu_4 = \nu_5 = 6, \nu_6 = 4$	]0.085,0.312[	0.227	1.548
15	$\nu_2 = \nu_3 = \nu_4 = \nu_5 = \nu_6 = 6$	]0.057,0.312[	0.255	1.609

**Table 1.** Jacobian eigenvalues,  $\mu_i$ , for ( $i = 2, 3, 4, 5, 6$ ), which correspond to the transversal Lyapunov exponents, synchronization interval, its amplitude, network topological entropy and the number of edges from 8 to 15 (complete network).



**Fig. 6.** The network topological entropy increases as the the number of edges of the network increases.

## 5 Conclusions and discussion

We started our simulations, considering the network with 8 edges and without the edges 1 – 2, 3 – 5, 5 – 6, 3 – 4, 4 – 6, 2 – 5 and 3 – 6, and in each step we add the last edge of this list. In each step of this construction, we obtain the Laplacian matrix and compute the eigenvalues  $\mu_i$  ( $i = 1, 2, 3, 4, 5, 6$ ) of the Jacobian matrix, the parallel and transversal Lyapunov exponents, the



synchronization interval, the network topological entropy and the  $I_{C_i}$  for the networks with 8, 9, 10, 11, 12, 13, 14 and 15 edges (complete network). For all these cases  $\mu_1 = c$  and this eigenvalue correspond to the synchronization manifold. The others  $\mu_i$  correspond to the transversal Lyapunov exponents and are presented in Table 1. In this table is also presented the synchronization interval and the network topological entropy, for all these cases. See in Figs.2, 4 and 5 the synchronization regions, in terms of the skew-tent map parameter  $a$  and of the coupling parameter  $\sigma$ . In Fig.6 we may see that the network topological entropy increases as we add one edge successively to the network.

From the numerical simulations shown in figures and Table 1, we conclude that, with the topological order established, the interval where the mutual information rate attains its maximum, the synchronization interval, increases its amplitude. Thus, we claim that, as larger the network topological entropy, the larger is the rate with which information is exchanged between nodes in the network.

## Acknowledgment

This work is funded by FCT through the National Funds - Foundation for Science and Technology within the project PEst-OE/MAT/UI0006/2011, CIMA-UE, CEAUL and ISEL.

## References

- 1.M. S. Baptista and J. Kurths, Chaotic channel, *Phys. Rev. E*, **72**, 045202R, (2005).
- 2.M. S. Baptista and J. Kurths, Information transmission in active networks, *Phys. Rev. E*, **77**, 026205, (2008).
- 3.S. Boccaletti, J. Kurths, G. Osipov, D.L. Valladares and C.S. Zhou, The synchronization of chaotic systems, *Physics Reports*, **366**, 1-101, (2002).
- 4.B. Bollobás and O.M. Riordan, *Handbook of Graphs and Networks: From the Genome to the Internet*, Wiley-VCH, 2003.
- 5.A. Caneco, S. Fernandes, C. Grácio and J.L. Rocha, Networks synchronizability, local dynamics and some graph invariants, *Dynamics, Games and Science I, Springer Proceedings in Mathematics*, **1**, 221-238, (2011).
- 6.A. Caneco and J.L. Rocha, Synchronization and information transmission in networks, *submitted*.
- 7.L. Ji, B.-H. Wang, W.-X. Wang and T. Zhou, Network entropy based on topology configuration and its computation to random networks, *Chin. Phys. Lett.*, **25**, 11, 4177, (2008).
- 8.D. Lind and B. Marcus, *Symbolic Dynamics and Coding*, Cambridge University Press, 1995.
- 9.L. M. Pecora and T. L. Carroll, Driving systems with chaotic signals, *Phys. Rev. A*, **44**, 2374-2383, (1991).
- 10.J.L. Rocha, C. Grácio, S. Fernandes, A. Caneco, Spectral and dynamical invariants in a complete clustered network, *submitted*.





## Synchronization in von Bertalanffy's models

J. Leonel Rocha<sup>1</sup>, Sandra M. Aleixo<sup>1</sup> and Acilina Caneco<sup>2</sup>

<sup>1</sup> Instituto Superior de Engenharia de Lisboa - ISEL, ADM and CEAUL, Rua  
Conselheiro Emídio Navarro, 1, 1959-007 Lisboa, Portugal  
(E-mail: [jrocha@adm.isel.pt](mailto:jrocha@adm.isel.pt), [sandra.aleixo@adm.isel.pt](mailto:sandra.aleixo@adm.isel.pt)),

<sup>2</sup> Instituto Superior de Engenharia de Lisboa - ISEL, ADM and CIMA-UE, Rua  
Conselheiro Emídio Navarro, 1, 1959-007 Lisboa, Portugal  
(E-mail: [acilina@adm.isel.pt](mailto:acilina@adm.isel.pt))

**Abstract.** Many data have been useful to describe the growth of marine mammals, invertebrates and reptiles, seabirds, sea turtles and fishes, using the logistic, the Gompertz and von Bertalanffy's growth models. A generalized family of von Bertalanffy's maps, which is proportional to the right hand side of von Bertalanffy's growth equation, is studied and its dynamical approach is proposed. The system complexity is measured using Lyapunov exponents, which depend on two biological parameters: von Bertalanffy's growth rate constant and the asymptotic weight.

Applications of synchronization in real world is of current interest. The behaviour of birds flocks, schools of fish and other animals is an important phenomenon characterized by synchronized motion of individuals. In this work, we consider networks having in each node a von Bertalanffy's model and we study the synchronization interval of these networks, as a function of those two biological parameters. Numerical simulation are also presented to support our approaches.

**Keywords:** Von Bertalanffy's models, synchronization, Lyapunov exponents.

### 1 Introduction and motivation

Several mathematical equations have been used to describe the growth of marine populations, namely fishes, seabirds, marine mammals, invertebrates, reptiles and sea turtles. Among these equations, three of the most familiar are the logistics, the Gompertz and the von Bertalanffy models, see [5] and references therein. For a certain population, the growth of an individual, regarded as an increase in its length or weight with increasing age, is commonly modeled by a mathematical equation that represents the growth of an "average" individual in the population. One of the most popular functions that have been used to analyze the increase in average length or weight of fish is von Bertalanffy's model, see for example [1] and [3].

Synchronization is a fundamental nonlinear phenomenon, which can be observed in many real systems, in physics, chemistry, mechanics, engineering, secure communications or biology, see for example [13]. It can be observed in living beings, on the level of single cells, physiological subsystems, organisms and even on the level of large populations. Sometimes, this phenomenon is essential for a normal functioning of a system, e.g. for the performance of a pacemaker, where the synchronization of many cells produce a macroscopic rhythm that governs respiration and heart contraction. Sometimes, the synchrony leads to a severe pathology, e.g. in case of the Parkinson's disease, when



locking of many neurons leads to the tremor activity. Biological systems use internal circadian clocks to efficiently organize physiological and behavioral activity within the 24-hour time domain. For some species, social cues can serve to synchronize biological rhythms. Social influences on circadian timing might function to tightly organize the social group, thereby decreasing the chances of predation and increasing the likelihood of mating, see [14]. Almost all seabirds breed in colonies; colonial and synchronized breeding is hypothesized to reduce predation risk and increases social interactions, thereby reducing the costs of breeding. On the other hand, it is believed that synchronization may promote extinctions of some species. Full synchronism may have a deleterious effect on population survival because it may lead to the impossibility of a recolonization in case of a large global disturbance, see [15]. Understand the aggregate motions in the natural world, such as bird flocks, fish schools, animal herds, or bee swarms, for instance, would greatly help in achieving desired collective behaviors of artificial multi-agent systems, such as vehicles with distributed cooperative control rules.

The layout of this paper is as follows. In Sec.2, we present a new dynamical approach to von Bertalanffy's growth equation, a family of unimodal maps, designated by von Bertalanffy's maps. In Sec.3, we present the network model having in each node a von Bertalanffy's model. The synchronization interval is presented in terms of the network connection topology, expressed by its Laplacian matrix and of the Lyapunov exponent of the network's nodes. In Sec.4, we give numerical simulations on some kinds of lattices, evaluating its synchronization interval. We present some discussion on how this interval changes with the increasing of the number of neighbors of each node, with the increasing of the total number of nodes and with the intrinsic growth rate. Also, we observe and discuss some desynchronization phenomenon.

## 2 Von Bertalanffy's growth dynamics approach

An usual form of von Bertalanffy's growth function, one of the most frequently used to describe chick growth in marine birds and in general marine growths, is given by

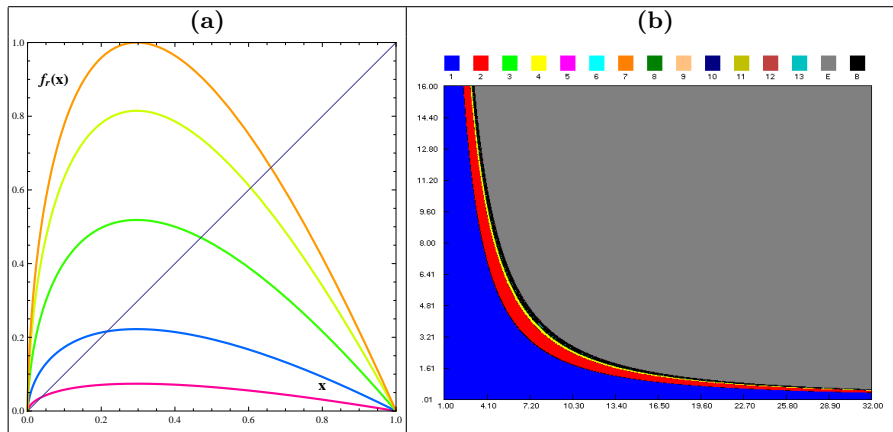
$$W_t = W_\infty \left(1 - e^{-\frac{K}{3}(t-t_0)}\right)^3, \quad (1)$$

where  $W_t$  is the weight at age  $t$ ,  $W_\infty$  is the asymptotic weight,  $K$  is von Bertalanffy's growth rate constant and  $t_0$  is the theoretical age the chick would have at weight zero. The growth function, Eq.(1), is solution of the von Bertalanffy's growth equation,

$$g(W_t) = \frac{dW_t}{dt} = \frac{K}{3} W_t^{\frac{2}{3}} \left(1 - \left(\frac{W_t}{W_\infty}\right)^{\frac{1}{3}}\right), \quad (2)$$

introduced by von Bertalanffy to model fish weight growth, see [11] and [12]. The *per capita* growth rate, associated to this growth model, is given by

$$h(W_t) = \frac{g(W_t)}{W_t} = \frac{K}{3} W_t^{-\frac{1}{3}} \left(1 - \left(\frac{W_t}{W_\infty}\right)^{\frac{1}{3}}\right). \quad (3)$$



**Fig. 1.** (a) Graphics of von Bertalanffy's maps  $f_r(x)$ , Eq.(4), for several values of intrinsic growth rate  $r$  (0.5 (magenta), 1.5, 3.5, 5.5 and 6.75 (orange)); (b) Bifurcation diagram of von Bertalanffy's maps  $f_r(x)$  in the  $(K, W_\infty)$  parameter plane. The blue region is the stability region. The period doubling and chaotic regions correspond to the cycles shown on top of figure. The gray region is the inadmissible region.

In this paper, we consider a family of unimodal maps, the von Bertalanffy maps, which is proportional to the right hand side of von Bertalanffy's equation, Eq.(2),  $f_r : [0, 1] \rightarrow [0, 1]$ , defined by

$$f_r(x) = r x^{\frac{2}{3}} \left(1 - x^{\frac{1}{3}}\right), \quad (4)$$

with  $x = \frac{W_i}{W_\infty} \in [0, 1]$  the normalized weight and  $r = r(K, W_\infty) = \frac{K}{3} \times W_\infty^{\frac{2}{3}} > 0$  an intrinsic growth rate of the individual weight, see Fig.1(a).

Remark that, the family of maps that we will study depends on two biological parameters: von Bertalanffy's growth rate constant  $K$  and the asymptotic weight  $W_\infty$ . The following conditions are satisfied:

- (A1)  $f_r$  is continuous on  $[0, 1]$ ;
- (A2)  $f_r$  has an unique critical point  $c \in ]0, 1[$ ;
- (A3)  $f'_r(x) \neq 0, \forall x \in ]0, 1[ \setminus \{c\}$ ,  $f'_r(c) = 0$  and  $f''_r(c) < 0$ ;
- (A4)  $f_r \in C^3(]0, 1[)$  and the Schwarzian derivative of  $f_r$ , denoted by  $S(f_r(x))$ , verifies  $S(f_r(x)) < 0, \forall x \in ]0, 1[ \setminus \{c\}$  and  $S(f_r(c)) = -\infty$ .

Conditions (A1)–(A4) are essential to prove the stability of the only positive fixed point, [10]. In particular, the negative Schwarzian derivative ensures a “good” dynamic behavior of the models. In general, the growth models studied have negative Schwarzian derivative and the use of unimodal maps is usual, see for example [8] and [9].

The dynamical complexity of the proposed models is displayed at  $(K, W_\infty)$  parameter plane, depending on the variation of the intrinsic growth rate  $r$ . The analysis of their bifurcations structure is done based on the bifurcation diagram, see Fig.1(b). For these models, the extinction region and the semistability



curve have no expressive meaning. Because it is difficult to identify *per capita* growth rates, Eq.(3), less than one for all densities, to the extinction case, and *per capita* growth rates strictly less than one for all densities, except at one population density, to the semistability case, except at most a set of measure zero. We verify that,  $\lim_{x \rightarrow 0^+} f'_r(x) > 1$  and the origin's basin of attraction is empty, except at most a set of measure zero. The fixed point 0 is unstable.

A behavior of stability is defined when a population persists for intermediate initial densities and otherwise goes extinct. The *per capita* growth rate of the population, Eq.(3), is greater than one for an interval of population densities. The lower limit of these densities correspond to the positive fixed point  $A_{K, W_\infty} \equiv A_r$ , of each function  $f_r$ , Eq.(4), see Fig.1(a). Furthermore, attending to (A2) and (A3) we have that  $f_r^2(c) > 0$ , then there is a linearly stable fixed point  $A_r \in ]0, 1[$ , whose basin of attraction is  $]0, 1[$ , for more details see [10].

The symbolic dynamics techniques prove to be a good method to determine a numerical approximation to the stability region (in blue), see Fig.1(b). For more details about symbolic dynamics techniques see for example [8]. In the  $(K, W_\infty)$  parameter plane, this region is characterized by the critical point iterates that are always attracted to the fixed point sufficiently near of the super stable or super attractive point  $\tilde{A}_r$ , defined by  $f_r(c) = c$ . Let  $\bar{A}_r \in ]0, 1[$  be the fixed points sufficiently near of  $\tilde{A}_r$ , then

$$\lim_{n \rightarrow \infty} f_r^n(c) = \bar{A}_r, \text{ for } \left(3K^{-1}A_r^{\frac{1}{3}}\left(1 - A_r^{\frac{1}{3}}\right)\right)^{\frac{3}{2}} < W_\infty(K) < \hat{W}_\infty(K)$$

where  $\hat{W}_\infty(K)$  represents the super stable curve of the cycle of order 2, given in implicit form by  $f_r^2(c) = c$ . In this parameter plane, the set of the super stable or super attractive points  $\tilde{A}_r$  defines the super stable curve of the fixed point. In the region before reaching the super stable curve, the symbolic sequences associated to the critical points orbits are of the type  $CL^\infty$ . After this super stable curve, the symbolic sequences are of the type  $CR^\infty$ . In this parameter region, the topological entropy is null, [6].

The period doubling region corresponds to the parameters values, to which the population weight oscillates asymptotically between  $2^n$  states, with  $n \in \mathbb{N}$ . In period-doubling cascade, the symbolic sequences correspondent to the iterates of the critical points are determined by the iterations  $f_r^{2^n}(c) = c$ . Analytically, these equations define the super-stability curves of the cycle of order  $2^n$ . The period doubling region is bounded below by the curve of the intrinsic growth rate values where the period doubling starts,  $\hat{W}_\infty(K)$ , correspondent to the 2-period symbolic sequences  $(CR)^\infty$ . Usually, the upper limit of this region is determined using values of intrinsic growth rate  $r$ , corresponding to the first symbolic sequence with non null topological entropy. Commonly, the symbolic sequence that identifies the beginning of chaos is  $(CRLR^3)^\infty$ , a 6-periodic orbit, see for example [8] and [9]. The unimodal maps in this region, also have null topological entropy, [6].

In the chaotic region of the  $(K, W_\infty)$  parameter plane, the evolution of the population size is *a priori* unpredictable. The maps are continuous on the interval with positive topological entropy whence they are chaotic and





the Sharkovsky ordering is verified. The symbolic dynamics are characterized by iterates of the functions  $f_r$  that originate orbits of several types, which already present chaotic patterns of behavior. The topological entropy is a non-decreasing function in order to the parameter  $r$ , until reaches the maximum value  $\ln 2$  (consequence of the negative Schwartzian derivative). In [8] and [9] can be seen a topological order with several symbolic sequences and their topological entropies, which confirm this result to others growth models. This region is bounded below by the curve of the intrinsic growth rate values where the chaos starts. The upper limit is the *fullshift* curve, defined by  $f_r(c) = 1$ . This curve characterizes the transition between the chaotic region and the inadmissible region. In the inadmissible region, the graphic of any function  $f_r$  is no longer totally in the invariant set  $[0, 1]$ . The maps under these conditions not already belong to the studied familie functions and are not good models for populations dynamics.

### 3 Synchronization and Lyapunov exponents

Consider a general network of  $N$  identical coupled dynamical systems, described by a connected, undirected graph, with no loops and no multiple edges. In each node the dynamics of the system is defined by the maps  $f_r$  given by Eq.(4). The state equations of this network, in the discretized form, are

$$x_i(k+1) = f_r(x_i(k)) + c \sum_{j=1}^N l_{ij} f_r(x_j(k)), \text{ with } i = 1, 2, \dots, N \quad (5)$$

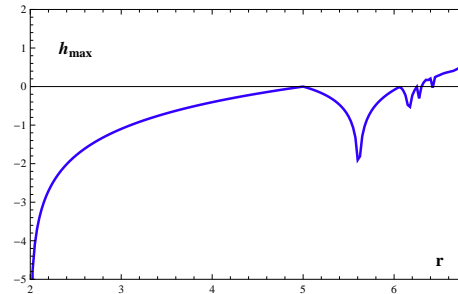
where  $c$  is the coupling parameter and  $L = (l_{ij})$  is the Laplacian matrix or coupling configuration of the network. The Laplacian matrix is given by  $L = D - A$ , where  $A$  is the adjacency matrix and  $D = (d_{ij})$  is a diagonal matrix, with  $d_{ii} = k_i$ , being  $k_i$  the degree of node  $i$ . The eigenvalues of  $L$  are all real and non negatives and are contained in the interval  $[0, \min \{N, 2\Delta\}]$ , where  $\Delta$  is the maximum degree of the vertices. The spectrum of  $L$  may be ordered,  $\lambda_1 = 0 \leq \lambda_2 \leq \dots \leq \lambda_N$ . The network (5) achieves asymptotical synchronization if

$$x_1(t) = x_2(t) = \dots = x_N(t) \xrightarrow[t \rightarrow \infty]{} e(t),$$

where  $e(t)$  is a solution of an isolated node (equilibrium point, periodic orbit or chaotic attractor), satisfying  $\dot{e}(t) = f(e(t))$ .

One of the most important properties of a chaotic system is the sensitivity to initial conditions. A way to measure the sensitivity with respect to initial conditions is to compute the average rate at which nearby trajectories diverge from each other. Consider the trajectories  $x_k$  and  $y_k$ , starting, respectively, from  $x_0$  and  $y_0$ . If both trajectories are, until time  $k$ , always in the same linear region, we can write

$$|x_k - y_k| = e^{\lambda k} |x_0 - y_0|, \text{ where } \lambda = \frac{1}{k} \sum_{j=0}^{k-1} \ln |f'_r(x_j)|.$$



**Fig. 2.** Lyapunov exponents estimates for von Bertalanffy's maps Eq.(4), as a function of the intrinsic growth rate  $r$ .

The Lyapunov exponents of a trajectory  $x_k$  is defined by

$$h_{\max} = \lim_{k \rightarrow +\infty} \frac{1}{k} \sum_{j=0}^{k-1} \ln |f'_r(x_j)| \quad (6)$$

whenever it exists. The computation of the Lyapunov exponent  $h_{\max}$  gives the average rate of divergence (if  $h_{\max} > 0$ ), or convergence (if  $h_{\max} < 0$ ) of the two trajectories from each other, during the time interval  $[0, k]$ , see for example [16]. We note that, the Lyapunov exponents depend on two biological parameters: von Bertalanffy's growth rate constant and the asymptotic weight. See in Fig.2 the Lyapunov exponents estimate for von Bertalanffy's maps Eq.(4).

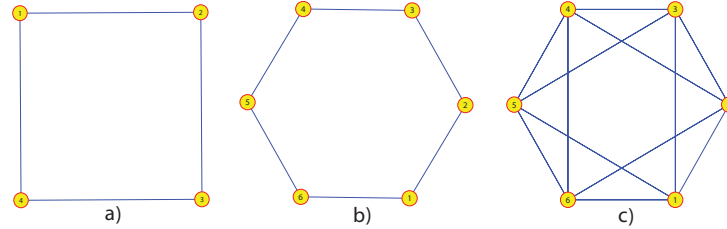
If the coupling parameter  $c$  belongs to the synchronization interval

$$\left] \frac{1 - e^{-h_{\max}}}{\lambda_2}, \frac{1 + e^{-h_{\max}}}{\lambda_N} \right[ \quad (7)$$

then the synchronized states  $x_i(t)$ , ( $i = 1, \dots, N$ ) are exponentially stable, [17]. The second eigenvalue  $\lambda_2$  is known as the algebraic connectivity or Fiedler value and plays a special role in the graph theory. As bigger is  $\lambda_2$ , more easily the network synchronizes. As much larger  $\lambda_2$  is, more difficult is to separate the graph in disconnected parts. The graph is connected if and only if  $\lambda_2 \neq 0$ . In fact, the multiplicity of the null eigenvalue  $\lambda_1$  is equal to the number of connected components of the graph. Fixing the topology of the network, the eigenvalues of the Laplacian  $\lambda_2$  and  $\lambda_N$  are fixed, so the synchronization only depends on the Lyapunov exponent of each node,  $h_{\max}$ . Remark that the synchronization interval also depends on two biological parameters: von Bertalanffy's growth rate constant and the asymptotic weight.

## 4 Numerical simulation and conclusions

To support our approaches, we consider a regular ring lattice, a graph with  $N$  nodes, each one connected to  $k$  neighbors,  $\frac{k}{2}$  on each side, having in each node the same model, the von Bertalanffy maps  $f_r$  given by Eq.(4). See in Fig.3



**Fig. 3.** Lattices. In a) with  $N = 4$  nodes and  $k = 2$ , in b) with  $N = 6$  nodes and  $k = 2$  and in c) with  $N = 6$  nodes and  $k = 4$ . From (a) to (b) the total number of vertices of the network increases maintaining the number of neighbors of each node, and from (b) to (c) increases the number of neighbors of each node, but the total number of vertices of the network remains the same.

some example of lattices. If, for instance,  $N = 6$  and  $K = 4$ , see Fig.3c), the adjacency matrix  $A$  and the Laplacian matrix  $L$  are

$$A = \begin{bmatrix} 0 & 1 & 1 & 0 & 1 & 1 \\ 1 & 0 & 1 & 1 & 0 & 1 \\ 1 & 1 & 0 & 1 & 1 & 0 \\ 0 & 1 & 1 & 0 & 1 & 1 \\ 1 & 0 & 1 & 1 & 0 & 1 \\ 1 & 1 & 0 & 1 & 1 & 0 \end{bmatrix} \quad \text{and} \quad L = D - A = \begin{bmatrix} 4 & -1 & -1 & 0 & -1 & -1 \\ -1 & 4 & -1 & -1 & 0 & -1 \\ -1 & -1 & 4 & -1 & -1 & 0 \\ 0 & -1 & -1 & 4 & -1 & -1 \\ -1 & 0 & -1 & -1 & 4 & -1 \\ -1 & -1 & 0 & -1 & -1 & 4 \end{bmatrix}.$$

So, the network correspondent to the graph in Fig.3 c) is defined by the system,

$$\begin{cases} \dot{x}_1 = f_r(x_1) + c(4x_1 - x_2 - x_3 - x_5 - x_6) \\ \dot{x}_2 = f_r(x_2) + c(-x_1 + 4x_2 - x_3 - x_4 - x_6) \\ \dot{x}_3 = f_r(x_3) + c(-x_1 - x_2 + 4x_3 - x_4 - x_5) \\ \dot{x}_4 = f_r(x_4) + c(-x_2 - x_3 + 4x_4 - x_5 - x_6) \\ \dot{x}_5 = f_r(x_5) + c(-x_1 - x_3 - x_4 + 4x_5 - x_6) \\ \dot{x}_6 = f_r(x_6) + c(-x_1 - x_2 - x_4 - x_5 + 4x_6) \end{cases}.$$

For this lattice the eigenvalues of the Laplacian matrix are  $\lambda_1 = 0$ ,  $\lambda_2 = \lambda_3 = \lambda_4 = 4$  and  $\lambda_5 = \lambda_6 = 6$ . If we consider, for instance,  $r = 6.60$ , the Lyapunov exponent of  $f_r(x)$  is 0.377, Eq.(6). Then, attending to Eq.(7), this lattice synchronizes if  $\frac{1-e^{-0.377}}{2} < c < \frac{1+e^{-0.377}}{6} \Leftrightarrow 0.079 < c < 0.281$  and the amplitude of the synchronization interval is 0.202. For more examples see Table 1. The lattice correspondent to the Fig.3 b) has eigenvalues of the Laplacian matrix  $\lambda_1 = 0$ ,  $\lambda_2 = \lambda_3 = 1$ ,  $\lambda_4 = \lambda_5 = 3$  and  $\lambda_6 = 4$ . Thus, for the same  $r = 6.60$ , the lattice synchronizes if  $0.313 < c < 0.421$  and the amplitude of this interval is 0.107. Moreover, to the lattice in Fig.3 a), the eigenvalues of the Laplacian matrix are  $\lambda_1 = 0$ ,  $\lambda_2 = \lambda_3 = 2$  and  $\lambda_4 = 4$ . For the same  $r = 6.60$ , the lattice synchronizes if  $0.157 < c < 0.421$  and the amplitude of this interval is 0.264. In Table 1 are presented more examples, where we computed the synchronization interval for several values of the intrinsic growth rate  $r$ , for all these lattices a), b) and c) of Fig.3. The results of Table 1 allow us to claim:

- (C1) From the lattice a) to lattice b) in Fig.3, the total number of vertices of the network increases maintaining the number of neighbors of each node.



$r$	$h_{max}$	Synchronization Interval			Amplitude		
		Lattice a)	Lattice b)	Lattice c)	Lattice a)	Lattice b)	Lattice c)
6.50	0.297	]0.128, 0.436[	]0.257, 0.436[	]0.064, 0.291[	0.308	0.179	0.226
6.55	0.347	]0.147, 0.427[	]0.293, 0.427[	]0.073, 0.285[	0.280	0.134	0.211
6.60	0.377	]0.157, 0.421[	]0.313, 0.421[	]0.079, 0.281[	0.264	0.107	0.202
6.65	0.406	]0.167, 0.417[	]0.334, 0.417[	]0.083, 0.278[	0.250	0.083	0.194
6.70	0.463	]0.185, 0.407[	]0.371, 0.407[	]0.093, 0.272[	0.222	0.037	0.179
6.73	0.506	]0.199, 0.401[	]0.397, 0.401[	]0.099, 0.267[	0.202	0.003	0.168
6.74	0.533	]0.207, 0.397[	(*)	]0.103, 0.265[	0.190	(*)	0.161
6.75	0.598	]0.225, 0.388[	(*)	]0.112, 0.258[	0.163	(*)	0.146

**Table 1.** Lyapunov exponent,  $h_{max}$ , synchronization interval,  $]\frac{1-e^{-h_{max}}}{\lambda_2}, \frac{1+e^{-h_{max}}}{\lambda_N} [$ , and amplitude of this interval,  $\frac{1+e^{-h_{max}}}{\lambda_N} - \frac{1-e^{-h_{max}}}{\lambda_2}$ , for several intrinsic growth rates  $r$ , for the lattices a), b) and c) of Fig.3. (\*) In this case, the desynchronization phenomenon occurs, see (C4).

We verify that the synchronization is worse, not only because it begins to synchronize at a higher value of the coupling parameter  $c$ , but also, because the synchronization interval is shorter.

- (C2) Comparing the results for the lattices b) and c) in Fig.3, we may conclude that maintaining the total number of vertices of the network, but increasing the number of neighbors of each node, the synchronization is better, not only because it begins to synchronize at a lower value of the coupling parameter  $c$ , but also, because the synchronization interval is larger.
- (C3) Observing the columns of Table 1, we verify that, as the intrinsic growth rate  $r$  increases, the synchronization is worse, not just because it begins to synchronize at a higher value of the coupling parameter  $c$ , but also, because the synchronization interval is shorter.
- (C4) Note that, for the intrinsic growth rate  $r = 6.74$  and  $r = 6.75$ , for the lattice b), the upper bound of the synchronization interval is lower than the lower bound. This means that, there is no synchronization for any value of the coupling parameter  $c$ . This desynchronization phenomenon was expected because the network (5) synchronizes only if  $h_{max} < \ln(2R + 1)$ , where  $R = \frac{\lambda_1 - \lambda_2}{\lambda_2 - \lambda_N}$ , see [17]. In the case of lattice b), we have  $\ln(2R + 1) = 0.511$ , so there is synchronization only if  $h_{max} < 0.511$ , which do not happens for  $r = 6.74$  and  $r = 6.75$ . In all the other studied cases, the Lyapunov exponent verifies  $h_{max} < \ln(2R + 1)$ , so we have a non empty synchronization interval.



## Acknowledgment

Research partially sponsored by national funds through the Foundation for Science and Technology, Portugal - FCT under the project PEst-OE/MAT/UI0006/2011, CEAUL, CIMA-UE and ISEL.

**FCT**

## References

- 1.G.M. Cailliet, W.D. Smith, H.F. Mollet and K.J. Goldman. Age and growth studies of chondrichthyan fishes: the need for consistency in terminology, verification, validation, and growth function fitting. *Environ. Biol. Fish.*, 77: 211–228, 2006.
- 2.A.B. Cooper. A Guide to Fisheries Stock Assessment. From Data to Recommendations. New Hampshire Sea Grant, 2006.
- 3.T.E. Essington, J.F. Kitchell and C.J. Walters. The von Bertalanffy growth function, bioenergetics, and the consumption rates of fish. *Can. J. Fish. Aquat. Sci.*, 58: 2129–2138, 2001.
- 4.J.A. Hutchings and J.D. Reynolds. Marine fish population collapses: consequences for recovery and extinction risk. *BioSci.*, 54: 297–309, 2004.
- 5.V.S. Karpouzi and D. Pauly. Life-History Patterns in Marine Birds. In M.L.D. Palomares and D. Pauly, editors, *Fisheries Centre Research Reports 16 (10), Von Bertalanffy Growth Parameters of Non-Fish Marine Organisms*, pages 27–43, Canada, 2008. The Fisheries Centre, University of British Columbia.
- 6.D. Lind and B. Marcus. An Introduction to Symbolic Dynamics and Codings. 2<sup>nd</sup> edition, Cambridge University Press, Cambridge, 1999.
- 7.J.A. Musick. Criteria to define extinction risk in marine fishes. *Fisheries*, 24: 6–14, 1999.
- 8.J.L. Rocha and S.M. Aleixo. An extension of gompertzian growth dynamics: Weibull and Fréchet models. *Math. Biosci. Eng.*, 10: 379–398, 2013.
- 9.J.L. Rocha and S.M. Aleixo. Dynamical analysis in growth models: Blumberg's equation. *Discrete Contin. Dyn. Syst.-Ser.B*, 18: 783–795, 2013.
- 10.S.J. Schreiber. Chaos and population disappearances in simple ecological models. *J. Math. Biol.*, 42: 239–260, 2001.
- 11.L. Von Bertalanffy. A quantitative theory of organic growth. *Human Biology*, 10: 181–213, 1938.
- 12.L. Von Bertalanffy. Quantitative laws in metabolism and Growth. *The Quarterly Review of Biology*, 32: 217–231, 1957.
- 13.A. Balanov, N. Janson, D. Postnov and O. Sosnovtseva. Synchronization: From Simple to Complex, Springer, 2009.
- 14.A.J. Davidson and M. Menaker, Birds of a feather clock together sometimes: social synchronization of circadian rhythms. *Curr. Opin. Neurobiol.*, 13 (6): 765–769, 2003.
- 15.J.A.L. Silva and F.T. Giordani, Density-dependent migration and synchronism in metapopulations. *Bull. of Math. Bio-*, 68: 451–465, 2006.
- 16.M.Hasler and Y.L. Maistrenko, An introduction to the synchronization of chaotic systems: coupled skew tent maps. *IEEE Trans. on Circ. Syst. - I*, 44 (10): 856–866, 1987.
- 17.X. Li and G. Chen, Synchronization and desynchronization of complex dynamical networks: An engineering viewpoint. *IEEE Trans. on Circ. Syst. -I*, 50 (11): 1381–1390, 2003.





## Analogue of Turan-Erdős-Koksma inequality for a discrepancy of complex PRN's

Vadim Rudetskiy<sup>1</sup>, Tran The Vinh<sup>2</sup>, Pavel Varbanets<sup>3</sup>, and Sergey Varbanets<sup>4</sup>

<sup>1</sup> I. I. Mechnikov Odessa National University, 65026 Odessa, Ukraine  
(E-mail: v.rudetsky@yahoo.com)

<sup>2</sup> I. I. Mechnikov Odessa National University, 65026 Odessa, Ukraine  
(E-mail: ttvinhcantt@yahoo.com.vn)

<sup>3</sup> I. I. Mechnikov Odessa National University, 65026 Odessa, Ukraine  
(E-mail: varb@sana.od.ua)

<sup>4</sup> I. I. Mechnikov Odessa National University, 65026 Odessa, Ukraine  
(E-mail: varb@sana.od.ua)

**Abstract.** There is built an analogue of Turan-Erdős-Koksma inequality for the discrepancy of the sequence of complex numbers from unit circle. The sequence of PRN's generated by the Gaussian integers with the norms comparable to 1 for given modulus has been considered. The estimate for discrepancy of this points was obtained.

**Keywords:** Gaussian integers, the sequence of pseudo-random numbers, discrepancy.

### 1 Introduction

We consider the sequence of complex numbers  $\{z_n\}$ ,  $|z_n| \leq 1$ . Let  $0 \leq \xi_1 < \xi_2 \leq 1$ ,  $0 \leq \varphi_1 < \varphi_2 \leq 2\pi$ , and let  $P(\xi, \varphi)$  denotes the sectorial region of unit circle  $|z| \leq 1$

$$P(\xi, \varphi) := \{z \in \mathbb{C} : \xi_1 < N(z) \leq \xi_2, \varphi_1 < \arg z \leq \varphi_2\}. \quad (1)$$

Denote by  $\mathfrak{F}$  the collection of sectorial region  $P(\xi, \varphi)$  for all  $\xi$  and  $\varphi$ .

The sequence  $\{z_n\}$  calls the pseudo-random in unit circle if it induces by a determinative algorithm and its statistic properties are "similar" on property of sequence of the random numbers. The "similarity" means that this sequence closely adjacent to uniformly distributed in the disk  $|z| \leq 1$ , and its elements are uncorrelated. On these properties of the sequence of pseudo-random numbers (abbreviation: PRN's) can define by value of discrepancy  $D_N$  of the points  $z_1, z_2, \dots, z_N$ :

$$D_N(z_1, \dots, z_N) := \sup_{P \in \mathfrak{F}} \left| \frac{A_N(P)}{N} - |P| \right|, \quad (2)$$

where  $A_N(P)$  is the number of points among  $z_1, \dots, z_N$  falling into  $P$ ,  $|P|$  denotes the volume  $P$ , supremum is extended over all sectorial region  $P$  of unit circle  $|z| \leq 1$ .

The similar definition of discrepancy  $D_N$  has for the  $s$ -dimensional sequence of complex points  $Z_n^{(s)} = (z_1^{(s)}, \dots, z_n^{(s)})$ ,  $z_j \in \mathbb{C}$ .

We say that the sequence  $\{z_n\}$  passes  $s$ -dimensional test on uncorrelatedness if it passes  $s$ -dimensional test on equidistribution (i.e.  $D_N^{(s)}(z_1^{(s)}, \dots, z_N^{(s)}) \rightarrow 0$



at  $N \rightarrow \infty$ ).

For the construction of the sequence of PRN's on  $[0, 1)$  use frequently the congruential recursion of the form

$$y_{n+1} \equiv f(y_n) \pmod{m},$$

where  $f(u)$  is an integral-valued function.

We will investigate the sequence of complex numbers produced by recursion

$$z_{n+1} \equiv z_0 \cdot (u + iv)^m \pmod{p^m} \quad (3)$$

where  $z_0$  and  $u + iv$  are the Gaussian integers,  $(z_0, p) = 1$ .

For real sequences  $\{x_n\}$  produced by congruential recursion, an estimate for  $D_N$  can be obtained by the Turan-Erdős-Koksma inequality (see, [3], Th. 3.10).

In our paper we get an analogue to the Turan-Erdős-Koksma inequality for the sequence of pseudorandom complex numbers.

## 2 Preliminary results

**Notations.** Let  $G$  denotes the ring of the Gaussian integers,  $G := \{a + bi : a, b \in \mathbb{Z}\}$ ;  $N(z) = |z|^2$  calls the norm of  $z \in G$ . For  $\gamma \in G$  denote  $G_\gamma$  (respectively,  $G_\gamma^*$ ) the complete system of residues (respectively, reduced residues system) in  $G$  modulo  $\gamma$ ;  $p$  is a prime number in  $\mathbb{Z}$ ;  $\mathfrak{p}$  is a Gaussian prime number. If  $q$  is a positive integer,  $q > 1$ , then we write  $e_q(x) = e^{2\pi i \frac{x}{q}}$  for  $x \in \mathbb{R}$ . Symbols "O" and " $\ll$ " are equivalent;  $\nu_p(\alpha) = k$  if  $p^k | \alpha$ ,  $p^{k+1} \nmid \alpha$ .

Let  $M > 1$  be a positive integer and let  $y_1, y_2, \dots, y_N$  be a some sequence of points from  $G_M$  and let  $Y_M = \{\frac{y_n}{M}\}$ ,  $n = 0, \dots, N - 1$ . For  $P \in \mathfrak{F}$  denote  $A(P, Y_M)$  the number of points from  $Y_M$  contained in  $P$ .

We will adapt the proof from [2] for a construction of an analogue of the Turan-Erdős-Koksma inequality.

We define the adequate approximation of sectorial region  $P \in \mathfrak{F}$ ,

$$P := \left\{ \frac{z}{q} : N_1 \leq N(z) \leq N_2, 0 \leq \varphi_1 < \arg z \leq \varphi_2 < 2\pi \right\}, q \in \mathbb{N}.$$

The set  $S(P)$  calls the adequate approximation of  $P$  if

- (i)  $A(P, Y_N(M)) = A(S(P), Y_N(M)) + O\left(N^{\frac{1}{2}}\right)$ ,
- (ii) volumes  $|P|$  and  $|S(P)|$  are "similar",
- (iii)  $A(S(P), Y_N(M))$  has a representation by an exponential sum.

Let  $N_1, N_2, \varphi_1, \varphi_2$  are the parameters in the definition of  $P$ . For  $r, s \in \mathbb{Z}_M$  we set  $\bar{r} = \frac{r}{M}$ ,  $\bar{s} = \frac{s}{M}$ .

Determine

$$S_{\bar{r}, \bar{s}} : \left\{ \beta = \frac{\alpha}{M} : \alpha \in G_M, \bar{r} < N(\beta) \leq \bar{r} + \frac{1}{M}, 2\pi\bar{s} < \arg \alpha \leq 2\pi \left( \bar{s} + \frac{1}{M} \right) \right\}. \quad (4)$$





Put

$$S(P) := \bigcup_{\substack{\bar{r}, \bar{s} \\ S_{\bar{r}, \bar{s}} \subset P}} S_{\bar{r}, \bar{s}}.$$

It is obvious that  $S(P) = P(\bar{N}_1, \bar{N}_2, \psi_1, \psi_2)$ , where

$$\begin{aligned} \bar{N}_1 &= \min \left\{ \frac{a}{M}, a \in \mathbb{Z}_M : N_1 \leq \frac{a}{M} \right\} \\ \bar{N}_2 &= \min \left\{ \frac{b}{M}, b \in \mathbb{Z}_M : N_2 \leq \frac{b}{M} \right\} \\ \psi_1 &= \min \left\{ \frac{2\pi a}{M}, a \in \mathbb{Z}_M : \psi_1 \leq \frac{2\pi a}{M} \right\} \\ \psi_2 &= \min \left\{ \frac{2\pi b}{M}, b \in \mathbb{Z}_M : \psi_2 \leq \frac{2\pi b}{M} \right\} \end{aligned}$$

We proved the following analogue of the Turan-Erdős-Koksma inequality (see, [3])

**Theorem 1.** *Let  $M > 1$  be integer. Then for any sequence  $\{y_n\}$ ,  $y_n \in G_M$ , the discrepancy  $D_N$  of points  $\{\frac{y_n}{M}\}$  satisfies to inequality*

$$\begin{aligned} D_N &\leq 2 \left( 1 - \left( 1 - \frac{2\pi}{M} \right)^2 \right) + \\ &+ \frac{1}{M} \sum_{\substack{\gamma \in G_M \\ \gamma \neq 0}} \min \left( \frac{1}{|\sin \pi \Re \gamma|}, \frac{1}{|\sin \pi \Im \gamma|} \right) \frac{1}{N} \left( |S_N| + O \left( N^{\frac{1}{2}} \right) \right), \end{aligned}$$

where  $S_N = \sum_{n=0}^{N-1} e_M(\Re(\gamma y_n))$ .

*Proof.* By an analogue with the work[2] we infer

$$R_N(S(P)) := \frac{A(S(P))}{N} - |S(P)| = \frac{1}{N} \sum_{n=0}^{N-1} \chi_{S(P)}(x_n) - |S(P)|, \quad (5)$$

where  $x_n = \frac{y_n}{M}$ ,  $\chi_\Delta$  is the characteristic function of the set  $\Delta$ .

By the equality

$$\chi_{S_{\bar{r}, \bar{s}}}(x) = \sum_{\alpha \in S_{\bar{r}, \bar{s}}} \frac{1}{M^2} \sum_{\gamma \in G_M} e_M(\gamma(\alpha - x))$$

we get

$$\begin{aligned} &|R_N(S(P))| \leq \\ &\leq \sum_{0 \neq \gamma \in G_M} \frac{1}{M^2} \left| \sum_{z(r,s) \in S_{\bar{r}, \bar{s}}} e_M(-\Re(\gamma z(r,s))) \right| \cdot \left| \frac{1}{N} \sum_{n=0}^{N-1} e_M(\Re(\gamma y_n)) \right|, \quad (6) \end{aligned}$$



where  $z(r, s)$  is the complex number such that

$$N(z(r, s)) = \frac{r}{M}, \quad \arg z(r, s) = \frac{2\pi s}{M}.$$

In order to calculate the first inner sum over  $S_{\bar{r}, \bar{s}}$  one needs an estimate of the sum

$$\sum_M = \sum_{\substack{N_1 < N(\omega) \leq N_2 \\ \varphi_1 < \arg \omega \leq \varphi_2}} e_M(\Re(\gamma\omega)), \quad (0 \neq \gamma \in G_M). \quad (7)$$

The sum  $\sum_M$  can be considered as a sum of coefficients of Dirichlet series for the Hecke Z-function over the Gaussian field  $\mathbb{Q}(i)$ :

$$Z_m(s, \delta_0, \delta_1) = \sum_{0 \neq \omega \in G} \frac{e^{2\pi i \Re(\omega \delta_1)}}{N(\omega + \delta_0)^s} e^{4mi \arg \omega}, \quad (\Re s > 1).$$

Putting  $\delta_0 = 0$ ,  $\delta_1 = \frac{\gamma}{M}$ , we obtain for any  $T > 1$  by a standard way the following estimates:

$$\begin{aligned} \sum_{N(\omega) \leq x} e_M(\gamma\omega) &= (\varphi_2 - \varphi_1) \sum_{N(\omega) \leq x} N(\omega) \leq x e_M(\gamma\omega) + O\left(\frac{1}{T} \sum_{N(\omega) \leq x} 1\right) + \\ &+ O\left((\varphi_2 - \varphi_1) \sum_{m=1}^T \left| \sum_{N(\omega) \leq x} e_M(\gamma\omega) e^{4mi \arg \omega} \right|\right). \end{aligned} \quad (8)$$

$$\sum_{N(\omega) \leq x} e_M(\gamma\omega) e^{4mi \arg \omega} \ll_\varepsilon \frac{x^{\frac{1}{2} + \varepsilon}}{M^{\frac{1}{4}}} + M^{\frac{1}{2}} (|m| + 3)^{1 + \varepsilon} \quad (9)$$

(for the details, see Chapter 2 of [1], for example).

Next, we have a simple analogue of the estimate of linear exponential sum over  $G$

$$\begin{aligned} &\left| \sum_{N_1 < N(\omega) \leq N_2} 2^{2\pi i \Re(\alpha\omega)} \right| \leq \\ &\leq (N_2 - N_1)^{\frac{1}{2}} \min\left((N_2 - N_1)^{\frac{1}{2}}, \frac{1}{|\sin \pi \Re \alpha|}, \frac{1}{|\sin \pi \Im \alpha|}\right). \end{aligned} \quad (10)$$

Now by (4)-(9), putting  $T = x^{\frac{2}{3}}$  and taking into account that  $|P| = \frac{\varphi_2 - \varphi_1}{2} (N_2 - N_1)$ , we obtain our assertion.  $\square$

### 3 Sequence of PRN's produced by the cyclic group $E_n$ .

Let  $p \equiv 3 \pmod{4}$  be a prime integer. Consider the set of the classes of residue  $(\text{mod } p^n)$  over  $G$ , such that for every  $\alpha \in E_n$  we have  $N(\alpha) \equiv \pm 1 \pmod{p^n}$ . Respectively a convolution of multiplication the set  $E_n$  forms a group. It is well known that a regular generative element of  $E_n$  is a generative element for any  $E_\ell$ ,  $\ell = 1, 2, \dots, n$ . Moreover,  $|E_n| = 2(p+1)p^{n-1}$  ( $|E_n|$  is the number of elements in  $E_n$ ).



We fix the generative element of  $E_n$  and let some  $z_0 \in G_n$ ,  $(N(z_0), p) = 1$ . We call  $z_0$  an initial value for the sequence  $\{z_m\}$ , where  $z_m = z_0(u + iv)^m$ ,  $m = 0, 1, \dots, N - 1$ .

**Lemma 1.** ([4], pp.232-233)

Let  $p \equiv 3 \pmod{4}$ ,  $n > 3$ , and let  $u + iv$  is a generative element of the group  $E_n$ . Then for every  $0 \leq \ell \leq p^{n-2}$ ,  $0 \leq k < 2(p + 1)$ , we have

$$(u + iv)^{2(p+1)p^\ell + k} \equiv A(\ell, k) + iB(\ell, k) \pmod{p^n},$$

where

$$\begin{aligned} A(\ell, k) &\equiv A_0(k) + A_1(k)\ell + \dots + A_{n-1}(k)\ell^{n-1} \pmod{p^n}, \\ B(\ell, k) &\equiv B_0(k) + B_1(k)\ell + \dots + B_{n-1}(k)\ell^{n-1} \pmod{p^n}. \end{aligned}$$

Moreover,

$$\begin{aligned} A_j(k) &= A_j u(k) - B_j v(k), \quad B_j(k) = A_j v(k) + B_j u(k), \quad j = 0, 1, \dots, n - 1; \\ A_0 &\equiv 1 \pmod{p}, \quad B_0 \equiv 0 \pmod{p}; \\ A_1 &\equiv 0 \pmod{p^3}, \quad A_2 = p^2 A'_2, \quad (A'_2, p) = 1; \\ B_1 &= p B'_1, \quad (B'_1, p) = 1, \quad B_2 \equiv A_3 \equiv B_3 \equiv \dots \equiv A_{n-1} \equiv B_{n-1} \equiv 0 \pmod{p^3}; \\ u(0) &= 1, \quad v(0) = 0, \quad (u(p + 1), p) = 1, \quad p \nmid v(p + 1); \\ (v(k), p) &= 1 \text{ for } k \neq \overline{0, p + 1}. \end{aligned}$$

**Corollary 1.**

$$\begin{aligned} p \nmid A_1(k), \quad A_j(k) &\equiv 0 \pmod{p^2}, \quad j = 2, 3, \dots; \quad k \neq \overline{0, p + 1}; \\ p^2 \nmid A_1(0), \quad A_j(0) &\equiv 0 \pmod{p^3}, \quad j = 2, 3, \dots; \\ p^2 \nmid A_1(p + 1), \quad p^2 \nmid A_2(k), \quad A_j(p + 1) &\equiv 0 \pmod{p^3}, \quad j = 3, 4, \dots; \\ p^2 \nmid B_2(k) \text{ if } k &\neq \overline{0, p + 1}; \quad B_2(k) \equiv 0 \pmod{p^3} \text{ else}; \\ B_j(k) &\equiv 0 \pmod{p^3}, \quad j = 3, 4, \dots; \quad \nu_p(B_1(k)) = 1, \quad k = 0, 1, \dots, 2p + 1. \end{aligned}$$

**Lemma 2.** Let  $\alpha \in G_{p^n}$ ,  $\alpha = p^h \alpha_0$ ,  $(\alpha_0, p) = 1$ ,  $h < n$ , and let  $z_m = z_0(u + iv)^m \pmod{p^n}$ ,  $m = 0, 1, \dots, 2(p + 1)p^{n-1} - 1$ .

Then

$$\left| \sum_{j=0}^{N-1} e_{p^{n-1}}(\Re(\alpha z_j)) \right| \leq 2p^{\frac{n-h-r-1}{2}},$$

where  $r$  is determined from (12) and depends on  $\alpha$ .

*Proof.* Let us denote

$$\begin{aligned} \nu_p(\alpha) &= h, \quad 0 \leq h < n - 1, \quad \alpha = p^h \alpha_0, \quad (\alpha_0, p) = 1; \\ M_h &= 2(p + 1)p^{n-1-h}. \end{aligned}$$



Then we have

$$\begin{aligned} & \left| \sum_{m=0}^{M_0-1} e_{p^{n-h-1}}(\Re(\alpha_0 z^m)) \right| = p^{2h} \left| \sum_{m=0}^{M_h-1} e_{p^{n-h-1}}(\Re(\alpha_0 z^m)) \right| = \\ & = p^{2h} \left| \sum_{k=0}^{2p+1} \sum_{\ell=0}^{p^{n-h-1}-1} e_{p^{n-h-1}}(aA_k(\ell) - bB_k(\ell)) \right|. \end{aligned} \quad (11)$$

For every  $k = 0, 1, \dots, 2p + 1$ , we consider the polynomial

$$aA_k(\ell) - bB_k(\ell) = \sum_{j=0}^{n-1} c_j(k)\ell^j,$$

where

$$c_j(k) = (aA_j - bB_j)u(k) + (bA_j - aB_j)v(k), \quad j = 0, 1, \dots, n - 1.$$

In particular,

$$\begin{aligned} c_1(k) &= (aA_1 - bB_1)u(k) + (bA_1 - aB_1)v(k) = \\ &= (au(k) + bv(k))A_1 - (bu(k) - av(k))B_1, \\ c_2(k) &= (aA_2 - bB_2)u(k) + (bA_2 - aB_2)v(k) = \\ &= (au(k) + bv(k))A_2 - (bu(k) - av(k))B_2. \end{aligned} \quad (12)$$

We see that for all values of  $k = 0, 1, \dots, 2p + 1$

$$\nu_p(A_1(k)) \neq \nu_p(B_1(k)), \quad \nu_p(A_2(k)) \neq \nu_p(B_2(k)).$$

Now if for given  $\alpha_0$  and  $k$  the inequality

$$\nu_p(c_1(k)) \geq \nu_p(c_2(k)) = r \quad (13)$$

holds, then the inner sum over  $\ell$  in (10) can be estimated as  $p^{\frac{n-h+r-1}{2}}$  (such sum by consequent slope leads to the Gaussian sum).

In other cases (i.e.,  $\nu_p(c_1(k)) < \nu_p(c_2(k))$ ) this sum is vanishes.

Hence, from (10)-(12) we infer the assertion of lemma.  $\square$

Lastly we prove the main result

**Theorem 2.** *Let the sequence  $\{z_n\}$  is generated by the recursion*

$$z_{m+1} \equiv z_m(u + iv) \pmod{p^n},$$

where  $z_0 \in G_{p^m}$ ,  $u + iv$  is a generative element of the group  $E_n$  of classes of residue modulo  $p^n$  with the norms that  $\equiv 1 \pmod{p^n}$ . Then the discrepancy of the points  $\left\{ \frac{z_m}{p^m} \right\}$ ,  $m = 0, 1, \dots, N - 1$ ,  $N \leq 2(p + 1)p^{n-1}$  satisfies the following inequality

$$D_N \leq 2 \left( 1 - \left( 1 - \frac{2\pi}{p^n} \right)^2 \right) + N^{-1} p^{\frac{n}{2}} \log p^n.$$



*Proof.* Indeed, for every  $h$ ,  $0 \leq h \leq n - 1$  there is at most  $O(p^{n-h-r})$  numbers  $\alpha_0, \alpha_0 \in G_{p^{n-h}}$  for which  $\nu_p(c_1(k)) \geq \nu_p(c_2(k)) = r$ , where  $c_1(k), c_2(k)$  determined by (11).

Now, by Lemma 2 and Theorem 1 we immediately obtain the proof of theorem.  $\square$

Theorem 1 makes possible to prove that the sequence of complex numbers  $z_n$  produced by the recursion

$$z_{n+1} \equiv \alpha z_n^{-1} + \beta + \gamma z_n \pmod{p^n},$$

$\alpha, \beta, \gamma, z_0 \in G$ ,  $(\alpha, p) = (z_0, p) = 1$ ,  $\beta \equiv \gamma \equiv 0 \pmod{p}$ , passes  $s$ -dimensional test on equidistribution and unpredictability.

## References

- 1.R. C. Baker. Diophantine Inequalities. *LMS Monographs (New Series)*, v.1(Clarendon Press, Oxford), 1986.
- 2.P. Hellekale. General discrepancy estimates the Walsh function system. *Acta Arith.*, 67:209-218, 1994.
- 3.H. Niederreiter. Random Number Generation and Quasi-Monte Carlo Methods, *SIAM, Philadelphia*, 1992.
- 4.S. Varbanets. The Norm Kloosterman Sums Over  $\mathbb{Z}[i]$ . *Analytic and Probabilistic Methods in Number Theory, Proc. Forth. International Conference in Honour of J. Kubilius, Palanga, Lithuania, 25-29 September*, 213-224, 2006.





## Linear-inversive congruential pseudo-random numbers with prime power modulus

Vadim Rudetskiy<sup>1</sup>, Tran The Vinh<sup>2</sup>, Pavel Varbanets<sup>3</sup>, and Sergey Varbanets<sup>4</sup>

<sup>1</sup> I. I. Mechnikov Odessa National University, 65026 Odessa, Ukraine  
(E-mail: v.rudetsky@yahoo.com)

<sup>2</sup> I. I. Mechnikov Odessa National University, 65026 Odessa, Ukraine  
(E-mail: ttvinhcntt@yahoo.com.vn)

<sup>3</sup> I. I. Mechnikov Odessa National University, 65026 Odessa, Ukraine  
(E-mail: varb@sana.od.ua)

<sup>4</sup> I. I. Mechnikov Odessa National University, 65026 Odessa, Ukraine  
(E-mail: varb@sana.od.ua)

**Abstract.** Studied the sequence of pseudo-random numbers produced by the linear-inversive congruential generator with the special conditions on the parameters of generator. Obtained the individual and averaged by initial value the estimates of exponential sums on the sequence of pseudo-random numbers.

**Keywords:** pseudo-random numbers, linear-inversive generator, discrepancy, exponential sum.

### 1 Introduction

The Nonlinear methods for pseudo-random number generation provide reasonable equidistribution and statistical independence properties. Unfortunately a classical standard method of generating the pseudo-random numbers in the interval  $[0, 1)$  by a linear recursion  $y_{n+1} \equiv ay_n + n \pmod{m}$  does not inquire with this problem.

A particularly promising nonlinear method is the inversive congruential method where nonlinearity is achieved by employing the operation of multiplicative inversion with a respect to given modulus of a typical representer of such generating is the following congruential recursion

$$y_{n+1} \equiv ay_n^{-1} + b \pmod{M}, \quad (1)$$

where  $u^{-1}$  is a multiplicative inverse mod  $M$  if  $(u, M) = 1$ .

Usually, modulus  $M$  select is equal to an odd prime (see, [1][2],[4]) or an odd prime power (see,[3],[6],[7],[8]). However, it has a priority of existence for the linear-inversive congruential generator.

$$y_{n+1} \equiv ay_n^{-1} + b + cy_n \pmod{p^m}. \quad (2)$$

Example, in [3] it is obtained the condition for which a generated sequence  $\{y_n\}$  has a period of maximal length for  $p = 2$ . In [8] it was studied the generator (2) with  $(y_0, p) = (a, p) = 1$ ,  $b \equiv c \equiv 0 \pmod{p}$  and inferred the condition when  $\{y_n\}$  has a maximal period  $\tau$ . For normalizing sequence  $\{\frac{y_n}{p^m}\}$  there is



obtained a non-trivial estimate of discrepancy  $D_N \left( \frac{y_1}{p^m}, \dots, \frac{y_N}{p^m} \right)$ ,  $N \leq \tau$ .

The sequence  $\{x_n\}$ ,  $x_n = \frac{y_n}{p^m}$  we call the sequence of pseudo-random numbers.

In present paper we investigate the linear-inversive generator (2) under conditions  $a \equiv b \equiv 0 \pmod{p}$ ,  $(c, p) = 1$ . Notice that the conditions  $a \equiv b \equiv 0 \pmod{p}$ ,  $(c, p) = 1$  or  $(a, p) = 1$ ,  $b \equiv c \equiv 0 \pmod{p}$  guarantee an existence of  $y_n$  for any value of  $n$  if  $(y_0, p) = 1$ .

W.-S. Chou[1] shows that for generator (1) the conditions  $a \equiv 0 \pmod{p}$ ,  $(b, p) = 1$  produce corresponding sequence  $\{y_n\}$  with a period  $\tau = 1$ . It is not alright for an applications. We will prove that the sequence  $\{y_n\}$  produced by (2) has reasonably large period. As well, we give the description of  $y_n$  as the polynomial on  $n$  and initial value  $y_0$ . It makes possible to obtain an acceptable estimate for the discrepancy function  $D_N$ .

Throughout this paper will be used the following

**Notation:**

For an integer  $q > 1$  we denote by  $\mathbb{Z}_q$  the residue ring of integers modulo  $q$ .

As usual, we denote  $\mathbb{Z}_q^*$  the set of invertible elements of  $\mathbb{Z}_q$ .

The notation  $e_q(x)$  stands for  $e^{2\pi i \frac{x}{q}}$ .

For  $u \in \mathbb{Z}_{p^m}^*$  we use the notation  $u^{-1}$  if  $uu^{-1} \equiv 1 \pmod{p^m}$ .

We write  $\nu_p(a) = k$  if  $p^k || a$ .

## 2 Auxiliary lemmas and preliminary results

In this section we shall gather some auxiliary results which we will use during the course of the proof of theorems.

**Lemma 1.** Let  $p$  be a prime and let  $f(x) \in \mathbb{Z}[x]$  be a polynomial of degree  $n$ ,  $n \geq 2$ ,

$$f(x) = a_1x + a_2x^2 + a_3x^3 + \dots + a_nx^n,$$

where  $\nu_p(a_j) \geq \nu_p(a_2) > 0$ ,  $j \geq 3$ .

Then the following estimates

$$\left| \sum_{x \in \mathbb{Z}_{p^m}} e_{p^m}(f(x)) \right| \leq \begin{cases} 0 & \text{if } \nu_p(a_1) < \nu_p(a_2), \\ 2p^{\frac{m+\nu_p(a_2)}{2}} & \text{if } \nu_p(a_1) \geq \nu_p(a_2). \end{cases}$$

hold.

This assertion is a corollary of the estimate of Gauss sum.

Let  $\{x_n\}$  is a sequence of numbers from  $[0, 1)$ . Form the sequence of  $s$ -dimensional points  $X_n^{(s)} = (x_n, x_{n+1}, \dots, x_{n+s-1})$ ,  $n = 1, s, \dots, N$ . We say that  $\{x_n\}$  passes the  $s$ -dimensional discrepancy test if for every  $j = 1, 2, \dots, s$  the sequence  $\{X_n^{(j)}\}$  has a discrepancy which tends to zero for  $N \rightarrow \infty$ .

Consider a point sets  $P_s$  from  $[0, 1)^s$  for which all coordinates of all points are





rational numbers of the form  $\frac{a}{q}$ ,  $0 \leq a < q$ . Let us denote  $C(q) = (-\frac{a}{2}, \frac{a}{2}] \cap \mathbb{Z}$ ,  $C^*(q) = \{a \in C(q) | (a, q) = 1\}$ . Let  $C_s(q)$  (respectively,  $C_s^*(q)$ ) be the inner product of  $s$  copies of  $C(q)$  (respectively,  $C^*(q)$ ).

**Lemma 2 (Niederreiter, [5]).** *For an integer  $M \geq 2$  and  $y_0, \dots, y_{N-1} \in \mathbb{Z}^s$ , let  $P$  be the point set consisting of the fractional parts  $\{M^{-1}y_0\}, \dots, \{M^{-1}y_{N-1}\}$ . Then*

$$D_N(P) \leq 1 - \left(1 - \frac{1}{M}\right)^s + \sum_{h \in C_s^*(M)} \frac{1}{r(h, M)} \left| \frac{1}{N} \sum_{n=0}^{N-1} e\left(\frac{1}{M}h \cdot y_n\right) \right|.$$

From this lemma it is seen that the non-trivial estimates of exponential sums over the sequence of  $\{X_n^{(s)}\}$  are important for the further investigation we presented.

**Proposition 1.** *Let  $\{y_n\}$  be the sequence produced by the recursion (2) with the parameters  $a \equiv b \equiv 0 \pmod{p}$ ,  $(c, p) = (y_0, p) = 1$ . There are exist the polynomial  $F_k(u, v) \in \mathbb{Z}[u, v]$  such that for  $k \geq m + 1$  we have*

$$\begin{aligned} y_k &\equiv F_k(y_0, y_0^{-1}) := A_{0k} + A_{1k}y_0 + B_{1k}y_0^{-1} + \\ &\quad + B_{2k}y_0^{-2} + B_{3k}y_0^{-3} + \dots + B_{m_1k}y_0^{-m_1} \pmod{p^m}, \\ B_{jk} &\equiv 0 \pmod{p^{m_0}}, \quad j \geq 4, \quad m_0 = 2\nu_p(a) + \nu_p(b), \quad m_1 \leq \left\lfloor \frac{m}{\nu_p(a \cdot b)} \right\rfloor, \end{aligned} \quad (3)$$

where the coefficients  $A_{ik}$ ,  $B_{jk}$  defined by the following relations (4) and (5).

*Proof.* By (2) we sequentially infer

$$\begin{aligned} y_1 &\equiv ay_0^{-1} + b + cy_0 \pmod{p^m} \\ y_2 &\equiv \frac{a}{ay_0^{-1} + b + cy_0} + b + c(ay_0^{-1} + b + cy_0) \equiv \\ &\equiv ac^{-1}y_0^{-1}(1 - c^{-1}y_0^{-1}(b + ay_0^{-1}) + c^{-2}y_0^{-2}(b + ay_0^{-1})^2 + \dots + \\ &\quad + b + c(ay_0^{-1} + b + cy_0)) \equiv \\ &\equiv A_{0,2} + A_{1,2}y_0 + B_{1,2}y_0^{-1} + B_{2,2}y_0^{-2} + B_{3,2}y_0^{-3} + \dots, \end{aligned}$$

where modulo  $p^{m_0}$ ,  $m_0 = 2\nu_p(a) + \nu_p(b)$ , we have

$$\begin{aligned} A_{0,2} &= b(1 + c), \quad A_{1,2} = c^2, \quad B_{1,2} = a(c + c^{-1}), \quad B_{2,2} = -abc^{-2}, \\ B_{3,2} &= ab^2c^{-3}, \quad B_{j,2} = 0, \quad j = 4, 5, \dots \end{aligned}$$

Let

$$y_k = A_{0,k} + A_{1,k}y_0 + B_{1,k}y_0^{-1} + B_{2,k}y_0^{-2} + B_{3,k}y_0^{-3} + B_{4,k}y_0^{-4} + \dots$$

Then modulo  $p^{m_0}$

$$\begin{aligned} y_{k+1} &= (b + cA_{0,k}) + cA_{1,k}y_0 + (cB_{1,k} + aA_{1,k}^{-1})y_0^{-1} + \\ &\quad + (cB_{2,k} - aA_{0,k}A_{1,k}^{-2})y_0^{-2} + (cB_{3,k} - aA_{1,k}^{-2}B_{1,k} + aA_{0,k}^{-2}A_{1,k}^{-3})y_0^{-3}. \end{aligned}$$



Hence, after simple calculations we deduce

$$A_{0,3} = b(1 + c + c^2), \quad A_{1,3} = c^3, \quad B_{1,3}a(c^2 + 1 + c^{-2}),$$

$$B_{2,3} = -ab(2c^{-1} + c^{-2}), \quad B_{3,3} = ab^2c^{-2} - a^2c^{-2}(c + c^{-1}) + ab^2c^{-6}(1 + c)^2,$$

and for  $k > 3$

$$\begin{cases} A_{0,k+1} = b \frac{c^{k+1}-1}{c-1}, \quad A_{1,k+1} = c^{k+1}, \quad B_{1,k+1} = a(c^2 + 1) + a(k-1)c^{-k}, \\ B_{2,k+1} = \begin{cases} -abc^{k-3}(2c^{-1} + c^{-2}) + abc^{-2(k-1)} \frac{c^{\lfloor \frac{k+1}{2} \rfloor} - 1}{c-1} & \text{if } c \neq 1, \\ 3ab + 2^{-1}abk & \text{if } c = 1. \end{cases} \end{cases} \quad (4)$$

Similarly,

$$B_{3,k+1} \equiv ac^{-2}(b^2g_1(k) + ag_2(k)) \quad (5)$$

where  $g_1(k), g_2(k) \in \mathbb{Z}[x]$ ,  $g_1(2) = g_2(2) = 0$ .  $\square$

**Corollary 1.** *Let  $\{y_n\}$  be the sequence produced by the recursion (2), moreover,  $\nu_p(b) < \nu_p(a)$ . Then in the assumptions of Proposition 1 for  $k \geq 3$ ,  $k \equiv z \pmod{\delta}$ ,  $0 \leq z \leq \delta - 1$ , where  $\delta$  is an index  $c \pmod{p}$ , we have*

$$y_k \equiv y_0 + kp^{\nu_p(u)+1}H_1(z, y_0, y^{-1}) + k^2p^{\nu_p(au)+1}H_2(z, y_0, y^{-1}) + k^3p^{\nu_p(au)+2} + \dots \pmod{p^m}$$

*Proof.* If  $c \equiv 1 \pmod{p}$  we have for  $p > 3$

$$c^k = (1 + pu)^k \equiv 1 + pa_1k + pa_2k^2 + pa_3k^3 + \dots + p^{\lambda_s}a_s p^s \pmod{p^m},$$

where  $\nu_p(a_j) = j\nu_p(u)$ ,  $j = 1, 2, 3, \dots$ ;

$$\nu_p(a_j) \geq 4\nu_p(u), \quad j = 4, 5, \dots$$

Hence, in this case we find from Proposition 1

$$y_k \equiv y_0 + kp^{\nu_p(u)+1}G_1(y_0, y_0^{-1}) + k^2p^{\nu_p(au)+1}G_2(y_0, y_0^{-1}) + k^3p^{\nu_p(au)+2}G_3(k, y_0, y_0^{-1}) \pmod{p^m}. \quad (6)$$

In the case  $c \not\equiv 1 \pmod{p}$  we denote through  $\delta$  an index of  $c$ ,  $1 < \delta \leq p - 1$ , modulo  $p$ .

Let  $k = \delta\ell + z$ ,  $0 \leq z \leq \delta - 1$ ,  $\ell \equiv k\delta^{-1} + z\delta^{-1} \pmod{p^m}$

$$c^k = (1 + pu)^\ell \cdot c^z = \left(1 + p\ell u + \frac{\ell(\ell-1)}{2}p^2u^2 + \dots\right) c^z,$$

$$c^{-k} \equiv 1 - p\ell u + \left(\ell + \frac{\ell(\ell-1)}{2}p^2u^2 + \dots\right) c^z.$$

And we again obtain the relation a type of (6)

$$y_k \equiv y_0 + kp^{\nu_p(u)+1}G'_1(z, y_0, y_0^{-1}) + k^2p^{\nu_p(au)+1}G'_2(z, y_0, y_0^{-1}) + k^3p^{\nu_p(au)+2}G'_3(z, k, y_0, y_0^{-1}) \pmod{p^m}, \quad (7)$$

where  $G_i, G'_i$  are the polynomials on  $k$  with the coefficients depending on  $y_0, y_0^{-1}, z$ .

The corollary is established.  $\square$



**Corollary 2.** *The period of the sequence  $\{y_n\}$  generated by (2) is equal to  $\tau = p^{m-\nu_p(b)}$  if  $\nu_p(b) < \nu_p(a)$ .*

Indeed, from (4), (5)

$$\begin{cases} A_{j,k+3} \equiv A_{j,3} \pmod{p^m}, \\ B_{j,k+3} \equiv B_{j,3} \pmod{p^m}, \\ j = 0, 1, 2, 3, \dots \end{cases}$$

if and only if  $k \equiv 0 \pmod{p^{m-\nu_p(b)}}$ .

### 3 Main results

First in this section we prove the Theorems 1-3 on the estimate of exponential sums of the sequences of PRN's  $\{y_n\}$  generated by recursion (2).

**Theorem 1.** *Let  $(h_1, h_2, p) = 1$ ,  $\nu_p(h_1 + h_2) = \alpha$ ,  $\nu_p(h_1k + h_2\ell) = \beta$  and let  $\{y_n\}$  be produced by (2). The the following estimates*

$$\left| \sum_{y_0 \in \mathbb{Z}_p^*} e_{p^m}(h_1y_\ell + h_2y_k) \right| \leq \begin{cases} 0 & \text{if } \alpha < \beta + \nu_p(b), \\ & m - \alpha - \beta > 0, \\ 2p^{\frac{m+\beta+\nu_p(b)}{2}} & \text{if } \alpha \geq \gamma + \nu_p(b), \\ & m - \alpha - \beta > 0, \\ p^{m-1}(p-1) & \text{in otherwise} \end{cases}$$

hold.

*Proof.* For  $0 \leq k, \ell < \tau = p^{m-\nu_p(b)}$  we have for  $c \neq 1$ :

$$h_1y_k + h_2y_\ell = B_0 + B_1y_0 + B_{-1}y_0^{-1} + B_{-2}y_0^{-2} + p^{\nu_0}H(y_0, y_0^{-1}),$$

where

$$\begin{aligned} B_1 &= b \left( \frac{h_1c^k + h_2c^\ell}{c-1} \right), \\ B_{-1} &= a(h_1 - h_2)(c^2 - 1) + a[(kh_1c^k + lh_2c^\ell) - (h_1c^k + h_2c^\ell)], \\ B_{-2} &= -ab(2c^{-1} + c^{-2})(h_1c^{k-1} + h_2c^{\ell-1}) + \\ &\quad + abc^2 \frac{h_1c^{k_1} + h_2c^{\ell_1} - (h_1c^{k_2} + h_2c^{\ell_2})}{c-1}, \\ \nu_0 &= \min(\nu_p(ab^2), \nu_p(a^2)). \end{aligned}$$

Substituting  $c^k$  and  $c^\ell$  by the polynomials on  $k$  or  $\ell$  and applying Lemma 1 we deduce the statement of the theorem.  $\square$

The case  $c = 1$  gives the same result.

**Theorem 2.** *Let a linear-inversive generator (2) generates the sequence of PRN's  $\{y_n\}$ . Then for  $N \leq \tau = p^{m-\nu_p(b)}$  we have the following bounds*

$$\left| \sum_{n=0}^{N-1} e_{p^m}(hy_n) \right| \ll \begin{cases} m & \text{if } m > \nu_p(bh), \\ p^{\frac{m+\nu_p(b)}{2}} \left( \frac{N}{\tau} + \log \tau \right) & \text{if } \nu_p(bh) < m, \\ N & \text{otherwise.} \end{cases}$$



This assertion follows from Corollary 1 and Lemma 1.

**Theorem 3.** *Let the sequence  $\{y_n\}$  be generated by (2) with parameters  $a, b, c, y_0, (y_0, p) = (c, p) = 1$  and  $\nu_p(a) > \nu_p(b) = \alpha \geq 1$ . Then for every  $h \in \mathbb{Z}$ ,  $\nu_p(h) = s$ , we have*

$$\frac{1}{\varphi(p^m)} \sum_{y_0 \in \mathbb{Z}_{p^m}^*} \left| \sum_{n=0}^{N-1} e_{p^m}(hy_n) \right| \ll N^{\frac{1}{2}} + Np^{-\frac{m-1}{2}}.$$

In order to prove this theorem it is sufficiently to apply the schema of argument from the proof of theorem 3 in [8].

Now, taking into account that equidistribution and statistical independency (unpredictability) properties of the uniform PRN's can be analyzed on the discrepancy of certain point sets in  $[0, 1)^s$  we state from the Theorems 2 and 3 and Lemma 3 the following statement:

**Theorem 4.** *Let  $\{y_n\}$  generated by (2) with  $(y_0, p) = (c, p) = 1$ ,  $\nu_p(a) > \nu_p(b) \leq 1$ . Then for the sequence  $\{x_n\}$ ,  $y_n = \frac{x_n}{p^m}$  we have*

$$D_N(x_0, x_1, \dots, x_{N-1}) \leq \frac{1}{p^m} + 2N^{-1}p^{\frac{m-\nu_p(b)}{2}} \left( \frac{1}{p} \left( \frac{2}{\pi} \log p^m + \frac{7}{5} \right)^2 + 1 \right).$$

Moreover, for almost all  $y_0 \in \mathbb{Z}_{p^m}$

$$D_N(y_0, x_0, x_1, \dots, x_{N-1}) \leq \frac{1}{p^m} + 3N^{\frac{1}{2}}p^{-\frac{m-\nu_p(b)}{4}} \log p^m.$$

So, the linear-inversive congruential generator (2) produces the sequences of PRN's  $\{x_n\}$  that involve the properties of equidistribution and unpredictability.

## References

- 1.W. S. Chou. The period lengths of inversive congruential recursions. *Acta Arith.*, 73(4):325–341, 1995.
- 2.J. Eichenauer, J. Lehn. A non-linear congruential pseudorandom number generator. *Statist. Hefte*, 27:315–326, 1986.
- 3.T. Kato, L.-M. Wu and N. Yanagihara. On a nonlinear congruential pseudorandom number generator. *Math. of Comp.*, 65(213):227–233, 1996.
- 4.H. Niederreiter. Recent trends in random number and random vector generation. *Ann. Oper. Res.*, 31:323–345, 1991.
- 5.H. Niederreiter. Random Number Generation and Quasi-Monte Carlo Methods. *SIAM, Philadelphia, Pa.*, 1992.
- 6.H. Niederreiter, I. Shparlinski. Exponential sums and the distribution of inversive congruential pseudorandom numbers with prime-power modulus. *Acta Arith.*, 90(1):89–98, 2000.
- 7.P. Varbanets, S. Varbanets. Exponential sums on the sequences of inversive congruential pseudorandom numbers with prime-power modulus, *Voronoi's Impact on Modern Science, Proc. of IV Intern. Conf. on Anal. Number Theory and Spatial Tessellations, Kyiv*, 4(1):112–130, 2008.



- 8.P. Varbanets, S. Varbanets. Generalizations of Inversive Congruential Generator.  
*Analytic and Probabilistic Methods in Number Theory, Proc. Fifth. International  
Conference in Honour of J. Kubilius, Palanga, Lithuania, 04-10 September 2011,*  
17:265-282, 2012.

